Nanometre-scale organization of the Natural Killer cell receptors KIR2DL1 and KIR2DS1 and its implications for signalling.

A thesis submitted to the University of Manchester for the degree of Doctor of Philosophy in the Faculty of Life Sciences

2016

Anna Oszmiana

Faculty of Life Sciences

The University of Manchester

Contents

Word count

62,877 words; excluding bibliography

List of figures

List of tables

Abbreviations

AA	an individual carrying only A KIR haplotypes
AB	an individual carrying A and B KIR haplotypes
A/D	analog to digital conversion
ADCC	antibody-dependent cellular cytotoxicity
AIDS	acquired immunodeficiency syndrome
APC	antigen presenting cell
ATP	adenosine triphosphate
BAT3	HLA-B-associated transcript 3
BB	an individual carrying only A KIR haplotypes
BCG	bacillus Calmette-Guérin
BSA	bovine serum albumin
CCL	C-C chemokine ligand
CMLE	classic maximum likelihood estimation
CTL	cytotoxic T lymphocyte
DAP	DNAX activation protein
DMEM	Dulbecco's Modified Eagle Medium
DC	dendritic cell
DMSO	dimethyl sulfoxide
DNA	deoxyribonucleic acid
dSTORM	direct STORM
EMCCD	electron-multiplying charge-coupled device
ERK	extracellular signal-regulated kinase
f-actin	filamentous actin
FBS	fetal bovine serum
Fc	fragment crystallisable region
FcR	Fc receptor
FCS	fluorescence correlation spectroscopy
FLIM	fluorescence lifetime imaging
FRET	Förster resonance energy transfer
Grb2	growth factor receptor-bound protein 2
GFP	green fluorescence protein
GM-CSF	granulocyte-macrophage colony-stimulating factor
GSDIM	ground-state depletion with individual molecule return
HA	hemagglutinin

HCMV	human cytomegalovirus
hESC	human embryonic stem cells
HIV	human immunodeficiency virus
HLA	human leukocyte antigen
HLA-C1	human leukocyte antigen C with asparagine at position 80
HLA-C2	human leukocyte antigen C with lysine at position 80
HSCT	hematopoietic stem cell transplantation
HN	hemagglutinin neuraminidase
HUGO	Human Genome Organization
ICAM	intercellular cell adhesion molecule
IFN	interferon
Ig	immunoglobulin
IL-	interleukin
IL-2Rα	interleukin 2 receptor subunit α
IQR	interquartile range
IRM	interference reflection microscopy
ITAM	immune tyrosine-based activating motif
ITIM	immune tyrosine-based inhibitory motif
KIR	killer-cell immunoglobulin-like receptor
KLRG1	killer-cell lectin like receptor G1
LAIR	leukocyte-associated immunoglobulin-like receptor
LAT	linker for activation of T cells
Lck	lymphocyte-specific protein tyrosine kinase
LD	linkage disequilibrium
LDL	low-density lipoprotein
LFA	lymphocyte function-associated antigen
LILR	leukocyte immunoglobulin-like receptor
LPS	lipopolysaccharide
mAb	monoclonal antibody
MAPK	mitogen-activated protein kinase
MEK	mitogen-activated or extracellular signal-regulated protein kinase kinase
MEM	Minimum Essential Medium
MHC	major histocompatibility complex
MIC	MHC class I chain-related
MTOC	microtubule organizing centre
NA	numerical aperture

NCR	natural cytoxicity receptors (of the family NKp30/NKp46/NKp44)
NHS	N-hydroxysuccinimide
NK	natural killer
NKAT	NK-associated transcript
NKG2D	NK group 2 member D
NOD	non-obese diabetic
NTAL	non-T cell activation linker
PAK1	p21-activated kinase 1
PALM	photoactivated localization microscopy
PLL	poly-L-lysine
PBMC	peripheral blood mononuclear cells
PBS	phosphate-buffered saline
PCR	polymerase chain reaction
PCNA	proliferating cell nuclear antigen
PFA	paraformaldehyde
PI3K	phosphoinositide 3-kinase
pMHC	peptide –MHC complex
PRR2	poliovirus receptor-related 2
PSF	point spread function
pY	phosphotyrosine
PVR	poliovirus receptor
RAG	recombination-activating gene
RPMI	Roswell Park Memorial Institute 1640 media
SD	standard deviation
SAP	SLAM-associated protein
SH	Src homology
SHIP	SH2 domain–containing inositol 5′ phosphatase
SHP	SH2 domain-containing tyrosine phosphatase
SLAM	signalling lymphocyte activation molecule
SLE	systemic lupus erythematosus
SLP-76	SH2 domain-containing leukocyte protein of 76 kD
SMAC	supramolecular activation cluster
STAT	signal transducer and activator of transcription 1
STED	stimulated emission depletion
STORM	stochastic optical reconstruction microscopy
Syk	spleen tyrosine kinase

TAP	transporter associated with antigen presentation
TCR	T cell receptor
TIGIT	T cell immunoreceptor with immunoglobulin and ITIM domains
TIRF	total internal reflection fluorescence
TNF	tumour necrosis factor
TRAIL	tumour necrosis factor-related apoptosis-inducing ligand
ULBP	UL-16 binding proteins
WT	wild-type
ZAP-70	ζ-associated protein kinase of 70 kD

The University of Manchester

Anna Oszmiana

Doctor of Philosophy

Nanometre-scale organization of the Natural Killer cell receptors KIR2DL1 and KIR2DS1 and its implications for signalling.

2016

Summary

Human Natural Killer (NK) cells are regulated by a variety of germ-line encoded activating and inhibitory receptors. Broadly, activating receptors detect ligands that are expressed or up-regulated on cancerous or infected cells, while inhibitory receptors bind self-molecules to induce tolerance against healthy cells. Highly homologous pairs of activating and inhibitory receptors are also expressed on NK cells, including Killer Ig-like Receptors KIR2DL1 and KIR2DS1, which bind the same ligands, class I MHC proteins from the C2 group. Here, two super-resolution microscopy techniques, stimulated emission depletion (STED) and ground state depletion microscopy followed by individual molecule return (GSDIM) were used to examine the nanometre-scale organization of KIR2DL1 and KIR2DS1, as well as molecules engaged in their signalling.

Both receptors were observed to constitutively assemble in nanometre-scale clusters at the surface of NK cells but displayed differential patterns of clustering - the activating receptor KIR2DS1 formed nanoclusters 2.3-fold larger than its inhibitory counterpart KIR2DL1. Site-directed mutagenesis established that the size of nanoclusters was controlled by transmembrane amino-acid 233, a lysine in KIR2DS1. Mutated variant of KIR2DS1 in which lysine 233 was substituted with alanine formed significantly smaller clusters than the wild-type KIR2DS1. Reciprocally, substitution of isoleucine found at position 233 in KIR2DL1 sequence with lysine resulted in the receptor assembling into larger clusters.

Super-resolution microscopy also revealed two ways in which KIR nanoclusters impact signalling. First, KIR2DS1 and DAP12 nanoclusters were juxtaposed in the resting-cell state but coalesced upon receptor ligation. Second, quantitative super-resolution microscopy revealed that membrane-proximal clusters of the kinase ZAP-70 or phosphatase SHP-1, as well as their phosphorylated active forms, were more often found in contact with larger KIR nanoclusters.

Together, this work has established that size of KIR nanoclusters depends on the transmembrane sequence and impacts downstream signalling.

Declaration

No portion of the work referred to in the thesis has been submitted in support of an application for another degree or qualification of this or any other university or other institute of learning.

The data presented in this thesis are my own work, with the following exceptions described below.

- The NKL/KIR2DL1-HA, NKL-KIR2DS1-HA, NKL/KIR2DL1-HA/KIR2DS1-FLAG and NKL/KIR2DL1-FLAG/KIR2DS1-HA cell lines and the retroviral vectors pIB2-KIR2DL1*002-HA and pIB2-KIR2DS1*00502-HA were kind gifts from Dr Shaun-Paul Cordoba and were created by him in our laboratory at Imperial College London.
- In Chapter 3, testing of the expanded human NK cell populations for the presence of the receptors KIR2DS1 and KIR2DL1 was performed in our laboratory at the University of Manchester by Kevin Stacey and Philippa Kennedy.
- In Chapters 3 – 5, David J. Williamson wrote the custom MATLAB scripts used for the super-resolution data analysis.

Copyright statement

i. The author of this thesis (including any appendices and/or schedules to this thesis) owns certain copyright or related rights in it (the “Copyright”) and s/he has given The University of Manchester certain rights to use such Copyright, including for administrative purposes.

ii. Copies of this thesis, either in full or in extracts and whether in hard or electronic copy, may be made only in accordance with the Copyright, Designs and Patents Act 1988 (as amended) and regulations issued under it or, where appropriate, in accordance with licensing agreements which the University has from time to time. This page must form part of any such copies made.

iii. The ownership of certain Copyright, patents, designs, trade marks and other intellectual property (the “Intellectual Property”) and any reproductions of copyright works in the thesis, for example graphs and tables (“Reproductions”), which may be described in this thesis, may not be owned by the author and may be owned by third parties. Such Intellectual Property and Reproductions cannot and must not be made available for use without the prior written permission of the owner(s) of the relevant Intellectual Property and/or Reproductions.

iv. Further information on the conditions under which disclosure, publication and commercialisation of this thesis, the Copyright and any Intellectual Property University IP Policy (see http://documents.manchester.ac.uk/display.aspx?DocID=24420), in any relevant Thesis restriction declarations deposited in the University Library, The University Library’s regulations (see http://www.library.manchester.ac.uk/about/regulations/) and in The University’s policy on Presentation of Theses.

Publications

- **Oszmiana, A**., Williamson, D. J., Cordoba, S. P., Morgan, D. J., Stacey, K. & Davis, D. M. The size of activating and inhibitory Killer Ig-like Receptor nanoclusters is controlled by the transmembrane sequence and impacts signaling. *Manuscript Submitted*.

- Lagrue, K., Carisey, A., **Oszmiana, A**., Kennedy, P. R., Williamson, D. J., Cartwright, A., Barthen, C. & Davis, D. M. 2013. The central role of the cytoskeleton in mechanisms and functions of the NK cell immune synapse. *Immunol Rev,* 256**,** 203-21.

- Pageon, S. V., Cordoba, S. P., Owen, D. M., Rothery, S. M., **Oszmiana, A.** & Davis, D. M. 2013. Superresolution microscopy reveals nanometer-scale reorganization of inhibitory natural killer cell receptors upon activation of NKG2D. *Sci Signal,* 6**,** ra62.

Acknowledgements

I would like to thank my supervisor, Professor Dan Davis, who has not only dedicated his time and energy to direct me throughout this project, but has also been extremely supportive and patient with my progress.

I would also like to thank the members of the Davis laboratory for their advice and constructive discussions, especially to David J. Williamson who has patiently guided me through the confusing world of single-molecule localisation data analysis. I am also grateful to Dominika Rudnicka and Shaun-Paul Cordoba who mentored me at the beginning of my PhD studies, to Pippa Kennedy who always offered a great advice about this project and provided me with excellent assistance during some of the experiments and to Alex Carisey who always found time to help me to improve and troubleshoot experiments. I would also like to acknowledge Kevin Stacey and David Morgan for their invaluable help with some of this work. I am also grateful to Adam Cartwright, Kathryn Lagrue, Mezida Bedru-Saed and Katja Srpan for being amazing friends during the long hours spent in the lab and also outside work.

Thank you to my co-supervisor and advisor, Professor Tracy Hussell, who was a great source of outside opinion and valuable advice throughout this project. I would also like to thank those within the Manchester Collaborative Centre for Inflammation Research and Faculty of Life Sciences who have offered their advice on this project, as part of internal assessments and other meetings.

I could never complete this PhD without the support from all my friends and family. Thank you to my parents, Izabela and Andrzej, and my sister Kasia, who made me believe that nothing is ever too difficult or impossible.

And finally, I would like to thank my amazing boyfriend Shoumit, for his support, patience and understanding. He was always there for me and always pulled me back when I was falling down. Thanks for having faith in me when I no longer had any faith in myself. I would never get this far without him.

Chapter 1: Introduction

1.1 Natural Killer cells and their medical importance

1.1.1 'Natural' cytotoxicity

In 1975, Kiessling *et al*. described cells isolated from spleens of unimmunized mice which demonstrated significant lysis of the tumour cells *ex vivo* [1]. Before this date, the term cytotoxicity was used to describe phagocytosis, antibody-dependent cellular cytotoxicity (ADCC) mediated by a mixed population of cell types and T cell responses, which were slow-starting and created long-lasting memory. Interestingly, cells described by Kiessling killed in a way independent of the known modes of cytotoxicity, presenting a rapid response which did not rely on pre-stimulation or presence of antibodies. In the same year, splenic cells from athymic nude mice with the same properties were described by Herberman *et al.* [2]. This new way of killing was named 'natural' cytotoxicity and the newly described lymphocyte subset 'natural killer' cells.

Today we know that natural killer (NK) cells are a distinct lineage developing from the common lymphoid progenitor in the bone marrow [3] and from committed NK precursors at other sites, as reviewed by Huntington *et al.* [4]. They are large granular lymphocytes comprising 5 – 15% of peripheral white blood cells [5] which are phenotypically defined by an absence of CD3 (a T-cell co-receptor) and expression of CD56 (an isoform of neural cell adhesion molecule) and NKp46, a member of natural cytotoxicity receptor (NCR) family [6, 7].

1.1.2 NK cells in various disease states

NK cells have diverse biological functions of which the best characterized one is to eliminate infected and malignant cells. Circulating NK cells are mostly in a resting state but activation by cytokines leads to their infiltration into tissues to screen for target cells with abnormal phenotype [8, 9]. Examples of the NK cells role in different medical conditions are presented in Table 1.1.

In immunity against viruses, their crucial role is evidenced by the reports of complete NK cell deficiencies in humans, each resulting in fatal infections developed during childhood [10]. Other evidence includes reports of decreased expression of activation-associated receptors, as well as compromised cytolytic function and cytokine production of NK cells observed in all groups of viral hepatitis [11]. The role of NK cells

in fighting human immunodeficiency virus (HIV), influenza virus, flaviviruses, cytomegalovirus and other viral infections has also been documented by multiple studies [12-18].

In addition to early control of infections, a large body of work proved that NK cells possess the capacity to recognize and kill tumour cells *in vitro* and serve to prevent growth and metastasis of certain tumours *in vivo* (reviewed in [19-21]). Most of the *in vivo* studies were performed by implanting syngeneic tumour cells in mice genetically deficient in NK cell function or depleted of NK cells by the administration of antibodies. In such models eliminating of NK cells often led to more aggressive tumour growth and metastasis. However, in most cases direct involvement of NK cells could not be clearly dissected, since genetic defects or administered antibodies did not exclusively target NK cells [20, 22, 23]. In an alternative approach, Schreiber and colleagues examined spontaneous and chemical carcinogen-induced tumour formation in mice combining deficiency specifically abrogating T cells (recombination-activating gene 2; RAG2 deficiency) with deficiency for signal transducer and activator of transcription 1 (STAT1), an important signal transducer of type I and type II interferon (IFN) receptors. Since NK cells share employment of these effectors with cytotoxic T cells, such setup allowed a more direct assessment of the NK cell contribution to tumour surveillance. Mice deficient for both RAG2 and STAT1 spontaneously developed adenocarcinoma at higher rates, as compared with mice deficient only for RAG2, thus implicating NK cells in tumour growth control [24]. In humans, most evidence for a role of NK cells in tumour surveillance comes from correlative studies, such as an epidemiologic survey of 11-year follow-up which showed a link between low NK cell activity in peripheral blood and increased cancer risk in adults [25].

As potent killers, NK cells have the potential to also harm the host and induce autoimmunity. In transgenic non-obese diabetic (NOD) mouse models of accelerated type 1 diabetes, depletion of NK cells was shown to substantially inhibit diabetes development [26, 27]. In human type 1 diabetes data are still sparse, although NK cells are thought to mediate pancreatic islet inflammation [28], and alterations in the NK cell phenotype at the onset of the disease or after long-term hyperglycemia have been observed [28].

On the other hand, NK cells seem to play a protective or disease controlling role in systemic lupus erythematosus (SLE). SLE patients show a moderate reduction of NK cell numbers [29, 30] and NK cells in these patients have a reduced cytotoxic activity [31, 32]. This defects of NK cells are associated with clinical conditions such as nephritis (inflammation of the kidneys) during SLE [30]. Therefore, in case of

autoimmune diseases, NK cells can be either disease-controlling or disease-enhancing.

Table 1.1 Role of NK cells in selected diseases

Type of disease	Examples	Role of NK cells	Possible therapeutic approaches
Viral infections	Hepatitis [11, 33], influenza [14, 15] HIV [12, 13], flaviviruses [16, 17], cytomegalovirus [18]	Immuno-surveillance, early control of infection [13, 14, 16-18]	Adoptive NK cell transfer, HIV-specific chimeric antigen receptors, enhancement of NK cell activation with cytokines, antibody tailoring for ADCC, hESC- and iPSC-derived NK cells transfer* [34-36]
Cancer	B cell lymphomas [37], hepatocarcinoma [34], colorectal cancer [38], neuroblastoma [39]	Immuno-surveillance, prevention of tumour growth and metastasis [19-21, 24, 25]	Adoptive NK cell transfer, NK activating gene therapy, chimeric antigen receptors, enhancement of NK cell activation with cytokines, ADCC , hESC- and iPSC-derived NK cells transfer* [19, 23, 34, 37, 40, 41]
Autoimmune conditions	Type 1 diabetes [26-28], systemic lupus erythematosus [29-32]	Not well established, might be disease controlling or enhancing [26-32]	Targeting NKp46 receptor to reduce destruction of pancreatic cells [42]

*hESC – human embryonic stem cells, iPSC – induced pluripotent stem cells

1.2 Effector functions of NK cells

The population of human NK cells is heterogeneous, both phenotypically and functionally. The majority of human NK cells found in blood have low surface density or 'dim' expression of CD56 and express higher levels of a low-affinity receptor for the constant region of immunoglobulin (Ig) G, FcγRIII (CD16). These cells display significantly higher cytolytic capacity against tumour targets [43], while having lesser activity to produce cytokines in response to activation [44]. In contrast, NK cells with high surface density of CD56 ($CD56^{bright}$) can secrete abundant amounts of cytokines and chemokines when activated [44], but are less cytotoxic [43]. Approximately 10% of circulating NK cells [43] and nearly all found in secondary lymphoid tissue [45] have a $CD56^{bright}$ and $CD16^{dim/neg}$ phenotype.

1.2.1 Cytotoxicity

Upon encountering of a target cell, NK cell forms an immune synapse. This specialized interface has been first described in the context of the helper T cell-antigen presenting cell (APC) contact [46] and its role in the cytolytic function of NK cells and cytotoxic T lymphocytes (CTL) was identified soon after that [47, 48].

Upon formation of an immune synapse, NK cells and CTL screen the target cell surface for the presence of specific ligands [47]. If a dominant activation signal is received, a multi-step cytotoxic response is initiated, as illustrated in the Figure 1.1. CTL and NK cell first respond by polarization of perforin and granzyme-containing granules to the immune synapse [49, 50]. In both cell types this is executed by first granules converging upon the microtubule organizing centre (MTOC) and then polarization of both to the synapse [51, 52].

The NK cell plasma membrane is supported by a dense actin meshwork. Cortical actin cytoskeleton is thought to constitute a physical barrier between the granules and the target cell, which has to undergo significant rearrangements to facilitate release of the granules into the target cell. This was first believed to be a complete clearance of actin from the lytic synapse area [53, 54]. However, more recent studies, an in particular application of super-resolution microscopy to study the NK cell synapse, helped to establish that upon activation actin mesh persists at the contact site, but is remodelled to create holes big enough for the granules to penetrate [55, 56].

NK cell lytic granules have been suggested to use two modes of fusion with the membrane: complete and incomplete. These distinct modes have been resolved by Liu

et al. who utilized fluorescent tagging of the two proteins present within the lytic granules. First, Fas ligand, a transmembrane protein contributing to NK cell- and CTL-mediated cytotoxicity was fused to pHluorin, a variant of the green fluorescence protein (GFP) whose fluorescence is restricted in acidic conditions i.e. inside the lytic granules. Second, granzyme B, a granule cargo protein, was tagged with red fluorescent protein (DsRed) [57]. During complete fusion, granule content is completely discharged and the contents diffuse rapidly at the plasma membrane, as visualised by a bright cloud of fluorescence dispersing within the membrane. During incomplete fusion, a transient fusion pore is formed at the plasma membrane and some granules content is released while most of it is retained, which can be seen as transient increase in fluorescence intensity in both the green and red channel within the synapse plane and limited diffusion of granules components within the plasma membrane [57]. The exact significance of these alternate forms of granule fusion in NK cells remains poorly understood. It has been proposed that incomplete fusion could facilitate a rapid killing of multiple targets through the recycling of granule contents. On the other hand, the sustained presence of the contents of fused granules at the synaptic membrane might serve other purposes, e.g. protecting the NK cell from cytotoxicity-induced suicide. In line with this, HeLa and 721.221 cells stably overexpressing CD107a, a protein often used as a degranulation marker, on their surface were reported to be more resistant to the NK cell–mediated killing, as compared with the control-transfected cells [58].

It is thought that target cell lysis is mainly caused by the apoptosis-triggering granzymes which enter the target cell cytosol through pores formed by perforin [59] or via endocytosis [60]. In an alternative pathway, binding of death receptors (e.g. Fas/CD95) on target cells with their equivalent ligands such as Fas ligand and tumour necrosis factor-related apoptosis-inducing ligand (TRAIL) on NK cells takes place, resulting in caspase-dependent apoptosis [61, 62].

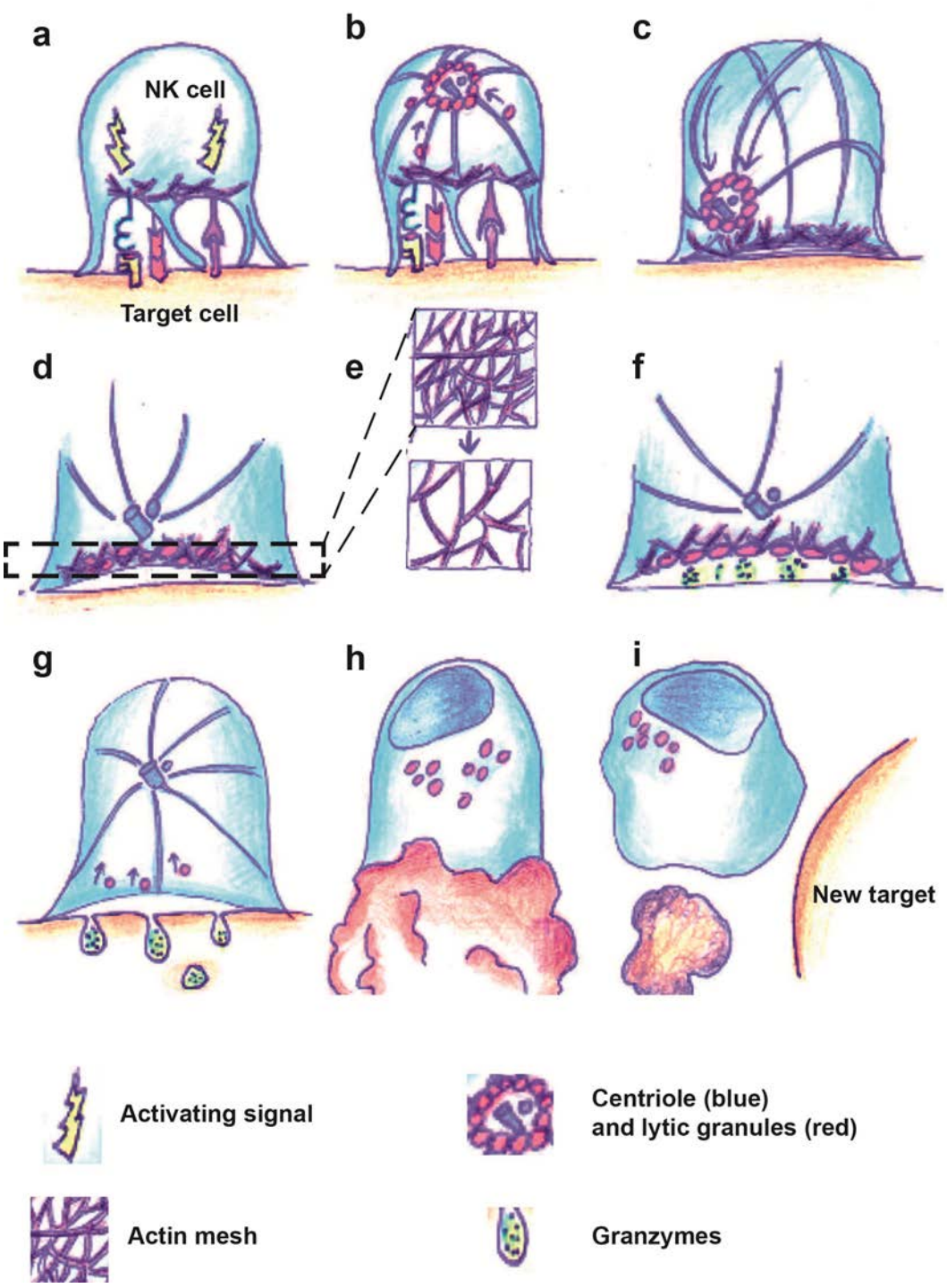

Figure 1.1 NK cell-mediated cytotoxicity
If upon encountering of a target cell by an NK cell a dominant activating signal is received (a), lytic granules converge around the MTOC (b) and both structures polarize towards the immune synapse (c). To allow the lytic granules to be released, cortical actin skeleton is remodelled at the immune synapse (d). En face view of the actin mesh opening is shown in (e). In the next step, contents of the lytic granules, including granzymes, are released into the synapse (f) and delivered to the target cell (g), resulting in the target cell death (h). The NK cell detaches from the dead target and proceeds to survey another target cell (i).

1.2.2 Cytokines secretion

Apart from lysis of aberrant cells, NK cells contribute to regulation of immune responses by secretion of pro-inflammatory and immunoregulatory cytokines and chemokines. The character of cytokine response was shown to be regulated by the type of stimulation received by an NK cell. Specifically, recognition of cancer cell or insect cell opsonised with antibodies against NK cell activating receptors by resting human NK cells induced secretion of a pro-inflammatory cytokine profile, characterized by C-C chemokine ligand (CCL)-3, CCL-4, CCL-5, tumour necrosis factor (TNF)-α, and IFN-γ secretion [63]. In such setting, the authors did not detect secretion of immunoregulatory cytokines, such as interleukin (IL)-5, IL-10, IL-13, or granulocyte-macrophage colony-stimulating factor (GM-CSF), which were more often reported to be secreted by NK cells upon stimulation with exogenous cytokines [64, 65].

Secretion of pro-inflammatory cytokines is yet another way in which NK cells contribute to the destruction of tumour cells. In a murine model, IFN-γ produced by NK cells is involved in eliminating of methylcholanthrene-induced tumour metastases and sarcoma [66]. Additionally, in combination with CD40 engagement, IFN-γ and TNF-α play a role in the stimulation of dendritic cells (DCs), which in turn secrete IL-12 [67, 68]. This crosstalk of NK cells with DCs helps to initiate and maintain an efficient T cell-mediated anti-tumour response [69].

1.2.3 Hierarchy of distinct effector responses

Importantly, although $CD56^{bright}$ NK cells are seen as the major source of cytokines and $CD56^{dim}$ NK cells are referred to as a subset specialized in cytotoxicity, $CD56^{dim}$ NK cells can also secrete pro-inflammatory cytokines in response to tumour cell lines [63, 70]. Interestingly, distinct responses of $CD56^{dim}$ NK cells were reported to be graded according to the relative expression of ligands for activating receptors. Specifically, chemokine production by resting primary human NK cells could be observed readily upon interaction with *Drosophila* insect cell line S2 transfected with at least one ligand for NK cell activating receptor, while degranulation response required stronger stimulation by cells co-expressing two different activating ligands. Finally, TNF-α and IFN-γ production was associated with the highest activation threshold and was significantly upregulated only upon interaction with S2 cells co-transfected with two activating ligands and intercellular cell adhesion molecule (ICAM)-1 [63]. This suggests that within the range of $CD56^{dim}$ NK cells responses, induction of TNF-α and IFN-γ is the most stringently controlled, with a greater requirement for receptor cooperation.

1.3 Regulation of the NK cell functions

Sharing a common early progenitor [3], NK cells display many similarities to other lymphocyte lineages, and in particular their response to activating signals is reminiscent of this of CTL. The most crucial difference between CTL and NK cells are their receptors. The T cell receptor (TCR) genes in somatic cells are assembled from a pool of discontinuous gene segments by genetic recombination machinery, which underlies a great diversity of TCR repertoire. The total αβ TCR diversity in the blood has been estimated as at least 25×10^6 different TCRs [71]. In contrast, activity of NK cells is governed by germline-encoded receptors which recognise conserved patterns on diseased cells. The frequency of NK cells with the same receptor for a specific ligand is higher than the frequency of T cells possessing TCR with the same specificity. As a consequence, NK cells do not need to proliferate as much as T cells to produce an effective immune response. This allows them act to more rapidly, the feature for which they have been first identified.

1.3.1 'Missing self' hypothesis – a model of innate recognition

Another important difference between NK cell- and T cell-mediated cytotoxicity has led to what was arguably the biggest break-through in the NK cell research after their initial discovery. Klas Kärre, working under the supervision of Rolf Kiessling, noticed that cells which often escaped killing by T cells were readily killed by NK cells. He realized that while T cells recognition of aberrant cells relies on the presence of major histocompatibility complex (MHC) molecules on the target cell surface, NK cells are the most efficient at killing when these proteins are absent [72].

A few years later, in 1990, Kärre published an important article in which he named his idea the 'missing self' hypothesis [73]. This hypothesis proposed that upon encountering a cell that has self-MHC at the surface NK cell receives a signal to not kill, but if this 'self' is missing - the cytotoxicity is triggered. The question provoked by this was how an NK cell can sense whether a normal molecule is missing and the most likely answer was that NK cells must possess receptors on their surface that survey other cells for the presence of the self-MHC. A search for 'missing self' receptor was started and soon after that an inhibitory receptor to self-MHC Ly49 was discovered in mice. This important discovery was made by the research group led by Wayne Yokoyama, who separated NK cells according to the expression of Ly49 and noticed that $Ly49^+$ cells did not lyse target cells which were efficiently killed by $Ly49^-$ cells. This resistance to NK cell-mediated killing correlated with expression of MHC class

l antigens on target cells [74]. Inhibitory receptors to self-MHC in humans were discovered later, almost at the same time by two research groups [75, 76].

1.3.2 Updated model – a role for activating receptors

It quickly became clear that although discovery of receptors mediating MHC-dependent protection from NK cell killing supported Kärre's original theory about NK cell recognition of target cells, NK cells also possess activating receptors which can trigger cytotoxicity in the absence of inhibition [77, 78]. We now know that a great diversity of activating receptors allows NK cells to recognize a broad spectrum of ligands associated with different states of disease. Overall, the modern view of NK cell recognition is that they integrate both the activating and inhibitory signals they receive and the balance of signals must favour activation for a response to occur. Current view of the NK cells regulation is illustrated in the Figure 1.2 and selected NK cell receptors and their ligands are summarized in the Table 1.2.

Table 1.2 Selected NK cell receptors and their ligands.

Receptor	Type of signal	Known ligands	References
NKp46	activating	HN of the Sendai virus, HA of influenza virus	[79, 80]
NKp44	activating	HN of the Newcastle disease virus, PCNA	[81, 82]
NKp30	activating	CMV pp65, BAT3, B7-H6	[83-85]
NKG2D	activating	MICA, MICB, ULBP1-6	[86-89]
CD16	activating	Human IgG	[90]
2B4	activating/inhibitory	CD48	[91]
CD94/NKG2C	activating	HLA-E	[92]
CD94/NKG2A	inhibitory	HLA-E	[92, 93]
DNAM-1	activating	PVR, PRR2	[94]
TIGIT	inhibitory	PVR, PRR2	[95]
CD96	activating/inhibitory	PVR	[96]

Activating KIR i.e. KIR2DS1	activating	MHC class I	[97]
Inhibitory KIR i.e. KIR2DL1	inhibitory	MHC class I	[75, 76]
Activating LILR i.e. ILT1	activating	MHC class I	[98]
Inhibitory LILR i.e. ILT2	inhibitory	MHC class I	[98, 99]
NKR-P1	inhibitory	LLT1	[100]
KLRG1	inhibitory	cadherin	[101]
LAIR-1	inhibitory	collagen	[102]

1.3.3 Inhibitory receptors

Numerous inhibitory receptors have been identified, representing a significant heterogeneity in terms of structure and ligand specificity. We now know that different individuals can possess completely different receptor repertoires and NK cells from one person can carry multiple different combinations of inhibitory receptors [103].

MHC-specific inhibitory receptors expressed in human NK cells include killer immunoglobulin-like receptors (KIR), which recognise classical MHC class I proteins - human leukocyte antigen (HLA)-A, -B, -C [75, 76], the CD94/NKG2 dimers, which ligate the non-classical MHC class I protein HLA-E [92, 104] and leukocyte immunoglobulin-like receptors (LILRs) which bind to a range of classical and non-classical MHC class I molecules [98, 105, 106]. In addition, a number of inhibitory receptors binding non-MHC ligands have been described in subsets of human NK cells. This includes killer-cell lectin like receptor G1 (KLRG1) which binds members of the classical cadherin family [101], NKR-P1 which binds related molecule lectin-like transcript 1 [100] and leukocyte-associated immunoglobulin-like receptor (LAIR)-1 recognizing collagen [102].

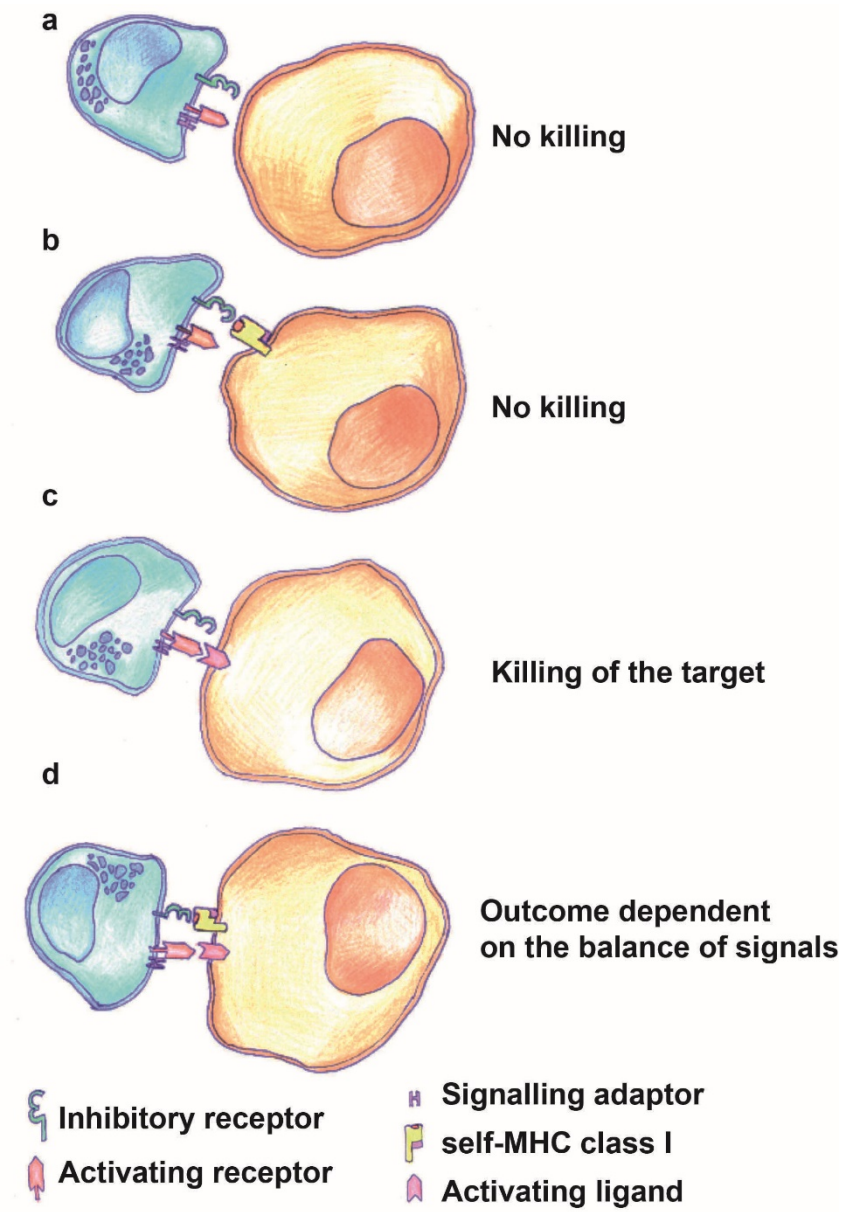

Figure 1.2 Regulation of NK cell-mediated cytotoxicity

For each target cell, a decision whether this particular cells is killed or spared is based on the signals from multiple activating and inhibitory receptors. Lack of both the inhibitory (self-MHC class I) and activating ligands does not activate the NK cell (a). Presence of the inhibitory ligands only is typical for healthy cells, which are protected from the NK cell-mediated lysis (b). In contrast, presence of ligands for the activating receptors in the absence of self-MHC leads to the target cell lysis (c). If both types of ligands are detected at the surface of the same cell, the outcome of the interaction depends on the balance between activating and inhibitory signals (d).

Signalling through inhibitory NK cell receptors is initiated by phosphorylation of an immunoreceptor tyrosine-based inhibition motifs (ITIMs) localised in their cytoplasmic domains [107, 108]. The definition of the ITIM sequence was established as V/I/LxYxxL/V, where x denotes non-conserved position, which is the sequence required

for the recruitment of tyrosine phosphatase SHP-1 to cytoplasmic phosphotyrosines of an inhibitory KIR [109]. Most of inhibitory receptors possess two ITIMs separated by approximately 25 amino-acids. Evidence for the contribution of both ITIMs to the inhibitory effect was provided by mutational analysis, but the membrane proximal tyrosine was suggested to play a more important role [110-112].

Although the concept and existence of the ITIM was first established for type IIb Fc receptor γ (FcγRIIb), which inhibits B cell receptor signalling by recruiting the Src homology (SH) 2 domain–containing inositol 5′ phosphatase (SHIP), inhibition by KIR was shown to rely on the recruitment of SH2 domain-containing tyrosine phosphatase (SHP)-1 or SHP-2, but not SHIP [109, 113]. Interaction of SHP-1 and SHP-2 with cytoplasmic tail of the receptors, and specifically binding of their tandem SH2 domains to ITIMs, releases the catalytic domain from an inhibitory, intramolecular interaction with the N-terminal SH2 domain [114].

Recruitment of SHP-1 by ITIM-bearing NK cell receptors is generally believed to block signalling from the activating receptors at a membrane-proximal step, resulting in most downstream signals being prevented from occurring at all [107]. Experiments employing a KIR–SHP-1 fusion protein that included a substrate-trapping mutation in SHP-1 led to identification of Vav1, a molecule known to act as a regulator of actin cytoskeleton, as a direct substrate of SHP-1 [115]. This suggests that inhibition of NK cells involves blocking the actin-dependent activation signals from different activating receptors [116].

1.3.4 Activating receptors

Identification of the role for activating receptors acting as regulators of NK cell function alongside inhibitory receptors led to modification of the original ‘missing self’ model, often called a ‘perturbed self’ model. NK cells are known to be sensitive to changes in the expression of various ligands triggered by different pathogens or malignant transformation. This is mediated by a variety of receptors, which differ in terms of structure, specificity and signalling pathways utilized. At present, our understanding of activating signalling in NK cells is skewed toward a few receptors for which signalling pathways have been best characterized.

Among the receptors which are considered dominant are those associated with immunoreceptor tyrosine-based activation motif (ITAM)-bearing signalling molecules, such as DNAX activation protein 12 (DAP12), CD3 ζ subunit and FcRγ subunit. This includes a family of NCRs: NKp46 and NKp30, which associate with FcRγ and/or CD3

ζ, and NKp44, which associates with DAP12 [7, 117, 118]. These receptors were grouped together based on their ability to activate NK cells and importance for the killing of tumour cells *in vitro* [119], but they do not share many similarities in their sequence or structure [120].

Ligands corresponding to the NCRs have largely remained elusive, but the molecules proposed so far to ligate NCRs include these of viral, bacterial and cellular origin. Reported viral ligands for NCRs include hemagglutinin neuraminidases (HN) of the Sendai virus and of the Newcastle disease virus, which were described as ligands for NKp46 and NKp44 [79, 81], hemagglutinin (HA) of influenza virus, identified as a ligand for NKp46 [79] and human cytomegalovirus tegument protein pp65, identified as a ligand for NKp30 [83]. Some bacterial components have also been reported to interact with NCRs. For example, fusion proteins of NKp44, but not other NCRs, showed a direct binding to *Mycobacterium bovis* (bacillus Calmette-Guérin; BCG) and NK cells were found to be directly activated upon incubation with the bacteria [121]. In addition, a number of interactions between NCRs and cellular ligands have been described, including binding of NKp30 to HLA-B-associated transcript 3 (BAT3) [84], an intracellular protein shown to be involved in the p53-mediated cellular response to stress and DNA damage [122] and to B7-H6, a transmembrane protein expressed on several tumour cell lines [85] and interaction of NKp44 with proliferating cell nuclear antigen (PCNA) [82], an intracellular molecule overexpressed in cancer cells. Importantly, for most of the cellular ligands proposed for NCRs, it remains highly controversial whether they truly bind to the receptors and contribute to regulation of NK cell activity. The full identification of NCR ligands still remains to be completed and verified in a more physiologically relevant setup than analysis of soluble ligands binding, a method often applied in the previous studies.

Another important and well characterized activating receptor is NK group 2 member D (NKG2D, also known as CD314). It binds to multiple ligands upregulated on cells in response to infection, transformation, or DNA damage which are generally absent from the surface of healthy cells or expressed at very low levels. In humans, NKG2D ligands include two proteins encoded by MHC class I chain-related (MIC) genes, MICA [86] and MICB [87], and six UL-16 binding proteins, ULBP1 - 6 [88, 89]. An important role for NKG2D in targeting NK cell responses toward abnormal cells was first suggested by *in vitro* experiments, in which natural or induced expression of NKG2D ligands enhanced the sensitivity of tumour cells to NK cell-mediated killing [123, 124]. Experiments in mouse models confirmed the importance of NKG2D for tumour

control: neutralization of NKG2D with antibodies enhanced the sensitivity of wild-type (WT) C57BL/6 and BALB/c mice to methylcholanthrene-induced fibrosarcoma [125] and mice deficient in NKG2D were more prone to spontaneous tumours in B cell lymphoma and prostate adenocarcinoma models [126]. Human NKG2D signals through its association with an adaptor molecule DAP10, which is genetically linked to DAP12 but carries a tyrosine-based motif (YxxM) different from the ITAM [127, 128].

Expression of an FcγRIIIa receptor, CD16, which associates with CD3 ζ and FcRγ subunits [90], makes the NK cells potent effectors of ADCC. CD16-mediated ADCC is believed to contribute to the therapeutic effects of clinically effective cytotoxic antibodies. One such therapeutic is rituximab, a monoclonal antibody against CD20 commonly used in the therapy of B cell malignancies [129, 130]. Rituximab-triggered NK cell-mediated ADCC is illustrated by Figure 1.3. Evidence for the role of CD16 in therapeutic effect of rituximab includes poor response to antibody treatment in mice deficient in activating Fc receptors [131]. Similarly in humans, a polymorphism in CD16 that showed increased binding to human IgG1 was associated with a better response to anti-CD20 antibodies (90% response rate) as compared to the patients with normal CD16a (51% response rate) [132].

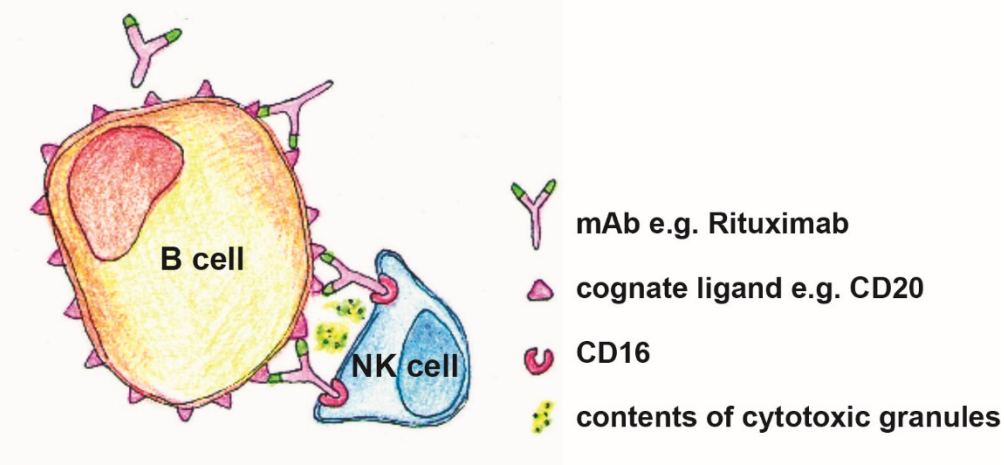

Figure 1.3 NK cell-mediated ADCC.
ADCC is a tripartite process in which $F(ab)_2$ fragment of an antibody (e.g. Rituximab) binds to a cognate ligand at the surface of a target cell (e.g. CD20 at the surface of a malignant B cell) and Fc portion of the same antibody binds to Fc receptor at the surface of an effector cell (e.g. CD16 on an NK cell), triggering a cytotoxic response.

Interestingly, some NK cell receptors can mediate activating or inhibitory functions depending on the presence of certain signalling molecules [133]. One such receptor is 2B4 (CD244), a member of the signalling lymphocyte activation molecule (SLAM) receptor family, which binds to Ig-like hematopoietic molecule CD48 [91]. Its activating

function requires association with SLAM-associated protein (SAP), which controls 2B4-dependent NK cell activation in two ways: by inducing phosphorylation of Vav1 by the Fyn kinase [134] and by blocking the recruitment of the inhibitory phosphatase SHIP-1 [135]. In the absence of SAP however, inhibitory molecules including SHIP, SHP-1 and SHP-2 are recruited to tyrosine-based motifs similar to ITIMs, present in the cytoplasmic tail of 2B4 [136, 137]. Such situation occurs in cells from patients with X-linked lymphoproliferative syndrome [136] but most probably also in heathy individuals, as suggested by reports of 2B4 inhibitory function being crucial for protection of activated $CD8^+$ T cells from NK cells during lymphocytic choriomeningitis virus infection of mice [138]. How the balance between the activating and inhibitory functions of 2B4 is set in normal individuals is not known.

The signalling events downstream of activating NK cell receptors are relatively complex. In general, ligation of ITAM-bearing receptor complexes is coupled to the activation of Src family of protein tyrosine kinases, such as lymphocyte-specific protein tyrosine kinase (Lck). Activated Lck mediates tyrosine phosphorylation of ITAMs, which can then recruit and activate members of Syk (spleen tyrosine kinase) family, such as Syk itself or ZAP-70 (ζ-associated protein kinase of 70 kD). Signalling adaptors that act downstream of Syk family members in NK cells include guanine nucleotide exchange factor Vav, SLP-76 (SH2 domain-containing leukocyte protein of 76 kD), Grb2 (growth factor receptor-bound protein 2), Shc, LAT (linker for activation of T cells) and NTAL (non-T cell activation linker) [139, 140]. Events in the downstream signalling cascade include activation of the MAPK (mitogen-activated protein kinase) ERK (extracellular signal-regulated kinase) through the cytoplasmic kinases PAK1 (p21-activated kinase 1) and MEK (mitogen-activated or extracellular signal-regulated protein kinase kinase) [141].

Phosphorylation of DAP10 triggers a distinct signalling pathway, including phosphoinositide 3-kinase (PI3K), Grb2 and Vav1 [142, 143]. Therefore, both ITAM- and DAP10-dependent pathways converge on a common signalling cascade Vav-Rac-PAK1-MEK-ERK which appears to be crucial NK cell cytotoxicity regulation. Figure 1.4 summarizes the signalling pathways downstream of the NK cell receptors.

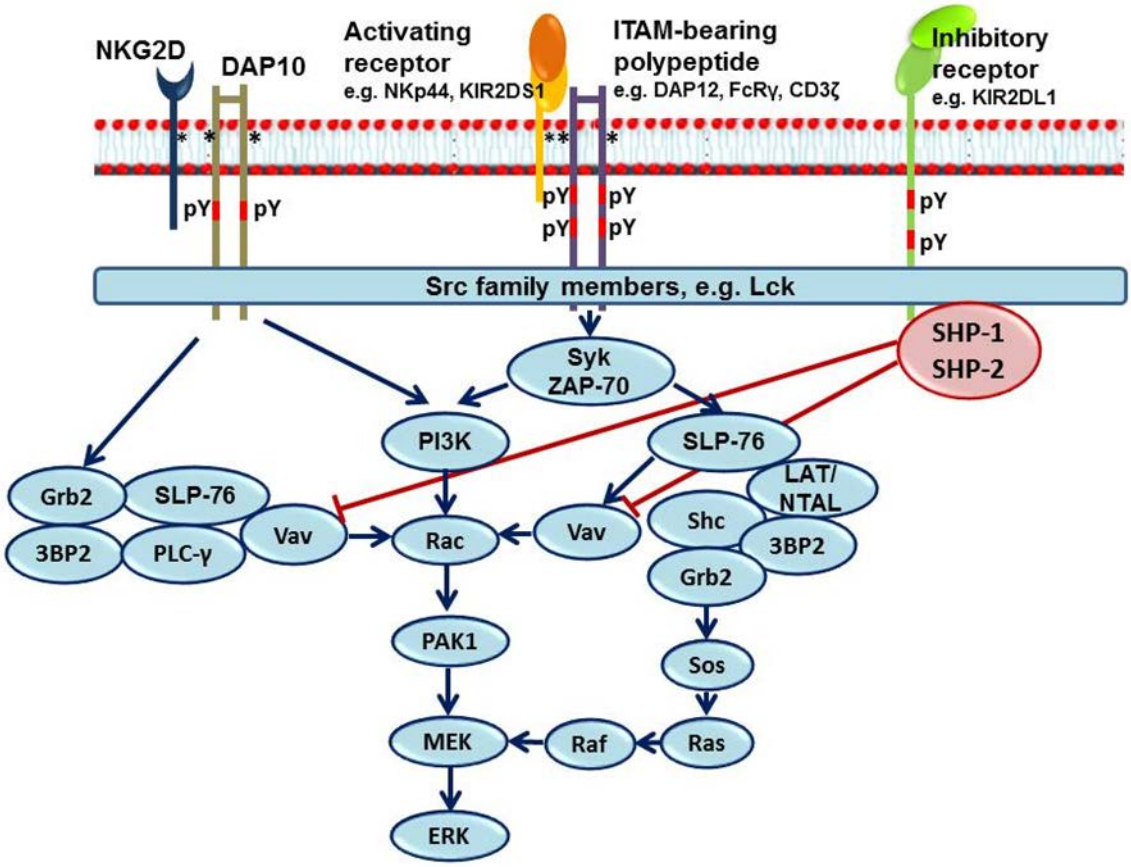

Figure 1.4 Signalling pathways downstream of NK cell receptors.
ITAM- and DAP10-dependent pathways converge on a common signalling cascade Vav-Rac-PAK1-MEK-ERK. The guanine nucleotide exchange factor Vav1 has been identified as a direct substrate of SHP-1 phosphatase acting downstream of inhibitory receptors. Based on [144].

1.3.5 NK cell receptors synergy

Considering how many different families of NK cell receptors were described within a relatively short time since the discovery of 'missing self' receptors, it was important to establish whether there is redundancy, hierarchy, or complementation among the multiple activating receptors on NK cells.

One way to determine the precise role of any given receptor on NK cells is to test them individually and in combination with others. Specific monoclonal antibodies are convenient tools for such analysis. Cross-linking of NK receptors with antibodies showed that the only receptor tested that was sufficient to activate degranulation in human primary resting NK cells was CD16. Other tested receptors - NKp46, 2B4, NKG2D, DNAM-1 and CD2 – triggered degranulation only in combination with others. In addition, only some pairwise combinations led to the synergy [145].

In an alternative approach, an insect cell line S2 was transfected to express ligands for NK receptors, one at a time or in combinations. For stimulation of CD16, the same

cells were coated with an anti-S2 polyclonal rabbit IgG. Similarly to results of crosslinking with antibodies, insect cells were only killed either by ADCC or when pairs of ligands for synergistic combinations of receptors were co-expressed [146]. A conclusion from these experiments is that no single receptor for natural cytotoxicity is sufficient to induce degranulation and none is necessary (CD16 is not an NCR because it relies on opsonizing antibodies).

More recent studies applying super-resolution microscopy to characterize activation-triggered actin remodelling in NK cells demonstrated that while ligation of some receptors, such as NKG2D and CD16, is sufficient for actin mesh opening up enough for the lytic granules to pass, other receptors, such as CD2 or NKp46, need co-ligation of an adhesion molecule lymphocyte function-associated antigen (LFA)-1 for the same effect [147]. One explanation of this would be that recognition of foreign proteins (such as NKp46 ligands of viral origin) needs to be more tightly regulated as a consequence of NK cells using germline-encoded receptors. Integrin recognition could serve to differentiate between free pathogens in blood and pathogen-infected cells [147]. This distinction would not be required for NK cell receptors recognizing host cell–encoded proteins which can only be found on diseased cells and not pathogens (such as NKG2D).

1.3.6 NK cell licensing

Dominant inhibitory receptors recognise a restricted range of self-ligands which are inherited independently (and therefore are not necessarily present with their receptor). Since these receptors are stochastically expressed within the NK cell population, a subset of NK cells that lack inhibitory receptors for self MHC would likely exist. These NK cells would have the potential to harm the host. To prevent such possibility, NK cells are subject to developmental controls.

It was initially thought that all NK cells had an inhibitory receptor for self [148]. However, this view was corrected by multi-colour flow cytometry of freshly isolated cells [149, 150]. We now know that inhibitory receptors expression pattern in humans is indeed close to stochastic, with only subtle exceptions, e.g. KIR tend to be expressed on the same cell more than expected by random chance and are less likely to be co-expressed with NKG2A [151]. None the less, NK cells with activating receptors, but no inhibitory receptors to self MHC, do exist in humans and mice [149, 150] (assuming that the major receptors for self MHC have been identified). And yet the host is protected, because these cells are hypo-responsive. Early in the NK cell development,

inhibitory receptors that encounter their ligand, presumably on bone-marrow stroma and hematopoetic cells, ‘educate’ [70] or ‘license’ [150] an NK cell to become fully reactive (here these terms are used interchangeably). If an NK cell happens to not possess an inhibitory receptor to self MHC, this ‘licensing’ never occurs and the cell remains non-responsive, even in the presence of activating signals [70, 149]. The exact molecular mechanisms of this process are poorly understood. However, some changes in the NK cell phenotype triggered by education have been described.

Firstly, fluorescence correlation spectroscopy (FCS) analysis of murine receptors in educated and uneducated NK cells by Guia *et al.* suggested that the confinement of activating receptors at the cell membrane changes upon education. The authors were able to distinguish the receptors which were confined in actin mesh from these that were partitioned in lipid domains and not constrained by actin. They did that by measuring how long fluorescently-labelled surface molecules stay within different focal volumes illuminated by laser light, which is directly related to their mobility [152]. In cells which did not undergo education, both activating and inhibitory receptors were confined within actin mesh, within close proximity of each other. Such arrangement was proposed to promote constant inhibition of activating receptors. In fully educated cells however, activating receptors were relocated into the lipid domains and not constrained by actin. This was proposed to terminate the close interaction between activating and inhibitory receptors and play a crucial role in NK cells gaining responsiveness [152].

The abilities of unlicensed NK cells to form conjugates with target cell and polarize lytic granules have also been investigated. While granule polarization was similar to that in licensed NK cells, there was a reduction in NK cell conjugation to target cells. This indicated that inside-out signalling from activating receptors to an adhesion molecule LFA-1 was impaired in unlicensed NK cells, while integrin outside-in signalling required for granule polarization was functional [153]. A more recent study used microchips composed of wells small enough to fit into the field of view of a confocal microscope to image and track the behaviour of NK cells co-incubated with cancer cell lines. Comparison between uneducated cells and these educated by NKG2A revealed that education was associated with a more dynamic migration behaviour and increased frequency of making contacts with target cells. An impaired adhesion response has also been observed in unlicensed cells, in line with previously suggested defects in integrin signalling. $NKG2A^+$ NK cells also more frequently killed the target cells once a conjugate had been formed, although duration of conjugation periods and NK cell spreading response in conjugates that led to killing were similar.

Summarizing these observations, the authors concluded that the high killing capacity of educated cells was linked to processes regulating events in the recognition phase of NK–target cell contact rather than events after cytotoxicity has been triggered [154].

1.3.7 Paired NK cell receptors

What makes the view of NK cell regulation even more complicated is that, like other immune cells, NK cells also express paired activating and inhibitory receptors which share their ligand specificity. The significance of such receptor pairing is poorly understood and remains one of the most intriguing questions regarding NK cell function regulation.

One extensively studied example of receptor pairing are DNAM-1 (also known as CD226), T cell immunoreceptor with immunoglobulin and ITIM domains (TIGIT) and CD96. DNAM-1 and TIGIT bind to plasma membrane glycoproteins CD155 (also known as poliovirus receptor; PVR) and CD122 (also called poliovirus receptor-related 2 (PRR2) and nectin 2), which are involved in different pathological conditions ranging from cancer to infectious diseases [94, 155, 156], and CD96 shares the specificity for CD155 [96]. DNAM-1 was originally described as an adhesion molecule that controls NK cell-mediated cytotoxicity [157] but later studies unravelled its role as a co-stimulating receptor, triggering NK cells cytotoxicity when acting in synergy with other activating receptors [145]. In contrast, TIGIT was shown to inhibit the NK cell functions [95, 158]. The function of CD96 is less well understood - it contains an inhibitory motif and in some setups has been shown to counterbalance the DNAM-1-mediated activation of NK cells [159], but other studies advocated its role in promoting the adhesion of NK cells to targets and co-stimulation of NK cells [96].

Binding of DNAM-1 to CD155 or CD122 at the cell surface of aberrant cells triggers the lysis by NK cells and was shown to play a crucial role in killing of the neuroblastoma cells, freshly isolated from patients [160]. Castriconi *et al.* found that susceptibility to lysis directly correlated with the surface expression of CD155 on neuroblasts, and masking of either DNAM-1 (on NK cells) or CD155 (on neuroblasts) with monoclonal antibodies resulted in strong inhibition of tumour cell lysis [160]. *In vivo*, DNAM-1 was demonstrated to play a role in the rejection of transplanted murine T-cell lymphoma, RMA. When RMA cells were transduced with DNAM-1 ligands prior to transplantation the tumour was rapidly rejected, while mock-transduced RMA tumour grew [161]. In addition, experiments in DNAM-1-deficient mice showed that the receptor also mediated production of IFN-γ *in vivo* - the frequency of IFN-γ^+ NK cells at

6h after the lipopolysaccharide (LPS) challenge was lower in DNAM-1-deficient mice than wild-type counterparts [159]. In the same study, a substantial increase in serum IFN-γ following LPS injection was reported for CD96-deficient mice, which suggests that DNAM-1 and CD96 oppose each other in the regulation of NK cell secretion of IFN-γ [159].

Engagement of TIGIT was reported to limit the NK cell-mediated cytotoxicity – transfection of NK cell line YTS with TIGIT led to abrogation of lytic granules polarization to the immune synapse [162] and killing of 721.221 cancer cell line transfected to express PVR [95, 162]. In line with this, blocking of TIGIT-PVR interaction by monoclonal antibodies resulted in a significantly increased killing of the 721.221-PVR cells by IL-2-activated primary NK cell cultures [95]. Furthermore, NK cells from TIGIT conditional knock-out mice produced much more IFN-γ than those of WT mice when cultured with Yac1, a murine cell line expressing PVR [163].

Paired receptors are also found within the CD94–NKG2 receptor family, which consists of the NKG2 family members (NKG2A, NKG2B, NKG2C, NKG2E or NKG2H) covalently associated with a CD94 unit. The prototypic member of this family, CD94–NKG2A, possesses an ITIM in the cytoplasmic tail and recruits SHP-1 to inhibit NK cell function, similarly to inhibitory KIR [93, 164, 165]. In contrast, CD94–NKG2C, CD94–NKG2E and CD94–NKG2H function as activating receptors via association with DAP12 [166]. The ligand for the CD94–NKG2 receptors in humans is the non-classical MHC class I molecule HLA-E [92, 93]. Since HLA-E is known to bind peptides derived from the leader sequence of classical MHC class I molecules, it has been suggested that in parallel to its main function of inhibiting the NK cell activity, the HLA-E-CD94–NKG2A interaction might also serve as yet another way for NK cell to monitor expression of other MHC class I molecules [92].

Amongst the activating members of the family, CD94–NKG2C has been proposed to play a role in host defence against viruses. Stimulation of peripheral blood mononuclear cells (PBMC) with human cytomegalovirus (HCMV)-infected fibroblasts promotes the clonal expansion of $NKG2C^{+}$ NK cells in HCMV-infected donors. The CD94–NKG2C complex itself is believed to be involved in driving NK cell clonal expansion in response to HCMV infection [167, 168], but the corresponding viral ligand remains elusive.

Finally, activating counterparts for multiple inhibitory KIR have been identified. The extracellular portions of paired KIR represent very high structural homology, which suggests that they should share the ligand specificity. However, the specificities of only

a few activating KIR have been firmly characterized [169-171]. Inhibitory and activating KIR are the main subject of this thesis and are described in detail below.

Significance of paired receptors

Some of the puzzling questions regarding paired NK cell receptors is why do NK cells need such systems and how is the response regulated in cells co-expressing activating and inhibitory receptors to the same ligand? An interesting hypothesis is that the primary function of these receptors is to fine-tune the activation thresholds of immune cells. Paired receptors often bind the ligand with different affinities [172], and as such, their signalling can be manipulated by the ligand expression levels at the surface of a target cell. A model of fine-tuning of NK cytotoxicity by adjusting the response to ligand densities under different conditions was proposed for the CD155-binding receptors by Noa Stanietsky and Ofer Mandelboim [173]. According to these authors, low levels of CD155, which are normally expressed on healthy cells, could be sufficient to stimulate the inhibitory TIGIT due to the high binding affinity of TIGIT to CD155. This would result in the inhibition of NK cell function, even in the presence of DNAM-1 and CD96. When tumours emerge, CD155 expression might be up-regulated to enable detachment and migration of cancer cells (CD155 is involved in regulation of formation of adherent junctions). This would enable co-stimulation by DNAM-1 and CD96 (which both bind to CD155 with lower affinity) and in concert with the appearance of other tumour-specific activating ligands (such as ligands for NKG2D and B7-H6 ligand for NKp30) trigger NK activation.

The role of activating and inhibitory receptors binding to the same self-MHC molecules is perhaps even more enigmatic (as further discussed below). Overall, detailed characterization of ligand specificity and signal integration for paired receptors is needed and will greatly advance our understanding of the tightly regulated NK cell activation.

1.4 Killer Immunoglobulin-like receptors

The KIR were first identified by their ability to control the specificity of NK cell-mediated cytotoxicity [174, 175]. Their discovery as inhibitory receptors for HLA class I molecules vindicated the role of HLA in protecting the healthy cells from killing by NK cells, originally proposed by the ‘missing self’ hypothesis. Later studies unravelled that

contribution of the KIR family to the regulation of immune responses is far more complex than initially thought, with some KIR being stimulatory rather than inhibitory.

1.4.1 *KIR* genes structure

The *KIR* gene family currently consists of 15 gene loci encoded within the *KIR* locus, a 100-200 Kb region of the Leukocyte Receptor Complex mapped to chromosome 19. Individual *KIR* genes can contain four to nine exons. The basic arrangement of exons and introns is relatively consistent for different *KIR* genes: the first two exons encode the signal sequence, exons 3 - 5 correspond to one Ig domain each (D0, D1, and D2, starting from the N-terminus), exons 6 and 7 correspond to the linker and transmembrane regions, respectively, and the two final exons encode the cytoplasmic domain [176, 177].

Based on the presence or absence of specific exons *KIR* genes are generally divided into three types, as illustrated by Figure 1.5. Type I *KIR2D* genes, which include *KIR2DL1-3* and *KIR2DS1-5* as well as the pseudogene *KIR2DP1* possess eight exons and a pseudoexon 3 sequence (which is inactivated) [75, 76, 178]. They all encode two extracellular domains with a D1 and D2 conformation, but since exon 3 is a pseudoexon in these genes, they are missing the D0 domain. Within the type I *KIR2D* group, the genes differ with regards to the length of particular exons, e.g. *KIR2DL1* and *KIR2DL2* share a common deletion in exon 7 and *KIR2DL1-3* differ from *KIR2DS1-5* in the length of their cytoplasmic tail.

The type II two-domain *KIR* genes, which include *KIR2DL4* and *KIR2DL5* [178], have deleted the region corresponding to exon 4 and therefore their protein product has no D1 domain [179]. But since they possess a translated exon 3, the extracellular domains of type II KIR proteins have D0 and D2 conformation. *KIR2DL4* is further differentiated from *KIR2DL5* (as well as from other *KIR* genes) by the length of its exon 1 sequence [178].

Finally, the type III *KIR* genes include the structurally related *KIR3DL1*, *KIR3DS1*, *KIR3DL2* and *KIR3DL3* genes. They possess nine exons (except for *KIR3DL3* which completely lacks exon 6) and therefore encode proteins with three extra-cellular Ig-like domains - D0, D1 and D2. Within the *KIR3D* group, the four genes differ in the length of the exon 9, leading to different lengths of their cytoplasmic tails [75, 180, 181].

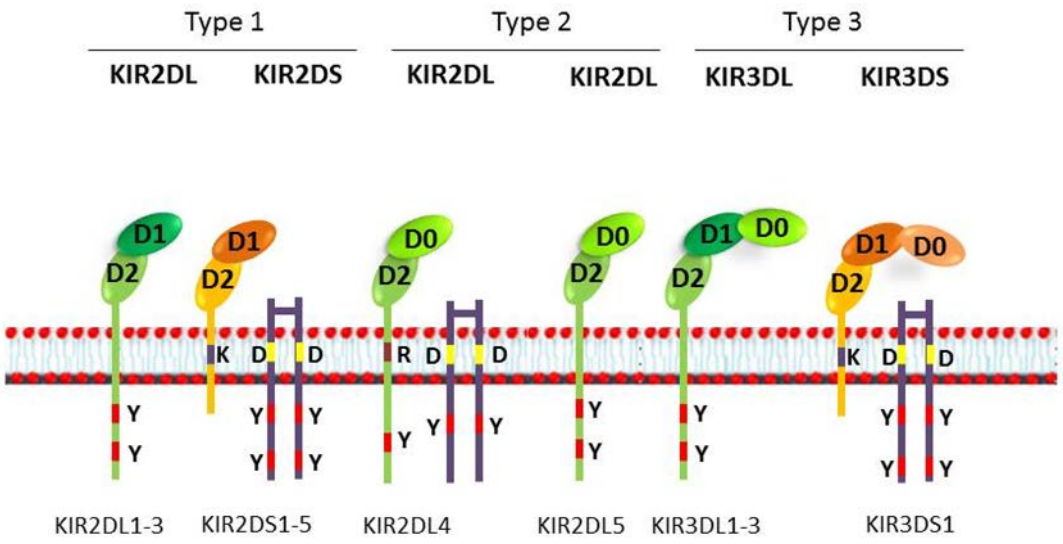

Figure 1.5 Structure of the KIR molecules.
KIR molecules possess two (Type 1 and 2) or three (Type 3) extracellular Ig-like domains. The cytoplasmic domains of the inhibitory receptors contain ITIM sequences, whereas a charged amino acid residue facilitating interaction with the adaptor molecule (such as DAP12), is located in the transmembrane region of the activating receptors. KIR2DL4 contains features of both activating and inhibitory receptors.

1.4.2 Genetic diversity of the KIR family

What makes the KIR family unique among other families of NK cell receptors is the extreme diversity at the *KIR* gene locus, arising from both multi-allelic and polygenic polymorphism [182]. Perhaps the most remarkable feature is that gene content varies between haplotypes. This is in part caused by the homology between family members which allows unequal crossing-over at meiosis.

A recent study in which over 3,000 Caucasians from family-based cohorts were typed for both the presence/absence of all individual *KIR* genes as well as copy number identified 71 different haplotypes [183]. Interestingly, just 11 of these haplotypes could account for 94% of all genotypes observed. These common haplotypes could be derived from combinations of only 3 centromeric and 3 telomeric motifs, as a result of reciprocal recombination at the site located near the central *KIR2DL4* gene. *KIR2DL4* is conserved in nearly all haplotypes, and so are *KIR3DL3* and *KIR3DL2*, which flank the *KIR* locus at the centromeric and telomeric ends, respectively. These genes are often called framework *KIR*. The intervening genes, however, vary between the haplotypes and these variations in gene content are the basis for dividing the haplotypes into two primary sets, termed A and B. These groups were originally distinguished by the presence of a 24 kb HindIII fragment on Southern blot analysis, which is present in group B haplotypes and absent from group A

haplotypes [182]. However, a more functionally relevant distinction between haplotypes A and B is the number of stimulatory receptors present. Haplotypes A contain only a single stimulatory *KIR* gene, *KIR2DS4*, which often carries an inactivating mutation [184], whereas haplotypes B contain various combinations of *KIR2DS1, KIR2DS2, KIR2DS3, KIR2DS5, KIR3DS1* and *KIR2DS4.* According to their genotypes, the individuals are therefore designated 'AA' 'AB' or 'BB'.

In Caucasian populations, the frequencies of haplotypes A and B are roughly equal, but haplotype B displays a substantial variety in gene content. The centromeric and telomeric motifs identified by Jiang *et al*. are linked to patterns of linkage disequilibrium (LD) – they exhibit very strong linkage disequilibrium within them, but not between them. For the A haplotypes, patterns of linkage disequilibrium between *KIR* loci are fixed and therefore A haplotypes differ at the allelic level, but not in gene content [185]. Among the B haplotypes many pairs of genes seem to have quite strong LD, as suggested by *KIR* profiling of unrelated individuals [182, 186, 187]. Notably, some *KIR* haplotypes can have two (or more) copies of a gene on a single haplotype. This copy number variation originates from the expansion and contraction events occurring within the *KIR* region and has been found to be much more frequent in *KIR* B haplotypes [183].

Allelic polymorphism provides additional diversity within the *KIR* locus. The sequence analysis of *KIR* cDNA has shown that most *KIR* genes contain variable sites [75, 76, 185, 188, 189], which can occur at positions encoding residues engaged in the interaction with HLA class I [190-192]. Due to similarity amongst *KIR* gene sequences and resulting from it possibilities of unequal crossing-over at meiosis, the definition of what is a gene and what is an allele is rather unclear and has changed over time. For example, *KIR2DS4* and *KIR2DS1* were originally suggested to be allelic variants of a single locus [182], but more recent data suggests that they represent distinct loci [176, 186]. Within the pairs of homologous activating and inhibitory *KIR*, some, such as *KIR2DL1* and *KIR2DS1*, are known to occupy separate loci, while others, such as *KIR3DL1* and *KIR3DS1,* appear to occupy the same locus within different haplotypes [176] and have been suggested to be alleles of a single locus based on the segregation analysis [188].

One quite polymorphic *KIR* is *KIR3DL1,* for which different allotypes where shown to be expressed at different levels, as determined by high, low or no binding of KIR3DL1-specific monoclonal antibodies. As a result, characteristic bimodal distributions in flow cytometry analysis of primary human NK cells can be sometimes observed, indicating that these donors are heterozygotes for high and low binding *KIR3DL1* alleles [188].

1.4.3 KIR nomenclature

The number of extracellular Ig domains is one of the features which were used to create the most commonly used nomenclature system for the KIR family, known as the Human Genome Organization (HUGO) nomenclature system. Two or three Ig domains present account for 2D or 3D in the *KIR* genes (and proteins) names. This system also takes into account characteristics of the cytoplasmic tail - irrespective of the number of Ig subunits, the cytoplasmic domain of KIR can be either long (designated as "L") or short ("S"). This corresponds to the functional divergence of KIR. KIR with long cytoplasmic tails are inhibitory due to the presence of ITIMs in their cytoplasmic domains [109] and short-tailed KIR transmit activating signals through their interaction with DAP12 [193].

KIR allele sequences are named in an analogous fashion to the nomenclature used for HLA alleles [194, 195]. The gene name is separated by an asterisk from a numerical allele designation, of which the first three digits are used to indicate alleles that differ in the sequences of their encoded proteins, the next two digits are used to distinguish alleles that only differ by synonymous differences within the coding sequence and the final two digits are used to distinguish alleles that only differ by substitutions in an intron, promoter, or other non-coding region of the sequence [195].

1.4.4 Ligand specificity of KIR proteins

Ligands reported for the KIR receptors are listed in the Table 1.3. The ability of KIR to distinguish between different HLA molecules has been attributed to only a few residues within the receptor and ligand sequences. For example, residues at positions 77 and 80 in HLA-C are critical for defining the two groups of allotypes - they can be either serine and asparagine (respectively) in the group 1 HLA-C (HLA-C1) allotypes, or asparagine and lysine in the group 2 allotypes (HLA-C2) [196]. On the receptor side, exchanging of a single residue, the methionine, at position 44 in KIR2DL1 with the lysine was sufficient to switch the specificity of KIR2DL1 from HLA-C2 to HLA-C1, and vice versa [197].

Table 1.3 Inhibitory and activating KIR and their ligands.

Inhibitory		**Activating**	
Receptor	**Ligand**	**Receptor**	**Ligand**
KIR2DL1	HLA-C2 [76, 97, 169, 190, 196, 198-200]	**KIR2DS1**	HLA-C2 [97, 169, 170, 198]
KIR2DL2	HLA-C1 including HLA-B*46 and B*73 (and weakly to HLA-C*02,*05 of the HLA-C2 class) [192, 201]	**KIR2DS2**	Homology to KIR2DL2/S2 suggests HLA-C1-like ligand, but only weak if any binding reported [reviewed in [202], HLA-A*1101 [203]
KIR2DL3	HLA-C1 including HLA-B*46 and B*73 [76, 199, 201, 204]	**KIR2DS3**	No evidence of an MHC ligand
KIR2DL4	In some studies [205, 206], but not others [207] binding to HLA-G detected	**KIR2DS4**	HLA-C1 (C*1601, C*0102, and C*1402), HLA-C2 (C*0501, C*0202, and C*0401), HLA-A (A*1101 and A*1102) [171]
KIR2DL5	No evidence of an MHC ligand	**KIR2DS5**	No evidence of an MHC ligand
KIR3DL1	HLA-Bw4 [208-210]	**KIR3DS1**	Homology to KIR3DL1 suggests an HLA-Bw4-like ligand, no evidence of binding found so far
KIR3DL2	Peptide-dependent binding to HLA-A*11 and HLA-A*03 [76, 211, 212], β2 microglobulin-free heavy chain forms of HLA-B27 [213], HLA-F [214]		
KIR3DL3	No evidence of an MHC ligand		

1.5 Activating receptors for self-MHC

The role for inhibitory receptors binding to self-ligands has been extensively studied and well established. Similarly, activating receptors that recognise ligands on stressed

or infected cells are a logical component allowing NK cell recognition of perturbed self. On the other hand, the existence of activating receptors for self MHC is surprising and their precise role in the process of NK cell recognition remains unknown. The fact that they have emerged in different receptor families suggests that these molecules are likely important for NK cell function. Ly49 family of murine NK cell receptors is not related to KIR in humans, but these two families share functional similarities – they have both evolved to facilitate the recognition of 'missing self' and are a classic example of convergent evolution. Among the human proteins, paired receptors for MHC can also be found it different families, i.e. activating CD94/NKG2C and inhibitory CD94/NKG2A both bind to HLA-E. It can be therefore assumed that arising of activating receptors for self-MHC was driven by some evolutionary advantage which it must give (or must have given).

1.5.1 Activating receptors and decoy ligands

One hypothesis trying to explain the significance of activating KIR proposes that MHC molecules are not their 'main' ligands. In fact, the ligand specificity of most activating KIR is unknown. Binding of only two activating KIR, KIR2DS1 and KIR2DS4, to MHC ligands has been reliably established [97, 169, 171, 215]. However, both receptors have a much lower affinity for HLA-C than inhibitory KIR2DL1. KIR2DS2 and KIR3DS1 are predicted to bind HLA based on their structural homology to inhibitory KIR2DL2 and KIR3DL1, but their interaction with HLA remains largely undetectable, probably due to its being very weak.

Weaker or no binding of activating KIR to MHC ligands compared to their inhibitory counterparts posed a question whether activating KIR might have evolved to recognize other pathogen- or tumour-derived ligands. This hypothesis originally arose from the observation that in mice the inhibitory Ly49I receptor and its highly homologous activating counterpart, Ly49H, share the same ligand - the m157 protein encoded by the mouse cytomegalovirus. Mice carrying the activating Ly49H are resistant to murine cytomegalovirus infection [216]. It is possible that pathogens first used decoy MHC-like ligands, such as m157, to escape the missing-self recognition by inhibitory receptors, such as Ly49I, and NK cells responded by developing the activating receptor that bound these decoy ligands with higher affinity than the true MHC ligands.

1.5.2 Activating receptors and unusual or pathogen-associated peptides

Alternatively, activating receptors could be more sensitive to unusual or pathogen-associated peptides held by self MHC. When cells are infected, activating KIR could sense the changes in peptide repertoire presented. In some cases recognition by inhibitory and activating KIR was shown to be affected by the peptide sequence. In a binding assay with soluble KIR proteins, KIR2DL1 and its activating homologue KIR2DS1 were shown to share sensitivity to peptide sequence alterations at positions 7 and 8 [169, 217]. Crystal structures of inhibitory KIR in contact with their ligands confirmed that KIR contact these two positions of the held peptide upon interaction with HLA-C [190, 192], suggesting a limited opportunity for peptide discrimination. Nevertheless, in the tetramer-based binding study using Epstein-Barr virus-transformed cell line, infection of cells led to expression of a detectable levels of an MHC class I ligand for KIR2DS1 [169].

In some cases, peptides were suggested to even antagonize the inhibitory receptor function. It is known that peptides affect the stability of HLA molecules. But not always the same peptide that provides good stability also triggers strong binding or signalling. Fadda *et al.* described one such peptide, which was able to stabilize HLA-C*0102 but was not recognized by its cognate receptors KIR2DL2/3. Importantly, this peptide was able to antagonise the inhibitory effects of a different, recognised peptide [218]. Thus, in this experimental setting, the existence of peptide antagonism rendered the NK cells sensitive to even small changes in the peptide content of MHC class I. It is possible that pathogens could evolve specific peptides to prevent this antagonism and escape from the recognition by inhibitory KIR. Activating KIR could therefore be a host response to such pathogen-derived peptides. This argument however, would not explain the evolution of activating receptors from the Ly49 family, which do not contact the peptide binding groove [219].

1.5.3 Activating receptors and fine-tuning of activation thresholds

Another possibility is that similar to the role proposed for paired receptors binging to non-MHC ligands, the role of paired KIR is to fine-tune the threshold for the NK cell activation. In support of this idea, inhibitory KIR have been shown to bind their ligands with very fast on/off kinetics, which was proposed to facilitate the rapid immunosurveillance of cells [220]. Moreover, different levels of HLA-C protein expressed at the surface of the 721.221 were shown to determine the efficiency of the inhibition in primary human NK cells [221].

1.6 KIR2DL1 and KIR2DS1

1.6.1 Identification of KIR2DL1 as an NK cell inhibitory receptor

In 1993, Moretta *et al.* observed that NK clones which stained with the monoclonal antibody EB6, but did not stain with the GL183 antibody (which is now known to target KIR2DL3/2 and KIR2DS2), failed to lyse $Cw4^+$ C1R target cells [199, 222]. They have demonstrated that the protein bound by the EB6 antibody was directly responsible for this protection, because adding of this antibody, its $F(ab')_2$ fragment and the XA141 mAb (IgM antibody also binding KIR2DL1) reconstituted the lysis of $Cw4^+$ C1R cells. In contrast, adding of the entire EB6 antibody but not its $F(ab')_2$ fragment, inhibited the lysis of an unprotected cell line P815, which binds murine antibody via surface Fc receptors, resulting in an antigen-like effect mimicking the interaction between the NK receptor and its specific ligand [199].

Two years later the molecular cloning of the members of KIR family (back then known as p58 family or NK-associated transcripts; NKAT), including the *KIR2DL1* (also known as NKAT1) gene was reported almost simultaneously by two different groups [75, 76]. Furthermore, these two reports confirmed the clonal distribution of these receptors and suggested a phosphorylation of the receptor on the tyrosine-based motifs in their cytoplasmic domains as a possible mechanism of the signal transduction.

1.6.2 Identification of KIR2DS1 as an activating NK cell receptor

Soon after that it was realized that alongside the inhibitory receptor bound by the EB6 antibody, human NK cells also expressed the EB6-binding molecules which trigger the NK cell cytolytic activity and an increase in the intracellular calcium [97]. This activating EB6 ligand, which was later identified as KIR2DS1 receptor, was found to be present only in certain donors, and in these donors only a fraction of $EB6^+$ NK clones expressed the activating form of EB6 ligands, while the remaining clones expressed the inhibitory receptors.

This newly described activating receptor had a molecular mass of approximately 50 kD and thus differed from the 58-kD inhibitory form. Moreover, contrary to the results of EB6 masking of the inhibitory receptor, in clones expressing the activating receptor EB6 masking led to the inhibition of the cytolytic activity against $Cw4^+$ target cells [97].

Further characterization of these two receptors established that their extracellular domains reacting with the EB6 antibody only differed for 2-7 residues, while major differences existed in their transmembrane and cytoplasmic portions [223]. The inhibitory form was characterized by a longer tail and the activating one had a shorter cytoplasmic portion and contained a polar lysine residue within its transmembrane domain, which was identified as a potential site of association with proteins involved in signal transduction [223]. This lysine residue has been later confirmed to be crucial for the receptors' signalling and is involved in its interaction with the signalling adaptor DAP12 [193].

1.6.3 Frequency of *KIR2DL1* and *KIR2DS1* genes

The frequencies of both *KIR2DL1* and *KIR2DS1* genes vary between different populations. In Caucasians, *KIR2DL1* gene is generally carried more often than *KIR2DS1*. In European populations, *KIR2DL1* is very common and often found in over 95% of individuals (Figure 1.6 a). In contrast, *KIR2DS1* frequencies in the same populations are typically within the 30 – 50% range (Figure 1.6 b). *KIR2DS1* is most commonly found in the Australian Aboriginal populations – i.e. in the Aboriginal population of the South Australia, *KIR2DS1* frequency is reported as 82% and *KIR2DL1* frequency as 72% (*allelefrequencies.net*).

1.6.4 KIR2DL1 and KIR2DS1 specificity

Both KIR2DL1 and KIR2DS1 bind to the HLA-Cw molecules that have asparagine 77 and lysine 80 (Cw*02/4/5/6/707/12042/15/1602/17) [97, 169, 170, 196]. However, the inhibitory form has a much higher affinity for these ligands, as demonstrated by the soluble receptors binding to 721.221-Cw4 transfectants [198].

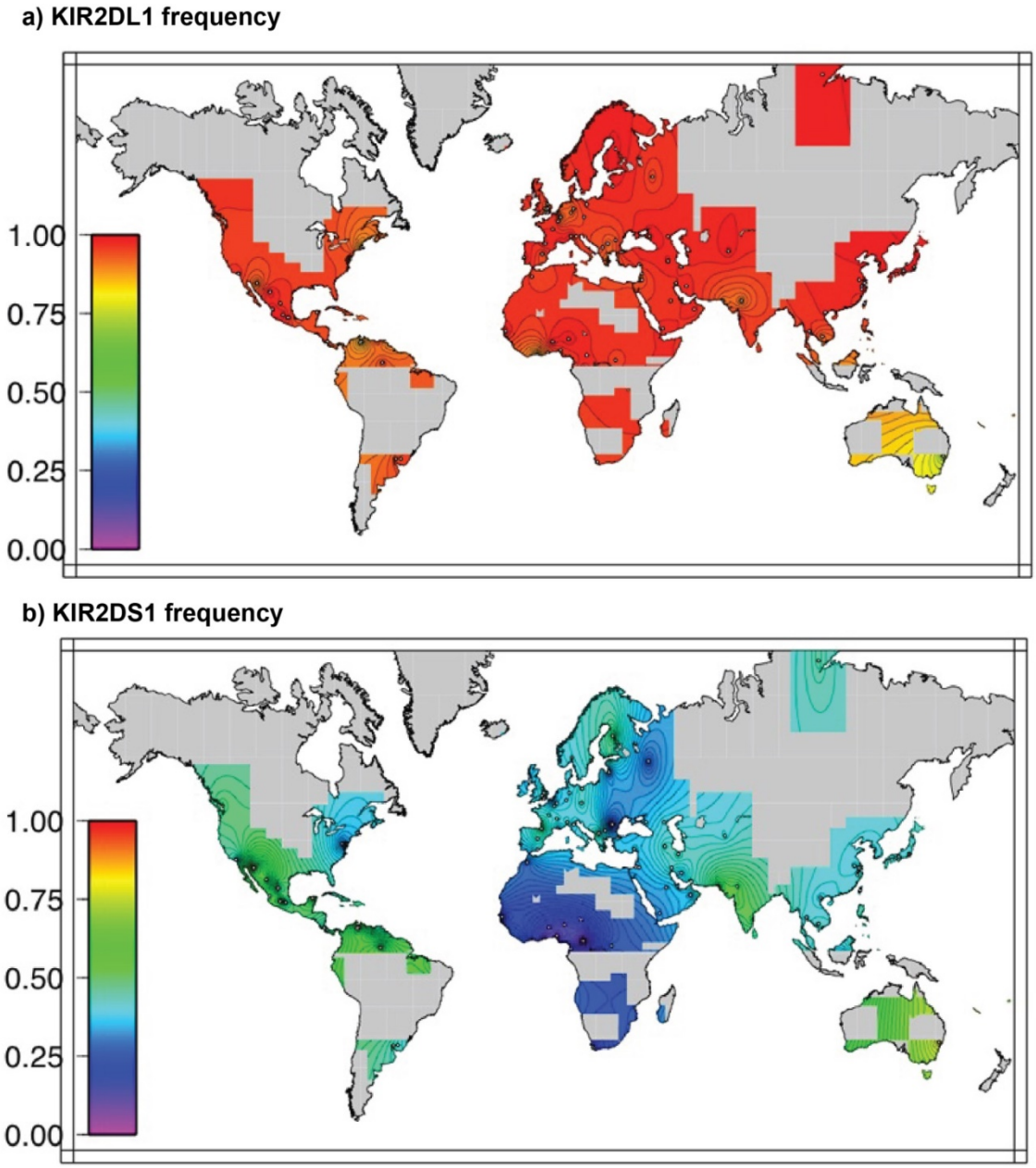

Figure 1.6 Frequency of *KIR2LD1* and *KIR2DS1* genes in different populations.
On the colour scale, value of one (red) corresponds to 100% of population carrying the gene. [Taken from allelefrequencies.net]

The difference in the affinity has been attributed to the amino-acid residue at the position 70 – the substitution of lysine 70 in KIR2DS1 by threonine (typical of the KIR2DL1 molecule) resulted in an increased binding affinity, comparable to that of KIR2DL1. Similarly, substitution of threonine 70 by lysine in KIR2DL1 reduced its binding to 722.221-Cw4 cells [198].

KIR2DL1 and KIR2DS1 also share the sensitivity to the changes in amino-acid residues at the positions 7 and 8 in the peptide bound in the MHC class I groove, i.e.

the negatively charged residues at these positions are incompatible with their binding [217]. This was first discovered for KIR2DL1 by the analysis of soluble receptors binding to the transporter associated with antigen presentation (TAP)-deficient RMA-S cells on which the Cw4 molecule was loaded with peptides of variable sequences [217]. The same sensitivity to peptide sequence alterations was later identified for KIR2DS1 [169].

1.6.5 KIR2DL1 and KIR2DS1 functions

The role of KIR2DL1 in inhibiting the NK cell effector functions is very well established [75, 76, 224-226]. In fact, the expression of KIR2DL1 was shown to determine the thresholds (described as the levels of MHC I protein on target cells) required for inhibition of NK clones, while the expression of other receptors was found less important [226].

Despite the weaker binding, KIR2DS1 has been demonstrated to mediate different effector functions in NK cells expressing KIR2DS1, but not KIR2DL1. In addition to already mentioned cytotoxicity towards the Cw4-expressing cell lines, the interaction of KIR2DS1 with $Cw4^+$ transfectants was also reported to trigger the secretion of IFN-γ in the clones of three different types of killer lymphocytes: the CD8+ γδ T cells, the CD8+ αβ T cells and NK cells [215, 227].

The fact that KIR2DS1 can mediate cytotoxicity opens the question of how $KIR2DS1^+$ NK cells are tolerant to host tissues. One study trying to address this problem analysed the anti-HLA-C2 activity of $KIR2DS1^+$ clones from donors homozygous for *HLA-C1 or HLA-C2* or heterozygous [228]. This demonstrated that donors homozygous for *HLA-C2* had significantly reduced frequency of anti–HLA-C2 reactive clones compared with all other donors but –more surprisingly - no significant difference was seen in the frequency of anti–HLA-C2 cytotoxicity in donors heterozygous for *HLA-C2* and donors without *HLA-C2* ligand. This suggests that the HLA-C2 expression level in the *HLA-C2* homozygous host cells might be sufficient to induce tolerance in $KIR2DS1^+$ NK cells, while the amount expressed by *HLA-C2* heterozygous donors might be insufficient for activation of KIR2DS1. The tolerance of $KIR2DS1^+$ clones from HLA-C2 homozygous donors was not dependent on ligand-mediated downregulation of the receptor and the authors proposed that it could be rather explained by *in cis* interactions between KIR2DS1 and HLA-C2 on the individual NK cell or some changes in the localization of inhibitory and activating receptors [228].

In the above study, anti–HLA-C2 cytotoxicity was nearly exclusively seen in KIR2DS1-single positive clones lacking inhibitory KIR and clones that expressed inhibitory KIR for self–HLA class I were commonly non-cytotoxic [228]. This domination of inhibitory KIR over an activating counterpart has been also observed in other studies [97, 229] and is in line with the strong inhibitory signals being generally able to override the activation [230-232].

1.6.6 KIR2DL1 and KIR2DS1 polymorphism

Like other KIR, KIR2DL1 and KIR2DS1 display a significant allelic polymorphism. More than 40 alleles were described for KIR2DL1, while KIR2DS1 appears to be relatively less polymorphic with 16 alleles found so far (*http://www.ebi.ac.uk/ipd/kir/*). Alleles of KIR2DL1 were shown to display a functional heterogeneity [233]. For instance, the alleles with arginine at position 245 were reported to have stronger ability to inhibit degranulation of YT-Indy cells, INF-γ production, and cytotoxicity against target cells expressing the HLA-Cw6 ligand, as compared to arginine 245-negative alleles. This stronger inhibition was mediated by more efficient recruitment of SHP-2 and β-arrestin 2 to arginine 245-containing KIR2DL1 as well as stronger inhibition of lipid raft polarization at the immune synapse, and less down-regulation of the surface expression upon interaction with the ligand [233].

Phylogenetic analysis of the coding sequence of 26 *KIR2DL1* and 7 *KIR2DS1* alleles, published recently by Peter Parham's group, identified four clades which correlated with genomic location in the Cen A, Cen B, or Tel B regions of *KIR* haplotypes. The analysis of the capacity of binding to a panel of nine HLA-C1 and seven HLA-C2 allotypes demonstrated that KIR2DL1 encoded by Cen A alleles binds C2 with greater avidity than does Cen B–encoded KIR2DL1, which appears to be associated with four D2 domain substitutions, all contributing to the binding.

The same study analysed the avidity and specificity of KIR2DS1 alleles, by constructing KIR-Fc fusion proteins for the four KIR2DS1 allotypes that differ in the amino-acid sequences of the D1 and D2 domains. This demonstrated that KIR2DS1*001 has the highest avidity for C2, which correlates with arginine at position 70 (where the other KIR2DS1 allotypes have lysine). The lowest avidity was observed for KIR2DS1*008, which correlates with serine at the position 123 (where the other KIR2DS1 allotypes have tryptophan).

1.7 KIR receptors in disease

Diversity at the *KIR* locus may be the result of selection pressures. Therefore, disease resistance or susceptibility conferred by the *KIR* locus is likely to vary in a haplotypic manner depending on disease type. A number of studies addressing genetic associations between *KIR* genes and specific diseases have been published to date, most of which stemmed from the very recent advances in characterization of the genes and their haplotypes. Examples of published associations are listed in the Table 1.4.

1.7.1 KIR3DS1 and KIR3DL1 influence on HIV infection

One of the most rigorously investigated associations is related to the progression of the HIV infection. Identification of HLA-Bw4 epitope as a protective factor for AIDS progression [234] was followed by the investigation of the influence of *KIR3DL1/S1* locus, which is known to bind HLA-Bw4, on disease progression. Mary Carrington's group confirmed the protective influence of HLA-Bw4 on the rate of progression to AIDS and found that this protective effect could be specifically attributed to the alleles of HLA-Bw4 that have isoleucine at position 80 (Bw-80I) [235]. The same study established that HLA-Bw4 is associated with delayed progression to AIDS only in the presence of the activating allele *KIR3DS1* (in survival analyses of combined cohorts, the relative risk hazard (RH) associated with the combination of *KIR3DS1* and *Bw4-80I* was equal 0.58 – 0.74 for different AIDS end points). Strikingly, when carried in the absence of the *HLA-Bw4*, *KIR3DS1* appeared to be associated with rapid progression to AIDS (RH = 1.23) [235]. Although these observations and the homology between KIR3DS1 and KIR3DL1 suggest an interaction between KIR3DS1 and HLA-Bw4, KIR3DS1 has never been shown to directly interact with HLA-Bw4 [236, 237]. However, it cannot be excluded that KIR3DS1 could bind a virally-altered form of HLA-Bw4. Alternatively, *KIR3DS1* could be not directly responsible for the observed protection, but rather be a marker of a haplotype that contains the actual locus responsible for this effect, which would still have to interact with *HLA-B Bw4-80Ile* or with a locus in linkage disequilibrium with *HLA-B Bw4-80Ile*.

KIR3DL1 has been later found to also influence the progression to AIDS. In the absence of *KIR3DS1*, combinations of *KIR3DL1* and *HLA-Bw4* alleles with the greatest inhibitory capacity were found to be associated with early control of viral load [238]. Specifically, when the mean viral load (MVL, measured as RNA copies per ml plasma) was compared between the individuals who carried the high-expression alleles of

KIR3DL1 and *Bw4-80I* and the reference group of individuals with *Bw6/Bw6* genotype, the relative frequency of high-expression alleles of *KIR3DL1 and Bw4-80I* combination was higher than that of *Bw6/Bw6* in the MVL < 2,000 grouping (odds ratio (OR) = 0.24). The opposite was observed in the MVL > 10,000 grouping [238].

The finding that both strong inhibition and activation are protective is surprising and suggests that KIR3DS1 and KIR3DL1 might mediate the protection against HIV in different ways. One possibility would be that KIR3DS1 directly recognises virus and KIR3DL1 tunes the responsiveness of the cell through education or leads to higher expression of KIR3DS1 via some unknown mechanisms. Notably, these reports are not entirely free from controversy, as other groups have failed to find an association between KIR3DS1, HLA-Bw4 and HIV progression [239, 240]. These discrepancies could be the result of different genetic backgrounds, viral strains or sample sizes, as well as different symptoms used to define AIDS as a disease outcome of HIV.

1.7.2 KIR2DL3 association with HCV infection

Another clearly established association is that of KIR2DL3 and HLA-C1 with hepatitis C (HCV) resolution [241]. The presence of genes encoding both proteins has a beneficial effect in individuals with expected low infectious doses (i.e. who got infected by the use of infected needles). Among these individuals, 20.4% of those resolving infection had the compound genotype *KIR2DL3/KIR2DL3-HLA-C1C1*, as compared with 9.9% with persistent infection (OR = 2.33). However, *KIR2DL3/KIR2DL3-HLA-C1C1* genotype showed no protection among the individuals with high-dose exposure (who received infected transfusions) – possibly due to innate immunity being overwhelmed by large doses of the virus. This effect was conserved in Caucasians and African Americans, implying this interaction with HCV as a fundamental part of the KIR system, possibly relevant to other viral infections. Although HCV-controlling subpopulation was found in both *KIR2DL3* homozygous and heterozygous individuals, the protective association with *HLA-C1C1* genotype was only significant among individuals homozygous for *KIR2DL3* (OR = 3.01). Notably, individuals heterozygous for *KIR2DL3* would carry *KIR2DL2*, which interacts with *HLA-C1* with a greater affinity than *KIR2DL3*. This is because *KIR2DL2* and *KIR2DL3* are found on opposite haplotypes. This indicates that strong inhibition mediated by *KIR2DL2* is less easily overridden by activating signals and thus can be detrimental during the HCV infection [241].

1.7.3 KIR2DL1 and KIR2DS1 significance in transplantation

The presence of *KIR2DL1* and *KIR2DS1* loci and the associated allelic variability have been also reported to be of medical importance. One such setting is allogeneic hematopoietic stem-cell transplantation (HSCT) to treat leukaemia. A clinical study involving 1277 patients with acute myeloid leukaemia who had received HSCT from unrelated donors demonstrated that patients who received allografts from *KIR2DS1*$^+$ donors had a lower probability of relapse than those with allografts from donors who were negative for *KIR2DS1* (26.5% vs. 32.5%; hazard ratio (HR) = 0.76) but only if the donor was not homozygous for *HLA-C2* (24.9% with homozygosity or heterozygosity for HLA-C1 vs. 37.3% with homozygosity for HLA-C2; HR = 0.46) [242]. The authors of this study hypothesized that high levels of the HLA-C2 self-ligand in the latter donors would induce tolerance in KIR2DS1$^+$ NK cells and diminish their activity, the effect which was later confirmed by *in vitro* studies [228]. Furthermore, in *HLA-C2* homozygous patients there was no difference in relapse between patients receiving a *KIR2DS1*$^+$ allograft, compared to those receiving a *KIR2DS1*$^-$ allograft. In contrast, there was a lower risk of relapse in *HLA-C1/C1* and *HLA-C1/C2* patients receiving a *KIR2DS1*$^+$ allograft, compared to those receiving a *KIR2DS1*$^-$ allograft (relapse rate 24.8%, vs. 31.5%; HR = 0.72). It is hard to explain how KIR2DS1$^+$ NK cells could mediate this anti-leukemic effect in *HLA-C1* homozygous recipients, as there would be no ligand for KIR2DS1 expressed by the recipient's leukaemia blasts. It is however possible that leukaemia blasts express some currently unknown non-HLA class I ligand which could mediate the recognition by KIR2DS1.

In addition, a study by Pende *et al*. provided a direct evidence for the KIR2DS1 role in the induction of alloreactivity against C2-positive leukaemia cells. They have demonstrated that NK cell clones characterized by the presence of KIR2DS1, derived from both the transplant donor and recipient, were highly cytolytic against patient's leukaemia blasts and Bw4$^+$ B-EBV cell lines. The lysis was specifically inhibited by blocking of KIR2DS1 with a monoclonal antibody [243].

Due to the assumptions of the 'missing self' hypothesis, it seems intuitive that the absence of C2 ligand on the recipient cells would be beneficial when combined with the presence of KIR2DL1 in the donor. Studies reporting such association for KIR2DL1 and other inhibitory KIR can be indeed found in the literature [244-247]. In a study by Hsu *et al*. testing the missing KIR ligand effect in HLA-identical sibling transplantation, missing KIR ligand in the recipient led to a decrease in disease relapse in acute myeloid leukaemia and myelodysplastic syndrome [244]. Similar effects were later reported for unrelated donor allogeneic HCT [246, 247].

Further advocating the importance of KIR2DL1 for the outcome of HSCT, Bari *et al.* found that allelic polymorphism at position 245 has influence on the survival rate and the incidence of disease progression in pediatric patients who had received allogeneic HSCT. Their study has shown that patients who received a donor graft containing the functionally stronger KIR2DL1 allele with arginine at amino-acid position 245 had better survival (HR for patients who received KIR2DL1-R^{245} homozygous graft was 0.4) and lower cumulative incidence of disease progression (HR for patients who received KIR2DL1-R^{245} homozygous graft was 0.38) than those patients who received a graft containing only the functionally weaker KIR2DL1 allele with cysteine at the same position [248].

1.7.4 KIR2DL1 and KIR2DS1 in pregnancy disorders

NK cells represent the dominant leukocyte subset in the decidua (uterine endometrium in pregnancy) and have been found vital for the healthy placentation [249]. Placental cells in direct contact with the maternal blood that supply the nutrients and oxygen are known as villous trophoblast. These cells are deficient in HLA molecules [250] and common activating ligands for NK cells, such as MICA, MICB or ULBP [251]. On the other hand, extra-villous trophoblast, which originates from trophoblast cells that broke away and migrated through the decidua itself, is known to express HLA-E, HLA-G, and HLA-C, but not HLA-A and HLA-B which makes them good targets for NK cells which they encounter in decidua [250, 252-254]. However, decidual NK cells differ significantly from peripheral blood NK cells, i.e. they are only weakly cytotoxic [255-257]. In contrast, they are known to be important for regulating of the trophoblast invasion and remodelling of arteries [249, 258].

Ashley Moffett and colleagues compared maternal *KIR* genotypes in combination with fetal *HLA-C* genotypes in pregnancies where complications arose from poor trophoblast invasion (pre-eclampsia, fetal growth restriction or recurrent miscarriage) compared with ethnically-matched controls who had a normal first pregnancy [258-262]. In all analysed populations (UK, Norwegian and Ugandan populations) the frequency of maternal KIR AA genotypes in combination with a HLA-C2 epitope inherited from the father was increased in women with affected pregnancies. As the main difference between the KIR A and B haplotypes is the number of activating *KIR* genes, this genetic evidence indicated that excessive inhibition of uterine NK cells associated with two A *KIR* haplotypes present may be detrimental for healthy placentation.

The activating *KIR* genes associated with the lower risk of pre-eclampsia vary in different populations. In Europeans, *KIR2DS1* in the telomeric region of the *KIR B* haplotype has a protective effect [258, 259]. Hiby *et al.* who studied the combined cohorts with pregnancy disorders found that the telomeric end of the *KIR B* haplotype was present in 45% of controls but only in 33% of affected pregnancies (OR 0.60) and in particular *KIR2DS1* gene was present in 32% of affected pregnancies compared with 43% of controls (OR 0.63). In the same study, KIR2DS1 expressed on the uterine NK cells was shown to specifically bind to the $C2^{+}$ trophoblast cells [259]. In Ugandan population, protection from pre-eclampsia was found to be associated with particular centromeric regions characterized by the presence of KIR2DS5 (OR = 0.59) [262].

1.7.5 KIR2DL1 and KIR2DS1 in cancer and autoimmune conditions

The role of activating and inhibitory KIR2D receptors in cancer is not well understood and seems to vary with type of cancer, therapy and clinical measurement. Amongst the reported associations, *KIR2DS1* gene frequency was found to be higher in breast cancer patients than in healthy controls (54.5% vs. 31.2%), while the frequency of KIR2DL1 was lower in the patient group compared to the controls (90.0% vs. 100%) [263]. In addition, a study including chronic myeloid leukaemia patients receiving a therapeutic antibody Imatinib, identified KIR2DS1 as an independent predictor for shorter progression-free survival (relative risk (RR) = 3.1) and overall survival (RR = 2.6) [264].

A number of associations with autoimmune diseases has been reported for KIR2DS1, suggesting that it can mediate contradictory effects in different conditions. For instance, *KIR2DS1* gene was found to be less common in patients with atopic dermatitis than in healthy controls (OR = 0.629) [265], but was carried with higher frequency in patients with SLE (OR = 4.544) [266], suggesting that KIR2DS1 might play opposite role in the pathogenesis of these two conditions.

KIR2DS1 and KIR2DS2 were also suggested to be associated with an increased susceptibility to psoriatic arthritis, but only in the absence of their cognate HLA ligands (27% individuals in patients group and 15% in controls had *KIR2DS1* and/or *KIR2DS2* without the corresponding ligand) [267]. A contrasting finding was later reported for *Psoriasis vulgaris*, where *KIR2DS1* and its cognate ligand *HLA-Cw6* were found to be more frequent in the patients group compared to the healthy controls (OR = 16.44 for Cw4 and 5.55 for KIR2DS1). Moreover, the association of *HLA-Cw*06* in the

absence of *KIR*2DS1 was two times weaker than in its presence, suggesting that these two detected associations are not entirely independent [268].

Table 1.4 Association of KIR receptors with selected medical conditions

Clinical context	Receptor implicated	Reported association	References
HIV infection	KIR3DS1	Delayed progression to AIDS in the presence HLA-Bw4, rapid progression to AIDS in the absence of HLA-Bw4	[235]
	KIR3DL1	Early control of viral load when in combination with HLA alleles with the greatest inhibitory capacity	[238]
HCV infection	KIR2DL1	When co-carried with HLA-C1, beneficial effect in individuals infected with low doses	[241]
Hematopoietic stem-cell transplantation to treat acute myeloid leukemia	KIR2DS1	Allografts from KIR2DS1^{+} HLA-C1^{+} donors are associated with lower probability of relapse	[242]
	KIR2DL1	Lack of HLA-C2 ligand for donor KIR2DL1 leads to decreased risk of relapse and improves survival outcome, donor grafts containing the functionally stronger KIR2DL1 allele are associated with better survival and lower cumulative incidence of disease progression	[244, 247, 248]
Pre-eclampsia	KIR2DS1 in the telomeric region of B haplotype	Protective in European population, associated with enhanced placentation	[258, 259]
	KIR2DS5 in centromeric regions	Protective in Ugandan population	[262]
Breast cancer	KIR2DS1	Gene frequency increased in patients vs healthy controls	[263]
Chronic myeloid leukemia	KIR2DS1	Identified as predictor for shorter progression-free and overall survival	[264]

Atopic dermatitis	KIR2DS1	Gene frequency lower in patients than in healthy controls	[265]
Systemic lupus erythematous	KIR2DS1	Gene frequency increased in patients than in healthy controls	[266]
Psoriatic arthritis	KIR2DS1, KIR2DS2	In the absence of their cognate HLA ligands associated with an increased susceptibility	[267]
Psoriasis vulgaris	KIR2DS1	Combination with HLA-Cw6 ligand more frequently found in patients than healthy controls	[268]

1.8 Surface organization of NK cell receptors – insights from imaging studies

Since NK cell recognition is mediated by surface expression of certain molecules on target cells, it seemed intuitive that direct contact between an NK cell and a potential target would have to occur. Imaging of such intercellular contacts in the *in vitro* co-cultures has led to the discovery that upon the contact, receptors and adhesion molecules at the NK-target cell interface are rapidly re-arranged into a highly organized structure – today known as immune synapse [47]. Following that initial discovery, it has quickly become clear that alongside the ligand specificity and binding affinity which control the signalling through NK cell receptors, the way these molecules are organized at the plasma membrane is also important. Our knowledge about the relation between the receptor patterns and NK cell activation has been progressing together with the development of microscopy. Imaging techniques which have proved exceptionally useful for studying the immune cells contacts are summarized below, together with the specific insights that came from these studies.

1.8.1 Fluorescent labelling of proteins

The first step to studying a protein localization by fluorescence microscopy is attaching a chemical compound that can re-emit light upon light excitation, called fluorophore, to it in a highly-specific manner. Although a number of new labelling strategies have been recently proposed, the two strategies that were developed first still remain the most common ways to fluorescently stain cellular components. These

include (1) using molecular biology to construct fusion proteins, which include the protein of interest tagged with a fluorescent protein (such as GFP from the jellyfish *Aequoria Victoria*), and (2) attaching a fluorophore to an antibody, either targeting a protein of interest or an Fc portion of that specific antibody.

Both these ways have their advantages and disadvantages. The strength of fluorescent proteins is that they can be used in live cells (or even in live organisms), allowing studying of dynamic processes in real-time. However, preparation of such probes is a lot more time-consuming and more importantly, they are often subject to significant photobleaching when higher laser power is used, and therefore are not suitable for all applications (e.g. they have limited use in most super-resolution microscopy techniques). In contrast, fluorescently-tagged antibodies allow quick and efficient labelling of many cellular proteins and can be conjugated with a large variety of fluorescent compounds of different spectral properties and often a superior stability. Unfortunately, they are not suitable for use in live cells and require chemical fixation and often permeabilization of the cells.

The molecular basis of fluorescence is in principle the same for fluorescent proteins and compounds with lower molecular weight. In a resting fluorophore, electrons populate the relatively low-energetic ground state. When they absorb a photon of appropriate wavelength (i.e. are excited by the laser beam), transition to the higher energy level occurs followed by the relaxation of electrons from the excited state to the ground state.

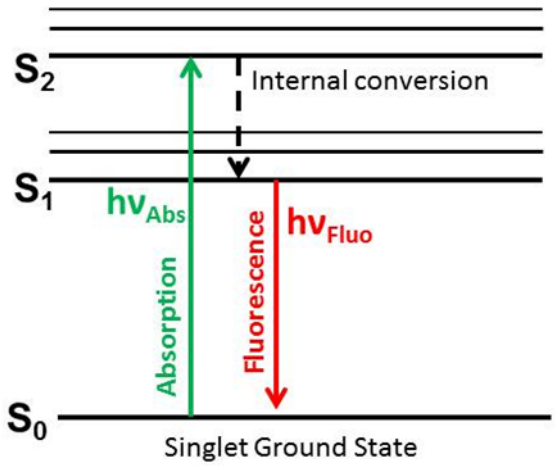

Figure 1.7 Jablonski diagram.
In a resting state, electrons populate the low-energetic ground state. When they absorb a photon of appropriate wavelength, transition to the higher energy level occurs followed by the relaxation of electrons from the excited state to the ground state. Part of the excess energy is emitted as fluorescence. The diagram shown here is a simplified version of the original and only transitions resulting in fluorescence are shown.

During the process of relaxation, the excess energy is emitted as fluorescence – characterized by the longer wavelength (and thus lower energy) than the originally absorbed photon. This has been illustrated by the Polish physicist Aleksander Jabłoński in a diagram depicted in Figure 1.7.

1.8.2 Imaging of immune synapse

The immune synapse has been originally described in the context of directed cytokine secretion between T cells and APCs [46]. The NK cell synapse was described soon after that by Daniel Davis and colleagues who studied the contact interfaces between NK cell line YTS and 721.221 cells transfected to express HLA-Cw3-GFP or HLA-Cw4-GFP fusion proteins [47]. This was achieved using laser scanning confocal microscopy.

Laser scanning confocal microscope was developed in response to the problems of wide-field fluorescence microscopy, in which the whole field of view is evenly illuminated and photons from the entire image are collected at the same time, resulting in high background noise from out-of-focus planes obscuring the image. In confocal microscopy, fluorophores are excited by a point illumination (a laser source) that is scanned line by line across the sample. The fluorescence signal is detected by a point detector (achieved by using a pinhole in front of the detector). The combination of selective illumination and point detection eliminates the out-of-focus light and produces clearer images. The first confocal laser scanning microscope was developed by M. David Egger and Paul Davidovits in 1969 has quickly proved useful for studying biological structures [269, 270].

In the experiments by Davis *et al.,* the confocal microscopy revealed clustering of target cell HLA-GFP proteins and NK cell KIR receptors (labelled with a fluorescently-conjugated antibodies) at the site of the contact. Prompted by this observation, the authors used a motorized stage to take images of multiple confocal planes and discovered that while in unconjugated cells the GFP-tagged HLA proteins has uniform distribution, a ring of HLA protein was clearly visible in the plane of the contact between 722.221/Cw4-GFP cell and YTS cell transfected to express KIR2DL1. Staining of an adhesion molecule ICAM-1 with antibodies revealed that this molecule concentrated at the centre of the HLA ring. The formation of such synapses required a divalent transition metal cation but was not dependent on adenosine triphosphate (ATP) or cellular cytoskeleton [47].

1.8.3 Diversity of immune synapses

The synapses described by Davis *et al.* served to transduce an inhibitory signal – and therefore have been named inhibitory, as opposed to the synapses formed between an NK cell and a susceptible target cell leading to cytotoxic events (activating) and more recently discovered 'regulatory' synapses formed between NK cells and DCs [271] or macrophages [272].

The inhibitory and activating NK cell synapses differ in some ways and for instance, actin cytoskeleton has been shown to polarize to the activating synapse and accumulate at its periphery forming a dense ring of filamentous actin (f-actin) [54-56, 147]. In contrast, accumulation of actin at the inhibitory synapses has not been observed [273, 274]. In the centre of an activating synapse, the actin mesh has been shown to increase its periodicity to allow the movement of the lytic granules through the mesh. At the inhibitory synapse however, this actin remodelling does not occur, as shown in the Figure 1.8 [55, 56].

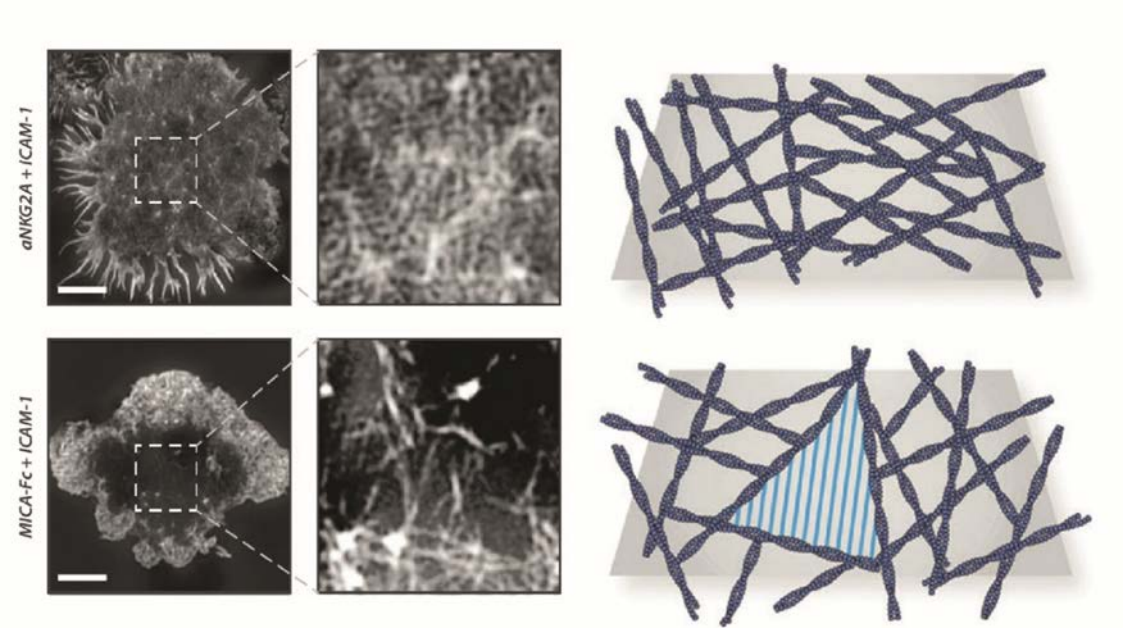

Figure 1.8 Remodelling of the actin mesh at an activating NK cell synapse.

Extract from [275]; data taken from Brown et al. [56]. Images show NK cells with F-actin stained with fluorescently-labelled phalloidin and visualized by 3D-structured illumination microscopy. When cells are not activated, i.e. plated on surface coated with antibodies against inhibitory receptor NKG2A and an adhesion molecule ICAM-1, actin forms a dense mesh (top row). When cells are activated on surfaces coated with activating ligand MICA and ICAM-1, the periodicity of the actin mesh increases (bottom row) to reveal regions (blue hatched area) predicted to be penetrable by lytic granules or vesicles containing cytokines. Scale bar = 5 µm.

Interestingly, one NK cell can sustain multiple immune synapses simultaneously, even interacting with both resistant and susceptible targets at the same time [47]. The signalling occurring at each synapse seems to be spatially restricted – the experiments in which the effector-target cell contacts were micromanipulated using optical tweezers to allow temporal and spatial control demonstrated that NK cells which already bound to a resistant target cell may simultaneously bind and kill a susceptible target cell [276].

1.8.4 Structure of immune synapse

The structure of an immune synapse was initially compared to the 'bull's-eye' pattern and concentric ring-shaped domains to which distinct molecules localized were designated as the central, peripheral and distal supramolecular activation cluster (c-, p- and dSMAC), respectively [54, 277]. However, it was later established that NK cell synapses do not always display this 'bull's-eye' pattern. Confocal microscopy of 721.221 cells transfected with GFP-tagged HLA-Cw6 and co-incubated with YTS cells transfected with KIR2DL1 revealed that alongside the ring-shaped pattern, other patters can be formed as well to achieve the segregation of inhibitory receptors from adhesion molecules. Which specific pattern is applied appears to be dictated by the expression levels of HLA-C on target cells. When the YTS NK cells formed synapses with target cells expressing low levels of HLA-C, a multifocal patterning of MHC class I protein was found dominant, whereas higher levels of expression were correlated with HLA-C more commonly forming structures which were homogeneous, ring-shaped, or containing multiple exclusions. Basing on these observations, the authors proposed that controlled patterning of proteins at intercellular contacts could be a way to transmit the information about protein expression levels between cells [226].

1.8.5 Importance of immune synapse

The importance of the NK cell immune synapse has been supported by a huge body of work and in particular by imaging studies. It provides a platform where ligands can be recognized accurately by their cognate receptors among the prevalence of non-relevant ligands. It is clearly the site of active signalling – the recruitment of downstream signalling molecules to the membrane domains occupied by the receptor assemblies has been observed using confocal microscopy. Importantly, this has been observed for both activating receptors - such as NKG2D, which was shown to co-localize at the synapse with Grb2 and Vav1 [147], and inhibitory receptors – such as KIR2DL1, whose phosphorylation is spatially restricted to the immune synapse, as

evidenced by the localization of anti-tyrosine-derived fluorescence and triggers the recruitment of Lck kinase to the synapse [278]. This is related to another role of an immune synapse – facilitating of the signal integration. The ability of KIR2DL1 to inhibit the NKG2D-mediated activation has been shown to be dependent on these receptors co-localizing at the immune synapse [279]. A study from Eric Long's group identified Crk, an adapter protein associated with cytoskeleton scaffold complexes as a regulator of signal integration in NK cells [232]. Crk was required for both CD16-derived activation signals and their inhibition upon CD94/NKG2A ligation. The authors proposed that Crk contributes to the signal integration in two ways – via disruption of actin-dependent processes such as the clustering of CD16 at the synapse and through relaxing the confinement of receptors within the mesh of cortical actin leading to more efficient engagement of activating receptors once inhibition is removed [232].

In addition, the assembly of immune synapse enables a directional secretion of cellular components. The polarization of the intracellular transport machinery to the synapse and reorganization of cortical actin mesh allow the lytic granules to be secreted directly at the contact interface [51, 280]. A polarization of cytokines at the immune synapse has also been reported and for example the directional secretion of preassembled stores of IL-12 by DCs toward the NK cell was shown to require formation of the synapse [271].

A recent study from our laboratory reported a novel function of the immune synapse and demonstrated that it can exclude molecules above a certain size from the site of the contact, in a zipper-like manner [281]. This was demonstrated by quantifications of relative intensity of fluorescence derived from differentially-sized dextran molecules at the synapses formed by primary NK cells and NK cell lines. Dextran sized ≤ 4 nm could move in and out of the immune synapse, but 10 – 13 nm dextran had a reduced access, and dextran ≥ 32 nm was virtually absent from the synapse. This was also true for proteins and for example, low-density lipoprotein (LDL) which has a diameter of 21.4 ± 1.3 nm was largely excluded from the synapse. This size-dependent exclusion is likely to be important for the NK cell mediated cytotoxicity, since LDL can inhibit the action of perforin [282], but also for the efficacy of antibodies-based therapies targeting synapse components - the full antibodies were also excluded from the synapse, while Fc fragments were not [281].

1.8.6 Imaging of NK cell surface with higher resolution

The above studies have mostly applied confocal microscopy to study the organization of NK cell synapse, but some of them also used a different microscopy technique, called total internal reflection fluorescence (TIRF) microscopy (also known as evanescent wave or evanescent field microscopy). This technique is particularly useful for visualization of the fluorescent structures in the close proximity to the glass slide, and as such it is widely used for studying the minimalistic model of the immune synapse where cells are interacting with glass surfaces coated with purified ligands or antibodies specifically targeting the receptors.

TIRF microscopy is based on selective excitation of the fluorophores near the glass surface (e.g. within the plasma membrane) and minimizing the fluorescent signals from the intracellular regions localized higher up [283, 284]. This is achieved by illuminating the sample at a critical angle so that the light is totally internally reflected at the glass coverslip-aqueous sample interface. Thus, no direct illumination reaches the sample. Instead, an evanescent wave is created within the sample, which decays exponentially from the interface and penetrates the sample to a depth of only approximately 100 nm. As a result, only the fluorophores within this evanescent field are excited and the background out-of-plane fluorescence is eliminated.

1.8.7 Formation of the receptor microclusters

Advances within the field of microscopy, and in particular TIRF microscopy, helped to establish that receptors and other membrane-proximal proteins at the immune synapse commonly organize into discrete micrometre-scale assemblies. Such microclusters of proteins have been observed in T cells, B cells, and NK cells and were for a long time considered to be a basic unit of lymphocyte signalling [49, 53, 231, 285, 286].

The microcluster formation has been extensively studied for TCR. TCR microclusters can be readily observed within seconds of ligand binding, as established by live-cell TIRF microscopy of the activated AND TCR transgenic T cells in contact with supported lipid bilayer incorporating agonist peptide-MHC (pMHC) and ICAM-1 [53]. In this system, already within 30 s after contact with the bilayer, TCR microclusters are co-localized with activated forms of Lck and ZAP-70 kinases and LAT adaptor. As the contact persists, the kinases disappear from the older centrally located microclusters and are enriched within the newer peripheral TCR clusters, which then move in an actin-dependent manner from the periphery towards the centre, where they become

signalling-deficient [53, 287]. Recruitment of the downstream signalling molecules and their subsequent loss in the centre of the synapse indicated that microclusters of TCR could serve as actin-dependent scaffold regulating the signal propagation.

In a similar experimental setup, where NK cells interacting with activating lipid bilayers were imaged in real-time by TIRF microscopy, a centripetal trafficking has been observed for the NKG2D receptor [231]. In contrast to the TCR, NKG2D clusters do not fuse into a central SMAC. Instead, within minutes of the contact with bilayer, NKG2D clusters were shown to merge with other clusters into a ring-shaped structure surrounding a central domain where lytic granules dock [49, 231]. Similar to clusters of TCR, the evidence for active signalling occurring at the NKG2D microclusters was found - in NKL cells that were fixed on bilayers containing ULBP3 and ICAM-1 and then stained with antibodies against phosphotyrosine (pY), the pY-derived signal was overlapping with the NKG2D microclusters. Similar to observations for TCR, the phosphotyrosine staining was more intensive within the peripheral microclusters [231]. In addition, live-cell imaging of the conjugates formed between Daudi B cells transfected with MICA and NKL cells expressing Vav1-GFP and Grb2-mCherry fusion proteins revealed that both Vav1 and Grb2 co-localized with the NKG2D microclusters during their trafficking [56].

An Fc receptor CD16 was observed to form similar microclusters in NK cells incubated on lipid bilayers carrying Fc fragments [232]. This was visualised by TIRF microscopy of fluorescently-labelled bilayer-bound Fc fragments, which upon the contact with human primary NK cells formed peripheral microclusters, which moved towards the centre, where they accumulated. The three-dimensional confocal imaging of the cells fixed on the same bilayers and stained with phosphospecific antibodies to Vav1 revealed that staining for pY174-Vav1 displayed a significant overlap with the Fc clusters, indicating again that the receptor microclusters are the active signalling sites [232].

Formation of the microclusters has been also reported for the inhibitory NK cell receptors. Treanor *et al.* used fluorescence lifetime imaging (FLIM) to study KIR phosphorylation in YTS cells contacting target cells expressing cognate HLA ligand [288]. This approach is used to quantify Förster resonance energy transfer (FRET), which involves the non-radiative transfer of energy from an excited donor fluorophore to a nearby acceptor and can be used to detect molecular interactions on the nanometre scale [289]. In these experiments, the energy donor was GFP fused to the cytoplasmic portion of KIR2DL1 and the FRET acceptor was a Cy3 molecule, conjugated with a generic anti-pY antibody. Since the most robust way to detect FRET

is through recording a decrease in the fluorescence lifetime of the donor fluorophore (in this case GFP), the KIR phosphorylation was investigated by comparing the fluorescence lifetime of GFP-tagged KIR2DL1 between unstained cell conjugates and conjugates stained with Cy3-labelled anti-pY antibody [288]. The phosphorylation of KIR could be indeed detected using this method - the mean lifetime of GFP signal in conjugates stained for pY was 5–10% lower than unstained control cells. Importantly, the phosphorylation of KIR was confined to discrete microclusters, implying their role in the signalling. In addition, when YTS/KIR2DL1 cells were transfected to express an Lck-YFP fusion protein and co-incubated with 721.221 cells expressing HLA-Cw6, the Lck kinase readily assembled into microclusters at the contact site, further supporting the role for microclustering in the signal transduction [278].

Microclusters of the NK cell inhibitory receptors were also described by Morgan Huse's group, who used a photochemical approach, in which a semisynthetic pMHC complex that is nonstimulatory to KIR2DL2 could be converted into the functioning ligand by irradiation with UV light [231]. Photostimulation of KIR2DL2-expressing NKL cells on surfaces containing this reagent triggered the formation of inhibitory receptor microclusters accompanied by retraction of cells and inhibited the formation of activating receptor microclusters [231].

1.9 Application of super-resolution microscopy to study NK cell surface

1.9.1 Limitations of traditional microscopy

The traditional fluorescence microscopy techniques are all subject to the resolution limitations referred to as the diffraction barrier, which restrict the ability of optical microscopes to distinguish between two objects separated by a lateral distance less than approximately half the wavelength of light used to illuminate the specimen. This is the consequence of one of the fundamental physics laws which was described by Ernst Abbe in 1873 using the following equation:

$$Abbe\ resolution_{x,y} = \lambda/2NA \qquad \text{(Equation 1)}$$

where λ is the wavelength of light used to excite the specimen, and NA is the numerical aperture (for a microscope objective, it describes the aperture angle).

In practice, this is imposed by the diffraction of visible light wave fronts as they pass through the circular aperture at the rear focal plane of the objective. The only mechanism for optimizing spatial resolution is to minimize the size of the diffraction-limited spots by decreasing the imaging wavelength, but even under ideal conditions and with the most powerful objectives, lateral resolution is limited to about 200 to 250 nm, due to transmission characteristics of glass at wavelengths below 400 nm and the physical constraints on numerical aperture. The smallest representation of a single object that the imaging system can create is called a point spread function (PSF) and is used to reflect the quality of the microscope. If the PSFs of two neighbouring fluorophores overlap, the microscope is unable to resolve them as two distinct objects. Since most biological specimens, such as membranes, are composed of the basic units (i.e. lipids and proteins) which are densely packed and a lot smaller than 200 nm, the exact arrangement of these components could never be resolved with the traditional approaches. Until recently, the main way to study the organization of membrane proteins at the nanometre-scale resolution was by using electron microscopy to visualize proteins which had been immunogold-labelled – targeted with an antibody conjugated with gold particles of nanometre-scale sizes.

The last decade however, brought some superior advances in the field of fluorescent microscopy. A number of techniques has been developed, which use different approaches to break the diffraction barrier and are collectively known as super-resolution microscopy techniques. The super-resolution microscopy has been celebrated by the 2014 Nobel Prize in Chemistry, awarded to Stefan W. Hell, for the development of a method called stimulated emission depletion (STED) microscopy, and Eric Betzig and William Moerner, who working separately laid the foundation for the second method, single-molecule microscopy.

1.9.2 Super-resolution microscopy

Single-molecule localization microscopy has proved exceptionally useful in studying the nanometre-scale organization of immune receptors. The idea behind this group of techniques is that if the signal from the individual fluorophores within the specimen could be resolved in time, and only a few of them would be active at any particular moment, this would effectively improve the spatial resolution of the image. Therefore, in the single-molecule localization techniques, the images are reconstructed from thousands of frames recorded one after another, each one containing the localisations of only a few fluorescent molecules. This resolution in time is achieved by selective

switching of a fluorescent molecule between either a bright and dark state (photoswitching) or between one fluorescence emission spectrum and another (photoconversion). The principle of image reconstruction in single-molecule localization techniques is presented in Figure 1.9.

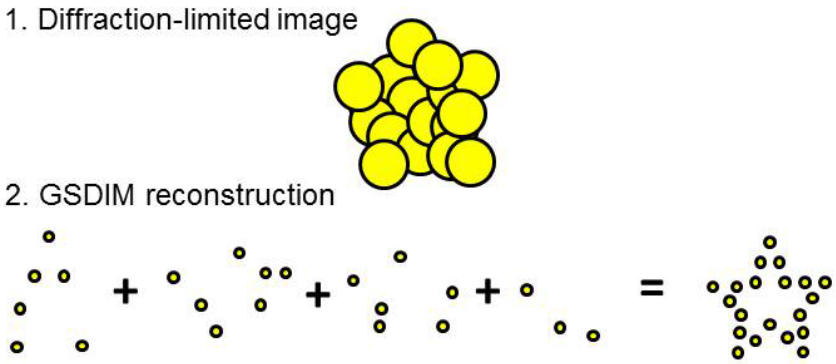

Figure 1.9 Principle of image reconstruction in single-molecule localization techniques.
In traditional fluorescence microscopy, the PSFs of two neighbouring fluorophores localized within ~ 200 nm, or closer, overlap and therefore the microscope is unable to resolve them as two distinct objects. In single-molecule localization techniques, the signal from individual fluorophores within the specimen is resolved in time by selective photoswitching or photoconversion of fluorophores. The images are reconstructed from multiple frames, each one containing the localisations of only a few fluorescent molecules.

Two widely used single-molecule localization techniques are photoactivated localization microscopy (PALM) and stochastic optical reconstruction microscopy (STORM). The main difference between them is the fluorescent probes used for imaging - PALM exploits photoactivatable and photoswitchable fluorescent proteins, while STORM is mostly based on labelling of the proteins with antibodies conjugated with fluorophores.

PALM was originally demonstrated using the photoactivatable proteins Kaede and dEosFP to image specific proteins in various cellular structures, such as mitochondria, lysosomes, lamellipodia and the plasma membrane [290]. Virtually at the same time, an almost identical technique was described by another group, who validated it by imaging photoactivatable GFP proteins on glass and on a terraced sapphire crystal surface and named it fluorescence photoactivation localization microscopy [291]. A great advantage of PALM microscopy is its compatibility with live-cells imaging. The fluorescent probes are fused to the proteins of interest using means of molecular biology. However, most of the studies are still performed in fixed cells, due to the long acquisition time required to obtain a PALM image. Nevertheless, efficient live cell

PALM imaging has been demonstrated by multiple groups and was used to study diverse cellular components [292-295].

STORM was originally based on the photoswitching of cyanine dyes when located in close proximity to each other (less than 2 nm). It was first demonstrated using the pair of Cy3 and Cy5 dyes to label short DNA molecules [296]. Since then, it has been widely used to study proteins labelled with antibodies and several improvements to this technology have been introduced, such as the possibility of multi-channel imaging [297] and three-dimensional STORM [298]. A variant of STORM extending the use of this technique to conventional dyes, such as popular Alexa Fluor (AF) dyes, has also been developed and named direct STORM (dSTORM) [299]. Ground-state depletion with individual molecule return (GSDIM) microscopy used in this study is a technique almost identical to dSTORM. Both these methods utilize highly powerful lasers to photoswitch conventional dyes into dark state, from which they stochastically return producing a short-lived fluorescent signal.

The reversible photoswitching of standard dyes requires the presence of oxygen scavengers, such as glucose oxidase, and thiols, such as β-mercaptoethylamine or β-mercaptoethanol [299, 300]. This and the common use of antibodies for labelling result in the most important limitation of STORM and GSDIM approaches – it is not well suited for live-cells imaging. However, STORM imaging in life cells although challenging, can be still performed using for example the recently described SNAP and CLIP fusion proteins, which can be labelled with different fluorophores in living cells [300, 301].

Alongside the single-molecule localization techniques, STED is another approach enabling studies of biological structures on nanometre scale. In this method, a controlled de-excitation of previously excited fluorophores is used to shape the PSF. This is executed by illuminating the sample with two laser beams simultaneously: a focal spot stimulates fluorescent molecules to glow, while a second, doughnut-shaped beam of longer wavelength (STED beam) depletes the fluorescence from the molecules in the outer part of the excitation PSF, minimising the volume in which the fluorescence is emitted. The STED principle is presented in Figure 1.10. This technique was first developed and successfully implemented by Stefan Hell and colleagues [302]. In theory, the resolution of this technique can be infinitely small and in practice, the resolution of 20 nm is often achieved by the STED systems [303-305]. This approach can work with a variety of fluorophores, some of which are suitable for live-cells imaging [306].

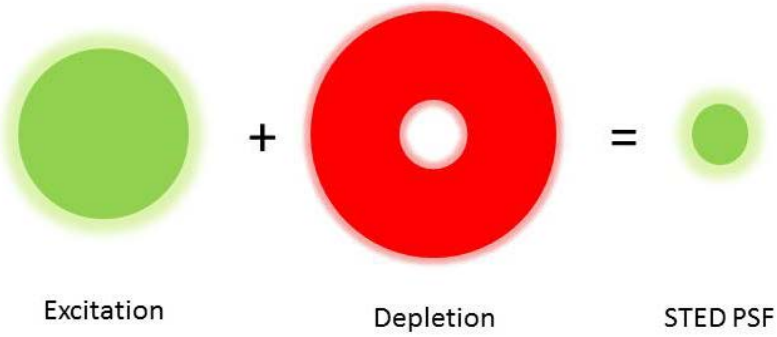

Figure 1.10 Principle of STED microscopy.
The sample is illuminated with two laser beams simultaneously: a focal spot excites fluorescent molecules, while a doughnut-shaped beam of longer wavelength (STED beam) selectively de-excites the fluorophores in the outer part of the excitation PSF, minimising the volume in which the fluorescence is emitted.

1.9.3 Studying of NK cell surface with super-resolution

Application of super-resolution microscopy to study plasma membrane organization in immune cells quickly demonstrated that most of the imaged surface molecules were not homogenously distributed in the plasma membrane, and instead formed nanometre-scale assemblies, termed nanoclusters. Examples of structures of different sizes that can be observed at the NK cell surface using particular microscopic techniques are shown in Figure 1.11.

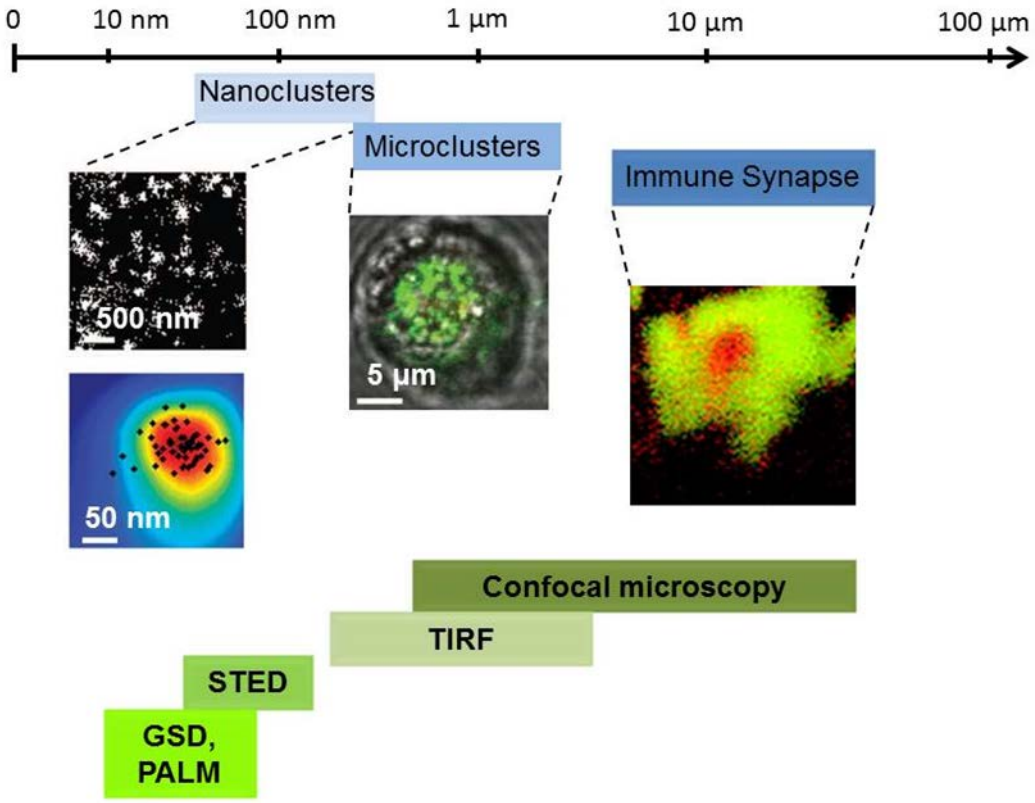

Figure 1.11 Different scales of NK cell receptors organization
Developments in the field of fluorescent microscopy enabled studying different levels of organization of the NK cell receptors. Confocal microscopy has been originally used to describe the NK cell immune synapse. Later, together with TIRF microscopy, it revealed the existence of the receptors microclusters. Most recently, super-resolution techniques, such as STED and GSD microscopy led to the discovery of pre-formed nanoclusters of NK cell receptors at the plasma membrane.

The link between the nanoclustering of surface molecules and the cellular activation has been best explored in T cells. Formation of TCR oligomers at the surface of non-stimulated T cells has been first suggested by the biochemical studies and electron microscopy [307]. More recently, nanometre-scale assemblies of TCR and LAT were observed in PALM images of the plasma membrane sheets from quiescent T cells by Lillemeier *et al.*, who named these structures protein islands [308]. Such pre-clustering of TCR and LAT in the membrane of resting T cells was also reported in another study by Sherman *et al.* [309]. The important difference between these two studies is what was proposed to happen at the T cell membrane following the activation. Lillemeier *et al.* found that upon TCR ligation, the protein islands concatenated into larger structures (which were suggested to be the microclusters, observed earlier by diffraction-limited microscopy), but remained as discrete subunits within microclusters without

exchanging their content [308]. In contrast, Samelson's group reported that during microcluster formation, molecules of TCR, LAT, and kinase ZAP-70 become mixed to some extent [309]. These differences might be likely caused by different experimental systems used in the above studies – while Lillemeier *et al.* used plasma membrane sheets generated from 5c.c7 primary T cells isolated from lymph nodes of transgenic mice, Sherman and colleagues performed their imaging studies in Jurkat T cell line.
Furthermore, a study from the group of Katharina Gaus combining imaging of LAT with PALM and phosphorylated form of LAT with dSTORM, demonstrated that phosphorylation of LAT was largely limited to clusters of approximately 80 nm in diameter and identified these structures as intracellular vesicles [310]. These results indicated that pre-clustered LAT molecules did not participate in the signalling. The comprehensive review of the imaging data on signalling clusters in T cells has been recently published by Sherman *et al*. who attempted to combine the insights from these and other studies into a uniformed model of molecular clustering at the T cell plasma membrane [311].

` The proteins crucial for B cell signalling are also known to form nanoclusters at the surface or resting B cells. Facundo Batista's group visualized the molecular organization of endogenous BCR in primary B cells by dSTORM to check if similarly to TCR, BCR-mediated signalling was also associated with its reorganization in the membrane. Their work demonstrated that endogenous IgM-BCR, IgD-BCR, and a co-receptor CD19 all form clusters within the plasma membrane of resting primary B cells and their organization is altered upon BCR crosslinking with $F(ab)_2$ fragments. Specifically, both BCR isotypes displayed significantly increased clustering upon crosslinking [312]. In addition, a more recent study from Michael Reth and colleagues reported that IgM-BCR and IgD-BCR are found in a closer proximity upon activation. This finding was made using dSTORM approach and was further confirmed by electron microscopy analysis [313].

In NK cells, super-resolution microscopy has been successfully applied to study the rearrangement of actin cytoskeleton at the activating synapse [55, 147, 314]. However, the nanometre-scale organization of the NK cell receptors has been less well explored, with only a handful of observations found in the literature. The first study using single-molecule localization techniques, PALM and GSDIM, to probe the nanometre-scale arrangement of KIR2DL1 was published in 2013 by our laboratory. We found that KIR2DL1 forms nanoclusters of a diameter of approximately 110 – 150 nm at the surface of human primary NK cells, as visualised by GSDIM, and human NK cell lines, imaged by PALM [224]. Quantitative analysis of the KIR2DL1 clustering revealed that

KIR2DL1 clusters became smaller and denser when the cells interacted with anti-KIR2DL1 antibodies-coated slides. More importantly, the same effect was triggered by the activation of cells via NKG2D. The changes in KIR2DL1 clustering were not a result of some general activation-induced remodelling of the plasma membrane, since MHC class I molecules in the same cells imaged in a control experiment displayed the same patterns of organization under all investigated conditions. Moreover, ligation of a different activating receptor, CD28, did not alter the organization of KIR2DL1, implying that this was specifically related to signalling through the NKG2D [218].

The findings of the above study implied that nanometre-scale organization of the NK cell receptors might be, similarly to T cells and B cells, linked to the process of signal transduction. However, the precise significance of the nanoclustering in the NK cell activation, as well as factors governing the nanometre-scale architecture of the NK cell plasma membrane remain a gap in the knowledge and need further investigation.

1.10 Aims

The overall aim of my thesis is to further our understanding of how nanometre-scale organization of NK cell receptors relates to the processes of signal transduction and integration. Although some evidence that clustering of NK cell receptors is modified under different activation states exists in the literature, the details of this aspect of NK cell biology have practically not been explored at all. The most important question is whether or not specific patterns of organization could make the receptors more or less capable to signal.

The model that I chose to explore this consists of paired NK cell receptors binding to MHC class I molecules – inhibitory KIR2DL1 and activating KIR2DS1. This pair of receptors is a valuable model for two main reasons. Firstly, they display very high structural similarity in their extracellular domains – therefore they are an easier system to study the link between the structure and clustering than two completely unrelated receptors. Secondly, KIR2LD1 and KIR2DS1 share the ligand specificity, which offers a great opportunity to investigate whether the nanoclustering patterns could impact both the activating and inhibitory signals in response to the same ligand.
The specific questions which I tried to answer in this work were:

1. How are the NK cell paired receptors KIR2DL1 and KIR2DS1 organized at the surface of NK cells on nanometre-scale? (Chapter 3)
2. What governs the KIR2DL1 and KIR2DS1 nanometre scale organization at the surface of NK cells? Is the amino-acid sequence of the proteins important? (Chapter 4)
3. How are the nanometre-scale organization patters related to the signal transduction? Are the nanoclusters the site of active signalling? Is the signalling favoured in the clusters of a particular size? (Chapter 5)

These questions were addressed using a range of complementary techniques, including two different super-resolution microscopy techniques, STED and GSDIM and site-directed mutagenesis.

Chapter 2: Experimental Procedures

2.1 Cell lines

The NKL/KIR2DL1-HA, NKL-KIR2DS1-HA, NKL/KIR2DL1-HA/KIR2DS1-FLAG and NKL/KIR2DL1-FLAG/KIR2DS1-HA cell lines were kind gifts from Dr Shaun-Paul Cordoba in our laboratory at the Imperial College London. They had been created by retroviral transduction of NKL cells with a retroviral vector pIB2, in which the coding sequences of KIR2DL1*002 and KIR2DS1*00502 followed by the coding sequence for a glutamic acid-phenylalanine linker and HA or FLAG tag were inserted. The KIR-deficient NKL cell line was established in 1996 from the peripheral blood of a patient with $CD3^{-}CD16^{+}CD56^{+}$ large granular lymphocyte leukaemia [315].

The leukemic T cell line Jurkat E6.1 was purchased from the American Type Culture Collection (TIB-152) and used to create Jurkat/KIR2DL1-HA and Jurkat/KIR2DS1-HA cell lines by retroviral transduction, as detailed below.

The 721.221/Cw4 and 721.221/Cw4/MICA cell lines were obtained from the frozen stocks of the Davis laboratory. 721.221 is a lymphoblastoid cell line in which the classical HLA class I locus was lost through γ irradiation [316]. Therefore, they make good targets for NK cells and when transfected with HLA they express only a single classical class I allotype. Cell lines used in this study had been created by the retroviral transduction of the 721.221 cell line and had been successfully used as target cells in the experiments previously published by Pageon *et al.* [224].

The Phoenix Ampho cell line was obtained from the Nolan laboratory at Stanford University, where it was originally developed. This cell line is a variant of the 293T cell line that has been stably transfected to express Moloney Murine Leukaemia Virus packaging proteins and can serve for the production of amphotropic retroviruses.

Culturing of cell lines

All cell lines were cultured at 37°C and 5% CO_2 in Roswell Park Memorial Institute (RPMI) 1640 culture medium (Sigma) supplemented with 10% fetal bovine serum (FBS; Invitrogen), 2 mM L-glutamine, and 1 % penicillin and streptomycin (both Gibco). Cell lines growing in suspension (NKL, Jurkat, 721.221) were maintained in 10 ml of medium in a 25 cm^2 tissue culture flask (Corning, Sigma) and expanded twice a week by transferring 1 ml of the culture into 9 ml of fresh media in a new flask. An adherent cell line Phoenix Ampho was maintained in 20 ml of medium in a 75 cm^2 tissue culture flask and expanded twice a week by detaching the cells using sheer flow of medium and transferring 1.5 ml of the culture into 18.5 ml of fresh media in a new flask.
NKL cell line was cultured in the presence of IL-2 (100 U/ml; Roche). NKL and Jurkat cell lines created by retroviral transduction were maintained in the presence of 10 µg/ml of the selecting antibiotic, blasticidin (InvivoGen).

Although Dulbecco's Modified Eagle Medium (DMEM) is typically recommended as a base culture medium for Phoenix cells, in this study these cells were maintained in a medium based on RPMI 1640. This was due to a better compatibility with the transduction of NKL and Jurkat cells. In a direct comparison I did not observe any difference in growth rate or condition of Phoenix cells cultured in either DMEM or RPMI 1640.

All cell lines were routinely tested for mycoplasma infection using a PCR-based kit (PromoCell), which utilizes specific primers designed from DNA sequences coding for highly conserved ribosomal RNAs (16S-rRNA). The test was conducted according to the manufacturer's instructions.

2.2 Generation and culture of primary human NK clones

PBMC from normal healthy volunteers were obtained by separation on a Ficoll-Paque gradient and primary NK cells were isolated from PBMC by negative selection with an NK isolation kit (Mitlenyi Biotec, Bergisch Gladbach, Germany). NK clones were generated by plating single NK cells in individual wells of a 96-well plate. Cells were cultured at 37°C and 5% CO_2 in clone medium composed of DMEM (Sigma), 10% human serum (Sigma), 15% F-12 Ham's nutrient formulation (Sigma), 1% penicillin and streptomycin, 2mM L-glutamine, 1mM sodium pyruvate, 1% Minimum Essential Medium (MEM) non-essential amino acids (Sigma).

For the first week, clone medium was supplemented with 1 x 10^8/ml irradiated (40 Gy) PBMC from two allogeneic individuals, 5 x 10^6/ml irradiated (40 Gy) RPMI 8866 cells, IL-2 (400 U/ml) and 5 ng/ml of phytohemagglutinin (Sigma). On day seven, cells

were passaged into fresh clone media supplemented with 1 x 10^8/ml irradiated (40 Gy) PBMC from two allogeneic individuals, 5 x 10^6/ml irradiated (40 Gy) RPMI 8866 cells and IL-2 (400 U/ml). After further seven days, cells were cultured in clone media supplemented with IL-2 (400 U/ml) and cell passage was repeated every 3 - 4 days.

2.3 Plasmid construction

The retroviral vectors pIB2-KIR2DL1*002-HA and pIB2-KIR2DS1*00502-HA were kind gifts of Dr Shaun-Paul Cordoba from Imperial College London. They had been created by introducing the coding sequences of *KIR2DL1*002* and *KIR2DS1*00502* into the pIB2 backbone using the BamHI and EcoRI restriction sites. Following that, the coding sequence for HA or FLAG tag was inserted into the EcoRI site by non-directional ligation, resulting in a glutamic acid-phenylalanine linker.

2.3.1 Site-directed mutagenesis

Point mutations in KIR2DS1 and KIR2DL1 sequence were introduced by site-directed mutagenesis using Q5 Site-directed Mutagenesis Kit (New England Biolabs), according to the instructions provided by manufacturer. In this approach, the substitutions within the DNA sequence are created by incorporating the desired nucleotide changes in the centre of the forward primer. Unlike the kits that rely on the linear amplification, primers designed for this kit do not overlap. Instead, the reverse primer is designed so that the 5' ends of the two primers anneal back-to back, as illustrated by Figure 2.1.

Primers were designed and annealing temperatures were calculated using the New England Biolabs online primer design software, NEBaseChanger™. All primer sequences are listed in the Table 2.1. The presence of desired point mutations was confirmed by DNA sequencing performed by GATC Biotech.

For transfection of cells, plasmids containing mutated DNA sequences were purified from 200 ml of liquid cultures of NEB 5-alpha Competent *E. coli* (supplied as part of the Q5 Kit) transfected with the appropriate plasmids according to the instructions supplied with the kit. The cultures were grown in Luria-Bertani medium for 15-16 hours, at 37°C, under constant shaking and in the presence of 100 µg/ml of ampicillin (Sigma). Plasmids were purified using the PureYield Plasmid Maxiprep Kit (Promega) according to the protocol supplied with the kit

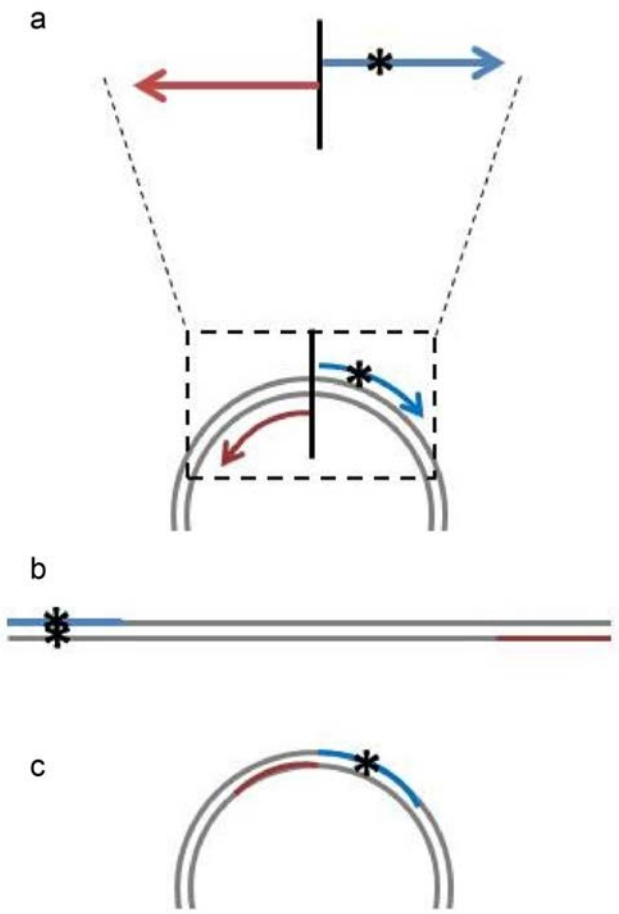

Figure 2.1 Site-directed mutagenesis.
In the mutagenesis approach used in this study desired nucleotide changes are introduced in the centre of the forward primer (blue, mutation marked with asterisk). The reverse primer (red) is designed so that the 5' ends of the two primers anneal back-to back (a). The linear product obtained from the PCR reaction (b) undergoes ligation in the following step (c).

Table 2.1 Primers used for site-directed mutagenesis.
Nucleotides corresponding to the desired change in the sequence are marked in red.

Mutation	Primer sequences	Annealing temperature
KIR2DS1 K233A	Forward 5'CTCAGTGGTCGCCATCCCTTTCACC3' Reverse 5'GTCCCAATCAGAACATGTAG3'	60°C
KIR2DS1 K233R	Forward 5'CTCAGTGGTCCGGATCCCTTTCAC3' Reverse 5'GTCCCAATCAGAACATGTAG3'	58 °C
KIR2DL1 I233K	Forward 5'CTCAGTGGTCAAGATCCTCTTCATC3' Reverse 5'GTCCCAATCAGAATGTGC3'	60 °C
KIR2DL1 Y281A/Y311A	Forward 5'CCCTTCTCAGAGGCCCAAGACACCCCCAACAGA TATCATCGTGGCCACGGAACTTCCAAATGCTG3' Reverse 5'CGAGTGATTTTTCTCTGTGTGAAAACGCAGTGAT TCAACTGTGTGGCTGTCACCTCCTGAGGGTC3'	63 °C

2.4 Retroviral transduction of cell lines

NKL and Jurkat cells were transfected to express KIR2DL1-HA, KIR2DS1-HA and their mutated forms by retroviral transduction using the packaging cell line Phoenix Ampho. In the first step, 10 µg of plasmid DNA was used to transfect approximately 80% confluent 75 cm^3 tissue culture flask of Phoenix Ampho cells. For this, 30 µl of cationic lipid/polymer-based cytofectin Lipofectamine 3000 (Invitrogen) was diluted in 0.5 ml of Opti-MEM I Reduced-Serum Medium (Gibco). The DNA was also diluted in 0.5 ml of Opti-MEM medium and 20 µl of P3000 Reagent (Invitrogen) was added. Next, the two solutions were mixed, incubated at room temperature for 5 min and added to the Phoenix cells in a dropwise manner, after which cells were incubated at 37°C and 5% CO_2 for 3 days.

The viral supernatant was then removed from the Phoenix cells, sterile filtered and used for infection of NKL or Jurkat cells. For this, 10^6 cells were placed in a well of a 6-well tissue culture plate in 1 ml of the normal culture medium (in the presence of IL-2 for NKL cells). The viral supernatant was supplemented with 5 µg/ml of polybrene and 10 mM HEPES buffer (Gibco) and 5 ml was added to the NKL/Jurkat cells.

Cells were then centrifuged at 400 g for 70 min at 32^{o}C and incubated for 2 hours at 37°C. The spinfection and incubation was repeated 3 times in total. At the end of this process, Phoenix cells were discarded and transduced cells were returned to the incubator and cultured in 6-well plates until they recovered. Two days after the infection 10 µg/ml of blasticidin was added to the culture medium for selection of transduced cells.

2.5 Flow cytometry

2.5.1 Staining of the transfected cell lines for flow cytometry

To assess the surface expression of KIR2DL1-HA, KIR2DS1-HA and mutated forms of the receptors in singly-transfected cell lines, cells were first counted using a Neubauer hemocytometer and 5 x 10^5 cells were transferred to a round-bottom 5 ml flow cytometry tube (BD Falcon). Samples were spun down at 500 g for 5 min (the same speed and duration applied to all the later centrifugations), re-suspended in 3 ml of pre-chilled washing buffer (1% FBS in phosphate-buffered saline; PBS) and spun down. Washing buffer was decanted and cells were re-suspended in the buffer remaining at the bottom of the tube. To block the samples, 2 µl of AB human serum was added. Samples were blocked at 4^{o}C for 20 min. An anti-KIR2DL/S1 antibody conjugated with APC, PE or Atto 488 was added (clone EB6, Beckman Coulter) to the final concentration of 5 µg/ml. In parallel, cells were stained with an isotype-matched control antibody (clone P3.6.2.8.1 from eBioscience or clone MOPC-21 from Biolegend). Cells were stained at 4^{o}C for 30 min, washed by addition of 3 ml of pre-chilled washing buffer and spun down. The excess washing buffer was decanted. Washing step was repeated twice in total, after which cells were re-suspended in the remaining buffer and fixed by adding 100 µl of 4% paraformaldehyde (PFA) in PBS to each tube.

To assess surface expression of KIR2DL1-HA and KIR2DS1-FLAG or KIR2DL1-FLAG and KIR2DS1-HA in double transfectants, cells were stained in a similar way with the following exceptions: (1) prior to the blocking step, the cells were fixed by re-suspending in 4% PFA in PBS, and incubated for 30 min at RT; (2) for permeabilization of the cells, 0.1% of saponin was present in the washing buffer at all times; (3) cells were stained with 5 µg/ml of anti-HA antibody (clone 6E2, Cell Signaling) conjugated with AF 647 and 5 µg/ml of anti-DYKDDDK (amino-acid sequence of FLAG) Tag antibody (rabbit polyclonal, Cell Signaling) conjugated with AF 488 or appropriate

isotype-matched control Abs (clone MOPC-21 from Biolegend conjugated with AF 647 and rabbit IgG control #4340 from Cell Signaling conjugated with AF 488).

2.5.2 Staining of NK clones for flow cytometry

To assess KIR2DL1 and KIR2DS1 expression on the NK clones, the flow cytometry method described by Fauriat *et al.* was used [317]. In this method, KIR2DS1^{+}/KIR2DL1^{-} and KIR2DS1^{-}/KIR2DL1^{+} NK cells are identified using monoclonal antibodies EB6 and 143211, which have competing epitopes. Clone EB6 binds to NK cells expressing either receptor, while 143211 binds only KIR2DL1 and blocks EB6 binding. Sequential staining with these antibodies thus allows the discrimination of cells displaying KIR2DS1^{+}/KIR2DL1^{-}, KIR2DS1$^{-/}$KIR2DL1^{+} , or KIR2DS1$^{+/}$KIR2DL1^{+} phenotypes.

Primary NK cells from the expanded populations were counted using a Neubauer hemocytometer and 5 x 10^5 cells from each population were transferred to a round-bottom 5 ml flow cytometry tube. Cells were spun down at 500 g for 5 min (the same speed and duration applied to all the later centrifugations), re-suspended in 3 ml of pre-chilled washing buffer (1% FCS in PBS) and spun down again. Washing buffer was decanted and cells were re-suspended in the buffer remaining at the bottom of the tube. To block the unspecific binding of antibodies, samples, 2 µl of AB human serum was added and samples were incubated at room temperature for 10 min. After that, antibodies were added and cells were stained at 4^{o}C for 20 min. Cells were washed by addition of 3 ml of pre-chilled washing buffer, spun down and the excess washing buffer was decanted. At the end, cells were re-suspended in the remaining buffer and fixed by adding 100 µl of 4% PFA/PBS to each tube.

NK clones identified by this procedure as KIR2DS1$^{+/}$KIR2DL1^{-} were additionally screened for the expression of KIR2DL3 in a separate experiment. This was due to the described cross-reactivity of the anti-KIR2DL/S1 antibody EB6 with KIR2DL3*005 allele [318]. For this, clones were stained with monoclonal antibody DX27 (Biolegend, three clones from the first donor), or with 180701 mAb (R&D Systems, two clones from the second donor). Clones identified as KIR2DS1^{+} KIR2DL3^{+} were excluded from the experiments.

Flow cytometry was carried out on a BD FACS Canto II flow cytometer (BD Biosciences). Analysis was carried out using FlowJo software (Treestar).

2.6 Enzyme-linked immunosorbent assay (ELISA)

To assess the influence of KIR2DL1 and KIR2DS1 ligation on the IFN-γ production by NKL cells, parental NKL cells and NKL/KIR2DL1-HA or NKL/KIR2DS1-HA transfectants were co-incubated with 721.221/Cw4 or 721.221/Cw4/MICA target cells. For this, 2 x 10^5 NK cells and 2 x 10^4 target cells were mixed in 100 µl of the normal culture medium in one well of a 96-well ELISA plate (Nunc) and incubated for 24 hours at 37°C and 5% CO_2. For each effector-target combination three replicates were prepared.

A capture antibody against IFN-γ (clone NIB42, BD Biosciences) was diluted in binding buffer (carbonate bicarbonate; Sigma) at the concentration of 1 µg/ml and 50 µl of the solution was added to each well of ELISA plate. The plate was incubated overnight at 4^{o}C. On the following morning, the antibody solution was removed and ELISA plate was blocked by adding 100 µl of blocking buffer (1% bovine serum albumin (BSA)/0.05% Tween-20/PBS). The plate was blocked for 1 hr at room temperature and blocking buffer was then removed.

The NK cell co-cultures with target cells were spun down at 500 g for 5 min. The supernatants were then mixed with 2 x concentrated PBS containing 2% of BSA at the volume ratio 1:1 and 100 µl of the blocked supernatant was added to each well.

As concentration standards, the recombinant human IFN-γ (R&D systems) was diluted in blocking buffer and 100 µl of serial dilutions with concentrations ranging between 500 and 25 pg/ml were added in duplicates to the wells. The plate was incubated for 1 hour at room temperature, after which the solutions were removed and the plate was washed three times with 300 µl of washing buffer (0.05% Tween-20 in PBS).

For detection of captured IFN-γ, a biotinylated IFN-γ mAb (clone 4S.B3, BD Biosciences) was diluted in the blocking buffer at the concentration of 1 µg/ml and 50 µl of the solution was added to each well. The plate was incubated for 1 hour at room temperature, after which the solution was removed and the plate was washed three times with 300 µl of washing buffer. In the next step, streptavidin-HRP conjugate (BD Biosciences) was diluted in the blocking buffer at the volume ratio 1:1000 and 50 µl of the solution was added to each well. The plate was incubated for 30 min at room temperature, after which the solution was removed and the plate was washed three times with 300 µl of washing buffer.

The plate was then developed by adding 50 µl of the TMB ELISA substrate solution (Sigma-Aldrich) to each well. Reaction was stopped by adding 100 µl of 1 N H_2SO_4 to

each well and absorbance at 450 nm was measured using Infinite M200 PRO microplate reader (Tecan). A 570 nm reference line was used.

2.7 Activation on slides assay

Formation of peripheral actin rings in response to the KIR2DL1 and KIR2DS1 ligation was assessed in cells incubated on glass slides coated with mAb. For this, poly-L-lysine (PLL, Sigma) was diluted in sterile water at the concentration of 0.01% and 200 µl was added to the wells of chambered glass coverslips (#1.5 Lab-Tek, Nunc). Lab-Teks were incubated at room temperature for 15 min, the solution was removed and Lab-Teks were dried in a heating chamber. The antibodies were diluted in PBS in following combinations:

a) 5 µg/ml of anti-KIR2DL/S1 (clone EB6) + 5 µg/ml of control murine IgG1 (clone MOPC-21, Biolegend)
b) 5 µg/ml of anti-NKG2D (clone 149810, R&D Systems) + 5 µg/ml of control murine IgG1
c) 5 µg/ml of anti-NKG2D + 5 µg/ml of anti-KIR2DL/S1
d) 10 µg/ml of control murine IgG1

For each combination of antibodies, 200 µl was added to the wells and Lab-Teks were incubated overnight at 4^{o}C. On the following morning, antibodies solutions were removed and wells were washed three times with 500 µl of PBS. Parental NKL, NKL/KIR2DL1-HA, NKL-KIR2DS1-HA, NKL/KIR2DL1-HA/KIR2DS1-FLAG and NKL/KIR2DL1-FLAG/KIR2DS1-HA cells were re-suspended in PBS at the concentration of 10^6 cells/ml and 300 µl of cell suspension was added to the pre-coated wells. Cells were incubated at 37°C for 10 min, after which the supernatant was removed and 200 µl of 4% PFA/PBS solution was added to each well. Cells were incubated at room temperature for 30 min and samples were washed with 500 µl of PBS three times. To fluorescently visualize actin, phalloidin conjugated with AF488 was diluted in PBS containing 0.1% saponin at the concentration of 33 nM (1U/ml) and 200 µl was added to each well. Samples were incubated at room temperature for 1 hour, washed with 500 µl of PBS three times and imaged by confocal microscopy as detailed below.

2.8 Fluorescent labelling of antibodies

Most of the primary antibodies used for immunostaining were conjugated in our laboratory using the method described below. AF 647 and AF 532 N-hydroxysuccinimide (NHS) esters were purchased from Invitrogen and Atto 488 NHS ester was from Sigma Aldrich. Upon arrival, dyes were dissolved in anhydrous dimethyl sulfoxide (DMSO) and aliquoted into tubes for a final 0.02 mg amount of dye per tube. All DMSO was removed using an evaporator. Aliquots were stored in dark at -20^{o}C.

For labelling of the antibodies, one vial of a dye (0.02 mg) was dissolved in 20 µl of anhydrous DMSO. A labelling reaction was set up in a 300 µl eppendorf tube: 52 µl of antibody solution (0.5 - 1 mg/ml) was mixed with 6 µl of 1 M $NaHCO_3$ solution in water and 2 µl of AF 647 solution. The tube was wrapped in aluminium foil and the reaction was run for 40 minutes at room temperature on a rocking platform.

While the reaction was progressing, a gel filtration column (Millipore) was equilibrated by running three column volumes of PBS through the column. At the end of the incubation, reaction was stopped by adding 140 µl of PBS and gentle vortexing. The entire volume was added to the centre of the column and sample was allowed to enter the column. Next, PBS was gradually added up to the volume sufficient to collect the fastest running coloured band. After collecting the first band, another 300 µl of PBS was added and the resulting eluent was collected. To calculate the antibody concentration and labelling efficacy the absorbance of the sample at the appropriate wavelengths was measured using the NanoDrop 200c Spectrophotometer (Thermo Scientific) and used in the following equations:

$$IgG\ concentration = \frac{A_{280\ nm} - (A_{Ex\ max} \times CF_{280nm})}{203{,}000} \qquad \text{(Equation 2)}$$

where $A_{280\ nm}$ is absorbance in a cuvette with a 1-cm pathlength at 280 nm, $A_{Ex\ max}$ is absorbance in a cuvette with a 1-cm pathlength at the maximum excitation wavelength λmax, $CF_{280\ nm}$ is a correction factor for the fluorophore's contribution to the absorbance at 280 nm and 203,000 is the molar extinction coefficient (ε) of a typical IgG at 280 nm.

$$Moles\ of\ dye\ per\ mole\ of\ protein = \frac{A_{Ex\ max}}{\varepsilon_{max} \times IgG\ concentration} \qquad \text{(Equation 3)}$$

where $A_{Ex\ max}$ is absorbance in a cuvette with a 1-cm pathlength at the maximum emission wavelength λ_{max} and ε_{max} is molar extinction coefficient of the dye at the maximum excitation wavelength λ_{max}.

Table 2.2 Spectroscopic data for dyes used for antibodies labelling.

	Atto 488	**Alexa Fluor 532**	**Alexa Fluor 647**
Excitation maximum, λ_{max} [nm]	501	530	650
Extinction coefficient at λ_{max}, ε_{max} [cm^{-1} M^{-1}]	90,000	81,000	239,000
Correction factor for the fluorophore's contribution to $A_{280\ nm}$ ($CF_{280\ nm}$)	0.1	0.09	0.03

2.9 Preparation of samples for imaging

2.9.1 Preparation of cells fixed on slides

To prepare glass slides for the incubation of cells, PLL was diluted in sterile water at the concentration 0.01% and 200 µl was added to the wells of Lab-Teks and incubated at room temperature for 15 min. The solution was removed and Lab-Teks were dried in a heating chamber. PLL-coated slides were used directly for imaging of unstimulated cells, or for stimulation of cells, 200 µl of PBS containing 5 µg/ml of anti-KIR2DL/S1 antibody (clone EB6) or 5 µg/ml of murine IgG1 was added to the wells and Lab-Teks were incubated overnight at 4^{o}C.

Cells were re-suspended in PBS at the concentration 10^6 cells/ml for cell lines and 1.5 x 10^6 cells/ml for primary NK cells and 300 µl of cell suspension was added to the pre-coated wells. Cells were allowed to settle for 10 min on PLL only-coated slides and for 5 min of antibodies-coated slides at 37°C. After the incubation, the supernatant was removed and cells were fixed by adding 200 µl of 4% PFA/PBS, followed by incubation at room temperature for 30 min and three washes with 500 µl of PBS each. The samples were then blocked in 300 µl of 4% BSA/PBS solution for 40 min at room temperature and the blocking buffer was removed.

For immunostaining, the antibodies were diluted at 5 µg/ml in 0.2% BSA/PBS (surface staining) or 0.1% saponin/0.2% BSA/PBS (for intracellular staining) and 200 µl of the solution was added to wells. All antibodies used for staining are listed in the Tables 2.3 and 2.4. Staining was performed at room temperature for 1 hour, after which

the antibodies solutions were removed and samples were washed five times for 3 min with 500 µl of PBS. If the primary antibodies were not directly labelled, fluorescently labelled secondary antibodies (listed in Table 2.4) were diluted at 5 µg/ml and 200 µl of the solution was added to wells. Staining was performed at room temperature for 1 hour, after which the antibodies solutions were removed and samples were washed five times for 3 min with 500 µl of PBS.

For GSDIM acquisition, 300 µl of GSDIM imaging buffer (50 mM Tris-HCl (pH 8.0), 10 mM NaCl, 10% (w/v)/Glucose, 1% (v/v) 2-mercaptoethanol, 0.7 mg/ml glucose oxidase, 42.5 µg/ml catalase) was added immediately before the start of imaging. Glucose oxidase and 2-mercaptoethanol were added to the buffer directly before use. Buffer was replaced with fresh one every 90 minutes.

Table 2.3 Directly labelled antibodies.

Target	Isotype	Clone	Fluorophore	Source
KIR2DL/S1	Mouse IgG1	EB6	Atto 488*	Beckman Coulter
KIR2DL/S1	Mouse IgG1	EB6	Alexa Fluor 532*	Beckman Coulter
KIR2DL/S1	Mouse IgG1	EB6	Alexa Fluor 647*	Beckman Coulter
HA tag	Mouse IgG1	16B12	Alexa Fluor 488	Invitrogen
FLAG tag	Mouse IgG1	M2	Alexa Fluor 532*	Sigma
Isotype control	Mouse IgG1	MOPC-21	Atto 488*	Biolegend
Isotype control	Mouse IgG1	MOPC-21	Alexa Fluor 532*	Biolegend
Isotype control	Mouse IgG1	MOPC-21	Alexa Fluor 647*	Biolegend
Isotype control	Mouse IgG1	MOPC-21	Alexa Fluor 488	Biolegend

*The antibodies were fluorescently labelled in our laboratory (See Antibodies labelling)

Table 2.4 Unconjugated primary antibodies and corresponding secondary antibodies

Target	Isotype	Clone/ Cat No.	Source	Secondary Ab
HA tag	Rabbit mAb, IgG	C29F4	Cell Signaling	Goat anti-rabbit IgG AF 568
IL-2R alpha	Mouse IgG2a	7G7/B6	Millipore	Goat anti-mouse IgG2a AF488
DAP12	Rabbit mAb, IgG	EPR5173	Abcam	Goat anti-rabbit IgG AF 568
ZAP-70	Rabbit polyclonal	ab134509	Abcam	Goat anti-rabbit IgG AF 568
ZAP-70 pY319	Rabbit polyclonal	ab131270	Abcam	Goat anti-rabbit IgG AF 568
SHP-1	Rat IgG2a	255402	R&D Systems	Goat anti-rat IgG AF 568
SHP-1 pY536	Rabbit polyclonal	AP08023PU-N	Acris GmbH	Goat anti-rabbit IgG AF 568
Isotype control	Rabbit mAb, IgG	EPR25A	Abcam	Goat anti-rabbit IgG AF 568
Isotype control	Rabbit polyclonal	ab27472	Abcam	Goat anti-rabbit IgG AF 568
Isotype control	Rat IgG2a	eBR2a	eBioscience	Goat anti-rat IgG AF 568
Isotype control	Mouse IgG2a	MOPC-173	Biolegend	Goat anti-mouse IgG2a AF488

2.9.2 Preparation of cells fixed in suspension

To check for changes in membrane organization induced by contact with a glass surface, KIR2DL1 and KIR2DS1 clustering was also compared in NKL cells fixed in suspension. For this, cells were suspended in 1 ml of 4% PFA/PBS at the concentration of 1.5 x 10^6 cells/ml. Samples were incubated for 30 min at room temperature and spun down at 300 g for 5 min (the same speed and duration applied

to all the later centrifugations). Cells were then washed three times by re-suspending in 1 ml of PBS, spinning down and discarding the supernatant. At the end of this process, samples were blocked by re-suspending cells in 4% BSA/PBS and incubating them for 20 min at room temperature. After that, cells were spun down and the supernatant was discarded. For immunostaining, cells were then incubated in 0.2% BSA/PBS in the presence of 5 µg/ml anti-KIR2DL/S1 mAb (clone EB6) conjugated with Atto 488, for 60 min at room temperature. After the incubation, cells were washed five times by adding 1 ml of PBS and spinning down, and then re-suspended in 1 ml of GSDIM imaging buffer. Cell suspension was added to chambered slides pre-coated with PLL (150 µl per well) and allowed to settle for 5 min before imaging.

2.10 Microscopy

2.10.1 TIRF and GSDIM microscopy

TIRF and GSDIM imaging was performed on a Leica SR GSD microscope using an 160× oil immersion objective (NA 1.43). The fluorescence was collected on an electron-multiplying charge-coupled device (EMCCD) camera (Andor iXon DU897E-C50-#BV) with a CCD sensitivity of 12.4 electrons per analog to digital (A/D) count, single pixel noise of 52.95 electrons and pixel size of 100 nm. During the acquisition, samples were illuminated with 488 and 642 nm lines of the laser. For 488 and 642 nm lines, 50% and 30% of the maximum laser power were used, respectively. Cells were illuminated in TIRF mode which limits the imaging to molecules that are within ≈200 nm of the glass surface. TIRF autoalignment was run each time at the start of the session and later every 2 hours. The electron-multiplying (EM) gain was set to 120. Up to 2×10^4 frames were acquired with a camera integration time of 15 ms (less if no photoswitching events could be detected in at least 2×10^3 consecutive frames).

2.10.2 Scanning confocal and STED microscopy

Scanning confocal and STED microscopy were performed on Leica TCS SP8 STED CW microscope with a 100× oil immersion objective (1.40 NA). The system was equipped with a continuous wave laser, which produces a continuous output beam allowing excitation of fluorophores precisely at their specific excitation maxima. Scan speed was set to 400 Hz and pinhole to 1 airy unit. Confocal images were taken in 512 pixels x 512 pixels format, for STED images the pixel size was automatically optimized

by the system to match the resolution that can be feasibly achieved using particular settings.

When 3D stacks were taken, cells were additionally imaged in interference reflection microscopy (IRM) mode, in which the intensity of the signal is a measure of proximity of the object to the glass surface. It takes advantage of the fact that the glass surface partially reflects the light, but light that is not reflected by the glass travels into the cell and is reflected by the cell membrane. When the membrane is close to the glass, the light reflected from the glass is shifted half of a wavelength (due to a change in refraction index), which results in a half a phase shift. In such situation the light waves reflected from the glass and from the membrane cancel each other out as a result of interference, resulting in a dark pixel in the final image. When the membrane is not attached to the glass, the reflection from the membrane has a smaller phase shift compared to the reflected light from the glass, and therefore they do not cancel each other out, resulting in a bright pixel. When there is no specimen, only the light from the glass is detected and appears as bright pixels in the final image [319].

STED was achieved using 592 nm continuous-wave fibre laser for STED of Atto 488, AF 488 and AF 532 and 660 nm continuous-wave fibre for STED of AF 568. STED beams were always autoaligned at the beginning of the session and then re-aligned every 90 min. For STED, fluorescence was always collected on hybrid photodetectors and time-gated detection with a gate of 0.9 − 6.0 ms was applied. Time gated detection has been demonstrated to significantly improve signal-to-noise ratio in a continuous wave-STED modality by suppressing low spatial frequencies in the image [320]. For two-colour STED microscopy, sequential scanning with switching between stacks was applied. To exclude cross-excitation of fluorophores in two-channel imaging, control images were acquired with only one of the two used laser lines (495 nm or 532/575 nm) active. Due to a smaller Stoke's shift between the excitation spectrum of AF 532 and 592 nm depletion laser line, there was a risk of AF 532 fluorescence emission excited by the STED laser (anti-Stokes fluorescence). To control for this, for each STED image of AF 532 an additional image with only the depletion laser active was taken and subtracted this image from its respective STED image (example of this procedure is shown in Figure 2.2). To ensure the specificity of the immuno-staining, all images were compared to images of respective cells stained with isotype-matched antibodies.

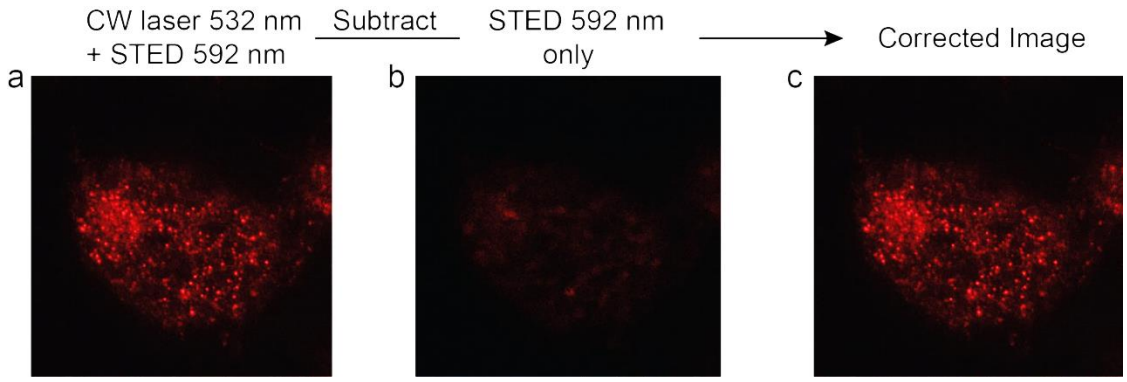

Figure 2.2 Correction for anti-Stokes excitation of AF 532 by the 592 nm STED laser line.
To correct for possible anti-Stokes excitation in such setup, for each STED image of AF 532 (a) an additional image with only the depletion laser active (b) was taken and subtracted this image from its respective STED image (c).

2.11 Microscopy data analysis

2.11.1 GSDIM data analysis

To obtain the x-y coordinates of molecules for a GSDIM image, a fluorescence intensity image captured by a camera was analysed with Thunderstorm software [321], which is available as a plug-in for ImageJ processing software (U.S. National Institutes of Health). Although a broad range of software dedicated to analysis of single-molecule localization data is currently available, the Thunderstorm was chosen due to its excellent performance in a direct comparison of different approaches published recently in *Nature Methods* by Sage *et al.* [322]. Data extraction process is illustrated by the Figure 2.3.

In the first step, a wavelet transform using a convolution kernel based on normalized B-spline basis function of the third order with a scaling factor of 2 was applied [323]. To calculate approximate positions of molecules, the local intensity maxima method was used. This method passes through each pixel of the image and determines if the pixel intensity is greater than a specified threshold and at the same time greater than or equal to all values within a 4- or 8-connected neighbourhood. For this step, a threshold value was set to 2 times the standard deviation of the intensity values from the first wavelet level F1, as suggested by Izeddin *et al*. [323], and a connectivity was set to 8-neighbourhood. Next, a sub-pixel localization of molecules was extracted employing a PSF Integrated Gaussian method. The Gaussian function has been shown to provide a very good approximation of the real PSF of a microscope [324, 325] and its integrated form takes into account the discrete nature of pixels present in digital cameras [326, 327]. A fitting radius of 5 pixels has been applied. Finally, x and y coordinates of

detected molecules were obtained using least-squares fitting method with initial sigma parameter (standard deviation of the Gaussian distribution) set to 1.6 pixel. The approach in this method is to minimise the sum of square residuals between the real observed intensity and the gaussian fit calculated. In the next step, poorly-localized molecules were discarded by filtering of molecules with parameters set to intensity > 400 photons, sigma > 9 and uncertainty ≤ 50 nm.

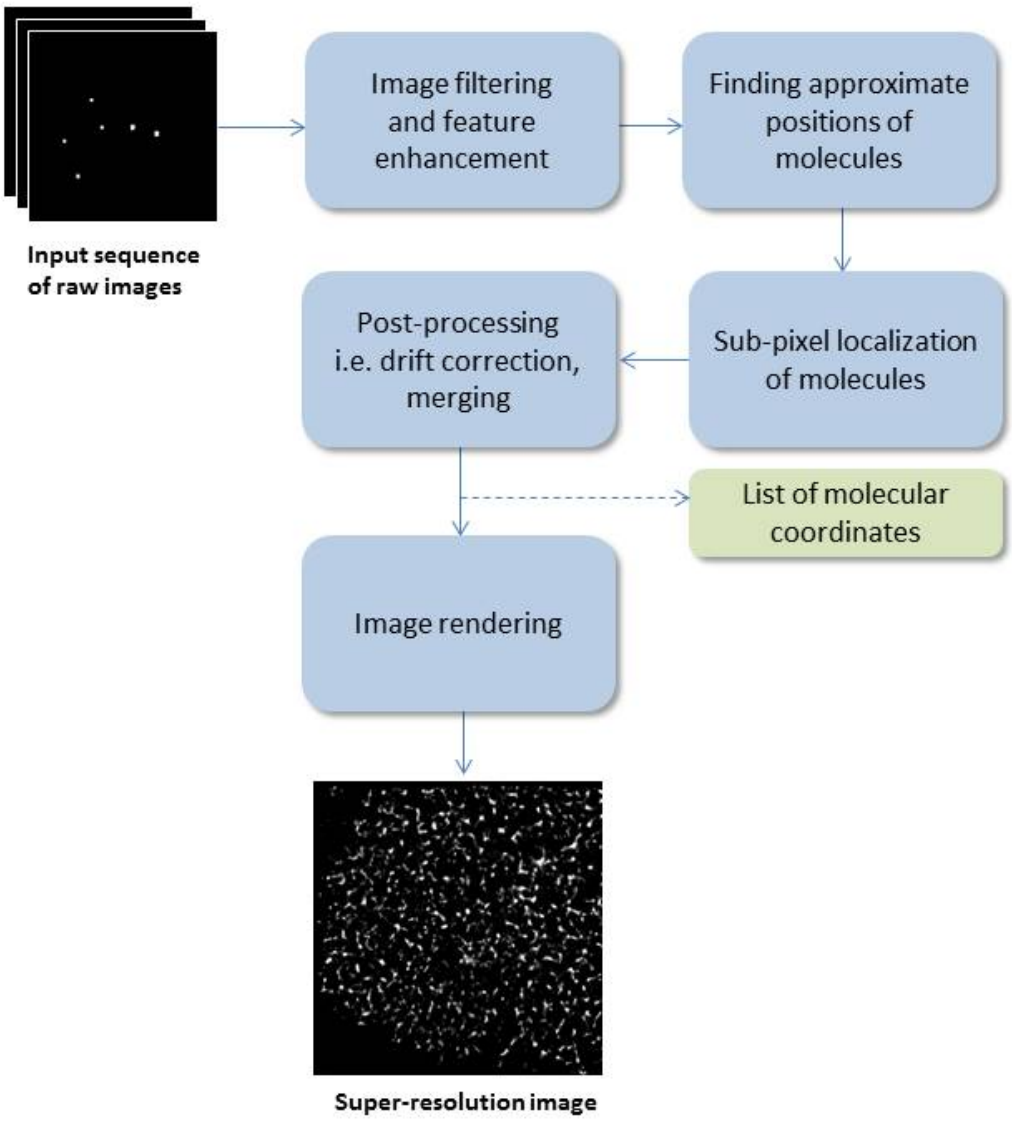

Figure 2.3 GSDIM image reconstruction workflow.

GSDIM and related single-molecule localization techniques are known to be prone to multiple rounds of photoactivation resulting in multiple localizations from the same molecule. One way commonly used to account for this sums the events whose localizations appeared in the same area within a defined number of consecutive frames (off-gap) and counts them as one molecule with a new position calculated as the mean value of the original data, as illustrated in the Figure 2.4.

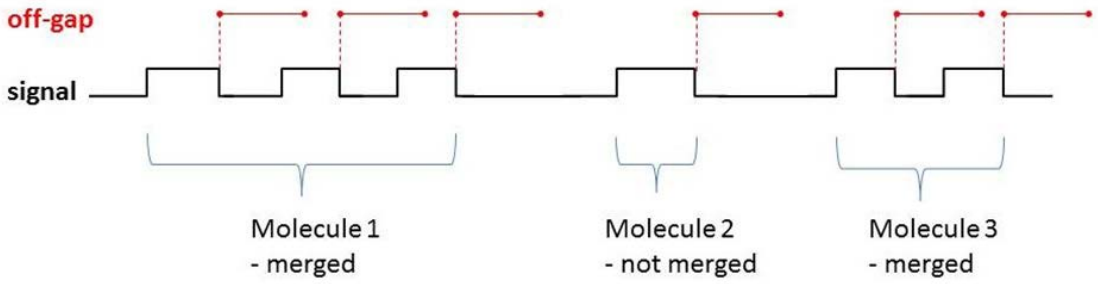

Figure 2.4 Elimination of re-appearing detections by merging.
If a fluorescent event appears in the same area within a defined number of consecutive frames (off-gap, shown in red) it is counted as one molecule with a new position calculated as the mean value of the original data.

Here, the molecules were merged within the radius of 30 nm and off-gap of 25 frames. The choice of radius was dictated by distribution of uncertainty of localization of detected molecules. It was assumed that for any molecule which has been detected once, if it recycles back to a fluorescent state it is likely to be localised to a similar position as the first time, e.g. within the original event's uncertainty distance. Therefore, 30 nm was chosen as radius within which molecules are merged, as > 95% of detected molecules were localized with uncertainty of ≤ 30 nm. The off-gap defines the time period (in frames) in which fluorescent events that localize to the same area were counted as one molecule.

Figure 2.5 a - c shows distribution of photon counts, uncertainty and sigma values for detections found within representative data sets for particular fluorophores. Threshold values applied are marked by vertical dashed lines to illustrate the influence of thresholding on the final list of molecules. In the Figure 2.5 d, the effect of increasing the off-gap on the number of molecules is plotted (radius of area within which molecules were merged was kept as 30 nm). Off gap times greater than 25 frames did not significantly reduce the number of detected molecules suggesting that molecules selection with threshold parameters set to radius of 30 nm and off-gap time of 25 frames is highly unlikely to include re-excited molecules.

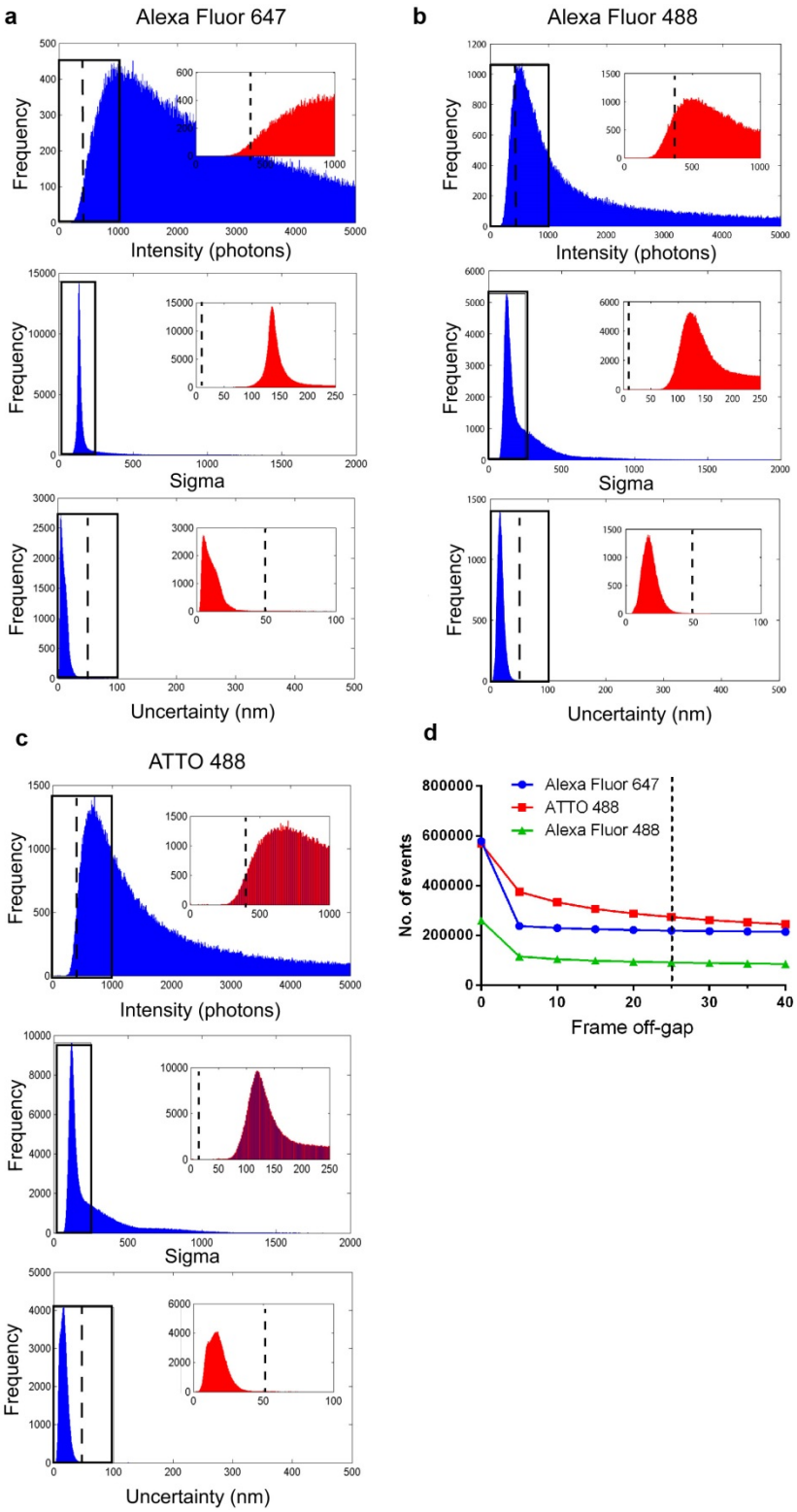

Figure 2.5 Parameters used for GSD data post-processing.
Photon counts, sigma and uncertainty for representative data sets are shown for AF 647 (a), AF 488 (b) and ATTO 488 (c). Black rectangles mark the graph sections enlarged in the insets. Dashed lines represent the threshold values used for post-processing filtering. (d) Influence of increasing off-gap on the number of total localizations. Off-gap value of 25 frames used for merging of re-appearing localizations is marked with a dashed line.

Due to the long times of acquisition, sample might be undergoing lateral drift. This was accounted for using the method of Mlodzianoski *et al.* [328]. The presumption of this method is that similar structures will appear in all reconstructed images. Cross-correlation methods are used to determine the shift between the first image and each of the subsequent images, leading to a set of cross-correlation images, where the shift in the position caused by the drift corresponds to the relative position between the global intensity maximum peaks. The original molecular coordinates are corrected for drift using the estimated values.

The steps following the detection of localizations in the GSDIM images are presented in the Figure 2.6. Once the events were detected, the data was exported as a table including information on the x-y coordinates of each molecule, the frame number in which the event was first detected, the photon count of the molecule, its associated background value, standard deviation of the Gaussian distribution used to fit the localisation of this molecule (sigma) and localization precision. These data was used to re-construct a 2D super-resolution image using Gaussian rendering. This method draws a normalized symmetric 2D Gaussian function integrated over the pixel area for every localized molecule, with a standard deviation equal to the computed uncertainty. For quantitative analysis, between 1 and 5 non-overlapping 3 µm × 3 µm regions Spatial pattern analysis was performed using Ripley's K-function calculated in SpPack, an add-in for Microsoft Excel [329], as:

For i ≠ j

$$K(r) = A\sum_{i=1}^{n}\sum_{j=1}^{n}\left(\frac{\delta_{i,j}}{n^2}\right) \text{where } \delta_{i,j} = 1 \text{ if } \delta_{i,j} < r \text{ otherwise } 0 \quad \text{(Equation 4)}$$

where A is the area of the analyzed region (here 3 x 3 µm), n is the number of points, r is the spatial scale (radius) for the K-function calculation and δ_{ij} is the distance between points i and j.

This counts the number of molecules localized within concentric rings centred on each molecule, normalized to the average molecular density of the entire region. This function was then linearized to generate the L-function according to:

$$L(r) = \sqrt{K(r)/\pi} \quad \text{(Equation 5)}$$

such that L(r) scales linearly with radius.

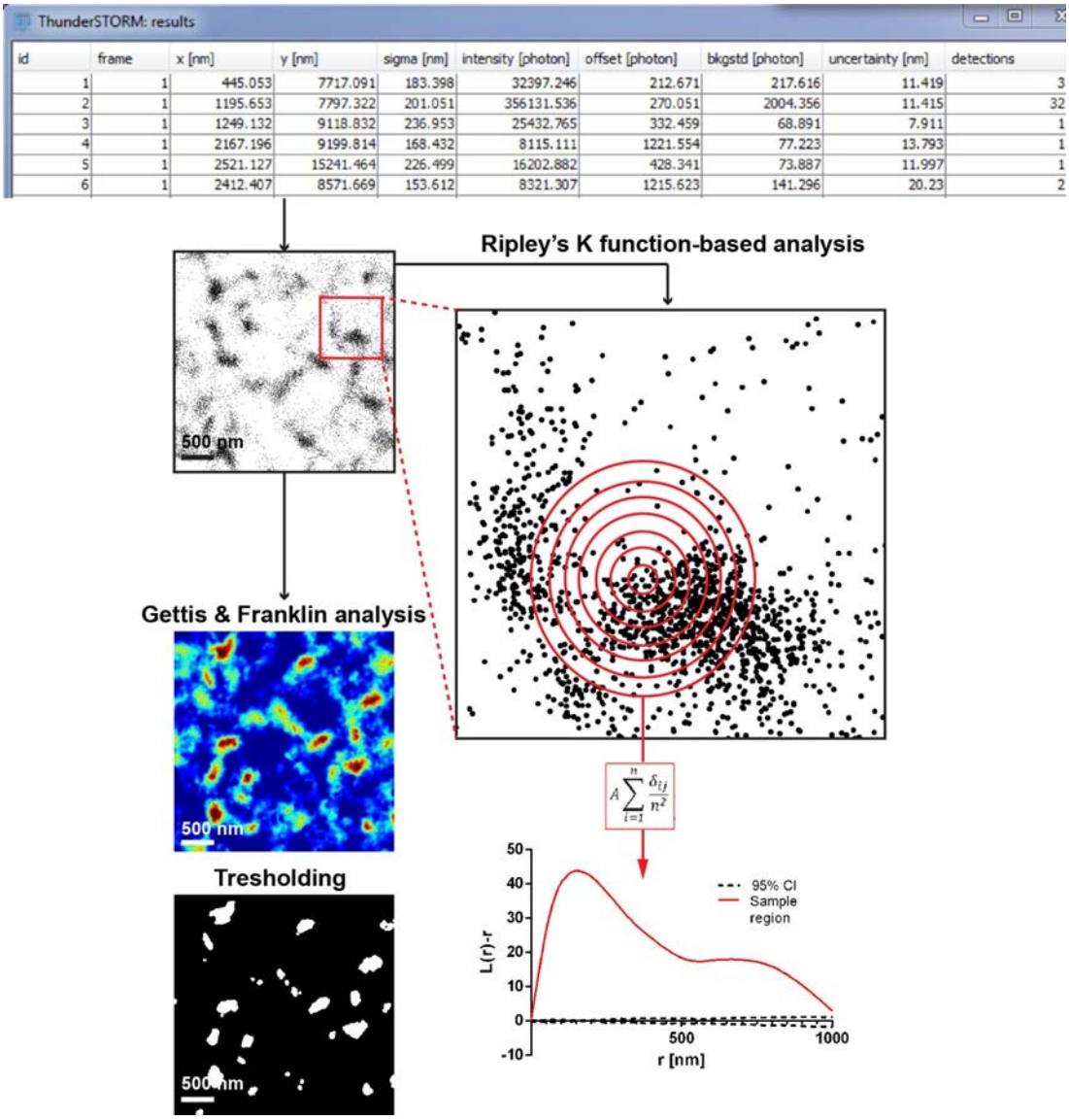

Figure 2.6 Post-detection GSDIM data analysis workflow.
The list of x-y coordinates of the detected molecules was used to reconstruct the super-resolution image and qualitatively analysed by Ripley's K function-based analysis as well as Getis and Franklin method allowing creation of pseudo-colour heat-maps and binary maps of receptor clustering.

For completely spatially random distributions of molecules, L(r) = r. Hence, L(r) - r (sometimes termed the H-function) was plotted against r such that a random distribution has L(r) - r = 0 for all r. Therefore, for length scales at which the distribution is more clustered than a random distribution, L(r) - r was positive, whereas L(r) - r was negative if the points are less clustered than for random events. Points at the edge of the distribution region were weighted to negate edge-related effects. Confidence intervals were generated by simulating 100 spatially random distributions with the same average molecular density as the data regions.

Quantitative colour-scale maps and binary maps of clusters were created using a custom MATLAB script written by Dr David J. Williamson from the University of Manchester. To create quantitative colour-scale cluster maps, values of L(r) for each point (ignoring the j-sum in Equation 4, according to univariate Getis and Franklin's local point pattern analysis method) at a value of r = 30 nm (L(30)) were calculated. The radius of 30 nm was chosen empirically by analysing the same representative dataset with identical parameters and only increasing the radius. The resulting images were then compared with regards to how precisely were the clusters localized using particular search radii, as depicted in the Figure 2.7. Two-dimensional pseudo-colour heat-maps were created by interpolating a surface plot of L(30) on a grid of resolution 5 nm.

For quantitative comparison of clustering patterns, binary maps were generated by overlaying a disc element of 25 nm radius around all point localizations with L(30) above a threshold value, L(30) ≥ 65. To choose an appropriate threshold, 3 randomised regions of the same area and number of molecules as representative regions selected in KIR2DL1 and KIR2DS1 images were generated. L(30) values were calculated for molecules within the randomised regions and distribution of L(30) values was compared between randomised regions and corresponding regions from our experimental data. This led to setting the threshold value to L(30) ≥ 65, above which molecules were identified as localized within a cluster and included in the binary maps. From the binary map, the number of clusters, cluster size and circularity (defined as 4π*area/perimeter^2, which equals to 1 for a perfect circle) were extracted using ImageJ and analysed.

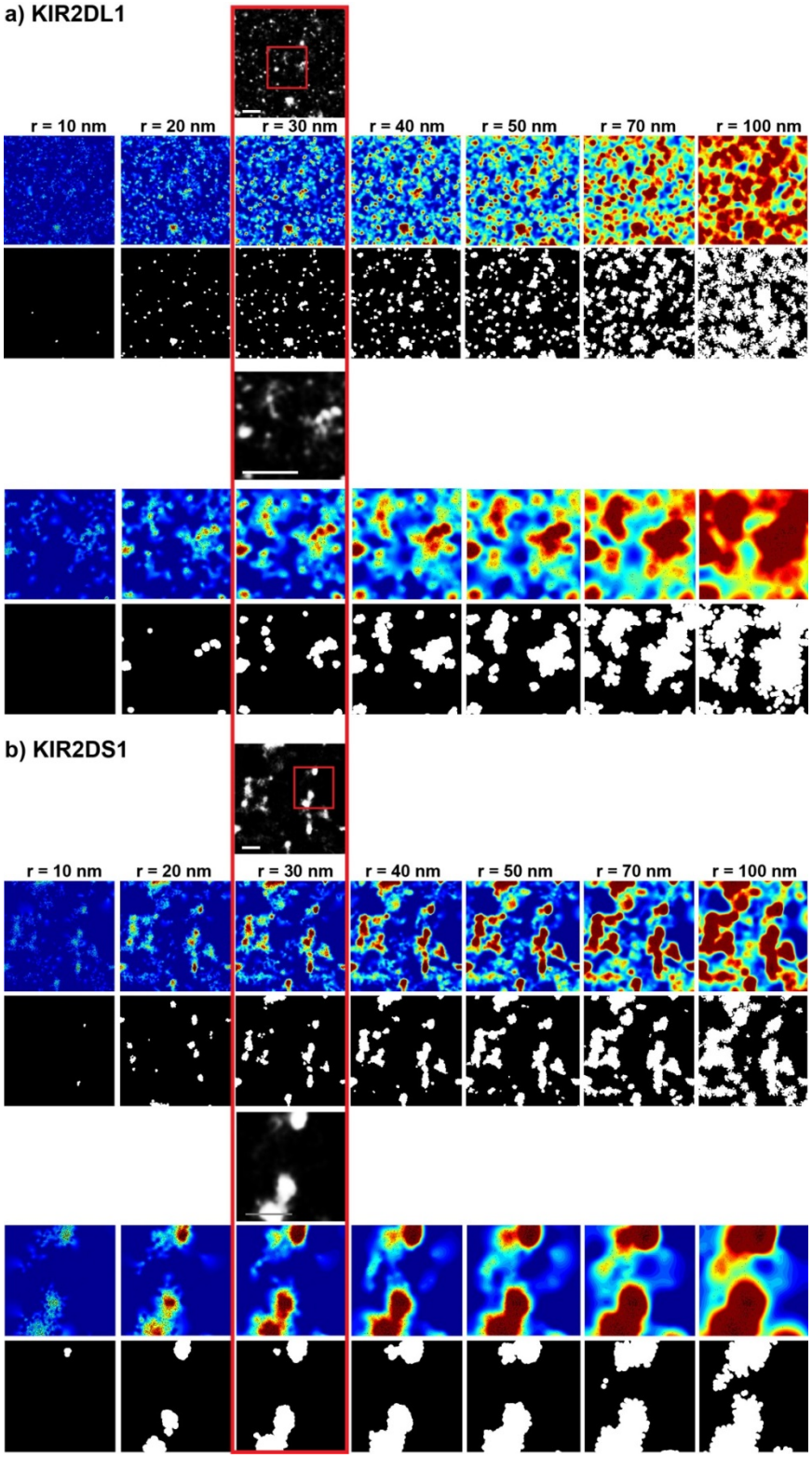

Figure 2.7 Finding of the appropriate search radius for Getis and Franklin analysis.

The radius of 30 nm was chosen by analysing the same representative datasets for KIR2DL1 (a) and KIR2DS1 (b) with identical parameters and only increasing the radius. The resulting maps (rows) were then compared with the corresponding images reconstructed in Thunderstorm (above each row) with regards to how precisely they localized the individual clusters. Representative 3 x 3 µm regions (upper sets in a and b) and enlarged 1 x 1 µm regions (lower sets) are shown. Scale bars 500 nm.

2.11.2 STED data analysis

For comparison of the intensity of fluorescence derived from signalling molecules labelled with antibodies, mean fluorescence intensity per pixel was measured in raw STED images using ImageJ software. The size of pixel in the compared images was kept constant.

To compare area of detected clusters, assess co-localization of proteins and identify clusters of receptors and signalling molecules which did not directly overlap but were localized within a close proximity, the images acquired by STED microscopy were in the first step deconvolved to improve the signal-to-noise ratio and facilitate more precise detection of protein clusters. Deconvolution was performed using Huygens Professional 10.1 software (Scientific Volume Imaging) with iterative Classic Maximum Likelihood Estimation (CMLE) algorithm using the following parameters: signal to noise ratio of 12, maximum of 40 iterations, threshold improvement value 0.05.

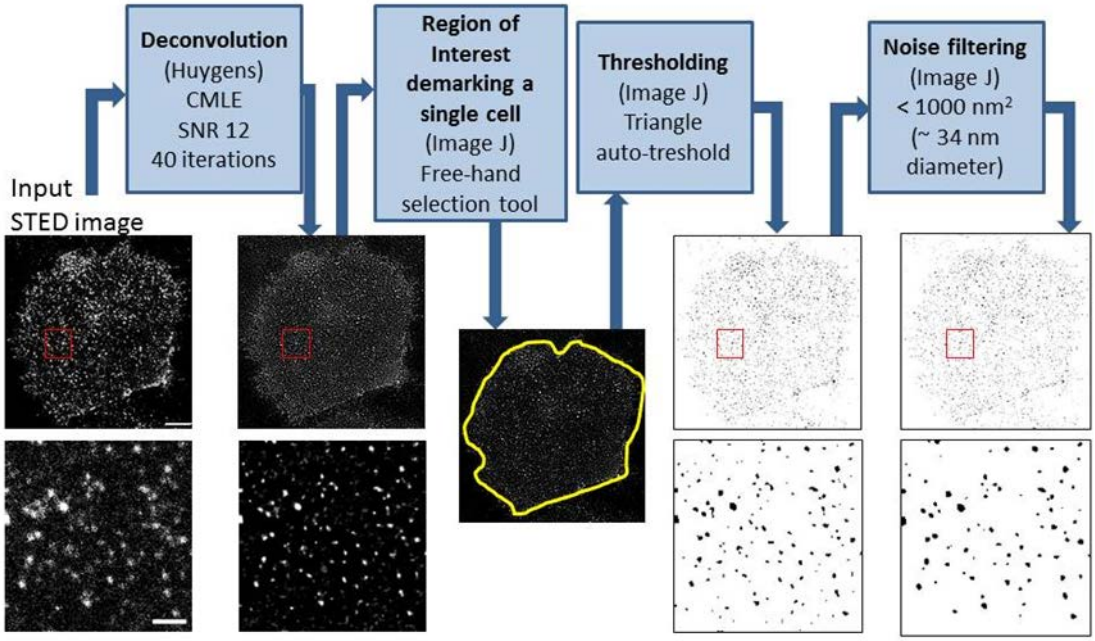

Figure 2.8 Processing of STED images for nanoclusters measurements.
The subsequent steps of STED data analysis are listed in the blue blocks. The example images represent NKL/KIR2DL1-HA cell stained with anti-HA antibody conjugated with AF 488. Bottom row images are enlarged regions from the corresponding images in the upper row marked by red squares. Scale bars 5 µm in the STED image (upper row) and 500 nm in the enlarged region (bottom row).

For measurements of nanoclusters, STED images were converted into binary maps by applying automatic triangle threshold implemented in the ImageJ software to regions-of-interest demarking a single cell, as illustrated in the Figure 2.8. To avoid false detections caused by noise fluctuations or motile unbound labelled antibodies objects with area smaller than 1,000 nm^2 were excluded from further analysis. Such

method has been previously successfully used for identification of TCRζ, LAT and pSLP76 nanoclusters in STED images of T cell synapses [330].

To assess co-localization of proteins, Pearson's correlation coefficients were calculated for the deconvolved multi-channel STED images using an ImageJ plug-in Coloc 2, which employs the Costes Auto threshold (written by Daniel J White, Tom Kazimiers and Johannes Schindelin and available on-line).

The Pearson's correlation coefficient is a common measure of correlation which ranges between 1 (perfect correlation) to -1 (perfect but negative correlation), with 0 denoting the absence of a relationship. Its application to the measurement of co-localization between fluorescently labelled molecules has been first described more than two decades ago [331] and today it still remains the most commonly used measure of co-localization. Pearson coefficient measures the pixel-by-pixel covariance in the signal levels of two images. Unlike Mander's overlap coefficient, it does not compare the absolute intensities but rather the deviation from the mean, which makes it a measure independent of signal levels and signal offset. The formula for Pearson correlation coefficient is given below:

$$Pearson\ Correlation\ Coefficient = \frac{\sum_i (R_i - \overline{R}) \times (G_i - \overline{G})}{\sqrt{\sum_i (R_i - \overline{R})^2 \times \sum_i (G_i - \overline{G})^2}} \qquad \text{(Equation 6)}$$

where R_i and G_i refer to the intensity values of the red and green channels, respectively, of pixel *i*, and $\overline{R}$ and $\overline{G}$ refer to the mean intensities of the red and green channels, respectively, across the entire image.

To identify clusters of signalling molecules overlapping, partially overlapping or remaining in contact at the edges, we converted STED images into binary maps as described above and found the x-y coordinates for each cluster centroid using a built-in ImageJ function Analyse particles. The area and integrated fluorescence intensity of each detected cluster were also measured. A custom- MATLAB script developed by Dr David J. Williamson from the University of Manchester was used to search a circular area around the centroid of each KIR2DL/S1 cluster for the presence of DAP12/SHP-1/ZAP-70 clusters. For each KIR cluster, the search radius was the sum of that cluster's own radius (calculated from the cluster area and assuming circularity) and the 75th-percentile value for cluster radii of the cognate signalling molecule (for DAP12 78 nm in unstimulated and 80 nm in activated cells; for total SHP-1 122 nm in

unstimulated and 114 nm in activated cells; for pY536 SHP-1 84 nm; for total ZAP-70 99 nm in resting and 126 nm in activated cells; for pY319 ZAP-70 90 nm).

Although such choice of the search radius is arbitrary, it was selected as a reasonable balance between the two extremal situations: (1) if the search radius was very small, i.e. much smaller than the average radius of a given signalling molecule cluster, the edge contacts with large clusters could never be detected, since the search radius would never reach their centroids position; (2) if the search radius was large. i.e. equal to the radius of the biggest cluster detected for a particular signalling molecule, it would be possible to detect the edge contacts with all the signalling molecule clusters, but the risk of including the centroids of smaller clusters that are not in contact would be considerably higher. This is illustrated by the Figure 2.9.

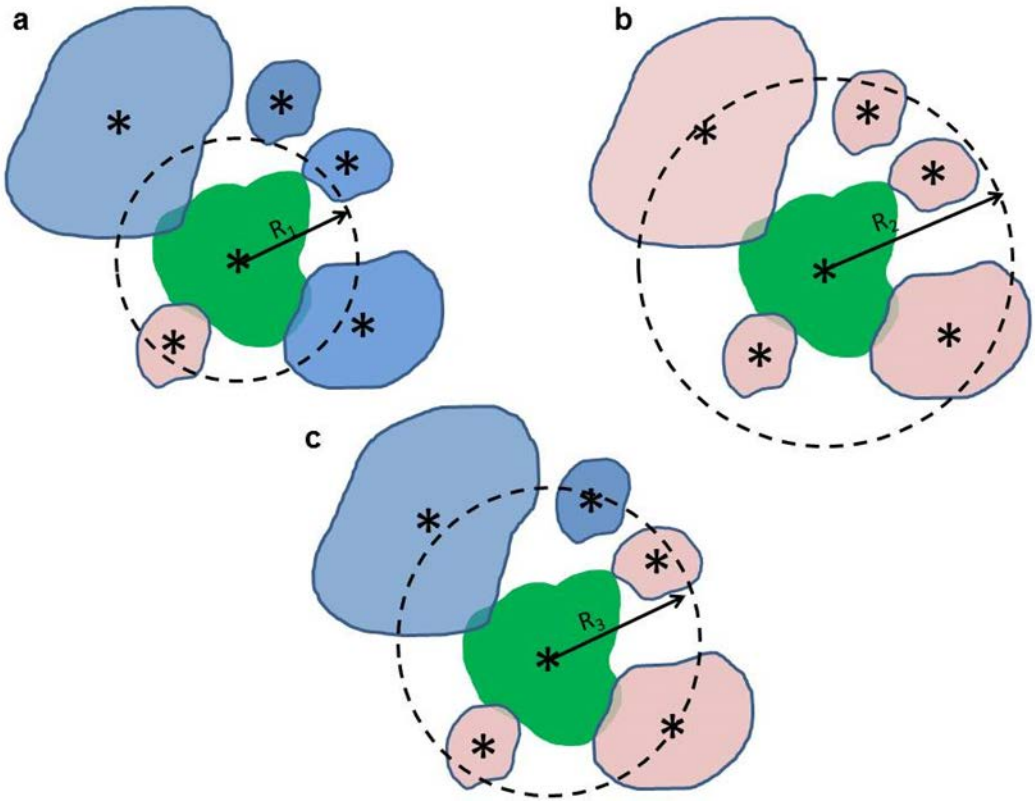

Figure 2.9 Influence of the choice of search radius on the cluster edge contacts detection.
KIR cluster is coloured green, signalling molecule clusters counted as *in contact* are coloured pink, signalling molecule clusters counted as *not in contact* are coloured blue. If the search radius is very small (a), the edge contacts with large clusters will not be detected, since the search radius would never reach their centroids position. If the search radius is large (b) it is possible to detect the edge contacts with all the signalling molecule clusters, but the centroids of smaller clusters that are not in contact might be often included. Therefore, an intermediate length of radius seems to be an optimal choice (c).

The distribution of areas of KIR2DL/S1 clusters for which at least one signalling molecule cluster was found nearby was compared against the distribution of all KIR cluster areas. For this, all detected KIR clusters were divided according to their size into the three bins. The bins corresponded to tertiles, i.e. each bin contained one third of the total number of KIR clusters. In the next step, the percentage of KIR clusters in contact with a particular signalling molecule cluster that falls into each of the designated bins was calculated. If the clusters in each size group were equally likely to recruit/trigger phosphorylation of the signalling molecules, approximately 33% of KIR clusters found in contact with DAP12/SHP-1/ZAP-70 would be found in every bin.

To assess whether covering a larger area by bigger clusters could account for these clusters forming more contacts with signalling molecules, data were compared against randomised equivalents. Here, the cluster segmentation data (comprising a list of cluster descriptors including centroid coordinates and the pixels comprising each segmented cluster) for the signalling molecule channel image were randomly assigned new centroid coordinates within a region of interest delineating the cell boundary. The pixel intensity values for each cluster were also repositioned about the new centroid location and the analysis (using the original cluster segmentation data for the KIR channel) was performed. In this way, signalling molecule clusters were disconnected from their original spatial locations (while retaining their original shape and intensity properties) and a measurement of a randomised, spatially unrelated co-clustering of KIR and signalling molecules could be obtained.

To assess relative efficiency of signalling molecules recruitment and phosphorylation within clusters of certain sizes, the median integrated fluorescence intensity of DAP12/SHP-1/ZAP-70 clusters found nearby the clusters of the certain size was plotted against area bins of KIR2DL/S1 clusters. Only KIR2DL/S1 clusters in contact with at least one cluster of a respective molecule were included in this analysis.

2.11.3 Statistical analysis

All statistical analyses were performed using GraphPrism 6.0 (GraphPad Software, Inc.). The statistical significance of differences between two data sets was assessed by Mann-Whitney test comparing ranks or Wilcoxon signed-rank test (for matched measurements). The multiple comparisons were made with Kruskal-Wallis test by ranks or matched-values Friedman test with Dunn’s post-testing.

Chapter 3: Comparison of KIR2DL1 and KIR2DS1 nanometre-scale organization

3.1 Introduction

Recent development of the super-resolution microscopy led to extensive studies of the nanometre-scale architecture of plasma membrane components in different cell types, including immune cells. Formation of nanoclusters has been rapidly reported for multiple immune receptors found at the surface of different cells. These include TCR in T cells [308-310], BCR in B cells [312, 313] and DC-SIGN in dendritic cells [332]. It is therefore possible that this type of organization might be a common feature amongst membrane-bound immune proteins.

Moreover, dynamic changes in nanometre-scale organization of the immune receptors have been observed upon cellular activation, such as mixing of TCR and molecules engaged in its downstream signalling [309]. In NK cells, there also is some evidence that nanometre-scale arrangement of the receptors might be linked to the signal transduction and integration. For instance, ligation of the activating receptor NKG2D was shown to trigger a change in the inhibitory receptor KIR2DL1 nanoclustering, leading to KIR2DL1 clusters becoming smaller and denser [224]. One implication of this observation is that in the presence of activating signals, changes in the arrangement of the inhibitory receptors could serve to sensitize the cell to the inhibitory ligands, in case they are present at the surface of the same target cell.

In a reciprocal process, ligation of the inhibitory NK cell receptors during the education of NK cells leads to relocation of the activating receptors, from the domains constrained by the cortical actin mesh to the less constrained lipid domains in the plasma membrane. This process was suggested to be crucial for the NK cell gaining a full responsiveness as a result of education [152].

Another hint for the importance of nanometre-scale organization of the receptors and ligands for the process of NK cell activation came from the study by Delcassian *et al.* In this study, primary human NK cells were incubated on nanopatterned surfaces with increasing distances between regularly spaced single ligands for an Fc receptor CD16.

The strength of NK cell activation was found to decrease as the spacing between ligand molecules increased.

Finally, a recent study from the group of Eric Long used bimolecular fluorescence complementation method to demonstrate that substitution of histidine 36 in the KIR2DL1 sequence with alanine triggers self-association and correlates with enhanced phosphorylation and recruitment of the phosphatase SHP-1 [333].

Taken together, although some indications that nanometre-scale clustering could affect the receptors signalling are found in the literature, the exact mechanisms for this are very poorly understood and require further studies.

3.2 Aims

My aim was to determine whether the way in which KIR2DL1 and KIR2DS1 are organized on nanometre-scale at the surface of NK cells is important for their signalling. The first step to achieve this goal was to characterize the nanometre-scale arrangement of KIR2DL1 and KIR2DS1 using super-resolution microscopy. Comparison between the organization patterns of these two receptors, which share ligand specificity and a significant sequence homology, might also indicate whether or not specific patterns might be more optimal for transduction of activating or inhibitory signals.

Surface organization of KIR2DL1 has been relatively well characterized, especially on micrometre-scale. It is well established that upon activation KIR2DL1 molecules coalesce into microclusters, which later merge as the stimulation persists [47, 221, 231, 278]. Moreover, KIR2DL1 is the only NK cell receptor to date for which the nanometre-scale organization has been directly imaged using PALM and GSDIM microscopy. Our group has reported that similarly to other immune receptors in T cells and B cells, KIR2DL1 constitutively forms nanometre-scale clusters at the surface of NK cells [224].

In contrast, KIR2DS1 has never been directly imaged on nanometre scale. This is partially due to the unavailability of monoclonal antibodies specifically targeting KIR2DS1 while not binding to the alleles of other KIR receptors. This chapter provides a thorough comparison of KIR2DL1 and KIR2DS1 nanometre-scale organization using two complementary super-resolution microscopy techniques.

3.3 Results

3.3.1 Analysis of KIR2DL1-HA and KIR2DS1-HA expression in transfected cell lines

To test the idea that organization of paired receptors KIR2DL1 and KIR2DS1 at the surface of NK cell could cause differences in their signalling capabilities, I first set out to characterize nanometre-scale scale arrangement of KIR2DL1 and KIR2DS1. For this purpose, two different cellular systems were used. First, NKL/KIR2DL1-HA and NKL/KIR2DS1-HA cell lines were obtained as a king gift from Dr Shaun-Paul Cordoba from Imperial College London. To create these cell lines, the KIR-deficient NK cell line NKL was stably transduced to express either receptor fused to an HA tag at the C-terminus by retroviral transduction. Cells expressing the desired receptors were selected by maintaining of an antibiotic, blasticidin, in the culture medium.

To ensure that transfected proteins are efficiently transported to the plasma membrane, the NKL/KIR2DL1-HA and NKL/KIR2DS1-HA cell lines were surface-stained with a monoclonal antibody EB6 conjugated to APC and analysed by flow cytometry (Figure 3.1). Clone EB6 has been previously demonstrated to bind both KIR2DL1 and KIR2DS1 [97]. In parallel, the same cells were stained with an isotype-matched control antibody. This demonstrated that both receptors were abundantly present at the surface of transfected cells.

To further investigate the cellular localization of fusion KIR-HA proteins and ensure that they can be efficiently labelled by targeting the intracellular HA tag, the same two cell lines were plated on PLL-coated glass slides, fixed, permeabilized and stained with an anti-HA mAb, or an isotype-matched control antibody, conjugated with AF 488. Samples were imaged by confocal microscopy using identical laser power and other parameters and the intensity of anti-HA and isotype control-derived fluorescence was directly compared, demonstrating that KIR2DL1-HA and KIR2DS1-HA indeed can be stained with the anti-HA antibodies (Figure 3.2 a - b and d - e).

To directly visualize the cellular localization of these receptors, 3D confocal stacks were acquired with a Z-plane step size of 220 nm. To localize the plane of contact between an NK cell and a glass slide, cells were simultaneously imaged in an IRM mode. In this approach, the intensity of the signal is a measure of proximity of the object to the glass surface – the areas of the membrane in contact with the glass are visible as dark pixels, while areas not attached to the glass result in bright pixels.

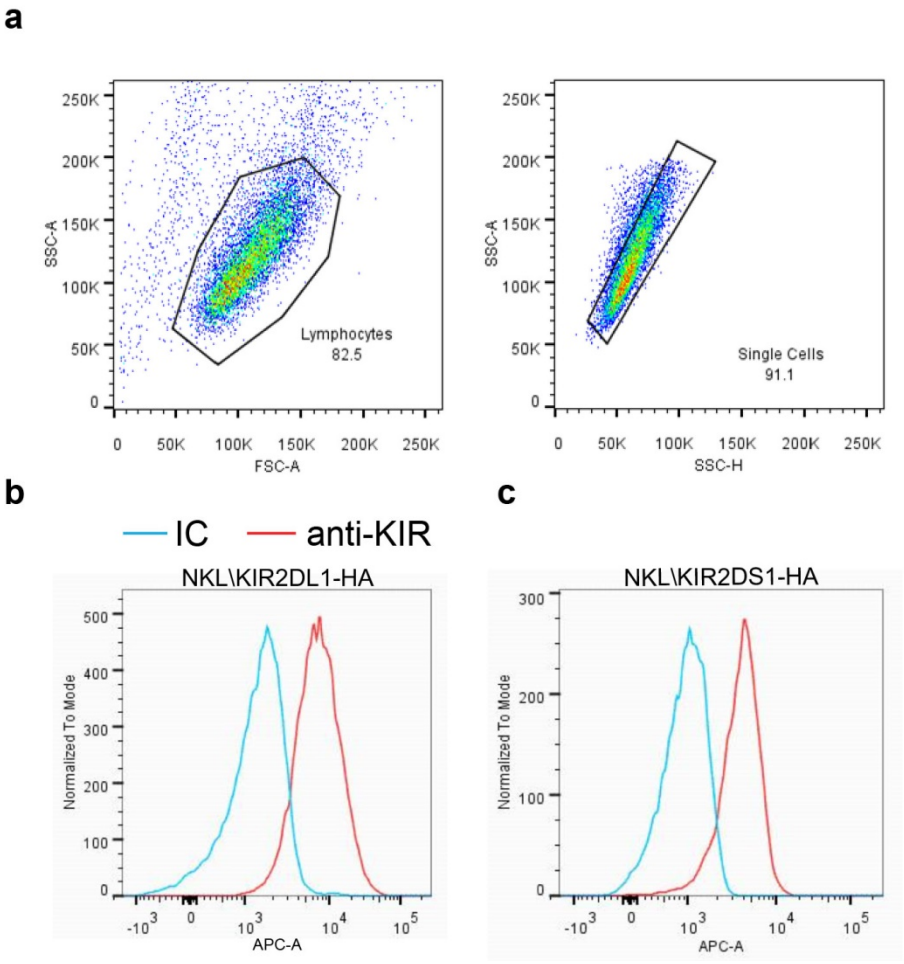

Figure 3.1 Analysis of the transfected receptors abundance in NKL/KIR2DL1-HA and NKL/KIR2DS1-HA by flow cytometry.
NKL/KIR2DL1-HA and NKL/KIR2DS1-HA transfectants were created by retroviral transduction of the human NK cell line NKL. Expression of the transfected receptors was assessed by flow cytometry, applying the gating strategy shown in (a). For this, NKL/KIR2DL1-HA (b, left) and NKL/KIR2DS1-HA (b, right) cells were stained with anti-KIR2DL/S1 mAb (clone EB6) conjugated with APC (red). Respective cells stained with isotype-matched control mAb (blue) were analysed as negative controls.

For both KIR2DL1 and KIR2DS1, bright fluorescent signal was observed in the contact plane, demonstrating that both receptors are present within the membrane attached to the slide (Figure 3.2 c and f). As the higher planes were imaged, the signal in the centre of the cell was rapidly decreasing but a bright staining could be still detected within the cell membrane. Some KIR-derived fluorescence was also detected intracellularly, visible as vesicular-like structures, which are likely to correspond to the fusion protein being transported to the membrane and internalized protein in lysosomal compartments.

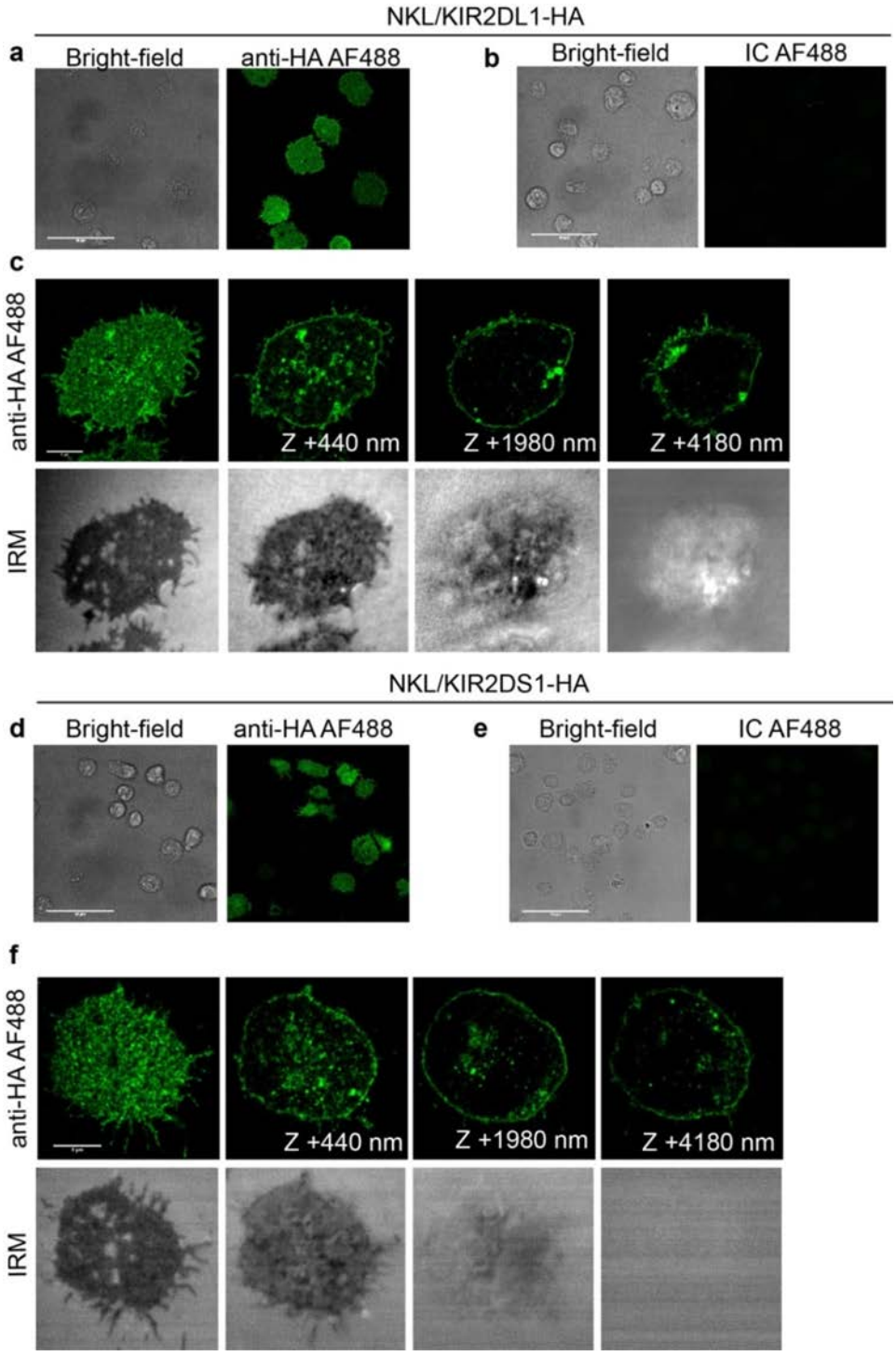

Figure 3.2 Visualization of the KIR2DL1-HA and KIR2DS1-HA localization in the transfected cell lines by confocal microscopy.

NKL/KIR2DL1-HA (a-c) and NKL/KIR2DS1-HA (d-f) cells were plated on PLL-coated glass slides, fixed, permeabilized, stained with anti-HA mAb (a,c,d,f) or isotype-matched control antibody (b, e) conjugated with AF 488 and imaged by confocal microscopy. Specificity of the staining was checked by directly comparing cells stained with anti-HA or control antibodies (compare a and b, d and e). Localization of KIR2DL1-HA (c) and KIR2DS1-HA (f) within the respective transfectants was assessed by visualization of KIR-derived fluorescence (upper rows) in different planes of the confocal Z stacks, for which a relative position in the Z plane was checked by imaging in IRM mode (lower rows). The most left images in (c) and (f) correspond to

the membrane proximal to the glass slide and the relative position of other images is indicated in the bottom of the micrographs. Scale bars 20 µm in (a, b, d, e) and 5 µm in (c and f).

Taken together, the above results establish that KIR2DL1-HA and KIR2DS1-HA are efficiently presented at the plasma membrane of transfected cells and can be visualized with both anti-KIR2DL/S1 and anti-HA antibodies.

3.3.2 Analysis of the KIR2DL1-HA and KIR2DS1-HA receptors functionality in the transfected cell lines

It was important to ensure that the fusion KIR receptors retained their functionality. One previously described hallmark of an NK cell activation is rearrangement of the cortical actin skeleton – depletion of f-actin from the centre of immune synapse and formation of a dense f-actin ring at the periphery [56, 334].

Therefore, NKL/KIR2DL1-HA and NKL/KIR2DS1-HA cells were incubated on glass slides coated with non-stimulatory IgG1 control mAb, anti-NKG2D mAb for activation of cells, anti-KIR2DL/S1 mAb (clone EB6) or a combination of anti-NKG2D and anti-KIR2DL/S1 antibodies. After 10 min of stimulation, cells were fixed, permeabilized and f-actin was visualized with fluorescently-conjugated phalloidin (Figure 3.3).

Formation of dense peripheral actin rings in parental NKL cells (Figure 3.3 a and d) could be observed when cells were incubated on anti-NKG2D antibodies, alone or in combination with anti-KIR2DL1 antibodies. Such result was expected, since the NKL cell line is known to express NKG2D but no KIR receptors.

In NKL/KIR2DL1-HA cells, formation of dense actin rings was observed in cells incubated on anti-NKG2D antibodies and was virtually absent from the cells incubated on other antibodies (Figure 3.3 b and d). Lack of actin rings in NKL/KIR2DL1-HA cells in which both NKG2D and KIR2DL1 were ligated demonstrated that NKG2D-mediated activation could be efficiently inhibited by KIR2DL1-HA ligation and therefore the transfected receptor was functional.

In NKL/KIR2DS1-HA cells, actin rings were present in cells incubated on either anti-NKG2D or anti-KIR2DL/S1, but not control IgG1 antibodies (Figure 3.3 c and d). This indicated that NKL/KIR2DS1-HA cells can be specifically activated via KIR2DS1-HA receptor, proving its functionality. In line with this, simultaneous ligation of NKG2D and KIR2DS1-HA in these cells led to further increase of the fraction of cells displaying actin rings.

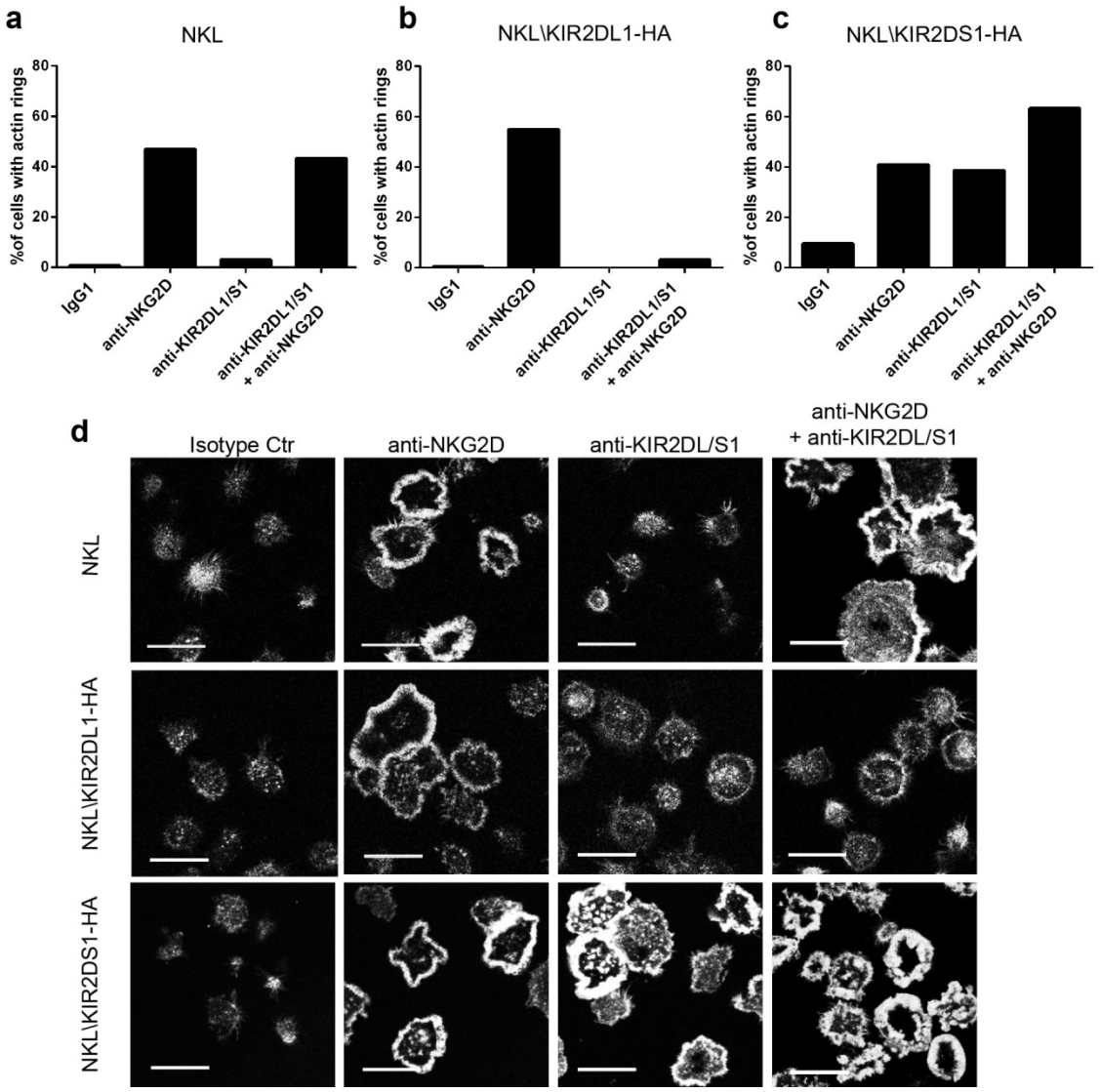

Figure 3.3 Effect of KIR2DL1-HA and KIR2DS1-HA ligation on the activation of NKL cells assessed by the formation of peripheral actin rings.
Parental NKL cells (a), NKL/KIR2DL1-HA (b) and NKL/KIR2DS1-HA (c) transfectants were incubated for 10 min at 37^{o}C on slides coated with anti-KIR2DL/S1 or anti-NKG2D mAb at 5 µg/ml plus 5 µg/ml of murine IgG1, 10 µg/ml of IgG1 or 5 µg/ml of anti-KIR2DL/S1 plus 5 µg/ml of anti-NKG2D mAb. Actin was visualized using fluorescently labelled phalloidin and percentages of cells forming peripheral actin rings were quantified. Results of one representative experiment are shown, n ≥ 100 cells per condition in each experiment. Representative fields of view are shown in (d). Scale bars 5 µm.

To further confirm the functionality of the fusion receptors, the effect of KIR2DL1 or KIR2DS1 ligation on secretion of IFN-γ was investigated (Figure 3.4). For this, parental NKL and NKL/KIR2DL1-HA cells were incubated for 24 hours with 721.221 target cells transfected with MICA (a ligand for NKG2D) and HLA-Cw4 (721.221/MICA/Cw4). Secretion of IFN-γ from NKL/KIR2DL-HA cells incubated with 721.221/MICA/Cw4 was largely reduced as compared with the parental NKL cells incubated with the same targets (Figure 3.4 a). This confirms, that ligation of KIR2DL1-HA efficiently abrogates NKG2D-mediated activation.

In a similar experiment, parental NKL and NKL/KIR2DS1 cells were incubated with 721.221 transfected to express HLA-Cw4 (721.221/Cw4). Although ligation of an activating KIR triggered less IFN-γ release than activation through NKG2D, it led to an increased response as compared to parental NKL cells incubated with 721.221/Cw4 targets (Figure 3.4 b). This confirms that transfected KIR2DS1-HA has retained its ability to activate NK cells in response to the Cw4 ligand.

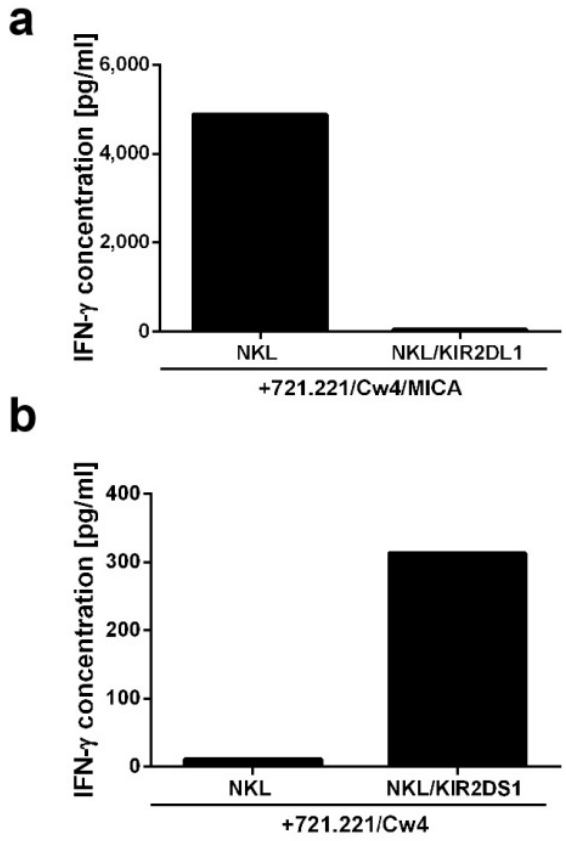

Figure 3.4 Influence of KIR2DL1-HA and KIR2DS1-HA ligation on the IFN-γ secretion by NKL cells.
Parental NKL cells and NKL/KIR2DL1-HA (a) or NKL/KIR2DS1-HA (b) were co-cultured for 24 hours with 721.221 transfectants expressing HLA-Cw4 and MICA (a) or -Cw4 only (b). IFN-γ release was measured by ELISA. E:T ratio was 10:1. Results of one representative experiment are shown.

3.3.3 Comparison of KIR2DL1 and KIR2DS1 nanometre-scale organization in NKL cells by GSDIM

To directly compare the nanometre-scale organization of KIR2DL1 and KIR2DS1, single-colour GSDIM experiments were performed first. This technique is based on stochastic switching of fluorophores and can be used to localize single fluorescently-

labelled molecules within a cell. When used in the TIRF mode, it is particularly useful for imaging of plasma membrane components.

For this, NKL\KIR2DL1-HA and NKL\KIR2DS1-HA cells were plated on PLL-coated slides, fixed and stained with an anti-KIR2DL/S1 antibody (EB6) directly labelled with AF647. The specificity of staining was assessed by a comparison with the images of NKL parental cell line stained with the same antibody (Figure 3.5). In parental NKL cells only residual staining could be observed in TIRF and during GSDIM acquisition less than 1% of the number of events typical for the transfected cells was detected (Figure 3.5 d). A significant improvement in the resolution was achieved in GSDIM images, as compared to TIRF images of the same cells.

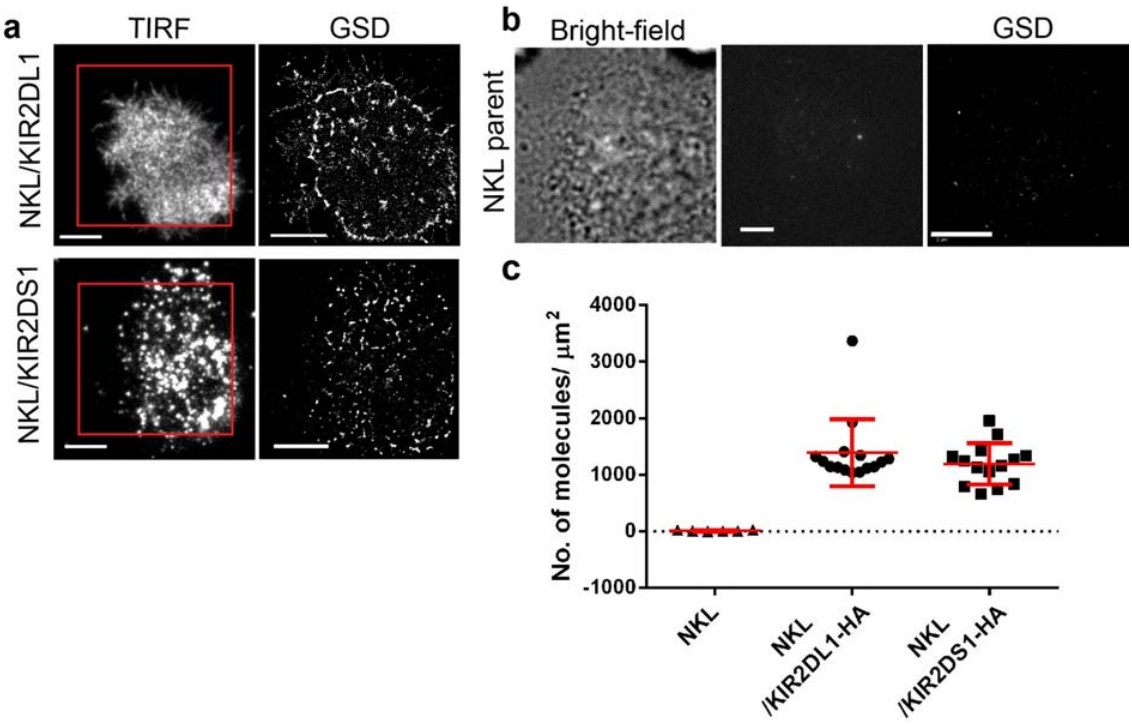

Figure 3.5 Specificity of fluorescent staining of KIR2DL1-HA and KIR2DS1-HA receptors with EB6 mAb in the transfected cell lines.
To assess the specificity of staining with EB6 mAb conjugated to AF 647 in NKL/KIR2DL1-HA and NKL/KIR2DS1-HA cells, the intensity of EB6-derived fluorescence was compared between the transfectants (a) and the parental cells (b) in TIRF and GSDIM images. For GSDIM microscopy, the average number of molecules detected in the transfectants and parental cells stained with EB6 was quantified in (c).

The obtained super-resolution images clearly showed that neither receptor was distributed randomly. Instead, both constitutively assembled in nanometre-scale clusters, which were larger for KIR2DS1 than KIR2DL1 (Figure 3.6 a and b). To quantitatively assess the clustering of receptors, the data was submitted to the analysis based on Ripley's K function [335]. Ripley's K function has been commonly used to

analyse single-molecule localisation data in earlier studies [224, 310, 312]. Briefly, for each molecule localized, this approach calculates the number of molecules found in the concentric rings of increasing radii centred at this molecule's position. These densities are then compared to the expected random distribution. The result is presented as a plot of L(r) - r values versus increasing radial scales, as in Figure 3.6 c and d. The positive values of L(r) - r indicate that points are more clustered than expected from a random distribution, and when L(r) - r is negative, the distribution is less clustered than would be expected from randomly distributed events. The radial scale at which the function peaks is indicative of the size of the clusters found in the region and the maximum value of the function can be used to asses a relative degree to which the molecules are clustered (i.e. it is higher for more clustered regions than for dispersed ones).

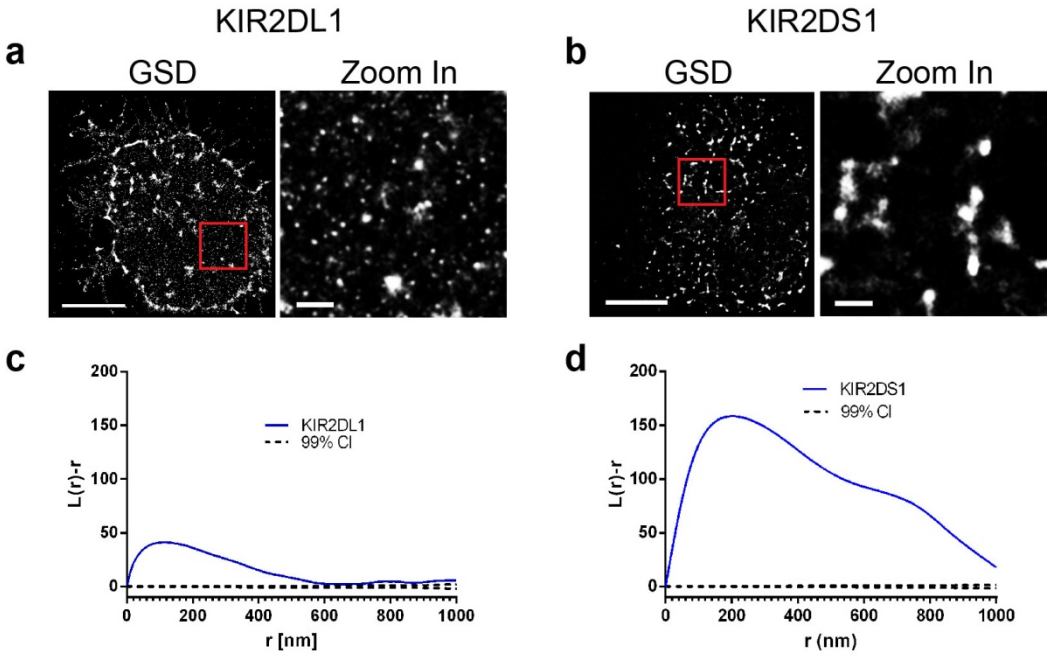

Figure 3.6 Distinct organization of KIR2DL1 and KIR2DS1 at the surface of NKL/KIR2DL1-HA and NKL/KIR2DS1-HA cells labelled with EB6 mAb and visualized by GSDIM.
NKL/KIR2DL1-HA (a) and NKL/KIR2DS1-HA (b) cells on PLL-coated slides were stained with anti-KIR2DL/S1 (EB6) mAb conjugated to AF 647. Representative GSDIM images of NKL/KIR2DL1-HA and NKL/KIR2DS1-HA cells are shown. Scale bars 5 µm. The 3 µm × 3 µm regions (red boxes in GSD images) are zoomed-in (scale bars 500 nm). (c and d) Ripley's *K* function of the events in the selected regions (red boxes) shown in (a and b). L(r) − r represents the degree of clustering at different spatial scales relative to simulated random distributions, indicated by the 99% confidence intervals (CI); r is the radial scale.

L(r) - r function plotted for the molecules of KIR2DL1 and KIR2DS1 localized within the representative 3 x 3 µm regions confirmed what was already apparent in the reconstructed images. Both receptors were pre-clustered in the plasma membrane, as

revealed by comparing the function values against the clustering of randomly distributed molecules, indicated by the dashed lines representing the 99% confidence intervals (99% CI). These confidence intervals were obtained by running 100 rounds of stochastic simulations of random distributions with the same number of events as the dataset studied. For both KIR2DL1 and KIR2DS1, the values for L(r) - r were higher for the data than for the random simulations. However, it could be observed that KIR2DS1 formed bigger clusters (as indicated by the larger radial scale for which the function reached its maximum) and was generally more clustered (as indicated by the higher value of the function maximum) than KIR2DL1.

While the Ripley's function-based analysis is a good method to obtain a global view of clustering of molecules, for extraction of the exact parameters of clusters the methods looking at local level of clustering are of more use. One such method is univariate Getis and Franklin's local point pattern analysis [224, 310, 336]. Using this approach, 2D pseudo-colour scale heat-maps of clustering were generated (Figure 3.7a).

The heat-maps were created in a custom MATLAB script by plotting the L(30) values in a pseudo-colour scale on a grid of resolution 5 nm (30 is the length of chosen sampling radius in nm). In the next step, binary maps of clusters were generated by overlaying a disc element of 25 nm radius around all point localizations with L(30) above a threshold value, $L(30) \geq 65$. To establish this threshold, the same analysis was run for randomized regions of the same area and number of molecules as the regions from the experimental data and the distribution of L(30) values for the experimental and randomized regions was plotted as a histogram (Figure 3.7 c). This has shown that L(30) values above 65 are very rarely observed for the randomized data, and thus they can be used to identify molecules clustered more than expected from the random distribution.

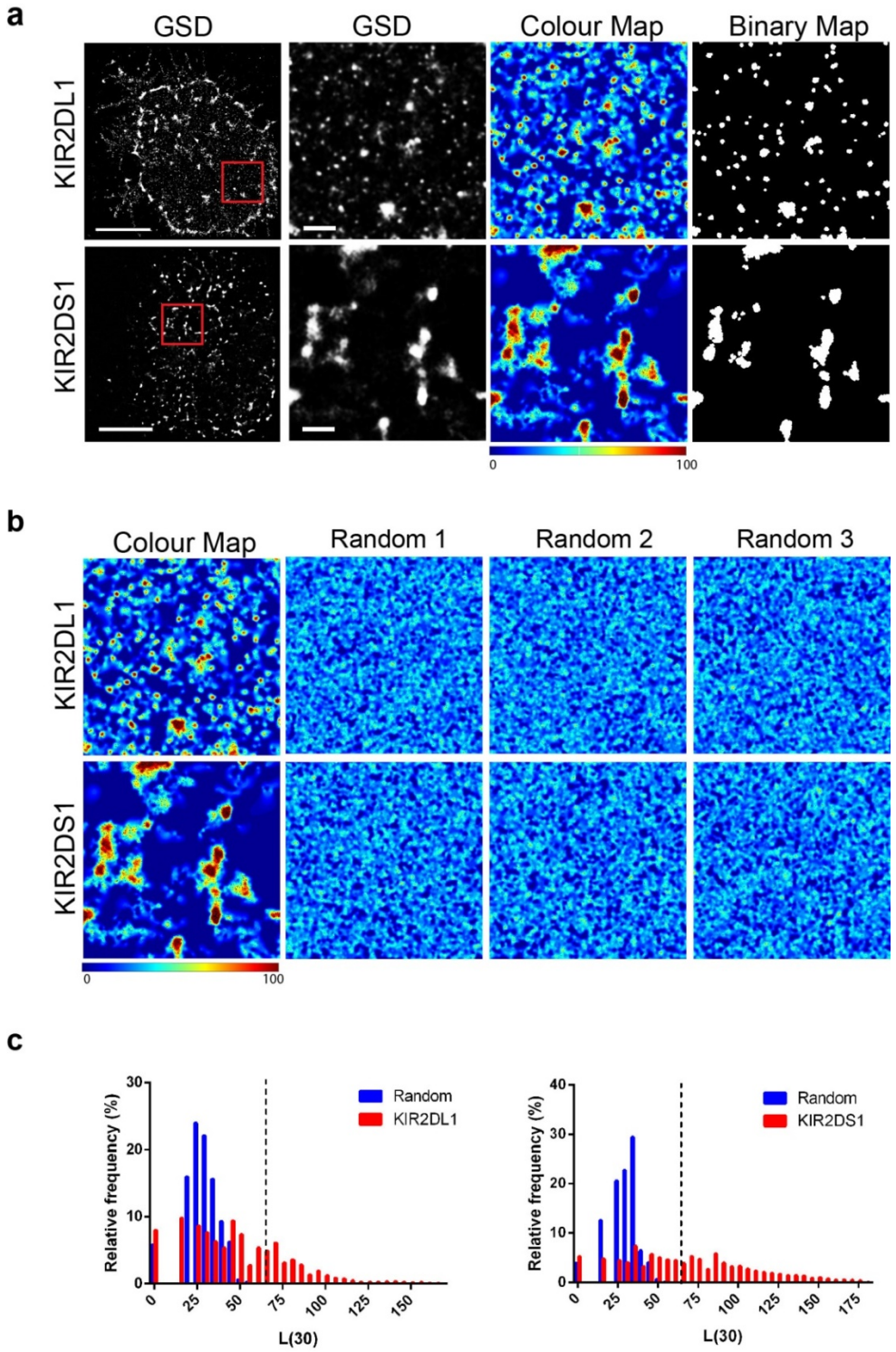

Figure 3.7 Pseudo-colour heat-maps and binary maps of clustering for KIR2DL1-HA and KIR2DS1-HA stained with EB6 mAb.

(a) To create the two-dimensional pseudo-colour heatmaps of clustering, L(30) values for KIR2DL1-HA (upper row) and KIR2DS1 (lower row) molecules detected in the representative 3 x 3 µm regions from the GSDIM images of NKL/KIR2DL1-HA and NKL-KIR2DS1-HA cells, respectively, were plotted in pseudo-colour scale on the grid of 5 nm resolution. Binary maps were created by overlaying a disc element around all point localizations with L(30) ≥ 65. To establish this threshold, the analysis was run for randomized regions of the same area and number of molecules and the distribution of L(30) values for the experimental and randomized regions was compared (c).

The obtained binary maps were then analysed in ImageJ to extract number of clusters, cluster size and other cluster parameters plotted in the Figure 3.8. Notably, quantifications of this type are sensitive to changes in parameters such as search radius. Therefore, precise values are indicative rather than definitive and this analysis is most effective in revealing relative differences between different receptors or conditions.

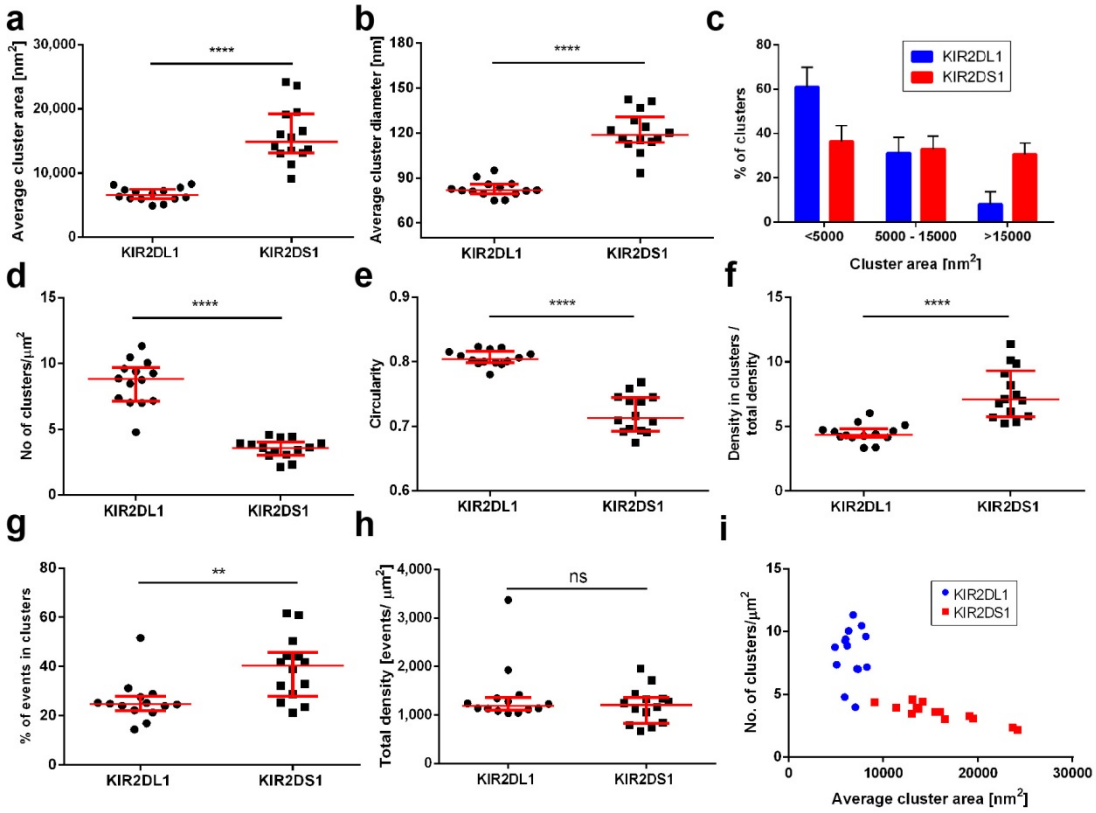

Figure 3.8 Quantitative analysis of KIR2DL1 and KIR2DS1 clustering in NKL/KIR2DL1-HA and NKL/KIR2DS1-HA cells stained with EB6 mAb.
Average cluster area (a) and diameter (b), size distribution of clusters (c), number of clusters per µm^2 (d), average cluster circularity (e), ratio of density of events in clusters to overall membrane density (f), fraction of molecules localized within clusters (g) and overall density of detected events (h). (i) Number of clusters per µm^2 plotted against average cluster area measured in individual cells. (a - b and d - i) Each symbol represents the mean from several regions within one cell. Horizontal bars and errors represent the medians and interquartile range. (c) Bars and errors represent means and SD. Data are from 14 cells per receptor from two independent experiments. ns non-significant, ** $p < 0.01$, **** $p < 0.0001$, Mann-Whitney test.

Quantitative comparison (Figure 3.8) showed that KIR2DS1 formed clusters of area ranging between 9,100 and 24,200 nm^2, with a median of 14,800 nm^2 (interquartile range (IQR) 13,000 -19,200 nm^2). The area of clusters detected for KIR2DL1 was smaller and ranged between 4,900 and 8,287 nm^2 with a median of 6,600 nm^2 (IQR 6,000 -7,500 nm^2). This corresponded to the median cluster diameters of 81 nm (IQR

80 – 86 nm) for KIR2DL1 and 119 nm (IQR 114 – 131 nm) for KIR2DS1 (Figure 3.8 a – b).

For both receptors, some intrinsic heterogeneity in cluster size within one cell could be noticed. For KIR2DL1, the majority of clusters (61 ± 9%) had an area ≤ 5,000 nm^2 (which corresponds to diameter ≤ 80 nm), and only 8 ± 6% were bigger than 15,000 nm^2 (diameter ≥ 138 nm). For KIR2DS1 however, roughly one third of the clusters (35 ± 9%) had area ≤ 5,000 nm^2 and a similar proportion of clusters was bigger than 15,000 nm^2 (31 ± 5%). Therefore, large clusters were 3.2 times more abundant for KIR2DS1 than KIR2DL1 (Figure 3.8 c).

Clusters of KIR2LD1 were more abundant at the surface of the cells, with a median of 8.8 and IQR 7.1 – 9.7 clusters detected per μm^2 (compared to the median of 3.6 and IQR 3 – 4 clusters/μm^2 detected for KIR2DS1). In addition, clusters of the two receptors presented a different morphology, more circular for the inhibitory receptor (median circularity 0.8 and IQR 0.79 – 0.81, on a scale between 0 and 1, where 1 means a perfect circle) than the activating one (median circularity 0.7; IQR 0.69 - 0.75). The density of KIR2DL1 within clusters was between 3.4 and 6.1-fold greater than the average membrane density, with a median of 4.4-fold increase. In contrast, KIR2DS1 was between 5 and 12.5 times more densely packed within the clusters, as compared to its global membrane density, with an median change of 7-fold. In addition, a smaller fraction of the total molecules number was found in clusters for KIR2DL1 (median 25%; IQR 22 – 28%) than for KIR2DS1 (median 40%, IQR 28 – 46%) (Figure 3.8 d – h).

To assess the variation of different parameters amongst individual cells expressing either KIR2DS1 or KIR2DL1, the average cluster size and number of clusters detected were cross-correlated for each analysed cell (Figure 3.8 i). This showed that for the inhibitory receptor, density of clusters at the cell surface varied more from cell to cell than average cluster area. In contrast, for KIR2DS1 the size of clusters changed more between cells than number of its clusters per unit of area.

Although the expression levels of KIR2DL1 and KIR2DS1, as measured by flow cytometry, were not identical, the observed differences in KIR2DS1 and KIR2DL1 nanometre-scale organization appear to not be due to variable numbers of events detected. This conclusion is supported by at least two lines of evidence. First, within the cell populations analysed, the total density of detected events for both receptors was comparable ($p = 0.6913$; Figure 3.8 h). Second, the particular patterns of organization observed for either of the receptors seem to be consistent across the range of different molecular densities. Figure 3.9 a shows example regions from the cells displaying comparative lower or higher molecular densities of KIR2DL1 and

KIR2DS1. It is clear that KIR2DS1 consistently forms larger clusters at both low and high densities of molecules.

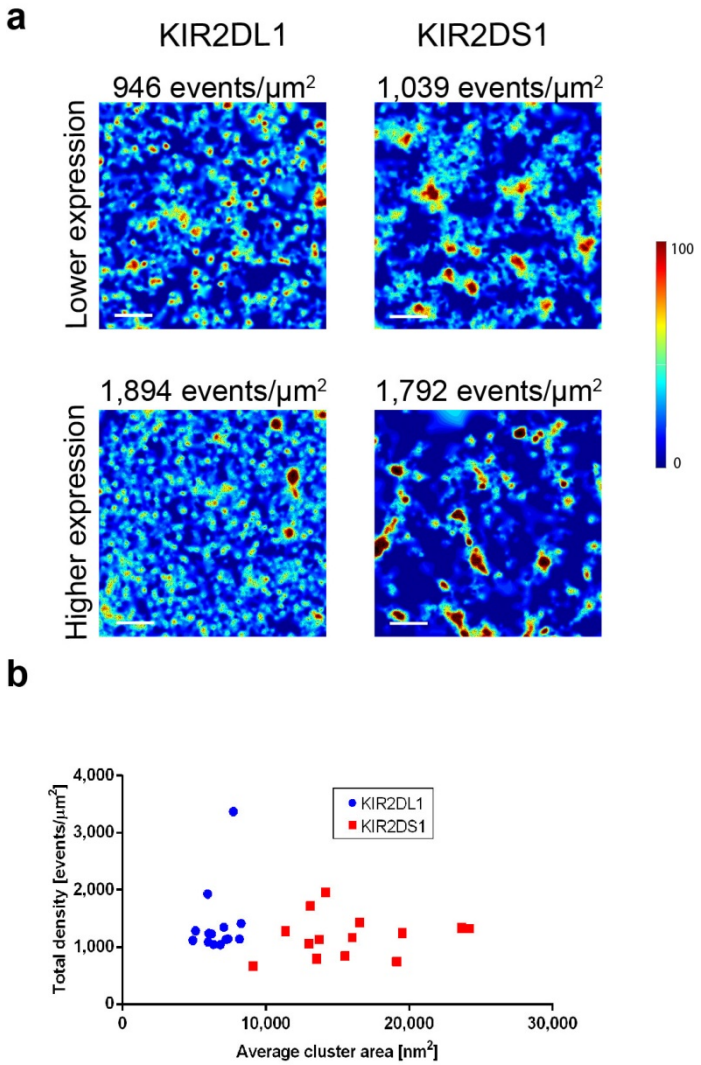

Figure 3.9 Differences in KIR2DL1-HA and KIR2DS1-HA clustering visualised by fluorescent staining with EB6 mAb are not due to differential expression levels.
NKL/KIR2DL1-HA and NKL/KIR2DS1-HA cells were stained with EB6 mAb conjugated with AF 647 and imaged by GSD microscopy. (a) Selected 3 μm × 3 μm regions are shown as colour maps where colours correspond to the extent of clustering according to pseudo-colour scale. Regions from cells with relatively low (upper row) and high (lower row) densities of detected events are shown. (b) Total density of events plotted against average cluster area measured in individual cells. Each symbol represents the mean from several regions within one cell. Data are from 14 cells per receptor from two independent experiments. Scale bars 500 nm.

This is further illustrated by panel b in the Figure 3.9, where the average cluster sizes measured in the particular cells are plotted against the overall density of receptors detected in these cells. While no obvious relation between the total molecules density and cluster size was found for either KIR2DL1 or KIR2DS1, across the range of molecular densities detected, the activating receptor formed larger clusters than KIR2DL1 at comparable density.

During the acquisition of GSDIM data, cells are illuminated in the TIRF mode and therefore collected information corresponds to the molecules remaining in close proximity of the glass slide. Thus, it is possible that uneven membrane topography, i.e. membrane ruffling could affect the appearance of fluorescently labelled molecules in the final image. Although it is challenging to probe the membrane topography in super-resolution, due to poor photoswitching capabilities of the common membrane dyes, some insights might be gained already from the TIRF images.

To investigate how even are the contacts between the cell membrane and glass slides typically observed in our experimental system, plasma membrane of the NKL/KIR2DL1-HA cells was fluorescently labelled with the lipophilic membrane stain DiO. Cells were then added to the PLL-coated slides, fixed and imaged by TIRF microscopy. To compare the distribution of DiO in the membrane with the distribution of KIR2DL1- or KIR2DS1-derived fluorescence, the relative intensity of fluorescence for each pixel was plotted on the z-axis of the three-dimensional plots of fluorescence (Figure 3.10). While the plots of KIR2DL1- and KIR2DS1-derived fluorescence displayed a huge variation in the intensity of discrete pixels, the intensity of DiO fluorescence was generally even across the entire region and significantly more homogenous than the receptors staining intensity.

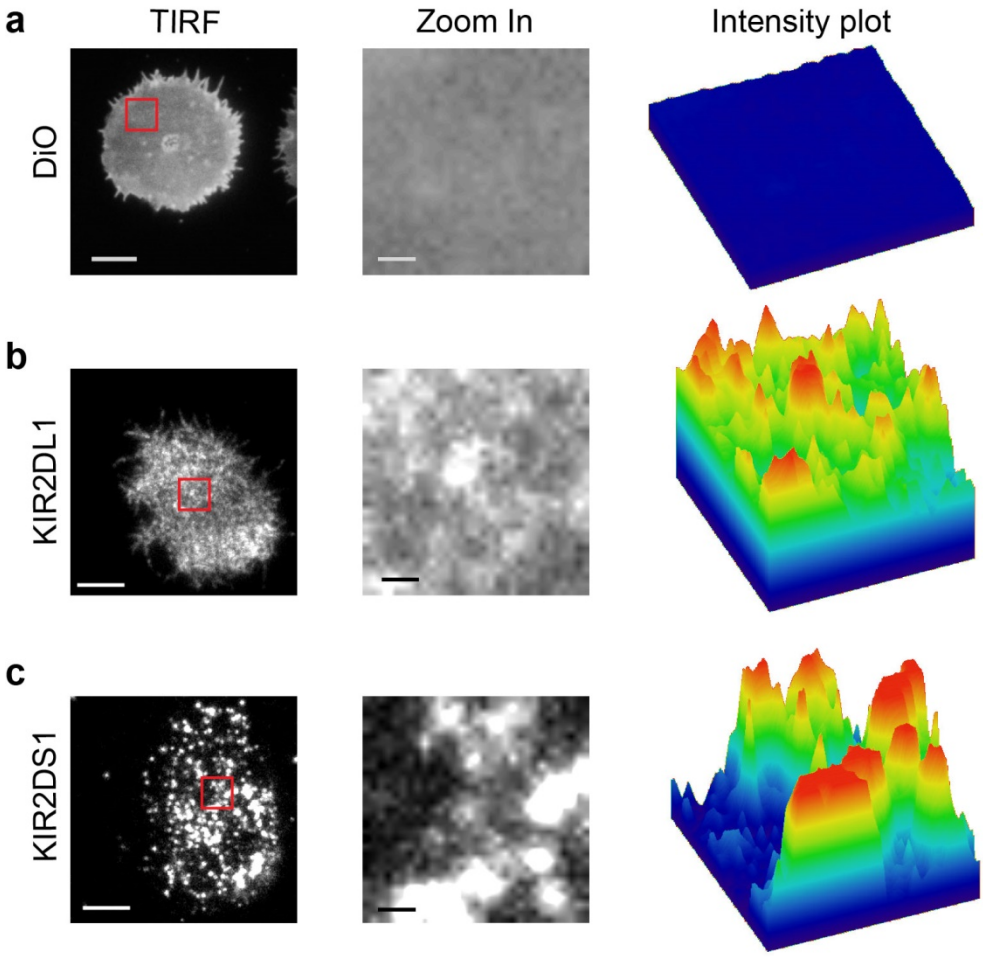

Figure 3.10 Clustering patterns observed for KIR2DL1 and KIR2DS1 are not caused by uneven topography of plasma membrane.
Plasma membrane of NKL/KIR2DL1-HA cells was fluorescently labelled with DiO and cells were then added to the PLL-coated slides, fixed and imaged by TIRF microscopy. Distribution of the DiO-derived fluorescent signal in the membrane was compared with the distribution of fluorescence derived from KIR2DL1-HA or KIR2DS1-HA stained with EB6 mAb conjugated with AF 647, by plotting the relative intensity of fluorescence for each pixel in the selected image regions (marked by red squares in TIRF images and enlarged in the middle column) on the z-axis of the three-dimensional plots (right column). Scale bars 5 µm in TIRF images and 500 nm in the enlarged regions.

Comparison of nanometre-scale organization of KIR2DL1-HA and KIR2DS1-HA in NKL cells stained with anti-HA antibody

It is important to note that such experiments provide information only on the molecules detected and therefore they crucially depend on the efficacy of fluorescent staining strategy. With this in mind, it was necessary to verify these observations in analogical experiments using a different mAb for labelling.

Therefore, NKL/KIR2DL1-HA and NKL/KIR2DS1-HA were fixed on PLL-coated slides like before and stained with an antibody targeting the HA tag present at the C-terminus of both receptors, directly conjugated with AF488. Again, the specificity of staining was checked by comparison with the staining in parental cells, which displayed a reduction in the number of molecules detected by 99% (Figure 3.11).

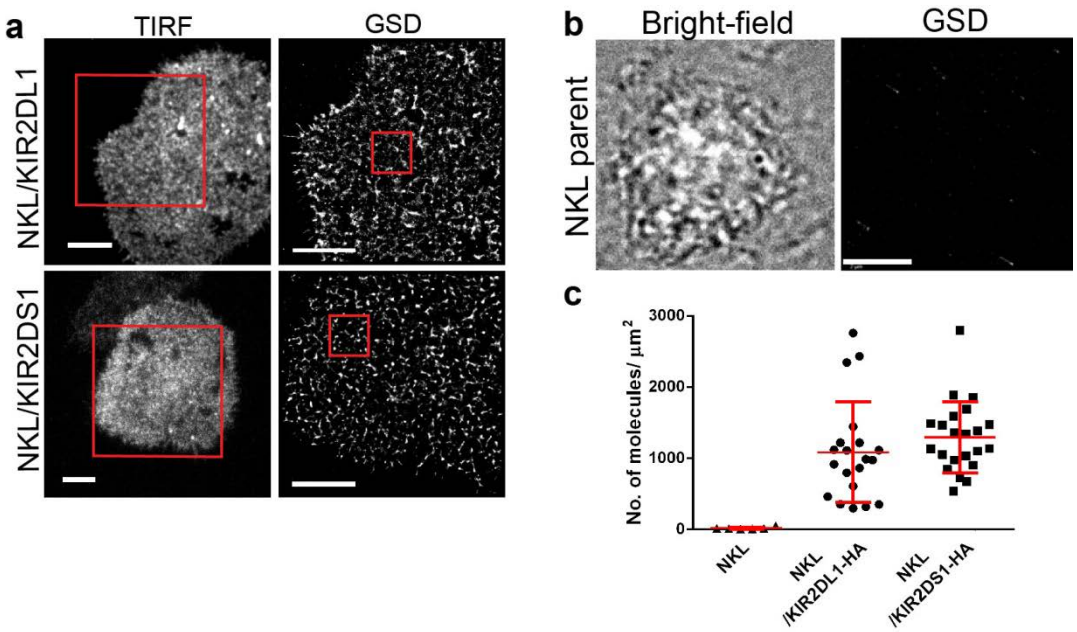

Figure 3.11 Specificity of fluorescent staining of KIR2DL1-HA and KIR2DS1-HA receptors with anti-HA mAb in NKL/KIR2DL1-HA and NKL/KIR2DS1-HA cells.
To assess the specificity of staining with anti-HA mAb conjugated with AF488 in NKL/KIR2DL1-HA and NKL/KIR2DS1-HA cells, the intensity of HA-derived fluorescence was compared between the transfectants (a) and the parental cells (b). For GSDIM microscopy, the average number of molecules detected in the transfectants and parental cells stained with anti-HA mAb was quantified (c).

As in the previous experiments, imaging by GSD provided a remarkable improvement in resolution, as compared to diffraction-limited techniques. This facilitated a direct comparison of KIR2DL1 and KIR2DS1 organization visualized with an anti-HA antibody. Visual inspection of images readily showed that the differences in the KIR2DL1 and KIR2DS1 clustering observed in the previous experiments could also be detected using this alternative labelling strategy (Figure 3.12 a). Clusters of KIR2DS1 clearly had a larger area and in line with this, L(r) – r function plotted for KIR2DS1 molecules peaked at larger radial scale and reached a higher maximum value (Figure 3.12 b).

The differences in clustering of the two receptors were again quantified using Getis and Franklin analysis. To check if the same parameters are suitable for identification of clusters in this data set, the heat-maps and distribution of L(30) values in the regions

from GSDIM images of KIR2DL1 and KIR2DS1 and randomized regions of the same area and density of molecules were compared. Similar to the experiments where anti-KIR2DL/S1 antibodies were used, a threshold value L(30) ≥ 65 was found to be appropriate for the cluster identification (Figure 3.12 c - d).

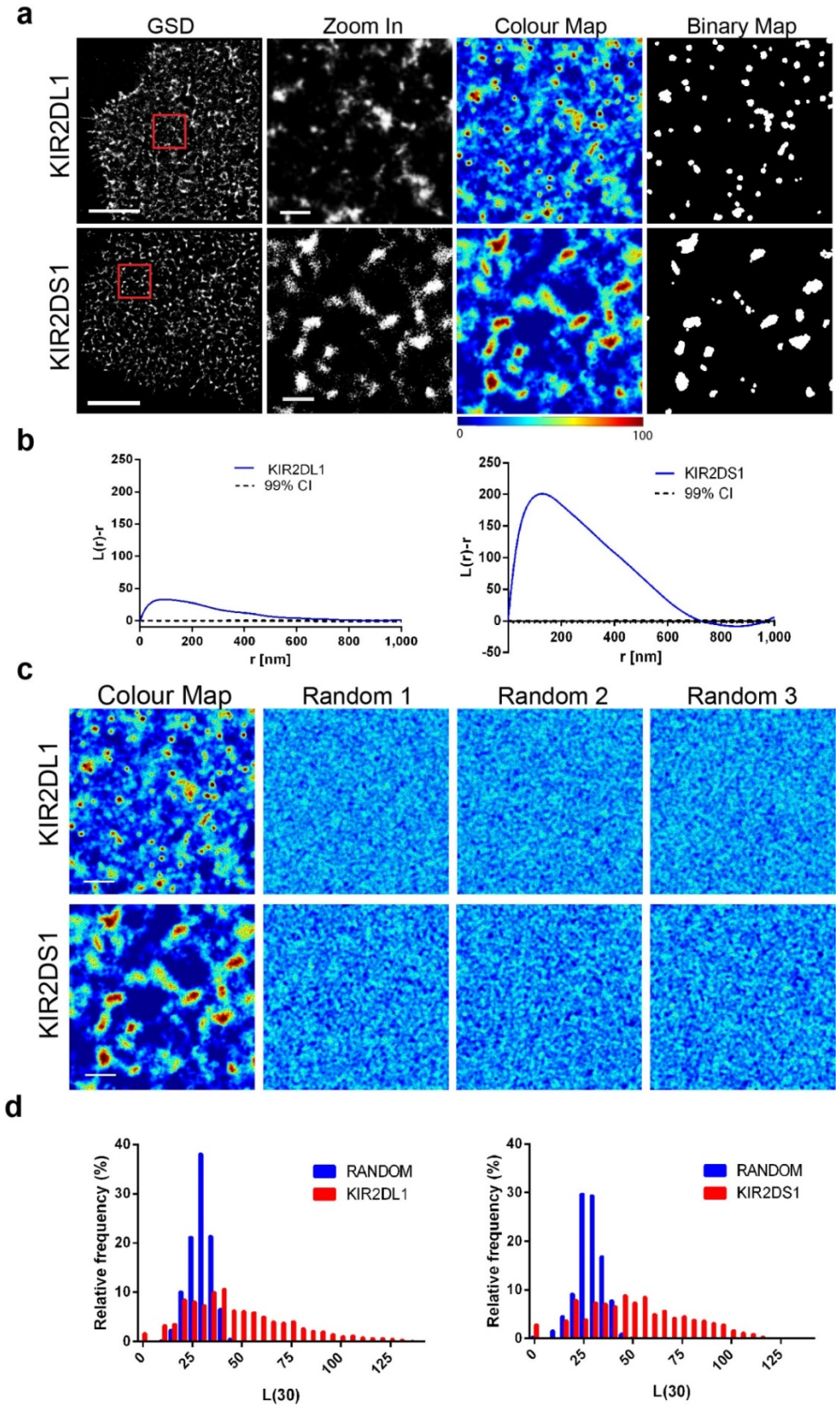

Figure 3.12 Differential clustering of KIR2DL1-HA and KIR2DS1-HA in NKL/KIR2DL1-HA and NKL/KIR2DS1-HA cells labelled with anti-HA mAb and imaged by GSDIM.

NKL/KIR2DL1-HA and NKL/KIR2DS1-HA cells on PLL-coated slides were fixed, permeabilized and stained with anti-HA mAb conjugated to AF 488. (a) Representative GSDIM images of

NKL/KIR2DL1-HA and NKL/KIR2DS1-HA cells are shown with corresponding colour maps where colours correspond to the extent of clustering according to pseudo-colour scale and binary maps of clusters. Scale bars 5 µm. The 3 µm × 3 µm regions (red boxes in GSD images) are zoomed-in (scale bars 500 nm). (b) Ripley's *K* function of the events in the selected regions (red boxes) shown in (a). L(r) − r represents the degree of clustering at different spatial scales relative to simulated random distributions, indicated by the 99% confidence intervals (CI); r is the radial scale. (c-d) Threshold value L(30) ≥ 65 used to create binary maps of clusters was determined by performing Getis & Franklin analysis for randomized regions of the same area and number of molecules (resulting colour maps are shown in (c)) and comparison of L(30) values in the experimental and randomized regions (d).

Analysis of cluster maps for KIR2DL1 and KIR2DS1 stained with anti-HA mAb enabled a quantitative comparison between the results obtained with two alternative methods of visualization. The sizes of KIR2DL1 and KIR2DL1 clusters stained with anti-HA mAb were relatively similar to those observed in the above experiments using EB6 mAb. Clusters of KIR2DS1 had a median area of 15,200 nm^2 and IQR 11,300 – 20,000 nm^2 (corresponding to median diameter of 139 nm), which was 1.9-fold larger than the median area of KIR2DL1 clusters (8,000 nm^2, IQR 6,900 – 8,800 nm^2; corresponding to median diameter of 101 nm, Figure 3.13 a – b).

Like previously, some heterogeneity in cluster sizes was detected within each cell for both KIR2DL1 and KIR2DS1. The distribution of KIR2DL1 cluster sizes was skewed towards smaller clusters (54% below 5,000 nm^2 vs 41% for KIR2DS1) and large clusters ≥ 15,000 nm^2 were 2.4 times more frequent for KIR2DS1 than KIR2DL1 (Figure 13.3 c).

Other differences previously observed in the experiments utilizing the EB6 mAb were also detected in this analysis: clusters of KIR2DS1 were found to be less abundant, less circular, more densely packed and contained a higher fraction of total molecules detected for the receptor (Figure 13.3 d – g). Importantly, the total molecule densities in the individual cells tested was in the same range for KIR2DS1 and KIR2DL1, which indicated that the results were not affected by expression levels (Figure 13.3 h). Again, density of clusters in the individual cells varied more than the average cluster size for KIR2DL1, while for KIR2DS1 cluster size was a more variable parameter (Figure 3.13 i).

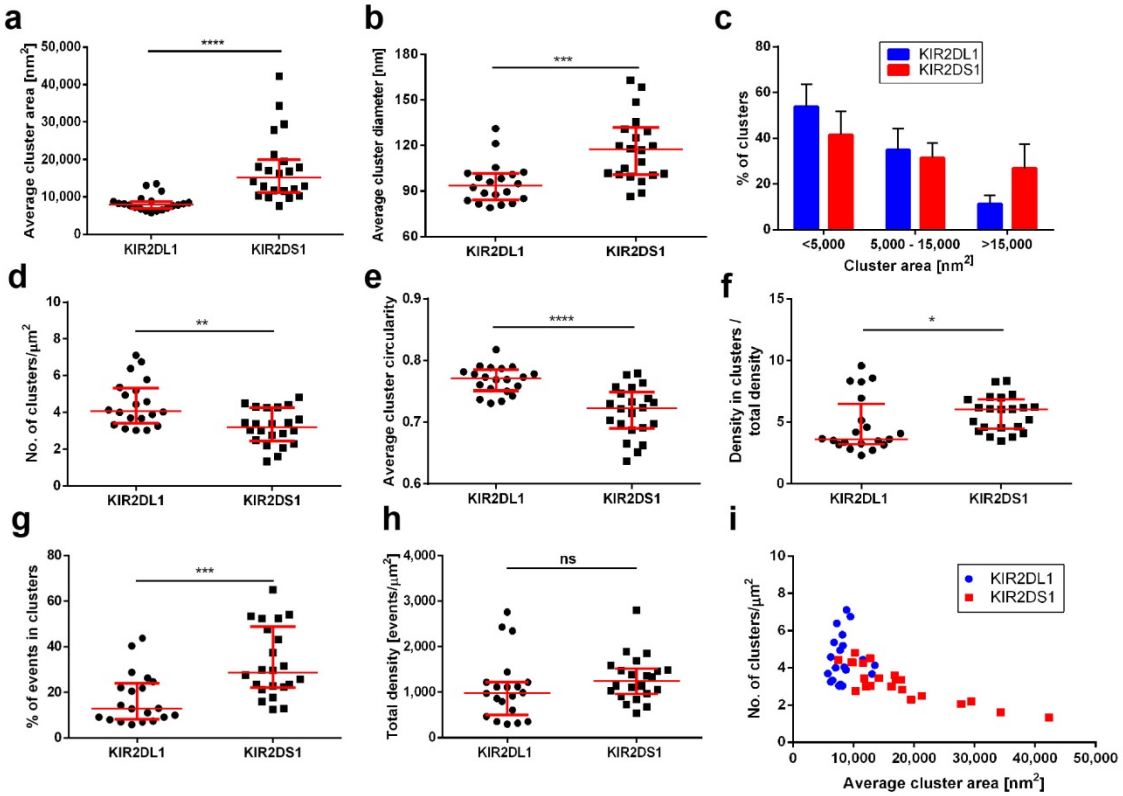

Figure 3.13 Quantitative analysis of KIR2DL1 and KIR2DS1 clustering in NKL/KIR2DL1-HA and NKL/KIR2DS1-HA cells stained with anti-HA mAb.
Average cluster area (a) and diameter (b), size distribution of clusters (c), number of clusters per µm^2 (d), average cluster circularity (e), ratio of density of events in clusters to overall membrane density (f), fraction of molecules localized within clusters (g) and overall density of detected events (h). (i) Number of clusters per µm^2 plotted against average cluster area measured in individual cells. (a - b and d - i) Each symbol represents the mean from several regions within one cell. Horizontal bars and errors represent the medians and interquartile range. (c) Bars and errors represent means and SD. Data are from 20 (KIR2DL1) and 22(KIR2DS1) cells from three independent experiments. ns non-significant, * $p < 0.05$, ** $p < 0.01$, *** $p < 0.001$, **** $p < 0.0001$, Mann-Whitney test.

As before, to further ensure that our observations are independent of the receptors relative abundance, organization of KIR2DS1 and KIR2DL1 was compared directly between cells for which comparable levels of each of the receptors were detected (Figure 3.14). Both heat-maps (Figure 3.14 a) and plotting of average cluster area versus molecular density for each cell (Figure 3.14 b) demonstrated that when visualized by the anti-HA staining, KIR2DS1 consistently forms larger clusters than KIR2DL1 at similar densities.

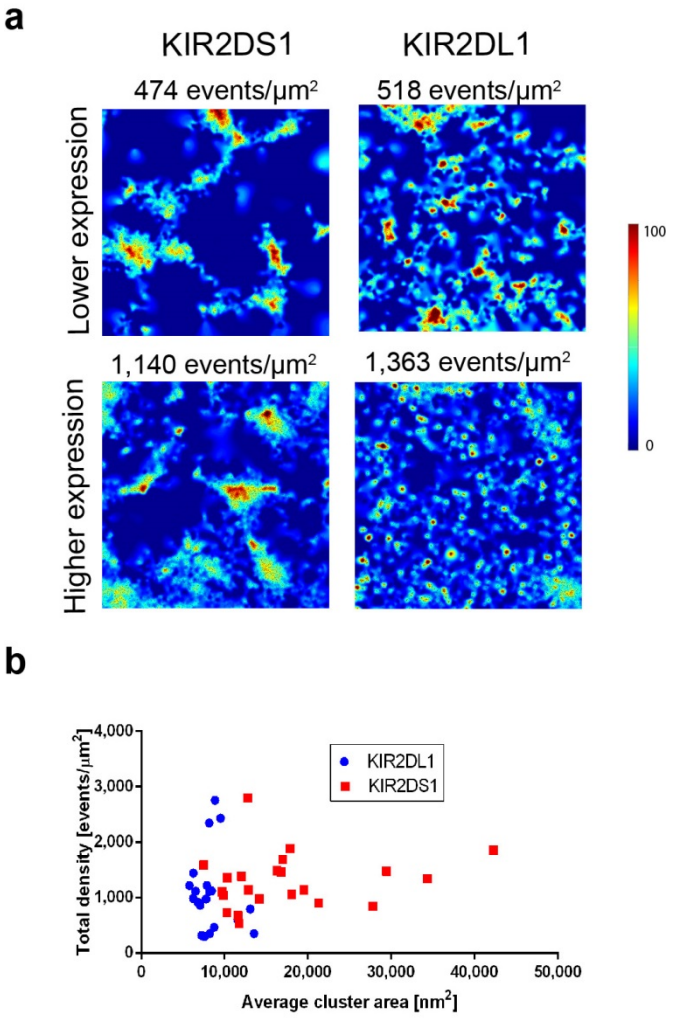

Figure 3.14 Differences in KIR2DL1-HA and KIR2DS1-HA clustering visualised by fluorescent staining with anti-HA mAb are not due to differential expression levels.
NKL/KIR2DL1-HA and NKL/KIR2DS1-HA cells were stained with anti-HA mAb conjugated with AF 488 and imaged by GSD microscopy. (a) Selected 3 µm × 3 µm regions are shown as colour maps where colours correspond to the extent of clustering according to pseudo-colour scale. Regions from cells with relatively low (upper row) and high (lower row) densities of detected events are shown. (b) Total density of events plotted against average cluster area measured in individual cells. Each symbol represents the mean from several regions within one cell. Data are from 20 (KIR2DL1) and 22 (KIR2DS1) cells from three independent experiments. Scale bars 500 nm.

Overall, the absolute values extracted from the images of KIR2DL1 and KIR2DS1 stained with either EB6 mAb conjugated with AF 647 or anti-HA mAb conjugated with AF488 were relatively similar (within the range of error) and most importantly, all the quantitative differences between the cluster parameters were consistently detected with both staining strategies. This indicated that the observations of KIR2DL1 and KIR2DS1 differential clustering patterns ware not dependent on a particular method of proteins visualisation.

3.3.4 Comparison of KIR2DL1 and KIR2DS1 nanometre-scale organization in NKL cells fixed in suspension by GSDIM

Glass slides are generally a stiff surface and most likely a stiffer one than substrates which NK cells might encounter *in vivo*. Therefore, one could imagine that interaction with PLL-coated glass slides might affect the organization of membrane-bounds proteins. To control for this, the experiments comparing KIR2DS1 and KIR2DL1 clustering were repeated in cells that were fixed and stained with the EB6 mAb conjugated to AF647 prior to adding them to chambered glass slides. Samples were imaged in the same way as in the previous experiments using the same mAb and obtained data was analysed in an identical way. Thus, it was possible to precisely dissect the effect of contact with glass slides on the organization of tested receptors.

Visual examination of the super-resolution images of KIR2DL1 and KIR2DS1 in NKL/KIR2DL1-HA and NKL/KIR2DS1-HA cells fixed in a suspension demonstrated that although in this setting cells did not spread on glass, imaging of the smaller contact areas was sufficient to visualize differential organization of the two receptors (Figure 3.15).

As before, KIR2DS1 was observed to form clusters of larger area (Figure 3.15 a) and this was further confirmed by the shift in the maximum value of L(r) – r function (Figure 3.15 b). Getis and Franklin analysis of the molecular organization in the pre-fixed cells revealed the same differences between the organization of KIR2DL1 and KIR2DS1. One exception was the relative increase in the molecular density in clusters compared to global membrane density (Figure 3.15 c - l). The two earlier datasets had clearly demonstrated that KIR2DS1 clusters are more densely packed, or in other words more enriched in molecules compared to the total membrane imaged, than clusters of KIR2DL1. Here however, although the median value for KIR2DS1 was higher than for KIR2DL1 (9.9-fold vs. 6.5-fold increase) the difference did not reach statistical significance ($p = 0.13$; Mann-Whitney test). It is possible that measurement of this particular parameter was more affected by the impaired spreading of the cells on glass and therefore it could not be precisely estimated in all the cells tested.

Importantly, a cross-correlation of average cluster sizes and molecular densities in particular cells images in these experiments once again confirmed that the observed differences are not caused by the numbers of molecules detected and KIR2DS1 forms bigger clusters than KIR2DL1 when they display the same molecular densities (Figure 3.15 l).

Taken together, these data clarifies that differential organization of KIR2DL1 and KIR2DS1 is not affected by the contact with glass surface and therefore this simplistic system can be successfully used for further experiments.

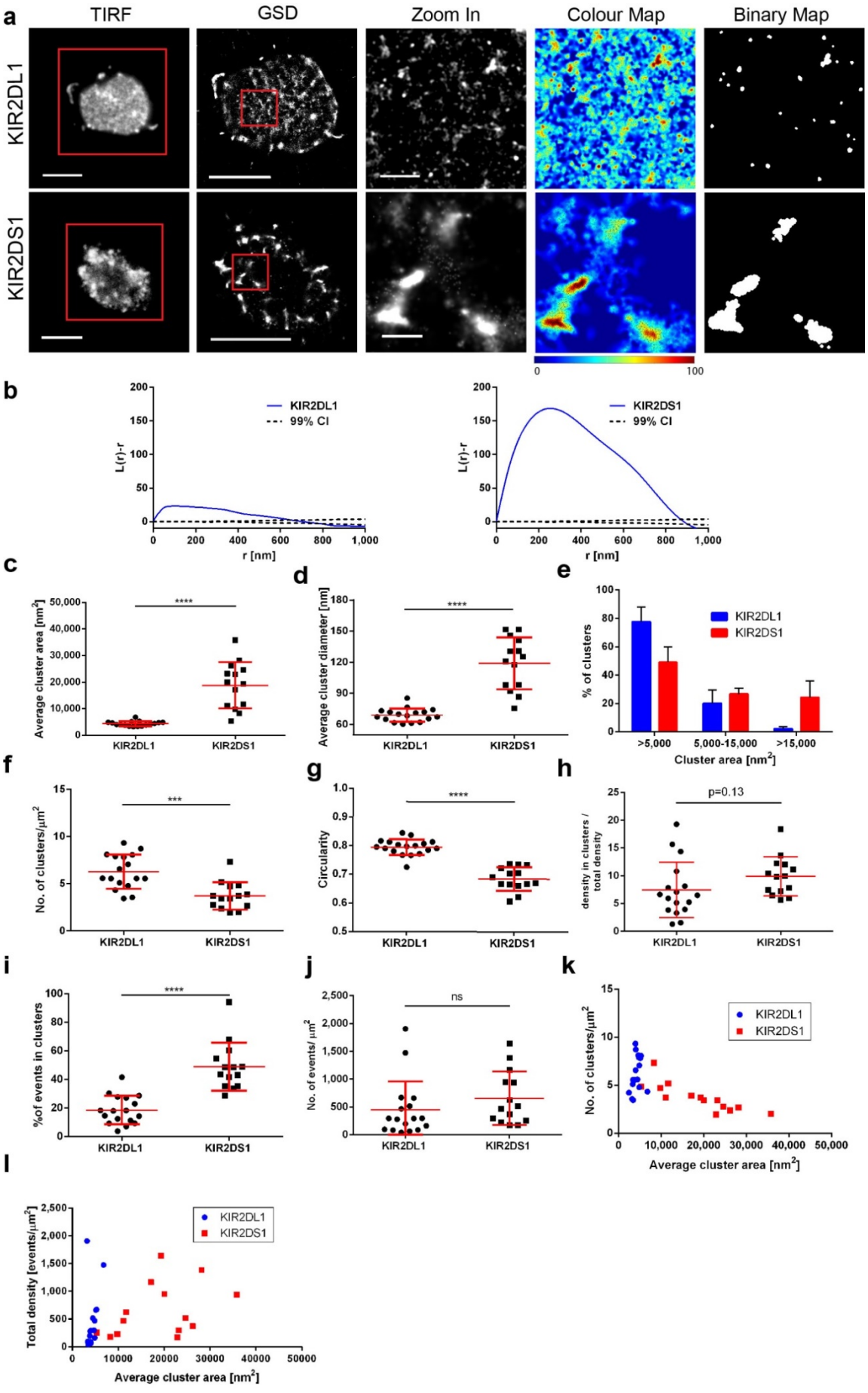
a
TIRF
GSD
Zoom In
Colour Map
Binary Map
KIR2DL1
KIR2DS1
0
100
b
KIR2DL1
99% CI
L(r)-r
r [nm]
KIR2DS1
99% CI
L(r)-r
r [nm]
c
Average cluster area [nm²]
****
KIR2DL1
KIR2DS1
d
Average cluster diameter [nm]
****
KIR2DL1
KIR2DS1
e
% of clusters
KIR2DL1
KIR2DS1
>5,000
5,000-15,000
>15,000
Cluster area [nm²]
f
No. of clusters/µm²
***
KIR2DL1
KIR2DS1
g
Circularity
****
KIR2DL1
KIR2DS1
h
density in clusters / total density
p=0.13
KIR2DL1
KIR2DS1
i
%of events in clusters
****
KIR2DL1
KIR2DS1
j
No. of events/ µm²
ns
KIR2DL1
KIR2DS1
k
No. of clusters/µm²
KIR2DL1
KIR2DS1
Average cluster area [nm²]
l
Total density [events/µm²]
KIR2DL1
KIR2DS1
Average cluster area [nm²]

Figure 3.15 Differential clustering of KIR2DL1 and KIR2DS1 at the surface of NK cells is not affected by contact with glass slides.
(a) Representative TIRF and GSD images of NKL/KIR2DL1-HA and NKL/KIR2DS1-HA cells fixed in suspension, stained with fluorescently labelled EB6 mAb, thoroughly washed and added to chambered glass slides pre-coated with PLL. Scale bars 5 μm. The 3 μm × 3 μm regions (red boxes in GSD images) are zoomed-in and shown with corresponding color maps and binary maps (scale bars 500 nm). (b) Ripley's *K* function of the events in the selected regions (red) shown in (a). (c to j) Quantification of KIR2DL1 and KIR2DS1 clustering in NKL/KIR2DL1-HA and NKL/KIR2DS1-HA cells fixed in suspension: average cluster area (c) and diameter (d), size distribution of clusters (e), number of clusters per μm^2 (f), average cluster circularity (g), ratio of density of events in clusters to overall membrane density (h), fraction of molecules localized within clusters (i) and overall density of detected events (j). (k - l) Number of clusters per μm^2 (k) or total density of detected events (l) were plotted against cluster area measured in individual cells. (c - d and f - l) Each symbol represents the mean from several regions within one cell. Horizontal bars and errors represent the medians and interquartile range. (e) Bars and errors represent means and SD, respectively. Data are from 17 (KIR2DL1) and 14 (KIR2DS1) cells from two independent experiments. ns non-significant, *** $p < 0.001$, **** $p < 0.0001$, Mann-Whitney test.

3.3.5 Comparison of IL-2Rα nanometre-scale organization in NKL/KIR2DL1-HA and NKL/KIR2DS1-HA cells by GSDIM

Although a rather unlikely possibility, it could not be excluded that there might be some general differences in the membrane organization between the NKL\KIR2DL1-HA and NKL\KIR2DS1-HA cell lines, which are mirrored by the organization of the two transfected receptors.

To explore this possibility, it was necessary to image another membrane-bound protein endogenously expressed by the NKL cell line. One such protein is α subunit of IL-2 receptor (IL-2Rα). Thus, the IL-2Rα in NKL\KIR2DL1-HA and NKL\KIR2DS1-HA cells plated and fixed on PLL-coated glass slides was stained using a mAb and a secondary antibody conjugated to AF 488. Cells were imaged by GSDIM microscopy and data was analysed as described before.

Reconstruction of super-resolution images has readily suggested that like the KIR, IL-2R assembles into the nanometre-scale clusters at the surface of NK cells (Figure 3.16 a). Crucially, there was no difference in IL-Rα organization at the surface of compared cell lines. Furthermore, plots of L(r) - r describing the IL-2Rα organization in these cell lines reached a very similar maximum value (264.6 for NKL\KIR2DL1-HA and 266.2 for NKL\KIR2DS1-HA) at a similar radial scale (150 nm for NKL\KIR2DL1-HA and 110 nm for NKL\KIR2DS1-HA) (Figure 3.16 b).

Thresholding of cluster maps for IL-2Rα demonstrated that this cytokine receptor forms bigger clusters than the KIR and their average size is not significantly different in NKL\KIR2DL1-HA (median of 25,700 nm^2, IQR 18,000 – 32,900 nm^2) NKL\KIR2DS1-HA (median of 30,500 nm^2 IQR 22,700 – 31,900 nm^2). Similar to KIR clusters, IL-2Rα

clusters found within one cell displayed a range of different sizes, but importantly, the relative distribution of cluster sizes appeared to be almost identical in both cell lines tested (Figure 3.16 e).

Organization of IL-2Rα in NKL\KIR2DL1-HA and NKL\KIR2DS1-HA cell lines was also indistinguishable with regards to other parameters, such as density of clusters, circularity, density of clusters relative to total membrane density, fraction of events localized in clusters and total density of molecules. According to Mann-Whitney test by ranks, no parameter was different for the IL-Rα imaged in NKL/KIR2DL1-HA and NKL/KIR2DS1-HA cells (Figure 3.16 c – j). When pairs of parameters measured in the same individual cells were plotted against each other (cluster size vs density of clusters and cluster size vs total molecular density) there was no segregation between the two populations imaged (Figure 3.16 k – l), which was different from the same type of graphs comparing KIR2DL1 and KIR2DS1. Overall, IL-2Rα appeared to be organized in an identical way at the surface of both cell lines used throughout this study. Therefore, it can be assumed that no general differences in the membrane organization between these two cells lines exist and all the quantitative differences noted for KIR2DL1 and KIR2DS1 are specific for these particular proteins.

In summary, the same dissimilarities between the activating KIR2DS1 and inhibitory KIR2DL1 receptors were consistently observed using a variety of staining strategies and experimental protocols. This indicated that specific patterns of KIR2DL1 and KIR2DS1 nanometre-scale organization are not caused by the experimental procedures applied and are the intrinsic feature of these receptors.

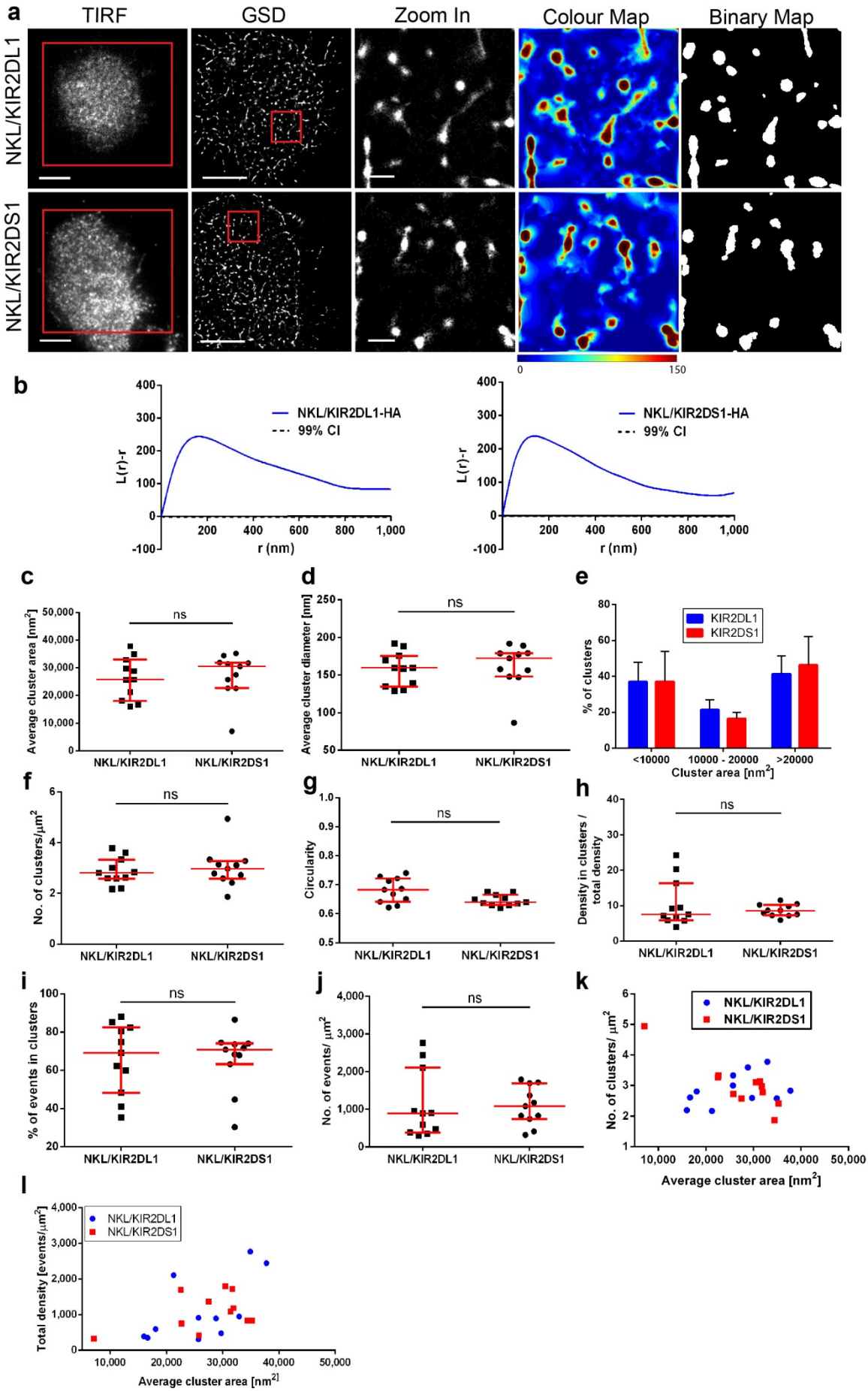
a
TIRF
GSD
Zoom In
Colour Map
Binary Map
NKL/KIR2DL1
NKL/KIR2DS1
0
150
b
NKL/KIR2DL1-HA
99% CI
L(r)-r
r (nm)
NKL/KIR2DS1-HA
99% CI
L(r)-r
r (nm)
c
Average cluster area [nm²]
ns
NKL/KIR2DL1
NKL/KIR2DS1
d
Average cluster diameter [nm]
ns
NKL/KIR2DL1
NKL/KIR2DS1
e
KIR2DL1
KIR2DS1
% of clusters
<10000
10000 - 20000
>20000
Cluster area [nm²]
f
No. of clusters/µm²
ns
NKL/KIR2DL1
NKL/KIR2DS1
g
Circularity
ns
NKL/KIR2DL1
NKL/KIR2DS1
h
Density in clusters / total density
ns
NKL/KIR2DL1
NKL/KIR2DS1
i
% of events in clusters
ns
NKL/KIR2DL1
NKL/KIR2DS1
j
No. of events/ µm²
ns
NKL/KIR2DL1
NKL/KIR2DS1
k
NKL/KIR2DL1
NKL/KIR2DS1
No. of clusters/ µm²
Average cluster area [nm²]
l
NKL/KIR2DL1
NKL/KIR2DS1
Total density [events/µm²]
Average cluster area [nm²]

Figure 3.16 Interleukin-2 Receptor has the same pattern of organization in NKL/KIR2DL1-HA and NKL/KIR2DS1-HA transfectants.
(a) Representative TIRF and GSD images of fluorescently labelled IL-2Rα in NKL/KIR2DL1-HA and NKL/KIR2DS1-HA cells on slides coated with PLL. Scale bars 5 μm. The 3 μm × 3 μm regions (red boxes in GSD images) are zoomed-in and shown with corresponding colour maps and binary maps (scale bars 500 nm). (b) Ripley's *K* function of the events in the selected regions (red) shown in (a). (c to j) Quantitative analysis of IL-2Rα clustering in NKL/KIR2DL1-HA and NKL/KIR2DS1-HA cells: average cluster area (c) and diameter (d), size distribution of clusters (e), number of clusters per μm^2 (f), average cluster circularity (g), ratio of density of events in clusters to overall membrane density (h), fraction of molecules localized within clusters (i) and overall density of detected events (j). (k - l) Number of clusters per μm^2 (k) or total density of detected events (l) were plotted against cluster area measured in individual cells. (c - d and f - l) Each symbol represents the mean from several regions within one cell. Horizontal bars and errors represent the medians and interquartile range. (e) Bars and errors represent means and SD, respectively. For each cell line, data are from 11 cells from two independent experiments. ns non-significant, Mann-Whitney test.

3.3.6 Comparison of KIR2DL1 and KIR2DS1 nanometre-scale organization in primary human NK cells by GSDIM

Next, it was necessary to characterize the nanometre-scale organization of KIR2DL1 and KIR2DS1 endogenously expressed by human primary NK cells. To facilitate imaging of the endogenous KIR2DL1 and KIR2DS1 receptors, clonal NK cell populations were established from the peripheral blood NK cells isolated from healthy donors. Although other NK cell receptors have been successfully imaged in bulk primary NK cells, using NK clones was necessary here due to unavailability of antibodies binding to KIR2DS1, but not to KIR2DL1.

Thus, human peripheral blood NK cells were plated in single wells at the desired density of 1 cell per well. This has resulted in obtaining of NK cell populations homogenous with regards to their KIR repertoire. $KIR2DS1^+/KIR2DL1^-$ and $KIR2DL1^+/KIR2DS1^-$ populations were identified by flow cytometry using a method proposed by Fauriat *et al*. [317], and validated in other studies [228, 258], which utilizes two monoclonal antibodies which compete for binding epitopes, EB6 and 143211. Clone EB6 binds to NK cells expressing either one or both of the receptors, while 143211 ligates only KIR2DL1. The procedures are described in detail in Chapter 2: Experimental Procedures. In most cases, the expanded populations have originated not from a single cell, but more likely from two different NK cells, and therefore not all the cells within the individual population had identical phenotype. This, however, did not interfere with the results of imaging experiments because only the populations identified as single positive for either KIR2DL1 or KIR2DS1 were included in the experiments. For simplicity, the expanded primary NK cell populations are referred to

as clones throughout this thesis. Example flow cytometry plots or the populations of each phenotype are shown in the Figure 3.17.

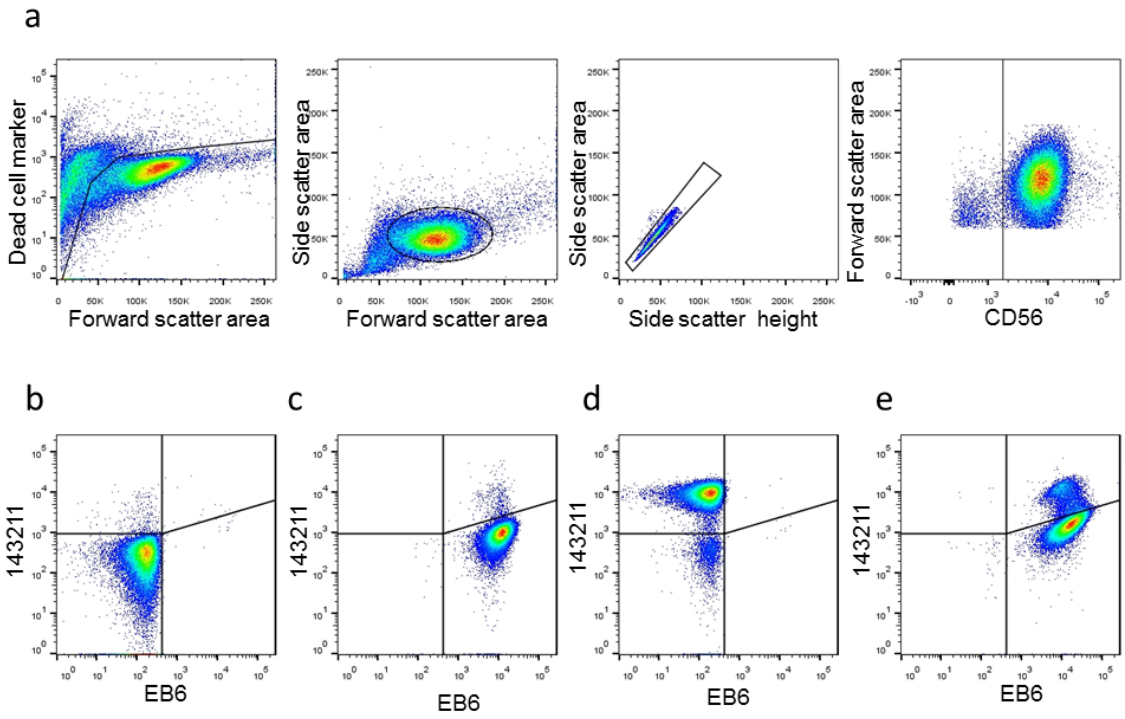

Figure 3.17 Identification of KIR2DL1-/KIR2DS1-, KIR2DL1+/KIR2DS1-, KIR2DL1-/KIR2DS1+ and KIR2DL1+/KIR2DS1+ NK clones.
To analyse the expression of KIR2DL1 and KIR2DS1, human primary NK clones were subsequently stained with an excess of 143211 mAb (which binds only KIR2DL1 and blocks the EB6 mAb binding) and then with EB6 mAb (binds both receptors). Gating strategy is shown in (a). Representative flow cytometry plots for KIR2DL1$^-$/KIR2DS1$^-$ (b), KIR2DL1$^-$/KIR2DS1$^+$ (c), KIR2DL1$^+$/KIR2DS1$^-$ (d) and KIR2DL1$^+$/KIR2DS1$^+$ (e) clones are shown.

In total, five KIR2DL1$^-$/KIR2DS1$^+$ populations were derived from the NK cells from two donors, alongside with five KIR2DL1$^+$/KIR2DS1$^-$ populations originating from the same two donors. For each clone, 3 - 5 cells were imaged by GSDIM and the results were pooled. For imaging, cells were plated on PLL-coated slides, fixed and stained with the EB6 mAb conjugated with Atto 488.

A striking difference in the organization of KIR2DL1 and KIR2DS1 at the surface of human primary NK clones was readily visible in the reconstructed super-resolution images (Figure 3.18 a), as well as pseudo-colour heat-maps and binary maps created for the representative regions from KIR2DL1$^-$/KIR2DS1$^+$ and KIR2DL1$^+$/KIR2DS1$^-$ clones.

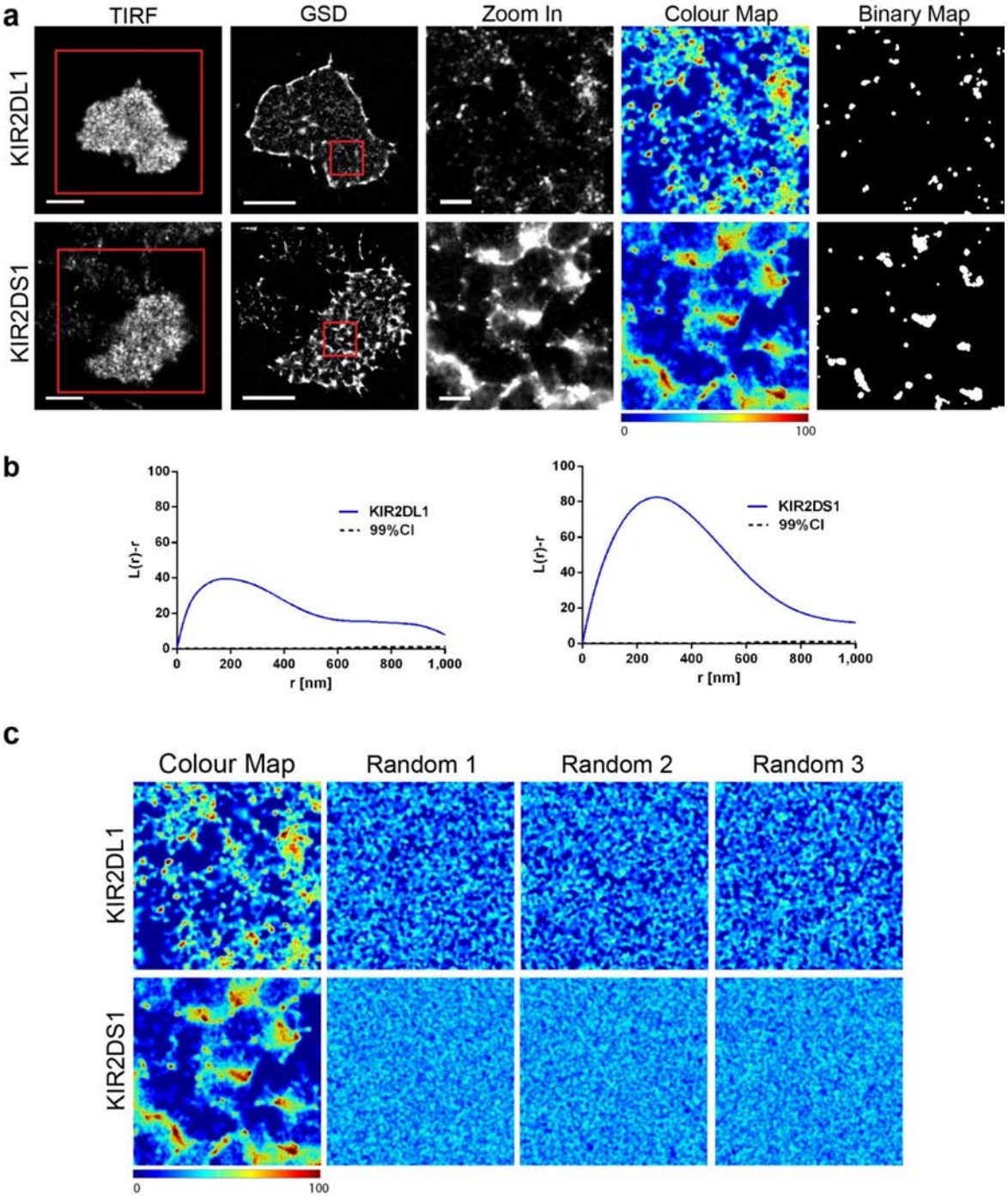

Figure 3.18 Differential clustering of KIR2DL1 and KIR2DS1 in KIR2DL1+/KIR2DS1- and KIR2DL1-/KIR2DS1+ primary human NK clones imaged by GSDIM.

KIR2DL1^{+}/KIR2DS1^{-} and KIR2DL1^{-}/KIR2DS1^{+} primary human NK clones on PLL-coated slides were fixed, permeabilized and stained with EB6 mAb conjugated to Atto 488. (a) Representative GSDIM images of KIR2DL1^{+}/KIR2DS1^{-} and KIR2DL1^{+}/KIR2DS1^{-} NK clones are shown with corresponding colour maps where colours correspond to the extent of clustering according to pseudo-colour scale and binary maps of clusters. Scale bars 5 µm. The 3 µm × 3 µm regions (red boxes in GSD images) are zoomed-in (scale bars 500 nm). (b) Ripley's *K* function of the events in the selected regions (red boxes) shown in (a). L(r) − r represents the degree of clustering at different spatial scales relative to simulated random distributions, indicated by the 99% confidence intervals (CI); r is the radial scale. (c) To establish if threshold value L(30) ≥ 65 is suitable for cluster detection in primary NK clones, Getis & Franklin analysis was run for

randomized regions of the same area and number of molecules and resulting colour maps were compared to the maps created for experimental data (c).

In line with this, L(r) – r function plotted for the molecules of endogenous KIR2DS1 reached a higher maximum value at larger radial scale than the same function plotted for the endogenously expressed KIR2DL1 (Figures 3.18 b). This indicated that similar to NKL, in primary NK cells KIR2DS1 assembled in larger clusters and generally had a more clustered phenotype.

Similar to the previous experiments, Getis and Franklin analysis was run for selected regions from the experimental data as well as three randomized regions of the same area and density. As demonstrated by the heat-maps obtained for the experimental and randomized data, in which the pseudo-colour scale corresponds to the L(30) values for particular molecules, the areas within the primary NK cells images could be identified where the molecules clustered more than expected from the random distribution (Figure 3.18 c).

Generation of binary maps and quantitative analysis of clustering allowed a direct comparison between the KIR2DL1 and KIR2DS1 organization at the surface of NK clones (Figure 3.19). Like in NKL, in primary cells KIR2DS1 formed significantly larger clusters (median area 16,600 nm^2, IQR 11,200 – 21,800 nm^2, which corresponds to median diameter of 145 nm) than KIR2DL1 (median area 6,700 nm^2, IQR 5,000 – 7,500 nm^2; corresponding to median diameter of 92 nm) (Figure 3.19 a – b). A majority (65 ± 9.7%) of KIR2DL1 clusters detected in clones had area below 5,000 nm^2 and clusters larger than 15,000 nm^2 were rarely detected for this receptor. In contrast, such large clusters were 4.5-fold more frequently found for KIR2DS1 (Figure 3.19 c).

Other differences observed in cell lines were also detectable in primary NK cells. Clusters of KIR2DL1 were more abundant at the cells surface (median of 5.4 and IQR 4.8 – 6.8 clusters/μm^2 for KIR2DL1 vs median of 3.9 and IQR 1.7 – 3.9 clusters/μm^2 for KIR2DS1) and more circular (median 0.79 and IQR 0.77 -0.81 vs median 0.71 and IQR 0.65 – 0.71 for KIR2DL1 and KIR2DS1, respectively). The molecular density within the clusters of KIR2DS1 in primary cells was 5-fold increased as compared to the density of molecules across the entire membrane, while increase in the density of KIR2DL1 molecules within clusters was less (3.9-fold). In addition, a fraction of the molecules detected within clusters was higher for KIR2DS1 (median 35%; IQR 26 – 40%) than for KIR2DL1 (median 14%; IQR 10 - 16%) (Figure 3.19 d – g). Importantly, although different molecular densities detected in individual $KIR2DS1^+$ cells covered a wider range, overall they were not significantly different from the densities of KIR2DL1

molecules detected (Figure 3.19 h). Similar to NKL, different parameters were more variable between individual KIR2DS1$^+$ and KIR2DL1$^+$ primary cells – for KIR2DL1, number of clusters tended to vary more than cluster area, while for KIR2DS1 average cluster area was a more variable measure (Figure 3.19 i).

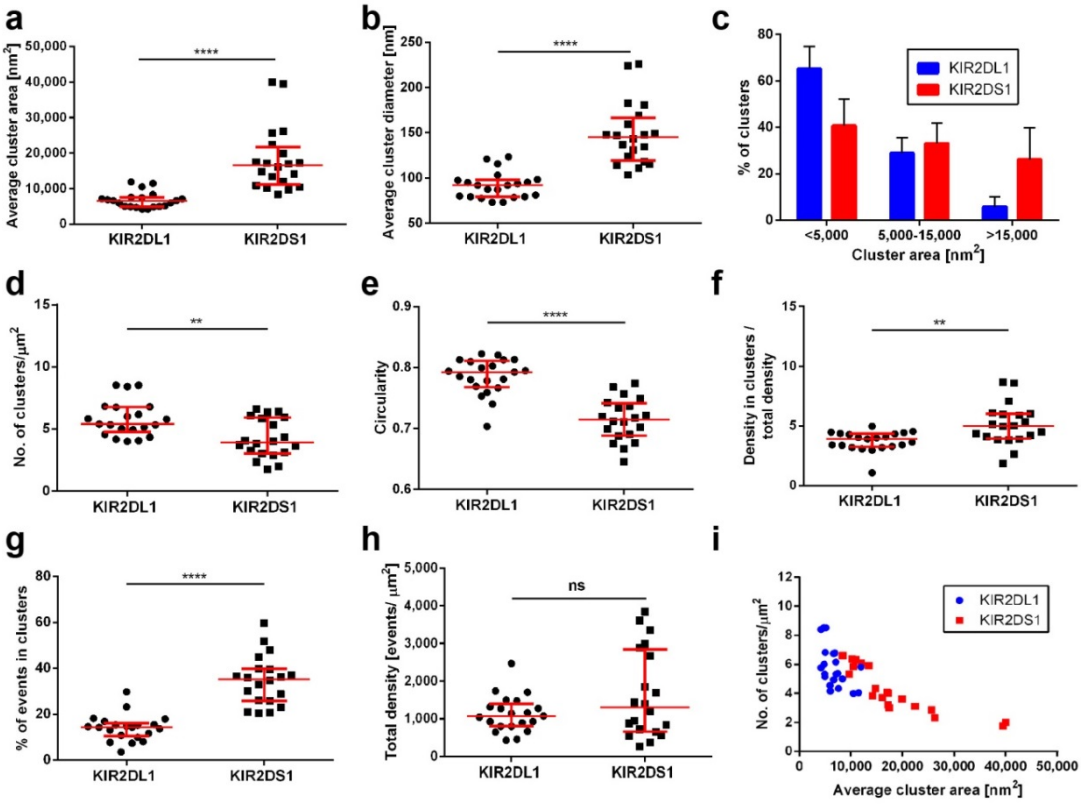

Figure 3.19 Quantitative analysis of KIR2DL1 and KIR2DS1 clustering in KIR2DL1+/KIR2DS1- and KIR2DL1-/KIR2DS1+ primary human NK clones labelled with EB6 mAb.
Average cluster area (a) and diameter (b), size distribution of clusters (c), number of clusters per µm^2 (d), average cluster circularity (e), ratio of density of events in clusters to overall membrane density (f), fraction of molecules localized within clusters (g) and overall density of detected events (h). (i) Number of clusters per µm^2 plotted against average cluster area measured in individual cells. (a - b and d - i) Each symbol represents the mean from several regions within one cell. Horizontal bars and errors represent the medians and interquartile range. (c) Bars and errors represent means and SD. Data are from 21 (KIR2DL1) and 20 (KIR2DS1) cells each from 5 clones derived from two donors. ns non-significant, ** $p < 0.01$, **** $p < 0.0001$, Mann-Whitney test.

Again, the differences in KIR2DL1 and KIR2DS1 organization seemed to be independent of the receptors relative expression in primary cells. Across a range of different molecular densities KIR2DS1 formed less clusters of larger area than KIR2DL1 when comparable densities of the receptors were detected (Figure 3.20).

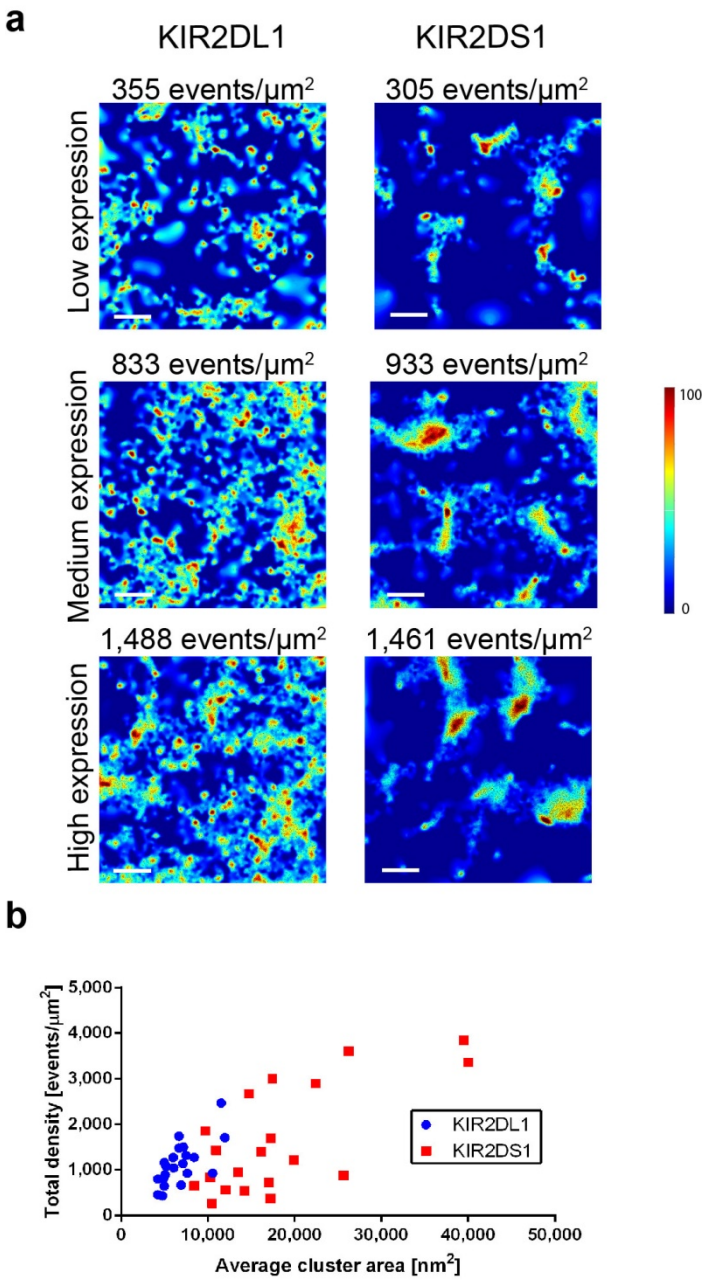

Figure 3.20 Differences in KIR2DL1 and KIR2DS1 clustering in KIR2DL1+/KIR2DS1- and KIR2DL1-/KIR2DS1+ primary human NK clones are not due to differential expression levels.

NKL/KIR2DL1-HA and NKL/KIR2DS1-HA cells were stained with EB6 mAb conjugated with AF 647 and imaged by GSD microscopy. (a) Selected 3 µm × 3 µm regions are shown as colour maps where colours correspond to the extent of clustering according to pseudo-colour scale. Regions from cells with relatively low (upper row) medium (middle row) and high (lower row) densities of detected events are shown. (b) Total density of events plotted against average cluster area measured in individual cells. Each symbol represents the mean from several regions within one cell. Data are from 21 (KIR2DL1) and 20 (KIR2DS1) cells each from 5 clones derived from two donors. Scale bars 500 nm.

Overall, similar values were obtained from measurements of KIR2DL1 and KIR2DS1 clusters at the surface of transfected cell lines and primary human NK cells. Most importantly, all the quantitative differences in the organization of the KIR2D receptors were consistently detected in these two complementary experimental setups.

3.3.7 Comparison of KIR2DL1 and KIR2DS1 nanometre-scale organization in NKL cells by STED

Each super-resolution technique has its caveats, and in particular GSDIM can be subject to oversampling via multiple rounds of photoactivation. Therefore, I next aimed to compare organization of KIR2DL1 and KIR2DS1 using a different super-resolution technique – STED microscopy. This technique does not rely on reconstruction of images from x-y coordinates of individual molecules. Instead, all the fluorophores are localized simultaneously and the improvement in resolution is achieved by shaping a PSF using a doughnut-shaped laser beam.

For single-colour STED imaging, NKL/KIR2DL1-HA and NKL/KIR2DS1-HA cells were plated on PLL-coated slides, fixed, permeabilized and stained with anti-HA mAb conjugated to AF488. Illumination of samples with STED laser led to the improvement in resolution and nanometre-scale clusters of KIR2DL1 and KIR2DS1 could be readily observed in obtained STED images (compare Figure 3.21 b and c).

To facilitate their quantitative characterization, it was necessary to threshold the images to create binary maps. This was achieved using auto-threshold tools in the image analysis software. For thresholding, it is very important to optimize the signal-to-noise ratio in the analysed images and here this was done by deconvolution of STED images using software recommended by the manufacturer of the STED microscope (Figure 3.21 d). This operation aims to recover the image degraded by optical systems by iteratively optimizing the likelihood of an estimate of the object, given the measured image and the PSF. Deconvolved images were used to create binary maps of clusters by applying a Triangle auto-threshold method implemented in ImageJ (Figure 3.21 e). This allowed a direct comparison of the KIR2DS1 and KIR2DL1 cluster dimensions in STED images.

Values measured in such way were similar to the results of single-channel GSDIM experiments. KIR2DS1 clusters detected in NKL/KIR2DS1-HA cells by STED had a median area of 15,000 nm^2, IQR 13,300 – 17,500 nm^2 (and median diameter of 138 nm), which was 1.75-fold larger than median area of KIR2DL1 clusters (8,600 nm^2, IQR 6,800 – 12,800 nm^2; median diameter 105 nm).

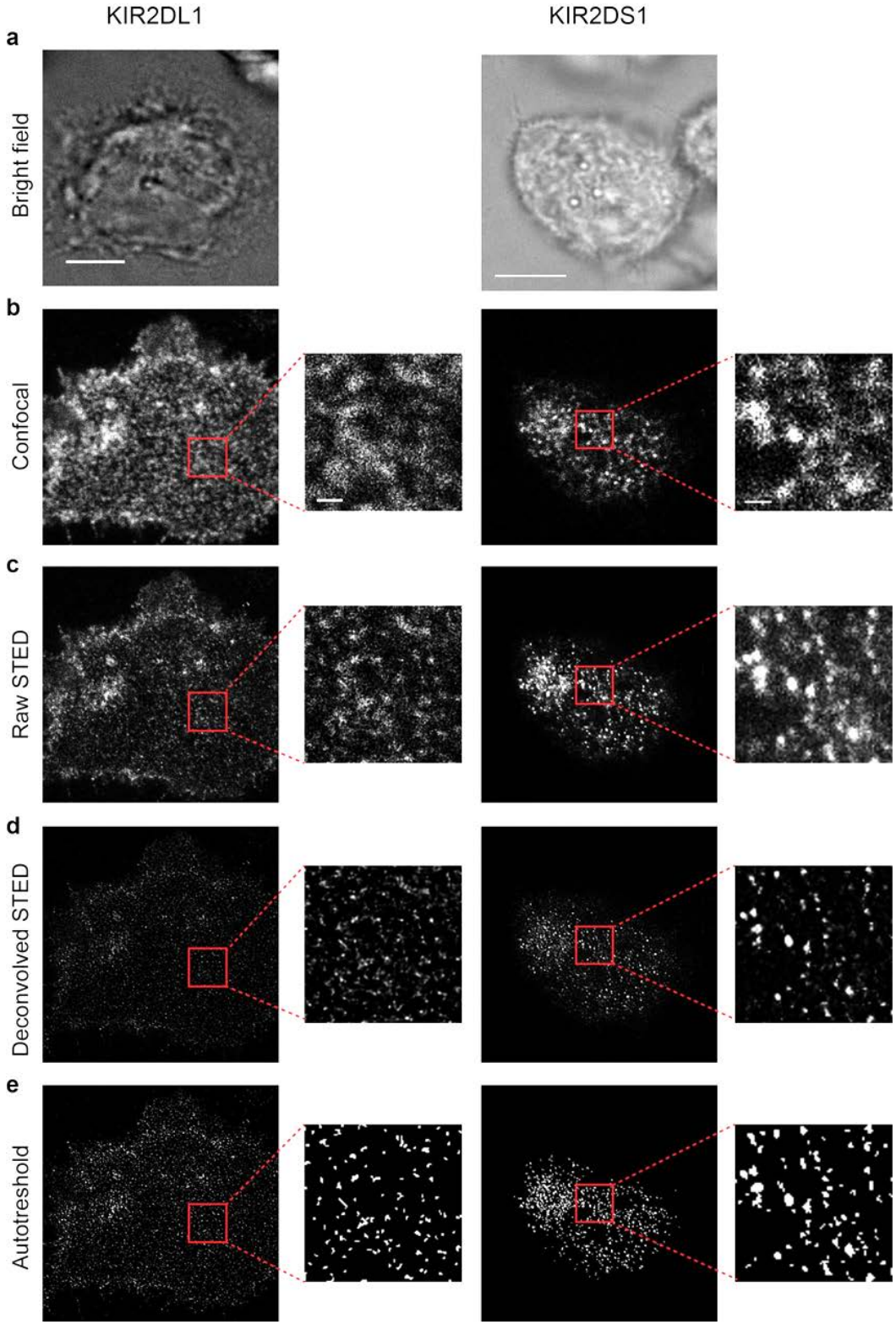

Figure 3.21 Differential clustering of KIR2DL1-HA and KIR2DS1-HA in NKL/KIR2DL1-HA and NKL/KIR2DS1-HA cells visualized by STED microscopy. NKL/KIR2DL1-HA and NKL/KIR2DS1-HA cells plated on PLL-coated slides were stained with anti-HA mAb conjugated with AF 488 and imaged by confocal and STED microscopy. Shown are representative bright-field (a), confocal (b), raw STED (c), deconvolved (STED) (d) images and thresholded binary maps of clusters (e). Scale bars 5 µm.

As in GSDIM data, clusters of both the receptors detected within the same cell displayed some size heterogeneity. Distribution of cluster sizes was skewed towards smaller clusters for KIR2DL1, for which 46 ± 11% of clusters were smaller than 5,000 nm^2, 35 ± 12 % of clusters had area between 5,000 nm^2 – 15,000 nm^2 and 15 ± 10 % were larger than 15,000 nm^2. In contrast, the smallest clusters were less frequent (30 ± 7%) and the largest clusters were 2.4–fold more frequent for KIR2DS1.

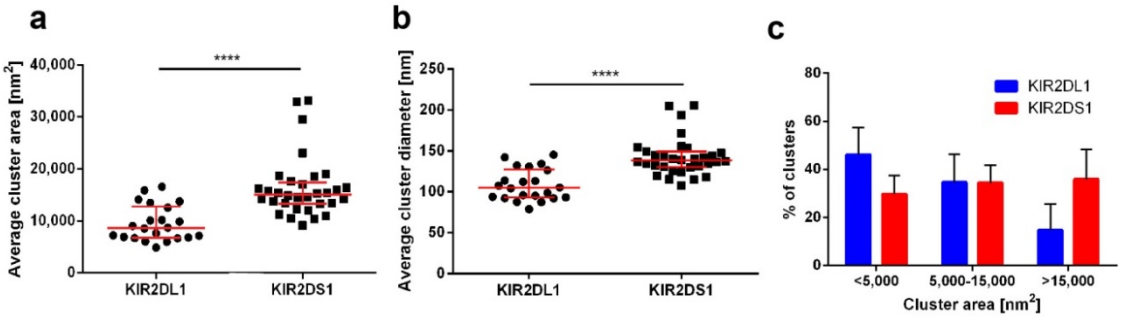

Figure 3.22 Comparison of KIR2DL1-HA and KIR2DS1-HA cluster sizes in NKL/KIR2DL1-HA and NKL/KIR2DS1-HA cells.
Cells were stained with anti-HA mAb and visualized by STED microscopy. (a) Average cluster area, (b) average cluster diameter and (c) size distribution of clusters. (a and b) Each symbol represents the mean from one cell. Horizontal bars and errors represent the medians and interquartile range. (c) Bars and errors represent means and SD. Data are from 22 (KIR2DS1) and 32 (KIR2DL1) cells from three independent experiments. **** $p < 0.0001$, Mann-Whitney test.

3.3.8 Comparison of KIR2DL1 and KIR2DS1 nanometre-scale organization in primary human NK cells by STED

To visualize endogenously expressed KIR2DL1 and KIR2DS1 by STED microscopy, $KIR2DL1^-/KIR2DS1^+$ and $KIR2DL1^+/KIR2DS1^-$ NK clones were plated on PLL-coated slides, fixed and stained with EB6 antibody conjugated with Atto 488. Obtained STED images were deconvolved and auto-thresholded to create binary maps of clusters (Figure 3.23).

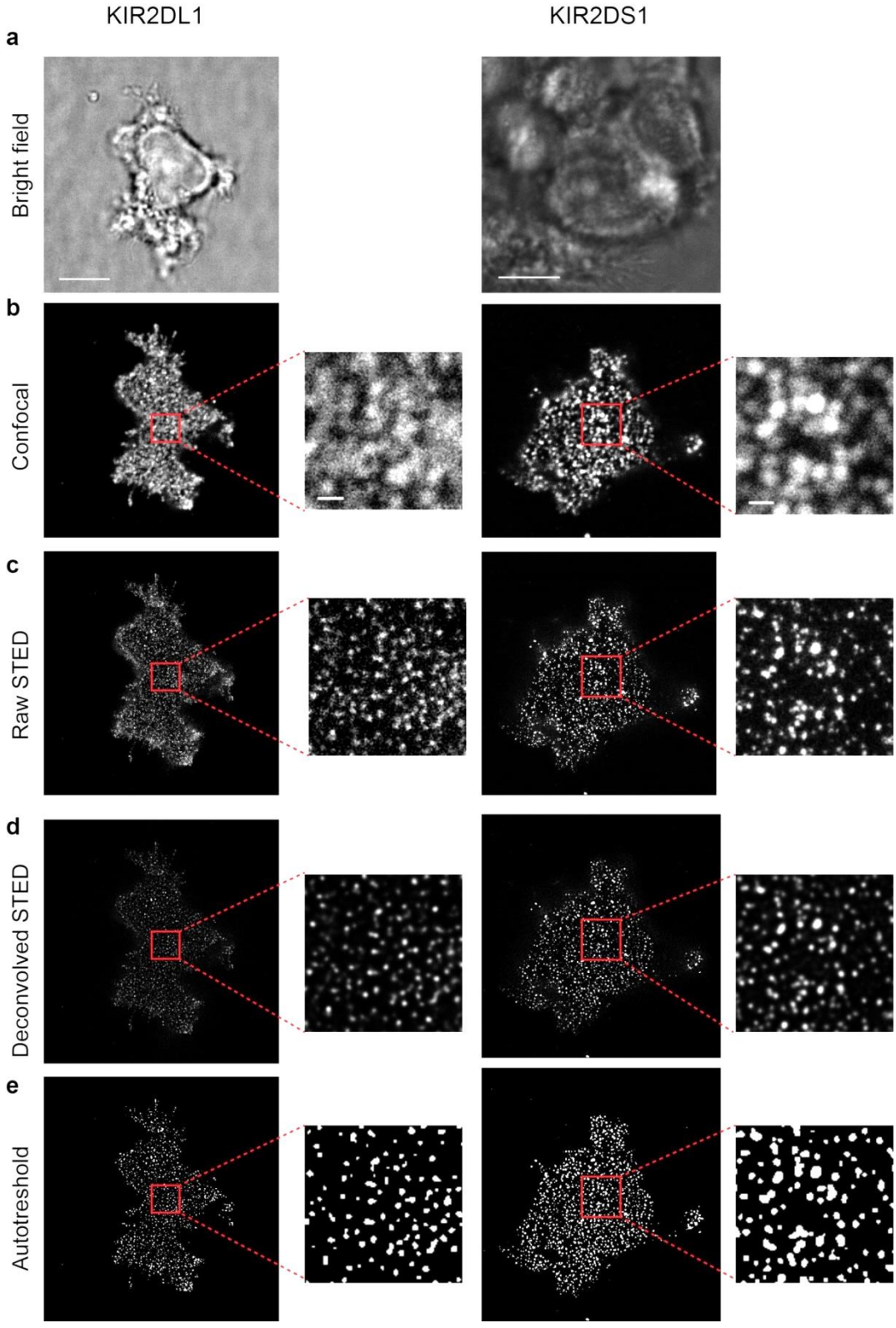

Figure 3.23 Differential clustering of KIR2DL1 and KIR2DS1 in KIR2DL1+/KIR2DS1- and KIR2DL1-/KIR2DS1+ primary human NK clones labelled with EB6 mAb visualized by STED microscopy.

KIR2DL1^{+}/KIR2DS1^{-} and KIR2DL1^{+}/KIR2DS1^{-} NK clones plated on PLL-coated slides were stained with EB6 mAb conjugated with Atto 488 and imaged by confocal and STED microscopy. Shown are representative bright-field (a), confocal (b), raw STED (c), deconvolved (STED) (d) images and thresholded binary maps of clusters (e). Scale bars 5 µm.

Quantitative analysis of the cluster maps demonstrated that in primary human NK cells clusters of KIR2DS1 visualized by STED were larger than clusters formed by KIR2DL1 (median area of 12,400 nm^2, IQR 9,500 – 16,300 nm^2 for KIR2DS1; and median 9,700 nm^2, IQR 7,100 – 10,800 nm^2 for KIR2DL1; corresponding to median diameter of 125 nm for KIR2DS1 and 111 nm for KIR2DL1, Figure 3.24 a - b). Analysis of size distribution for clusters of KIR2DL1 and KIR2DS1 detected by STED in primary cells showed that similarly to the transfected receptors, both receptors formed a range of differently sized clusters in each individual primary cell, however the smallest clusters were more often detected for KIR2DL1, while the biggest ones were for frequently seen for KIR2DS1 (Figure 3.24 c).

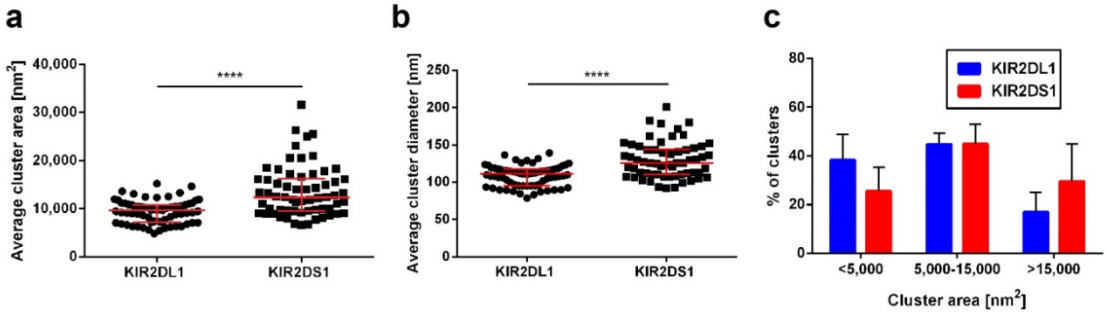

Figure 3.24 Comparison of KIR2DL1 and KIR2DS1 cluster sizes in KIR2DL1+/KIR2DS1- and KIR2DL1+/KIR2DS1- primary human NK clones labelled with EB6 mAb visualized by STED microscopy.
(a) Average cluster area, (b) average cluster diameter and (c) size distribution of clusters. (a and b) Each symbol represents the mean from one cell. Horizontal bars and errors represent the medians and interquartile range. (c) Bars and errors represent means and SD. Data are from 69 (KIR2DL1) and 62 (KIR2DS1) cells each from two clones derived from one donor. **** $p < 0.0001$, Mann-Whitney test.

Overall, imaging of KIR2DL1 and KIR2DS1 in cells lines and primary NK cells using two different super-resolution techniques clearly established that the activating receptor forms larger clusters at the surface of NK cells than its inhibitory counterpart.

3.3.9 Analysis of KIR2DL1 and KIR2DS1 expression in doubly-transfected NKL cell lines

One puzzling question in the field is whether or not the inhibitory and activating NK cell receptors need to be localized within immediate proximity for appropriate signal integration. Such requirement has been previously suggested by studies based on confocal microscopy. Specifically, Kohler *et al*. tested the impact of activating and inhibitory receptors co-localization at the synapse for the outcome of NK cell

interactions with 721.221 target cells transfected with appropriate ligands. The authors were able to force the segregation of NKG2D and KIR2DL1 at the synapse exploiting the principle of a so-called kinetic segregation model. In this model, different molecules are reorganized upon the synapse formation according to the length of their extracellular domains – these with longer domains are 'pushed' out of the area of tight intracellular contact. When segregation of KIR2DL1 and NKG2D was achieved by changing the sizes of the relevant molecules, the outcome of NK cell interactions was modified – KIR2DL1 could no longer inhibit the NKG2D-mediated degranulation. This indicated that activating and inhibitory receptors need to be localized within the same domains for the appropriate integration of NK cell signalling.

However, this study only explored the importance of receptor organization on micrometre scale and whether or not the same requirement applies on a smaller scale has never been rigorously tested.

Upon simultaneous encountering of activating and inhibitory ligands by an NK cell, a phenotypic dominance of inhibitory signals over activation has been observed and consistently, KIR2DL1 signals typically override KIR2DS1-mediated activation in NK cells expressing both receptors [7, 198, 229, 230]. To test whether this is mediated by KIR2DL1 and KIR2DS1 close proximity on nanometre scale, these two receptors had to be imaged by multi-channel super-resolution microscopy. Specifically, it was interesting to explore if activating and inhibitory clusters were localized within the same nanoclusters.

To answer this question, the NKL cell lines transduced to express both KIR2DL1 and KIR2DS1 were obtained as kind gifts from Dr Shaun-Paul Cordoba from Imperial College London. In these cell lines specific identification of each receptor by antibodies is facilitated by the presence of a short peptide tag – HA or FLAG tag – at the C-terminus of each receptor. Combinations of the tagged receptors were expressed in NKL cells to create NKL/KIR2DL1-HA/KIR2DS1-FLAG and NKL/KIR2DL1-FLAG/KIR2DS1-HA cell lines.

Expression of KIR2DL1 and KIR2DS1 in these cells was verified by intracellular staining using anti-HA antibody conjugated to AF 647 and anti-FLAG antibody conjugated to AF 488 for flow cytometry analysis (Figure 3.25). For both cell lines, small populations were observed that abundantly expressed only one of the receptors, while the other one was absent or very weakly expressed. However, the majority of cells (92% for NKL/KIR2DL1-HA/KIR2DS1-FLAG and 86% of NKL/KIR2DL1-FLAG/KIR2DS1-HA) abundantly expressed both receptors.

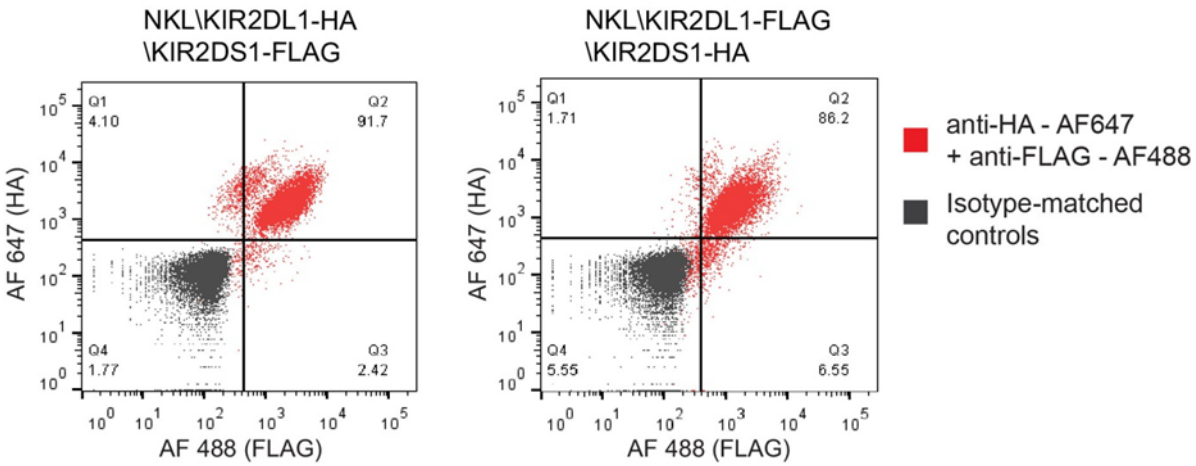

Figure 3.25 Flow cytometry analysis of KIR2DL1 and KIR2DS1 expression in NKL/KIR2DS1-HA/KIR2DL1-FLAG and NKL/KIR2DS1-FLAG/KIR2DL1-HA cells.
NKL/KIR2DL1-HA/KIR2DS1-FLAG and NKL/KIR2DL1-FLAG/KIR2DS1-HA cells were fixed, permeabilized, stained with anti-HA mAb conjugated with AF647 and anti-FLAG mAb conjugated with AF488 (red) and analysed by flow cytometry. Respective cells stained with isotype-matched control mAb (grey) were analysed as negative controls.

To additionally ensure that both cell lines could be reliably used for multi-channel imaging, cells were plated on PLL-coated slides, fixed, permeabilized and stained with anti-HA antibody conjugated with AF 488 and anti-FLAG antibody conjugated with AF 532 (Figure 3.26). For both cell lines, receptor-derived fluorescence was significantly brighter than suitable isotype control-derived signal. Again, this was true for both receptors in great majority of cells, while in small populations only one of the receptors was brightly stained. However, the relative expression of both receptors could be easily assessed prior to image acquisition and cells expressing only one receptor could be excluded from further analysis on this basis. Together, this indicated that both doubly-transfected cell lines facilitated multi-channel super-resolution imaging of KIR2DL1 and KIR2DS1.

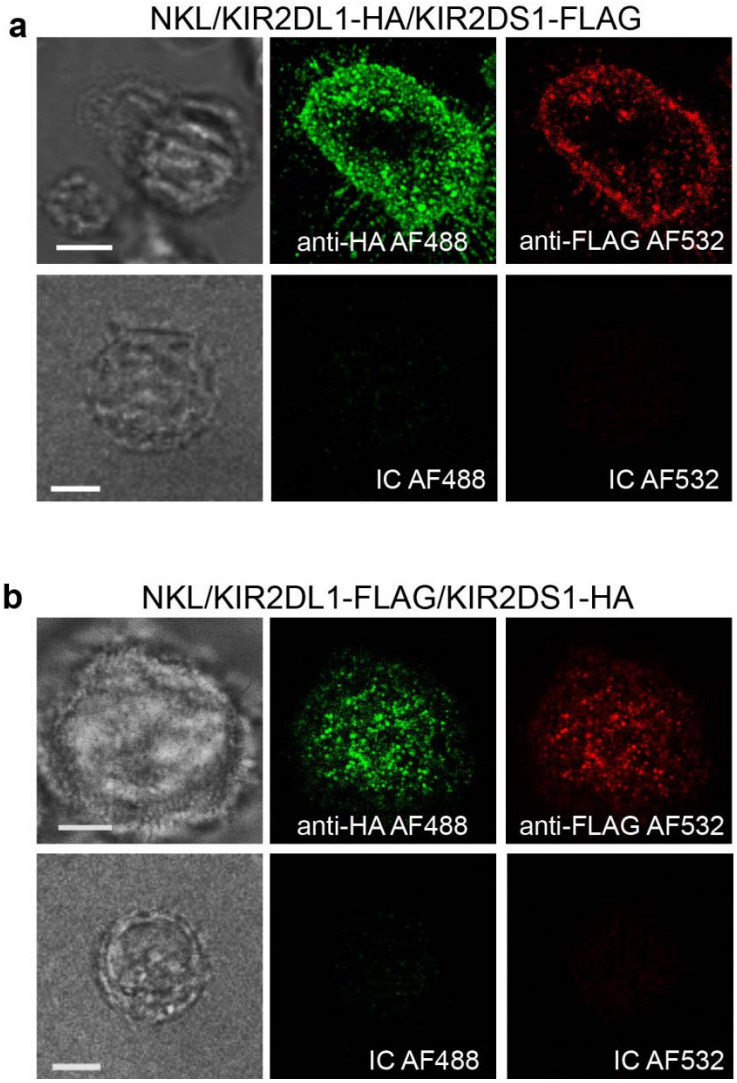

Figure 3.26 Confocal microscopy of KIR2DL1 and KIR2DS1 in NKL/KIR2DL1-HA/KIR2DS1-FLAG and NKL/KIR2DL1-FLAG/KIR2DS1-HA cells.
NKL/KIR2DL1-HA/KIR2DS1-FLAG (a) and NKL/KIR2DL1-FLAG/KIR2DS1-HA (b) cells were plated on PLL-coated slides, fixed, permeabilized, stained with anti-HA antibody conjugated with AF 488 and anti-FLAG antibody conjugated with AF 532 or isotype- and label-matched control antibodies and imaged by confocal microscopy. Scale bars 5 µm.

3.3.10 Analysis of KIR2DL1 and KIR2DS1 function in doubly-transfected NKL cell lines

To verify if upon ligation with EB6 mAb KIR2DL1-mediated inhibition dominates over the activation through KIR2DS1, similar to the outcome in primary NK cells, formation of peripheral actin rings was analysed for both double transfectants. As in earlier experiments with single transfectants, NKL/KIR2DL1-HA/KIR2DS1-FLAG and NKL/KIR2DL1-FLAG/KIR2DS1-HA cells were incubated on glass slides coated with non-stimulatory control antibody, anti-NKG2D antibody for activation of cells, anti-KIR2DL/S1 antibody (clone EB6) or a combination of anti-NKG2D and anti-KIR2DL/S1

antibodies. After 10 min of stimulation, cells were fixed, permeabilized and f-actin was visualized with fluorescently-conjugated phalloidin (Figure 3.27).

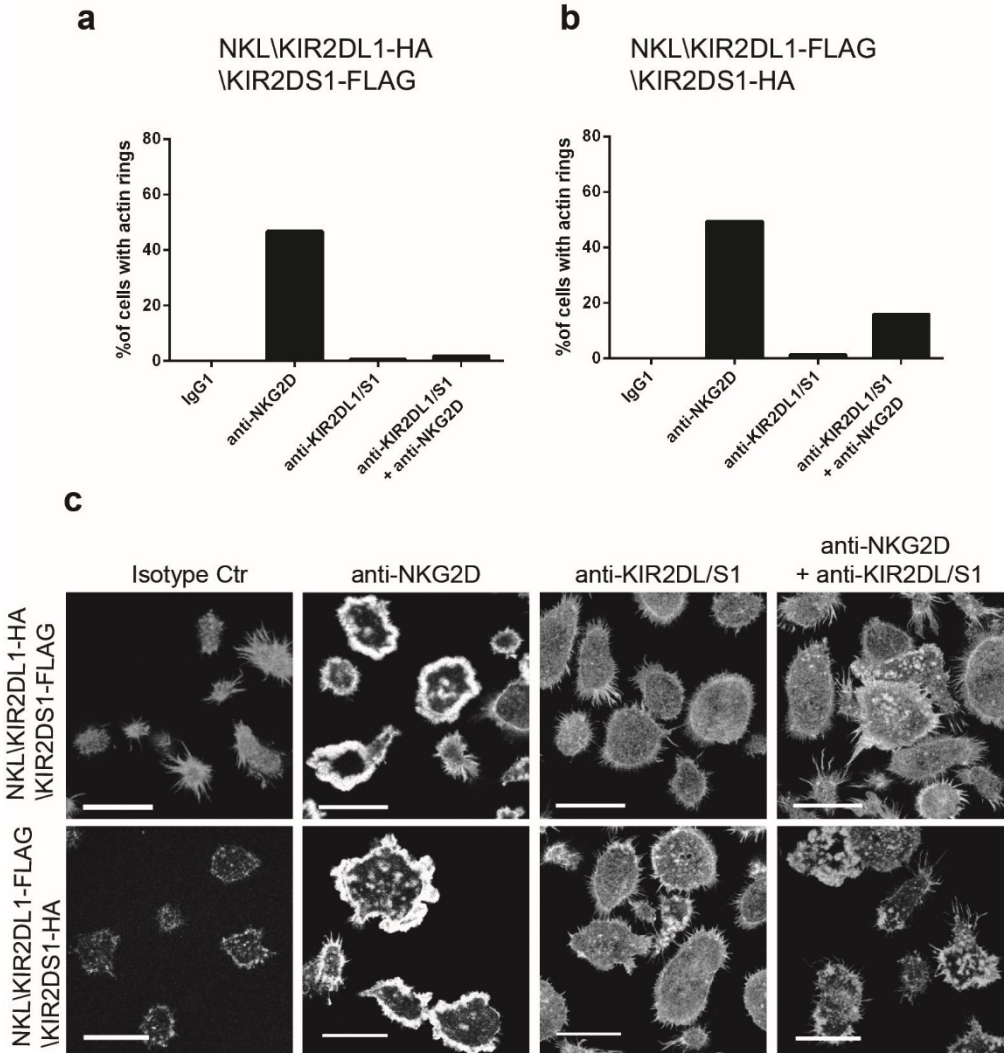

Figure 3.27 Effect of KIR2DL1-HA and KIR2DS1-HA ligation on the activation of NKL/KIR2DL1-HA/KIR2DS1-FLAG and NKL/KIR2DL1-FLAG/KIR2DS1-HA cells assessed by formation of peripheral actin rings.
NKL/KIR2DL1-HA/KIR2DS1-FLAG and NKL/KIR2DL1-FLAG/KIR2DS1-HA transfectants were incubated for 10 min at 37^{o}C on slides coated with anti-KIR2DL/S1 or anti-NKG2D mAb at 5 µg/ml plus 5 µg/ml of murine IgG1, 10 µg/ml of IgG1 or 5 µg/ml of anti-KIR2DL/S1 plus 5 µg/ml of anti-NKG2D mAb. Actin was visualized using fluorescently labelled phalloidin and percentages of cells forming peripheral actin rings were calculated. Results of one representative experiment of two are shown, n ≥ 100 cells per condition in each experiment. Representative fields of view are shown in (d). Scale bars 5 µm.

For both doubly-transfected cell lines, abundant actin rings could only be observed in cells stimulated through the anti-NKG2D antibodies alone, showing that such stimulation was sufficient to activate the cells. In cells incubated on anti-KIR2DL/S1 antibodies, peripheral actin rings were virtually absent. This indicated that in double transfectants, KIR2DL1 signals are able to override KIR2DS1-mediated activation,

which was earlier shown to trigger actin rings formation in KIR2DS1-single positive cells (Figure 3.3).

Moreover, in the presence of KIR2DS1, KIR2DL1 was still able to inhibit NKG2D-mediated activation, as indicated by a decrease in actin rings frequency in cells incubated on anti-NKG2D and anti-KIR2DL/S1 antibodies compared to cells on anti-NKG2D only. In cells incubated on the combination of activating and inhibitory antibodies, the actin rings were virtually absent in NKL/KIR2DL1-HA/KIR2DS1-FLAG cells and very rarely observed in NKL/KIR2DL1-FLAG/KIR2DS1-HA cells. It is difficult to explain why inhibition of NKG2D signals appeared stronger in one doubly transfected cell line than the other. It seems possible that while KIR2DL1 retains its functionality when tagged with either HA or FLAG tag, tag might have a small effect of its signalling efficiency.

Overall, as indicated by the reduction of KIR2DS1- and NKG2D-mediated actin rings formation in both NKL/KIR2DL1-HA/KIR2DS1-FLAG and NKL/KIR2DL1-FLAG/KIR2DS1-HA cells, in both doubly-transfected cell lines functional dominance of KIR2DL1 inhibition over KIR2DS1 activation is retained.

3.3.11 Characterization of KIR2DL1 and KIR2DS1 organization in in doubly-transfected NKL cell lines

To characterize the organization of KIR2DL1 and KIR2DS1 in NKL/KIR2DL1-HA/KIR2DS1-FLAG and NKL/KIR2DL1-FLAG/KIR2DS1-HA cells I first attempted to image the receptors by multi-channel GSDIM. However, this approach could not be reliably used to establish whether or not the two receptors localize within the same nanoclusters. This was due to a lateral shift between fluorescence in two channels which was detected for the samples stained in both channels for KIR2DS1 and imaged as positive control. Although some methods for correction of the inter-channel fluorescence shift are known, it was not possible to perfectly overlay the positive control images using those methods. Therefore, no conclusions about the mutual organization of KIR2DL1 and KIR2DS1 could be drawn from the multichannel GSDIM images.

Problems with overlaying of GSDIM images are likely to at least partially arise from lateral drift associated with very long acquisition times. Therefore, using other microscopy techniques in which acquisition times are shorter was likely to overcome this issue. In the next step, NKL/KIR2DL1-HA/KIR2DS1-FLAG and NKL/KIR2DL1-FLAG/KIR2DS1-HA cells were plated on PLL-coated slides, stained with anti-HA antibody conjugated with AF 488 and anti-FLAG antibody conjugated with AF 532 and

imaged by two-channel STED microscopy. Such approach enabled assessing of KIR2DL1 and KIR2DS1 localization in a lot more precise way than confocal imaging. Although in confocal images of doubly-transfected cells domains occupied by KIR2DL1 and KIR2DS1 seemed to overlay (Figure 3.28 a), STED images revealed that on nanometre-scale the activating receptor was not localized in the same clusters as the inhibitory one (Figure 3.28 b).

Importantly, when KIR2DS1-HA was stained with anti-HA mAb (labelled with AF 488) and EB6 mAb (labelled with AF 532) as a positive control for co-localization, clusters localized in both channels overlaid to much higher extent than in GSDIM images. This indicated that separation between KIR2DL1 and KIR2DS1 observed in STED images most likely represents the actual organization of these two receptors and is not a result of shift between fluorescent signals.

The relative intensities of fluorescence in green and read channels were compared in line profiles drawn across the multichannel images. While in the positive control images the relative intensities of anti-HA and anti-KIR2DL1 staining had almost identical profiles, in both NKL/KIR2DS1-HA/KIR2DL1-FLAG and NKL/KIR2DL1-HA/KIR2DS1-FLAG cells peaks of the relative intensities of staining for KIR2DS1 and KIR2DL1 were clearly segregated from each other (Figure 3.28 c).

To formally quantify degree of overlap between nanoclusters of KIR2DS1 and KIR2DL1, for every imaged cell a Pearson's correlation coefficient was calculated. Values of Pearson's correlation coefficient range between 1 and −1, where 1 means ideal co-localization and −1 means anticorrelation. Median correlation coefficient for KIR2DS1 and KIR2DL1 was -0.17 (IQR -0.22 - -0.08) in NKL/KIR2DS1-HA/KIR2DL1-FLAG and -0.22 (IQR -0.26 - -0.16) in NKL/KIR2DL1-HA/KIR2DS1-FLAG cells, as compared to 0.77 (IQR 0.64 – 0.84) in positive control (Figure 3.28 d). This indicates that when co-expressed, nanoclusters of KIR2DS1 and KIR2DL1 are in fact segregated from each other.

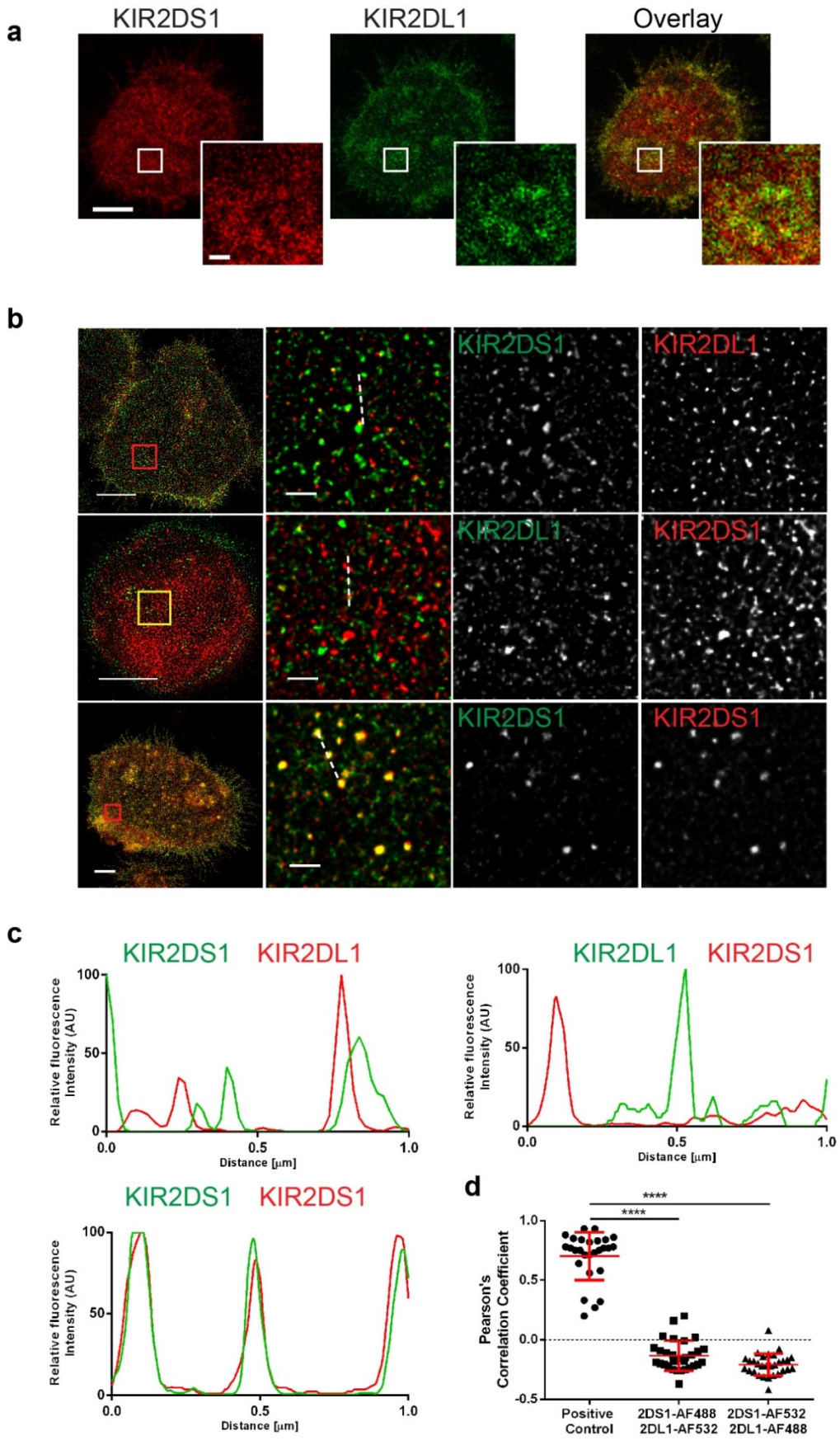

Figure 3.28 KIR2DS1 and KIR2DL1 are localized within separate nanoclusters.

NKL/KIR2DS1-HA/KIR2DL1-FLAG and NKL/KIR2DS1-FLAG/KIR2DL1-HA cells on PLL-coated slides were stained with anti-HA mAb conjugated with AF488 and anti-FLAG mAb conjugated with AF532 and imaged by confocal or STED microscopy. As a positive control, NKL/KIR2DS1-HA cells were stained with anti-HA mAb conjugated with AF488 and anti-KIR2DL/S1 mAb (clone EB6) conjugated with AF532. (a) Representative confocal images and enlarged 3 µm × 3 µm regions (white boxes) of NKL/KIR2DS1-FLAG/KIR2DL1-HA cell. (b) Representative STED images and enlarged 3 µm × 3 µm regions (red/yellow boxes) of NKL/KIR2DS1-HA/KIR2DL1-FLAG (top row), NKL/KIR2DS1-FLAG/KIR2DL1-HA (middle row) cells and KIR2DS1 stained in both channels as positive control of co-localization (bottom row) with channels overlaid and separated. Scale bars are 5 µm in STED images and 500 nm in enlarged regions. (c) Relative fluorescence intensity profiles along the dashed lines drawn across zoomed-in regions shown in (b). (d) Pearson's correlation coefficient values calculated for KIR2DL1 and KIR2DS1 in NKL/KIR2DS1-HA/KIR2DL1-FLAG and NKL/KIR2DS1-FLAG/KIR2DL1-HA cells compared to KIR2DS1 stained in both channels as a positive control. Each symbol represents one cell. For each cell line, data are from 30 cells from three independent experiments. Horizontal bars and errors represent the medians and interquartile range. **** $p < 0.0001$, Kruskal-Wallis test by ranks with Dunn's post-test.

Moreover, thresholding of the STED images to create binary maps and measuring the cluster dimensions demonstrated that differences between KIR2DL1 and KIR2DS1 cluster sizes were preserved in double-positive NK cells. In 96 % of NKL/KIR2DL1-HA/KIR2DS1-FLAG cells and 100% of NKL/KIR2DL1-FLAG/KIR2DS1-HA cells, KIR2DS1 formed larger clusters than its inhibitory counterpart at the surface of the same cell (Figure 3.29).

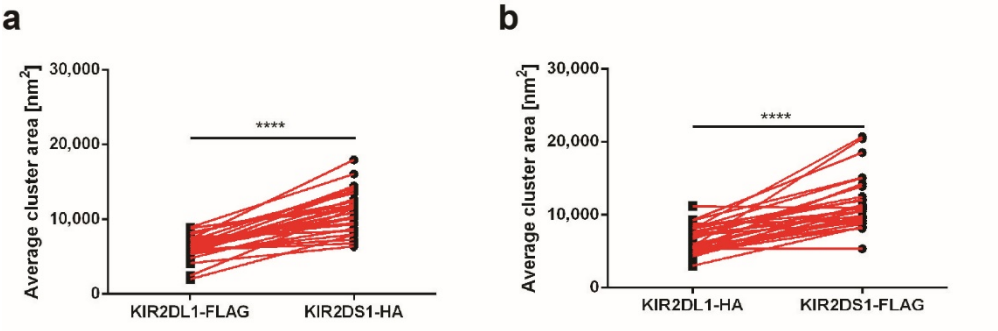

Figure 3.29 Comparison of average sizes of KIR2DL1 and KIR2DS1 clusters detected within the same cell in NKL/KIR2DS1-HA/KIR2DL1-FLAG and NKL/KIR2DS1-FLAG/KIR2DL1-HA cells.
Connected symbols represent values from the same NKL/KIR2DS1-HA/KIR2DL1-FLAG (a) or NKL/KIR2DS1-FLAG/KIR2DL1-HA (b) cell. For each cell line, data are from 30 cells from three independent experiments. **** $p < 0.0001$, Wilcoxon signed-rank test.

Together, these experiments demonstrate that in non-stimulated NK cells co-expressing KIR2DS1 and KIR2DL1, these receptors are localized within different nanoclusters which are spatially segregated from each other.

3.4 Discussion

3.4.1 Summary of results

The aim of this chapter was to characterize the nanometre-scale organization of NK cell paired receptors – inhibitory KIR2DL1 and activating KIR2DS1. This was achieved using two complementary super-resolution microscopy techniques, GSDIM and STED. The main findings presented in this chapter established that:

- Both KIR2DL1 and KIR2DS1 are not homogenously distributed in the membrane of NK cells but instead form nanometre-scale clusters. For KIR2DL1, this confirmed earlier observations published by our group. For KIR2DS1, the nanometre-scale clustering is described here for the first time.
- Despite their structural homology, nanoclusters of KIR2DL1 and KIR2DS1 display strikingly different features, with the activating receptor forming larger, denser and less circular clusters than its inhibitory counterpart. Clusters of KIR2DS1 are less abundant at the surface of NK cells but they contain a higher fraction of all KIR2DS1 molecules present at plasma membrane, as compared to clusters of KIR2DL1.
- When KIR2DL1 and KIR2DS1 are co-expressed at the surface of the same cell, they are localized within separate nanoclusters under non-stimulatory conditions. These clusters do not overlap, but often contact at the edges. In double-positive cells KIR2DS1 forms clusters larger than KIR2DL1 present at the surface of the same cell.

3.4.2 Relation to earlier studies

Formation of nanometre-scale assemblies in the plasma membrane has been described for multiple receptors and downstream signalling molecules involved in immune cells activation. However, majority of studies concentrate on studying clustering of TCR and BCR, while in NK cells this phenomenon is relatively little explored. The only study directly characterizing nanometre-scale organization of an NK cell receptor was published by our laboratory in 2013 and described formation of nanoclusters by KIR2DL1 [224]. The current study further confirmed the presence of KIR2DL1 nanoclusters at the surface of NK cell lines and primary human NK cells.

The absolute values reported here and in the earlier article by Pageon *et al.* are slightly different, although in a similar range. For instance, for KIR2DL1-FLAG fusion receptor transfected into NKL cell line and imaged by GSDIM, the study by Pageon *et*

al. reported an average cluster diameter of ~190 nm in cells incubated on non-stimulatory IgG1 antibodies. In the same study, PALM microscopy of KIR2DL1-tdEos expressed in the NKL cells was found to form clusters of average diameter of 110 nm. Here, diameter of KIR2DL1-HA clusters imaged at the surface of the same cell line was estimated to be smaller, with a median value of 82 nm and mean value of 83 nm. Similarly, clusters of KIR2DL1 at the surface of resting primary human NK cells reported in the earlier study had an average diameter of 146 nm, while here measurements of KIR2DL1 clusters in NK clones gave a median diameter of 92 nm and a mean diameter of 92 nm. Such difference in the size of clusters reported by the two studies from our group is mostly caused by slight differences in the data analysis.

Super-resolution microscopy has been popularized relatively recently and is developing very rapidly. Similarly, the methods of single-molecule data analysis are subject to continuous improvements and optimization. In the study by Pageon *et al.,* the pseudo-colour heat-maps were created by interpolating values of L(50) on a grid and binary maps were created by thresholding of these interpolated pseudo-colour heat-maps. It was later noticed that occasionally such way of cluster mapping led to merging of two or more clusters localized near each other but appearing as separate structures in the corresponding super-resolution images. To avoid such merging of clusters in the later studies, several changes in the data analysis strategy have been introduced and are applied here.

First, a user-defined search radius applied during Getis and Franklin analysis was reduced to 30 nm (this was 50 nm in Pageon *et al.*). Such radius was chosen in an empirical way by analysing the same data set using several different radii and selecting the value which allowed depicting of clusters in the binary maps with the best accuracy. Second, the binary maps used here were not generated by thresholding of the colour-maps. Instead, the exact L(30) values for each molecule were used directly. For each molecule for which $L(30) \geq 65$, a disc object was drawn around it with a diameter equal to the threshold uncertainty value (50 nm). The $L(30) \geq 65$ threshold was also carefully chosen by comparison of distribution of L(30) values in experimental and randomized regions.

These changes improved the precision with which individual clusters could be localized in the binary maps and as a consequence, resulted in smaller sizes of KIR2DL1 reported here than in our previous work. Most importantly however, regardless of the details of the analysis and selection of parameters, results of such measurements are always specific for the chosen search radius, threshold value etc., and should be considered indicative rather than definitive. In fact, they can be most

reliably used for comparison of two proteins imaged and analysed in an identical way, or to compare organization of the same protein under different conditions. Such practice is kept in both the study by Pageon *et al*. and here – every conclusion was drawn from a direct comparison of two data sets treated in an identical manner. Thus, despite minor differences in the absolute values reported, where these two studies overlap, they support each other's findings.

In contrast to KIR2DL1 whose organization has been extensively studied previously, little was known to date about how KIR2DS1 is organized at the surface of NK cells. Self-association of purified KIR2DS1 was detected by Hayley *et al.* who used a range of biophysical methods, including circular dichroism spectroscopy, dynamic light scattering, and atomic force microscopy, to study oligomerization of recombinant extracellular region of KIR2DS1 purified from bacterial expression system [337]. However, the authors did not study at all whether this is also true for the cell membrane-bound KIR2DS1. Our study is the first one to establish that KIR2DS1 forms nanoclusters at the surface of NK cells.

Whether or not the activating and inhibitory NK cell receptors must co-localize for appropriate signal integration has been a long-standing question in the field of NK cell signalling. This was often assumed to be a requirement, since the known substrates for SHP-1 - a tyrosine phosphatase crucial for NK cell inhibition, include molecules engaged in the membrane-proximal activating signals, such as Vav1 [115]. Therefore, it seems plausible that integration of signalling could indeed be a local process, in which SHP-1 physically associates with the ITIMs of inhibitory KIR, becomes activated and immediately dephosphorylates Vav1 recruited to the nearby activating receptors. However, there is not much experimental data to support this scenario. The study by Kohler *et al.* established that co-localization of the activating and inhibitory receptors on micrometre-scale is indeed required for appropriate outcome of signalling, but it did not provide any indication of what happens on a smaller scale [279].

The experiments in doubly-transfected NKL cells included in this chapter indicate that in fact, activating and inhibitory receptors do not have to be pre-mixed in the plasma membrane for the inhibitory receptor to be able to terminate the activating signals, at least not in this particular case of KIR2DL1 and KIR2DS1.

3.4.3 Significance of presented results

The experiments presented in this chapter clearly demonstrated that structurally-related NK cell receptors KIR2DL1 and KIR2DS1 display strikingly different patterns of

nanometre-scale organization at the NK cell surface. The activating KIR2DS1 forms larger and denser clusters which contain a higher percentage of the molecules present at the surface, while KIR2DL1 is generally more dispersed in the membrane, with lower fraction of molecules localized in the clusters that are smaller and less densely packed. It is interesting to speculate that such differential patters could be related to the type of signal transduced by a particular receptor and therefore represent more universal patterns characteristic for the inhibitory and activating NK cell receptors.

Clustering on a nanometre-scale could potentially affect the signalling capabilities of receptors in multiple non-exclusive ways. For instance, increased local density of receptors within a cluster could facilitate a phenomenon known as serial triggering. That is, a single ligand molecule could sequentially associate, activate and dissociate from multiple receptors without a need for its diffusion in the membrane. Therefore, a productive signal could be transduced at lower overall densities of the ligands. This mechanism has been suggested, for example, to mediate high sensitivity of TCR to low levels of cognate peptide MHC ligand, as a single pMHC complex at the surface of antigen-presenting cell was shown to serially trigger up to 200 TCRs [338].

However, dense packing of molecules within the nanoclusters could equally impair their ability to interact with ligands or downstream signalling molecules. One could imagine that when individual receptors are in tight contact, their binding sites might be buried inside the cluster where they are inaccessible for their binding partners. In the absence of specific ligands, such spatial segregation of receptors and other signalling components might serve to suppress the nonspecific activation and thus contribute to the maintenance of a quiescent state. It is further possible, that upon encountering of the ligand only molecules localized at the edges of protein clusters could readily initiate the signalling. This could in turn lead to the rearrangement of clusters and for example, increase the spacing between receptors, allowing more molecules to become signalling-competent and thus potentiate the signal. This second scenario seems especially plausible in case of KIR2DL1 and KIR2DS1. Quantification of the relative molecular densities within the clusters showed that KIR2DL1 tends to be less densely packed within the clusters than KIR2DS1. Although speculative, this could result in more KIR2DL1 molecules being able to transduce the signal immediately upon the ligand recognition, which would at least partially explain the phenotypic dominance of the inhibitory receptor. In this scenario, transducing of a productive signal through KIR2DS1 would require rearrangement of the molecules within membrane, presumably delaying KIR2DS1 signalling, and allow KIR2DL1 to quench activating signals at a very early stage.

Finally, mutual organization of different types of receptors at the cell membrane is likely important for integration of their signals. This seems especially important in NK cells which do not rely on one dominant activating receptor like T cells or B cells but instead are controlled by combined signals from multiple activating and inhibitory receptors. Organization of KIR2DL1 and KIR2DS1 at the surface of double-positive cells visualized in this study disproves some common assumptions that molecules of the activating and inhibitory receptors would have to be intermixed at the membrane to facilitate signal integration. Here, very little overlap between the KIR2DL1 and KIR2DS1 clusters was observed in resting NK cells, although these clusters often remained in contact at the edges. It is possible that flexible cytoplasmic tail of the inhibitory KIR2DL1 could be bent towards the side, allowing the two ITIMs located 38 and 68 amino-acid residues away from the membrane to reach the KIR2DS1 molecules localized at the cluster edges and facilitate a 'local' inhibition. This could in fact be sufficient to terminate the activating signals from KIR2DS1, if the centrally-located molecules had impaired signalling due to, for example, too high molecular density within clusters.

Interestingly, a study by Guia *et al*, suggested that in murine NK cells, the activating receptors were confined within cortical actin mesh network together with the inhibitory receptors only in hyporesponsive, uneducated NK cells [152]. Upon ligand recognition however, the activating receptors were relocated into the membrane nanodomains, while inhibitory receptors remained confined within the actin mesh. It is therefore possible that for the initiation of signal these two types of receptors have to be segregated on nanometre-scale. Their immediate proximity could feasibly cause too strong inhibition and render a cell hyporesponsive, similar to what was seen in uneducated cells.

3.4.4 Future directions

Experiments presented in this chapter established that KIR2DL1 and KIR2DS1 display distinct patterns of nanometre-scale organization at the surface of NK cells. This was done by imaging of fixed cells stained with antibodies. Thus, an important addition to this project would be imaging of KIR2DL1 and KIR2DS1 organization at the surface of living NK cells. Examples of super-resolution studies in live cells can be found in the literature. However, such studies are challenging due to multiple technical aspects of the super-resolution techniques. Out of the two techniques applied in our laboratory, GSDIM typically relies on using antibodies and requires specific imaging

buffers, which are often toxic to living cells. STED on the other hand, often requires illumination of cells with very high laser power, which might lead to significant photo-toxicity. However, several improvements have been recently introduced to address these issues and especially alternative ways to fluorescently label proteins, which are more compatible with live imaging, are becoming increasingly popular. Therefore, the next logical step to further support the findings of this chapter would be to optimize a system for live imaging of KIR2DL1 and KIR2DS1.

Furthermore, it would be very interesting to establish whether the organization patterns observed here are specific only to the KIR2DL1 and KIR2DS1 pair or relate to the general differences between activating and inhibitory NK cell receptors. It seems feasible that different types of organization can be more suitable for transducing a specific type of signal, especially since the activating NK cell receptors often lack ITAMs and their signalling relies on interactions with adaptor molecules.

Finally, differences between KIR2DL1 and KIR2DS described in this chapter provoked two important questions that are at least partially answered in the following chapters of this thesis. Specifically, I wanted to unravel the molecular basis for the KIR2DS1 and KIR2DL1 adopting differential patters of organization and establish whether or not these specific clustering patters are important for the KIR2DL1 and KIR2DS1 signalling.

Chapter 4: The link between nanometre-scale organization and amino-acid sequence of KIR2DL1 and KIR2DS1.

4.1 Introduction

Although formation of nanoclusters at the plasma membrane has been described for a broad range of immune receptors, relatively little is known about what controls the nanometre-scale organization. The most likely scenario is that protein clustering is not caused by any single feature of membrane or proteins themselves but instead is controlled by multiple factors.

A recent study using click chemistry to visualize membrane proteins in living cells and membrane sheets by STED has shown that formation of long-lived multi-protein assemblies is dependent on the presence of cholesterol and is eliminated after treatment of membranes with cholesterol-depleting agent methyl-β-cyclodextrin [339]. In addition, the same study and others advocated the importance of actin cytoskeleton underlying the plasma membrane for stabilizing of protein assemblies [312, 339-341].
However, it is relatively unexplored how the protein structure relates to organization of particular receptors within the membrane. For KIR2DL1, Kumar *et al.* have demonstrated that substitution of histidine 36 in in the first Ig domain sequence with alanine triggers constitutive self-association of the mutant receptor. The authors conclude that the bulky side-chain of histidine 36 acts as a steric hindrance limiting the KIR2DL1 association, because substitution with another bulky amino-acid, phenylalanine, did not trigger the self-association [333]. Importantly, in this study the increased self-association of the receptor was detected as changes in fluorescent signal in a bimolecular fluorescence complementation assay. This method is based on complementation of two non-fluorescent fragments of a protein called Venus, which refold into a fluorescent Venus when the receptors fused with these fragments are in close proximity. However, the authors did not visualize the changes in the protein organization directly.

4.2 Aims

The aim of this chapter was to establish what dictates the differential clustering patterns observed for KIR2DL1 and KIR2DS1.

To date, the only report of the link between sequence and clustering of KIR2DL1 is identification of histidine 36 as a steric hindrance limiting the receptor association in the membrane [333]. Intriguingly, the same residue is found at position 36 in the sequence of KIR2DS1, for which a significantly stronger clustering, as compared to KIR2DL1, was revealed in the previous chapter. This suggested that other structural properties of KIR2DS1 might act alongside the histidine 36-imposed hindrance to regulate the receptor clustering.

In this chapter, the link between the sequence and organization of KIR2DL1 and KIR2DS1 was addressed in a direct way: by introducing changes to amino-acid sequence of the receptors using site-directed mutagenesis and comparison of the wild-type and mutated receptors organization by super-resolution microscopy. Using this approach, I aimed to characterize the structural features causing the KIR2DS1 clusters to be larger and denser than KIR2DL1.

4.3 Results

4.3.1 Expression of mutated forms of KIR2DS1 in NKL cell line

Extracellular domains of KIR2DL1 and KIR2DS1 are highly homologous in terms of amino-acid sequence. Thus, it is not immediately obvious why these proteins organize differently at cell surfaces. The two alleles used in this study differ by only 7 amino-acids in their extracellular domain, which corresponds to 97% homology within this domain (See Appendix 1). The bulk of the differences between KIR2DL1 and KIR2DS1 sequence are located in the transmembrane and cytoplasmic domains. Therefore, to try and unravel the reason for these two receptors distinct organization at the cell surface, I decided to focus on the most important differences within the transmembrane and cytoplasmic domains, such as these associated with the type of signal transduced by each receptor.

To check the importance of the individual amino-acid residues, site-directed mutagenesis was employed to introduce the desired substitutions within the KIR sequences. I first decided to investigate the potential role of lysine residue present within transmembrane region of activating KIR. Activating KIR have no intrinsic

capacity to transduce the signal and their functionality has been shown to depend on the interaction with an adaptor molecule DAP12. Lysine residue present at 9th position in transmembrane region of the activating KIR (apart from KIR2DL4) has been shown to facilitate formation of complexes between KIR and DAP12. Inhibitory KIR do not have a positively-charged amino-acid within their TM domains.

To establish whether the presence of lysine residue in the transmembrane domain influences nanometre-scale organization of KIR2DS1, NKL cell line was stably transduced with two mutated forms of the receptor in which lysine 233 had been substituted with either neutral alanine (KIR2DS1^{K233A}) or positively-charged arginine (KIR2DS1^{K233R}), with an HA tag added at C-terminus. For easier comparison, in the figures comparing different variants of KIR2DS1, the wild type KIR2DS1-HA is referred to as KIR2DS1^{WT}.

Expression of the mutated receptors at the surface of NKL cells, relative to the wild-type form of KIR2DS1 was verified by flow cytometry. For this, parental NKL cells and cells transduced to express each of the receptors were surface-stained with mAb EB6 conjugated to Atto 488 (Figure 4.1a). This has established that both KIR2DS1^{K233A} and KIR2DS1^{K233R} were abundantly present at the surface of transfected cells, although their expression levels differed from the wild-type receptor. Specifically, KIR2DS1^{K233A} displayed a small increase and KIR2DS1^{K233R} a decrease in expression, as compared to KIR2DS1^{WT}. This shows that the amino-acid residue at the position 233 affects the relative expression of the receptor. However, there was a significant overlap between the expression levels of the three populations, meaning that this cellular system could be used to compare the receptors organization at similar molecular densities.

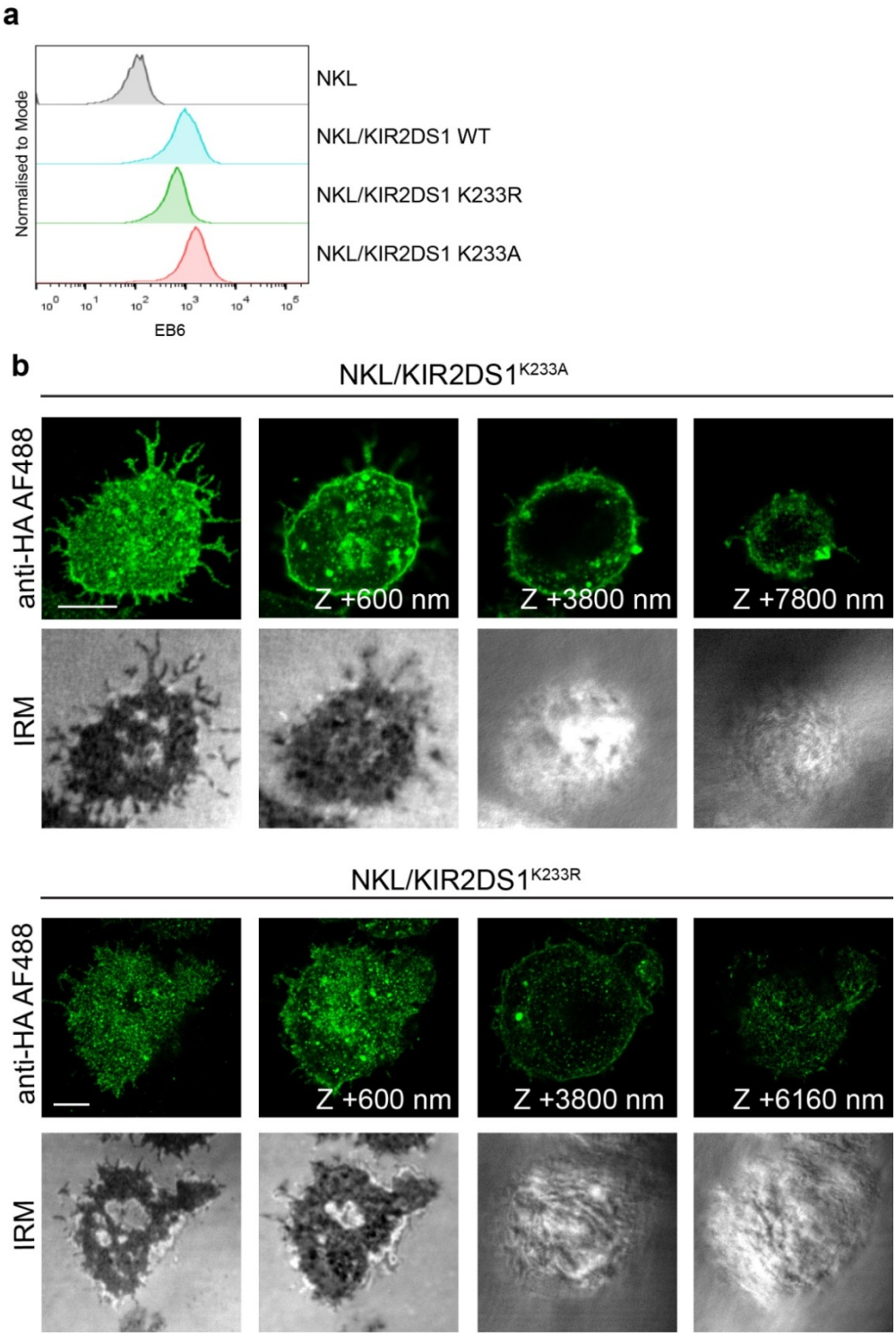

Figure 4.1 Expression of KIR2DS1 mutants in NKL cells.
(a) Parental NKL, NKL/KIR2DS1-HA, NKL/KIR2DS1^{K233A} and NKL/KIR2DS1^{K233R} cells were stained with anti-KIR2DL/S1 mAb (clone EB6) conjugated to Atto 488 and analysed by flow cytometry. (b) NKL/KIR2DS1^{K233A} and NKL/KIR2DS1^{K233R} cells were plated on PLL-coated glass slides, fixed, permeabilized, stained with anti-HA mAb and imaged by confocal microscopy. Localization of the proteins in the respective transfectants was assessed by visualization of KIR-derived fluorescence (upper rows) in different planes of the confocal Z stacks, for which a relative position in the Z plane was checked by imaging in IRM mode (lower rows). The most left images correspond to the membrane proximal to the glass slide and the relative position of other images is indicated in the bottom of the micrographs. Scale bars 5 µm.

In a complementary approach, cellular localization of the mutated receptors was visualized by confocal microscopy. For this, NKL/KIR2DS1^{K233A} and NKL/KIR2DS1^{K233R} cells were plated on the PLL-coated slides, fixed, permeabilized and stained with anti-HA mAb conjugated to AF 488. For both mutated receptors, bright fluorescent signal could be observed in the plane of the membrane contact with glass slide as well as across the whole of the higher located parts of the cell (Figure 4.1 b). Similar to the wild-type KIR2DS1, a fraction of both KIR2DS1^{K233A} and KIR2DS1^{K233R} was also visible inside the cytoplasm.

In summary, both mutated receptors were present at the surface of the transfected cell lines and as such could be used for GSDIM experiments.

4.3.2 Analysis of the importance of lysine 233 residue for nanometre-scale organization of KIR2DS1

To compare the nanometre-scale organization of KIR2DS1^{K233A} and KIR2DS1^{K233R} to this of the wild-type receptor, NKL/KIR2DS1-HA, NKL/KIR2DS1^{K233A} and NKL/KIR2DS1^{K233R} cells plated on the PLL-coated slides were fixed and stained with anti-HA mAb conjugated to AF 488. The cells were then imaged by GSDIM microscopy. The super-resolution images were reconstructed as before, and their visual inspection has readily suggested that substitution of lysine 233 with arginine had little, if any effect on the receptor nanoclustering. In contrast, when the same residue was substituted with alanine, changes in the clustering were apparent - KIR2DS1^{K233A} formed clusters visibly smaller than KIR2DS1^{WT} and its organization was generally more reminiscent of the wild-type KIR2DL1 than KIR2DS1 (Figure 4.2 a).

The same could be concluded from the Ripley's K function-based analysis. L(r) – r function plotted for KIR2DS1^{K233R} reached a maximum value of 128.85, which was relatively similar to KIR2DS1^{WT} (156.63). Function maxima for these receptors were also reached at similar radial scales (250 nm for KIR2DS1^{K233R} vs 230 nm for KIR2DS1^{WT}). For KIR2DS1^{K233A} however, L(r) – r function had a maximum of 38.64, at lower radial scale (180 nm; Figure 4.2 b). Together, this indicates that KIR2DS1^{K233A} is generally less clustered and forms smaller clusters than KIR2DS1^{K233R} and KIR2DS1^{WT}.

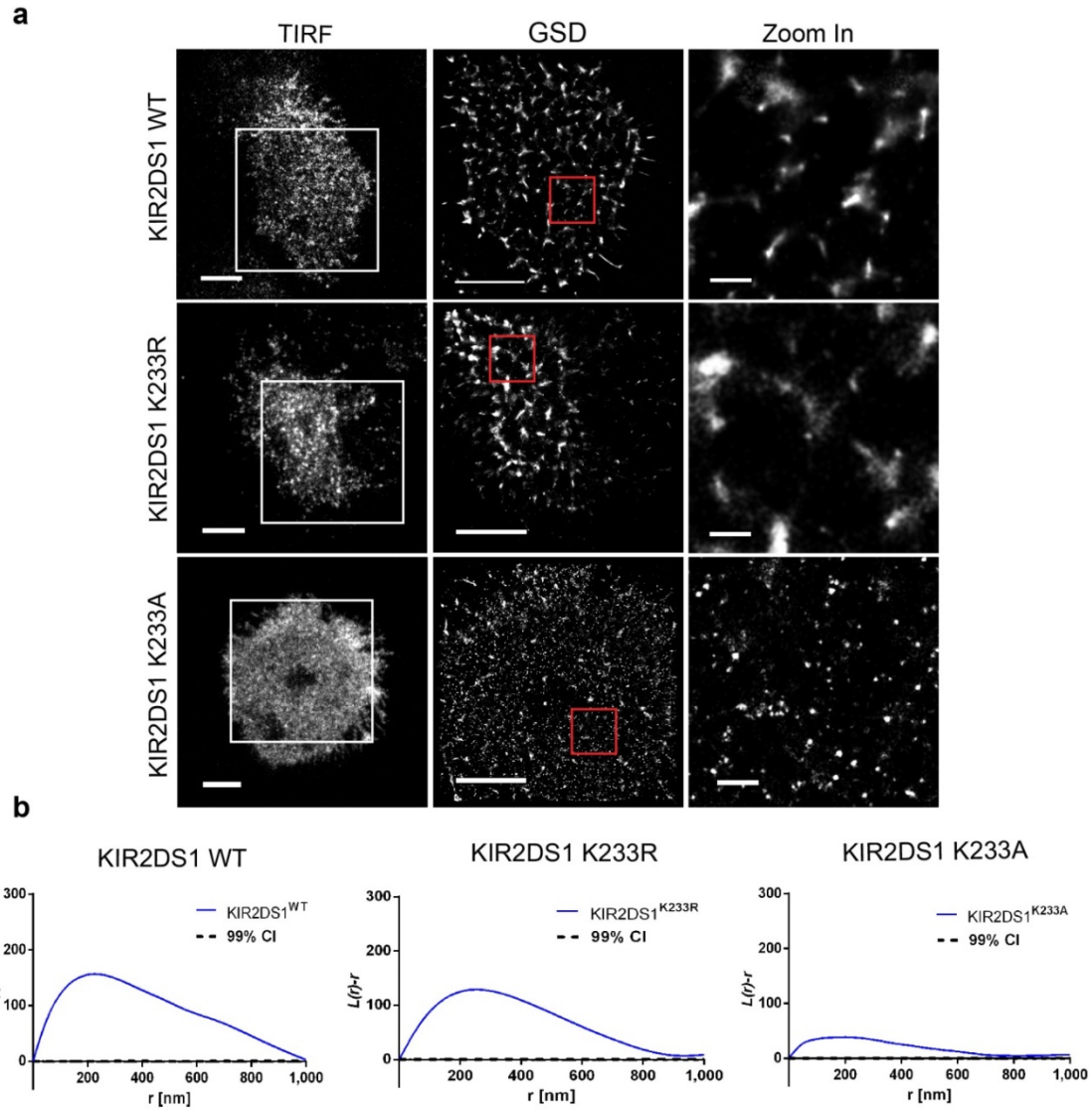

Figure 4.2 Organization of KIR2DS1^{WT}, KIR2DS1^{K233R} and KIR2DS1^{K233A} visualized by TIRF and GSDIM microscopy.
(a) Representative TIRF and GSD images of NKL/KIR2DS1-HA, NKL/KIR2DS1^{K233R} and NKL/KIR2DS1^{K233A} cells incubated on PLL-coated slides and stained with fluorescently labelled anti-HA mAb. Scale bars 5 µm. The 3 µm × 3 µm regions (red boxes in GSD images) are zoomed-in (scale bars 500 nm). (b) Ripley's *K* function of the events in the selected regions (red) shown in (a).

GSDIM data acquired for the three receptors were then subjected to Getis and Franklin local point pattern analysis. The resulting pseudo-colour scale heat-maps and binary maps of clustering confirmed that KIR2DS1^{K233A} displays a distinct nanometre-scale organization from KIR2DS1^{K233R} and KIR2DS1^{WT}, with less of its molecules localized within smaller-sized clusters, while KIR2DS1^{K233R} is organized in a similar manner to the wild-type receptor (Figure 4.3).

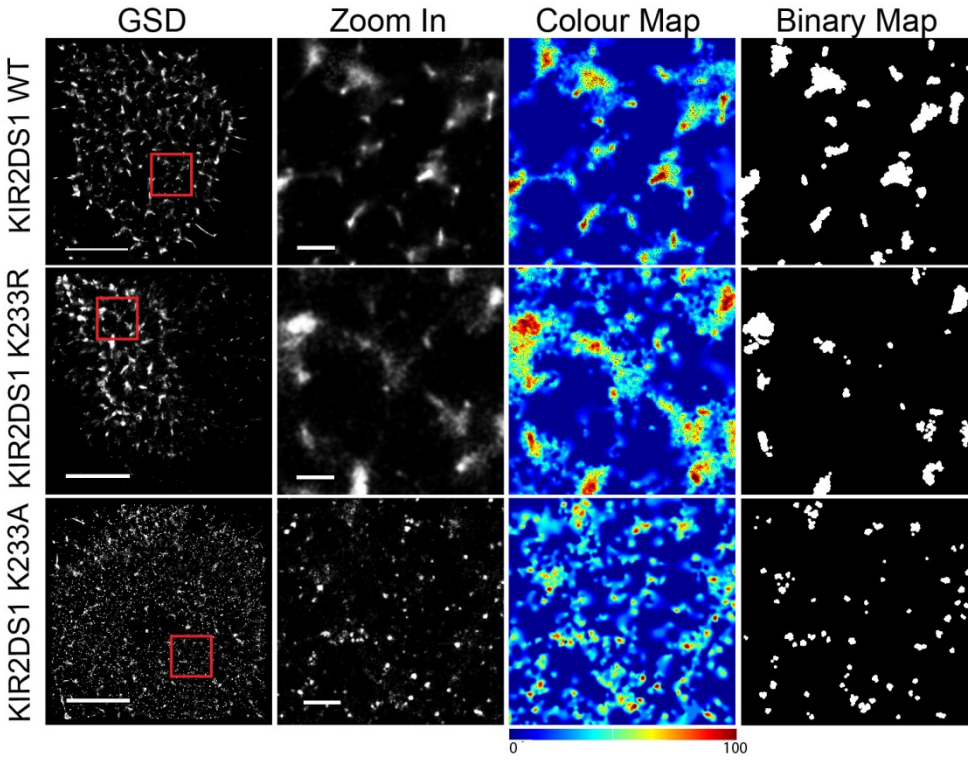

Figure 4.3 Pseudo-colour heat-maps and binary maps of clusters for KIR2DS1^{WT}, KIR2DS1^{K233R} and KIR2DS1^{K233A}.
GSDIM data acquired for NKL/KIR2DS1-HA, NKL/KIR2DS1^{K233R} and NKL/KIR2DS1^{K233A} cells were subjected to Getis and Franklin local point pattern analysis. The resulting colour-scale maps and binary maps of clusters are shown for selected 3 µm × 3 µm regions (red boxes in GSD images). Colours correspond to the L(30) values. To create binary maps, 50 nm disc objects were drawn around each molecule for which L(30) ≥ 65. Scale bars 5 µm in GSD images and 500 nm in zoomed-in regions.

The binary maps were then used to quantitatively compare the clustering of KIR2DS1^{WT}, KIR2DS1^{K233A} and KIR2DS1^{K233R} across all the cells imaged (Figure 4.4). This has shown that the area of KIR2DS1^{K233A} clusters (median 6,100 nm^2, IQR 4,500 – 8,600 nm^2, corresponding to median diameter of 88 nm) was significantly smaller than for the wild-type receptor (median area of 12,400 nm^2, IQR 9,800 – 18,000 nm^2). In contrast, the area and diameter of KIR2DS1^{K233R} clusters were not significantly different from the wild-type receptor (Figure 4.4 a – b). Comparison of the distribution of cluster sizes in individual cells showed that for KIR2DS1^{WT} and KIR2DS1^{K233R}, 41 ± 12% and 46 ± 9% of clusters, respectively, had area below 5,000 nm^2. These smallest clusters were more frequently observed for KIR2DS1^{K233A}, constituting 65 ± 11% of all clusters of this receptor. Conversely, the biggest clusters of area above 15,000 nm^2 were more abundant for KIR2DS1^{WT} and KIR2DS1^{K233R} (29 ± 13% and 22 ± 8%, respectively) than for KIR2DS1^{K233A} (8 ± 6%; Figure 4.4 c).

In terms of number of receptor clusters detected per µm^2, it is worth noticing that within the cells expressing KIR2DS1^{K233A} two different phenotypes could be observed.

In 7 out of 35 NKL/ KIR2DS1^{K233A} cells imaged, less than 2 clusters per μm^2 were detected. However, for the remaining 28 out of 35 NKL/ KIR2DS1^{K322A} cells, the number of clusters detected per μm^2 was higher than the median cluster density in KIR2DS1^{WT}. This means that KIR2DS1^{K233A} can either be generally more dispersed in the membrane and rarely form clusters at all, or form more clusters that are significantly smaller than clusters of the wild-type KIR2DS1. Overall, the median cluster density for KIR2DS1^{K223A} was 5.1 clusters/μm^2 (IQR 3.8 – 5.9 clusters/μm^2), and was significantly higher than for KIR2DS1^{WT} (Figure 4.4 d). In addition, clusters of KIR2DS1^{K233A} were more circular and less densely packed than clusters of KIR2DS1^{WT}. These parameters were indistinguishable between the KIR2DS1^{WT} and KIR2DS1^{K233R} (Figure 4.4 e –f). Moreover, fraction of the receptors found within clusters was significantly lower for KIR2DS1^{K233A}, but not for KIR2DS1^{K233R}, as compared to KIR2DS1^{WT} (Figure 4.4 g). Notably, in 7 out of 35 NKL/ KIR2DS1^{K233A} cells less than 2% of molecules was found in clusters, while for wild-type KIR2DS1 the lowest percentage of molecules in clusters that was ever observed was 12.5% and for KIR2DS1^{K233R} 23%.

Bulk analysis by flow cytometry demonstrated that mutated forms of KIR2DS1 had different expression levels from the wild-type receptor. In GSD experiments, however, where fewer cells are imaged, the density of detected molecules had relatively similar range and was not statistically different between all analysed receptors (Figure 4.4 h).
The relative variation of different parameters amongst individual cells expressing KIR2DS1^{WT}, KIR2DS1^{K233A} or KIR2DS1^{K233R} was assessed by plotting the average cluster size against the number of clusters detected in each individual cell (Figure 4.4 i). This showed that for KIR2DS1^{K233A} the density of clusters at the cell surface varied more from cell to cell than average cluster area, similar to what was seen earlier for KIR2DL1. This was different from KIR2DS1^{WT} and KIR2DS1^{K233R}, for which the cell populations mostly overlapped in the graph. For these receptors, size of clusters changed more between cells than density of clusters. Together with the above results, this demonstrates that patterns of clustering generally differ more between the KIR2DS1^{K233A} and KIR2DS1^{WT} than between KIR2DS1^{K233R} and the wild-type receptor.

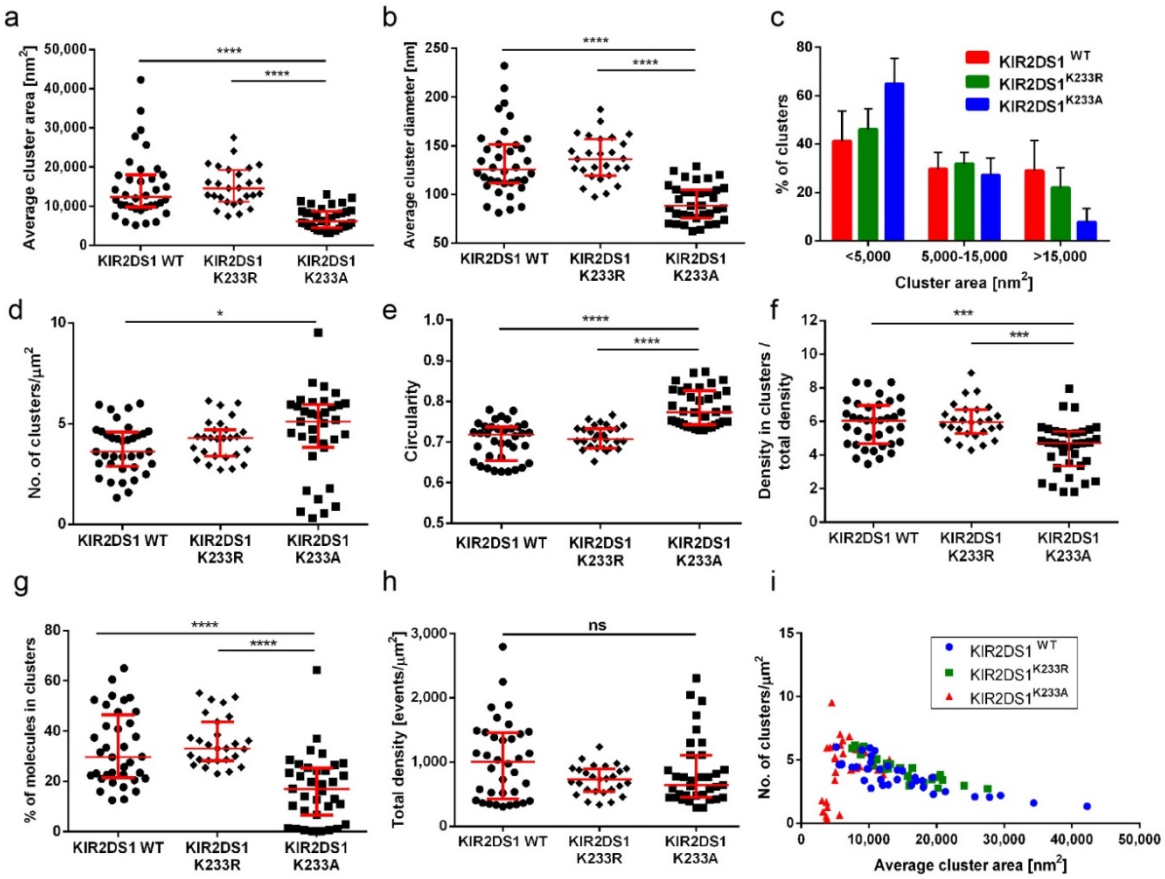

Figure 4.4 Quantitative analysis of KIR2DS1^{WT}, KIR2DS1^{K233R} and KIR2DS1^{K233A} clustering.
Average cluster area (a) and diameter (b), size distribution of clusters (c), number of clusters per µm^2 (d), average cluster circularity (e), ratio of density of events in clusters to overall membrane density (f), fraction of molecules localized within clusters (g) and overall density of detected events (h). (i) Number of clusters per µm^2 plotted against average cluster area measured in individual cells. (a - b and d - i) Each symbol represents the mean from several regions within one cell. Horizontal bars and errors represent the medians and interquartile range. (c) Bars and errors represent means and SD. Data are from 36 cells from five experiments (KIR2DS1^{WT}), 27 cells from three experiments (KIR2DS1^{K233R}) and 35 cells from four experiments (KIR2DS1^{K233A}). ns non-significant, * $p < 0.05$, *** $p < 0.001$, **** $p < 0.0001$, Kruskal-Wallis test with Dunn's post-test.

To further ensure that the observed patterns of clustering are not related to different expression levels of wild-type and mutated receptors, the pseudo-colour maps of clustering were directly compared between cells expressing KIR2DS1^{WT}, KIR2DS1^{K233R} or KIR2DS1^{K233A} at comparable lower or higher levels (within the bell-shaped distribution of the molecular densities). This demonstrated that at both low and high molecular densities, KIR2DS1^{K233A} formed smaller clusters than KIR2DS1^{WT} and KIR2DS1^{K233R} (Figure 4.5 a). In fact, this was true across the range of molecular densities detected, as further illustrated in the Figure 4.5 b, where average cluster sizes for the three receptors were plotted against the molecular densities in all individual cells analysed.

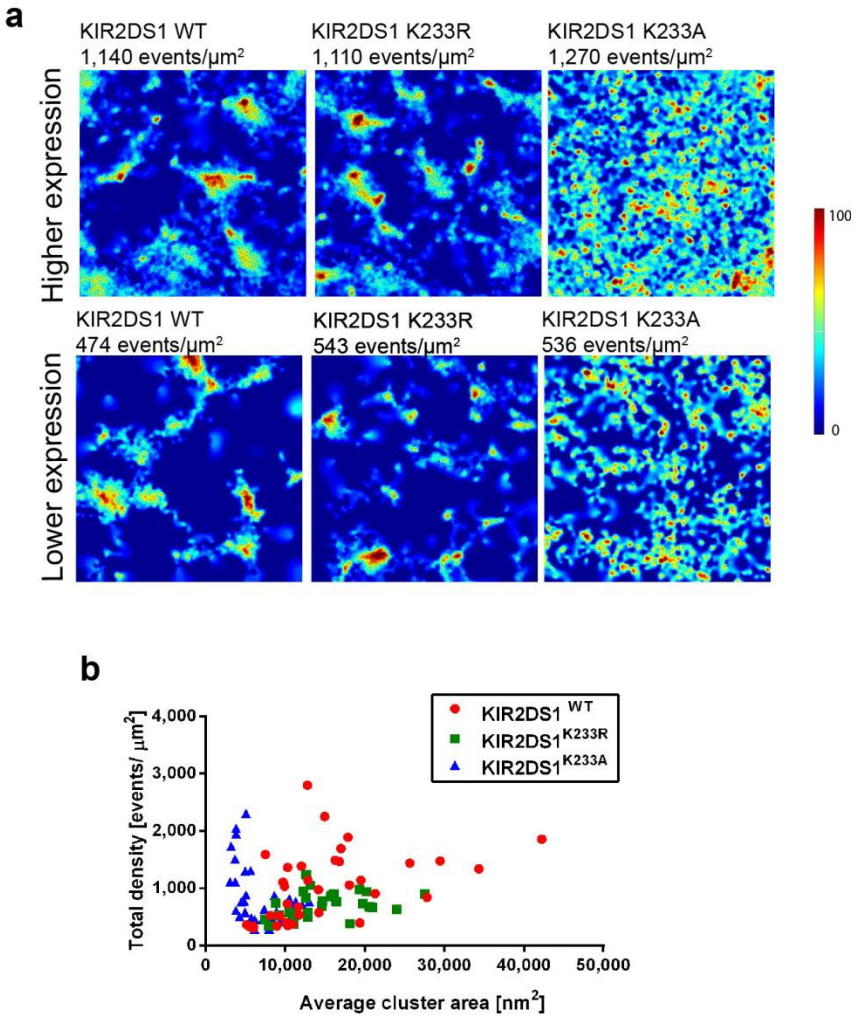

Figure 4.5 Differences in KIR2DS1^{WT}, KIR2DS1^{K233R} and KIR2DS1^{K233A} clustering are not due to differential expression levels.
NKL/KIR2DS1-HA, NKL/KIR2DS1^{K233R} and NKL/KIR2DS1^{K233A} cells were stained with anti-HA mAb conjugated with AF 488 and imaged by GSD microscopy. (a) Selected 3 µm × 3 µm regions are shown as colour maps where colours correspond to the extent of clustering according to pseudo-colour scale. Regions from cells with relatively high (upper row) and low (lower row) densities of detected events are shown. (b) Total density of events plotted against average cluster area measured in individual cells. Each symbol represents the mean from several regions within one cell. Data are from 36 cells from five experiments (KIR2DS1^{WT}), 27 cells from three experiments (KIR2DS1^{K233R}) and 35 cells from four experiments (KIR2DS1^{K233A}).

4.3.3 Expression of mutated forms of KIR2DL1 in NKL cell line

The changes in the KIR2DS1 clustering triggered by the lysine to alanine substitution at position 233 provoked the question whether the reciprocal effect would be achieved upon introduction of lysine to the same position in the KIR2DL1 sequence. The position 233 in the KIR2DL1 sequence (9th position in the transmembrane region) is occupied by isoleucine residue. The amino-acid context of the 233 residue is to some extent similar in KIR2DS1 and KIR2DL1. In both receptors, positions 230 – 232 are occupied

by serine, valine and valine residues, and position 234 is also occupied by the same amino acid, isoleucine.

To verify the importance of the residue 233 for the KIR clustering, the isoleucine 233 in KIR2DL1 sequence was substituted with lysine residue by site-directed mutagenesis. Mutated receptor, KIR2DL1^{I233K}, was stably expressed in the NKL cell line by retroviral transduction. In parallel, to analyse the importance of tonic signalling for the organization of KIR2DL1, another mutant receptor was created, in which the two tyrosine residues within the cytoplasmic ITIM motifs were mutated to alanine residues (KIR2DL1$^{Y281A/Y311A}$), and transfected into NKL cells. Both mutated receptors were fused to HA tag at a C-terminus. For easier comparison, in the figures comparing different variants of KIR2DL1, the wild type KIR2DL1-HA is referred to as KIR2DL1^{WT}.

To check the abundance of mutated KIR2DL1 receptors at the surface of transduced cells, parental NKL, NKL/KIR2DL1-HA, NKL/KIR2DL1^{I233K} and NKL/ KIR2DL1$^{Y281A/Y311A}$ cells were surface-stained with EB6 mAb conjugated to Atto 488 and analysed by flow cytometry (Figure 4.6 a). This has shown that both KIR2DL1^{I233K} and KIR2DL1$^{Y281A/Y311A}$ were abundantly expressed at the cell surface. The change of residue at position 233 affected the expression levels of KIR2DL1. Specifically, KIR2DL1^{I233K} was expressed at lower levels as compared to KIR2DL1^{WT}. In contrast, substitutions of the two signalling tyrosines had no effect on the receptor expression - KIR2DL1$^{Y281A/Y311A}$ was expressed at the same levels as the wild-type receptor. Nevertheless, the expression levels for the three receptors overlapped to some extent, enabling direct comparison of the wild-type and mutated KIR2DL1 organization in cells expressing the receptors at similar densities.

To assess the cellular localization of the KIR2DL1 mutants, NKL/KIR2DL1^{I233K} and NKL/KIR2DL1$^{Y281A/Y311A}$ cells were plated on PLL-coated slides, fixed, permeabilized and stained with an anti-HA mAb conjugated to AF 488. Confocal microscopy demonstrated that both KIR2DL1^{I233K} and KIR2DL1$^{Y281A/Y311A}$ were present in the cell membrane both at the contact plane with glass slide and in the higher planes (Figure 4.6 b). Some of the protein was also detected inside the cell.

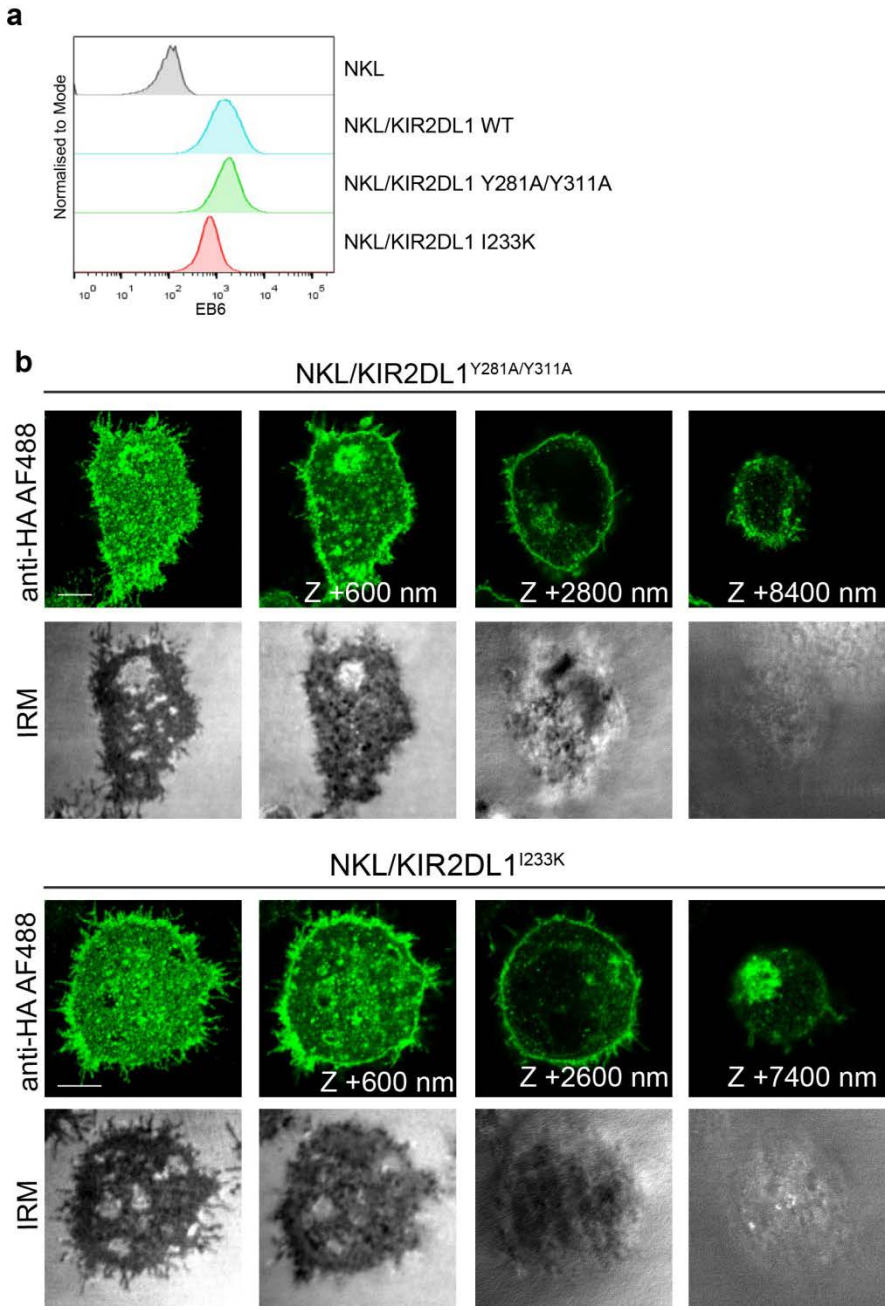

Figure 4.6 Expression of KIR2DL1 mutants in NKL cells.
(a) Parental NKL, NKL/KIR2DL1-HA, NKL/KIR2DL1$^{Y281A/Y311A}$ and NKL/KIR2DL1^{I233K} cells were stained with anti-KIR2DL/S1 mAb (clone EB6) conjugated to Atto 488 and analysed by flow cytometry. (b) NKL/KIR2DL1$^{Y281A/Y311A}$ and NKL/KIR2DL1^{I233K} cells were plated on PLL-coated glass slides, fixed, permeabilized, stained with anti-HA mAb and imaged by confocal microscopy. Localization of the proteins in the respective transfectants was assessed by visualization of KIR-derived fluorescence (upper rows) in different planes of the confocal Z stacks, for which a relative position in the Z plane was checked by imaging in IRM mode (lower rows). The most left images correspond to the membrane proximal to the glass slide and the relative position of other images is indicated in the bottom of the micrographs. Scale bars 5 µm.

4.3.4 Analysis of the effect of point mutations on the organization of KIR2DL1 at the surface of NKL cells.

To directly compare the nanometre-scale organization of KIR2DL1^{WT}, KIR2DL1^{I233K} and KIR2DL1$^{Y281A/Y311A}$, NKL cells expressing each of the receptors were fixed on PLL-coated slides, stained with anti-HA mAb conjugated to AF 488 and imaged by GSDIM. Visual inspection of the reconstructed super-resolution images has readily shown that isoleucine to lysine substitution at position 233 of KIR2DL1 indeed had an inverse effect to the lysine to alanine substitution at the same position of KIR2DS1. Clusters of KIR2DL1^{I233K} were visibly bigger than those of wild-type KIR2DL1. In contrast, no apparent differences in clustering of KIR2DL1^{WT} and KIR2DL1$^{Y281A/Y311A}$ could be observed in the GSDIM images (Figure 4.7 a). This was further confirmed by Ripley's K function-based analysis – L(r) – r plots for KIR2DL1^{WT} and KIR2DL1$^{Y281A/Y311A}$ reached similar maximum values (41.9 and 53.8, respectively) at similar radial scale (80 nm and 90 nm, respectively). In contrast, L(r) – r plot for KIR2DL1^{I233K} displayed a higher maximum value (139.8), suggesting that this molecule had a more clustered organization. In addition, the larger radial scale at which the function peaked (160 nm) indicated that substitution of isoleucine 233 with lysine leads to increase in the size of KIR2DL1 clusters (Figure 4.7 b).

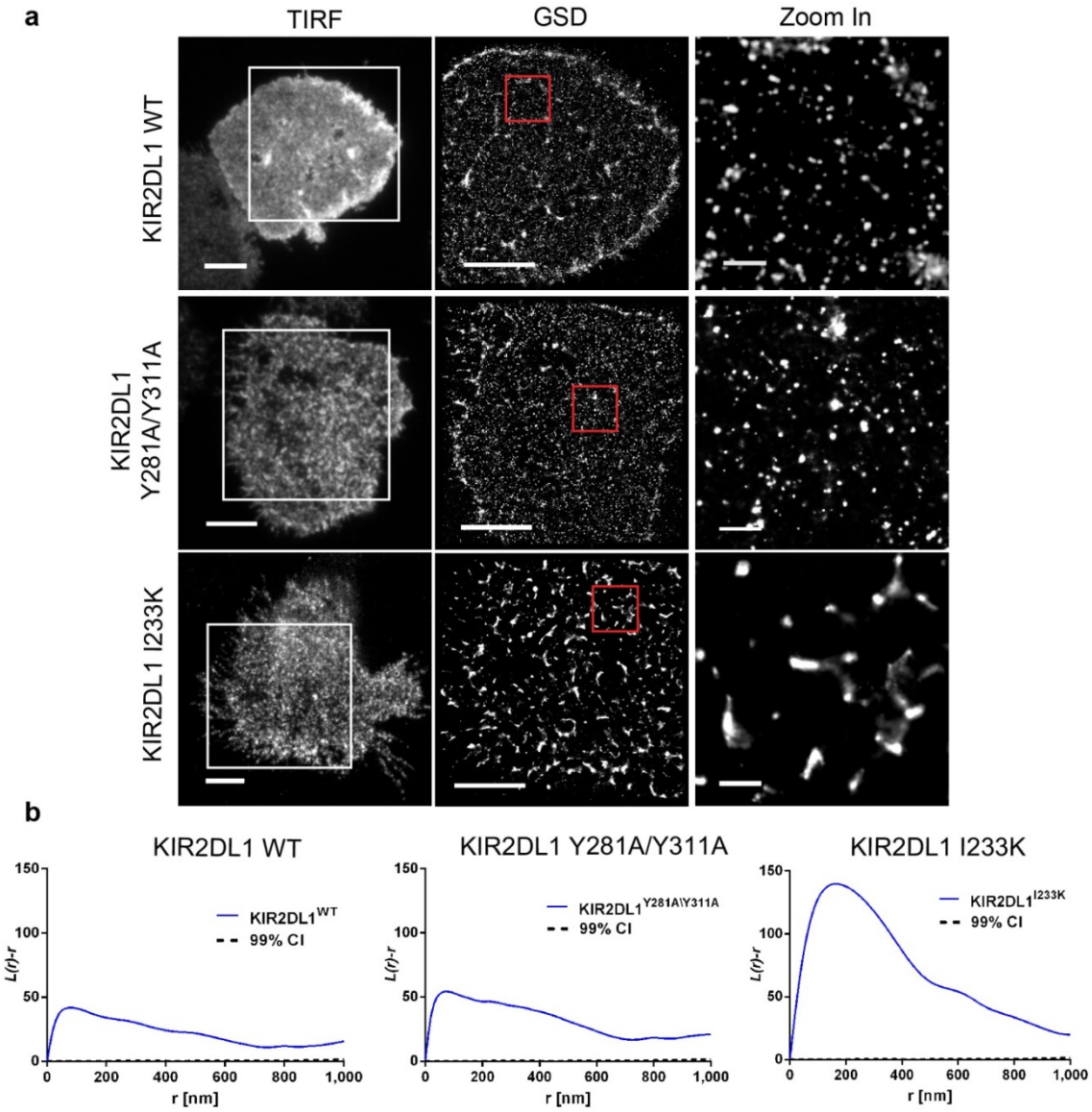

Figure 4.7 Organization of KIR2DL1^{WT}, KIR2DL1$^{Y281A/Y311A}$ and KIR2DL1^{I233K} visualized by TIRF and GSDIM microscopy.
(a) Representative TIRF and GSD images of NKL/KIR2DL1-HA, NKL/KIR2DL1$^{Y281A/Y311A}$ and NKL/KIR2DL1^{I233K} cells incubated on PLL-coated slides and stained with fluorescently labelled anti-HA mAb. Scale bars 5 µm. The 3 µm × 3 µm regions (red boxes in GSD images) are zoomed-in (scale bars 500 nm). (b) Ripley's *K* function of the events in the selected regions (red) shown in (a).

For more detailed comparison of clustering, GSDIM data acquired for KIR2DL1^{WT}, KIR2DL1^{I233K} and KIR2DL1$^{Y281A/Y311A}$ were subjected to Getis and Franklin analysis (Figure 4.8). The resulting pseudo-colour heat-maps of clustering and binary maps of clusters clearly demonstrated that KIR2DL1$^{Y281A/Y311A}$ formed clusters of similar size to the wild-type receptor, while clusters of KIR2DL1^{I233K} were much bigger, as compared to the latter receptors.

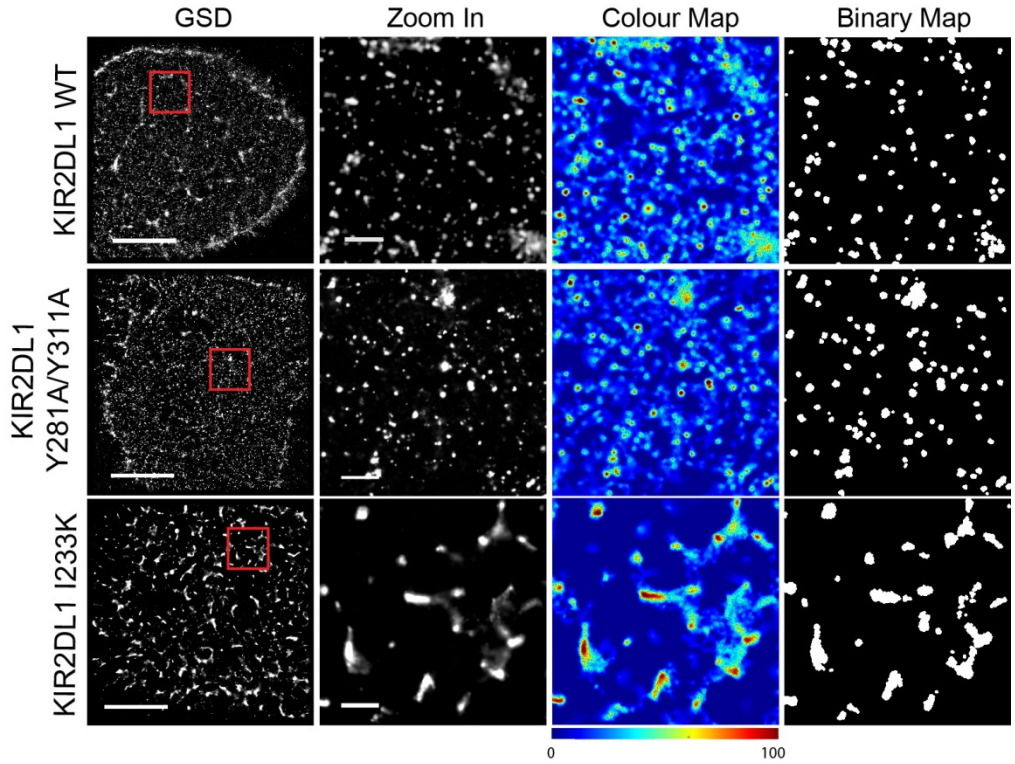

Figure 4.8 Pseudo-colour heat-maps and binary maps of clusters for KIR2DL1^{WT}, KIR2DL1$^{Y281A/Y311A}$ and KIR2DL1^{I233K}.
GSDIM data acquired for NKL/KIR2DL1-HA, NKL/KIR2DL1$^{Y281A/Y311A}$ and NKL/KIR2DL1^{I233K} cells were subjected to Getis and Franklin local point pattern analysis. The resulting colour-scale maps and binary maps of clusters are shown for selected 3 µm × 3 µm regions (red boxes in GSD images). Colours correspond to the L(30) values. To create binary maps, 50 nm disc objects were drawn around each molecule for which L(30) ≥ 65. Scale bars 5 µm in GSD images and 500 nm in zoomed-in regions.

Cluster parameters were then quantified and directly compared for all the cells imaged (Figure 4.9). This demonstrated that KIR2DL1^{I233K} formed larger clusters than wild-type receptor at the surface of NKL cells. Clusters of KIR2DL1^{I233K} had median area of 16,000 nm^2 (which corresponds to median diameter of 143 nm) and IQR of 11,900 – 18,800 nm^2, while for KIR2DL1 imaged in these experiments the median area was 7,800 nm^2 (corresponding to diameter of 100 nm) and IQR was 6,600 – 8,700 nm^2. In contrast, changing of the tyrosine residues within ITIMs to alanines had no effect on the size of KIR2DL1 clusters (Figure 4.9 a-b).

Analysis of cluster size heterogeneity in individual cells has shown that for KIR2DL1^{I233K}, clusters of area below 5,000 nm^2 were on average1.45 –fold less frequent than for the wild type receptor, while the fraction of clusters with area above 15,000 nm^2 increased from 9 ± 4% for wild-type to 25 ± 9% for KIR2DL1^{I233K}. The result of this analysis for KIR2DL1$^{Y281A/Y311A}$ was very similar to the wild-type KIR2DL1 (Figure 4.9 c).

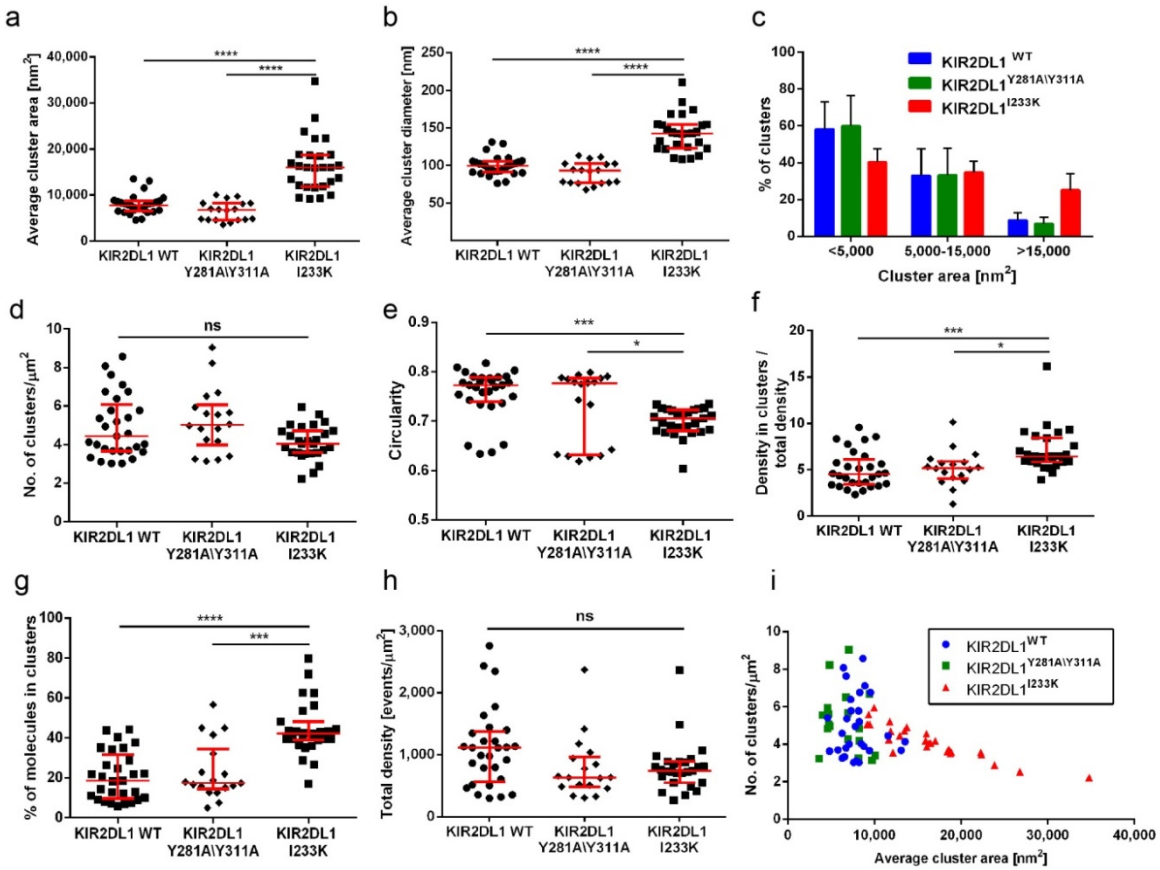

Figure 4.9 Quantitative analysis of KIR2DL1^{WT}, KIR2DL1$^{Y281A/Y311A}$ and KIR2DL1^{I233K} clustering.

Average cluster area (a) and diameter (b), size distribution of clusters (c), number of clusters per µm^2 (d), average cluster circularity (e), ratio of density of events in clusters to overall membrane density (f), fraction of molecules localized within clusters (g) and overall density of detected events (h). (i) Number of clusters per µm^2 plotted against average cluster area measured in individual cells. (a - b and d - i) Each symbol represents the mean from several regions within one cell. Horizontal bars and errors represent the medians and interquartile range. (c) Bars and errors represent means and SD. Data are from 29 cells from five experiments (KIR2DL1^{WT}), 27 cells from four experiments (KIR2DL1^{I233K}) and 18 cells from three experiments (KIR2DL1$^{Y281A/Y311A}$). ns non-significant, * $p < 0.05$, *** $p < 0.001$, **** $p < 0.0001$, Kruskal-Wallis test with Dunn's post-test.

The number of clusters formed by wild type and mutated variants of KIR2DL1 was not significantly different between the receptors (Figure 4.8 d). However, KIR2DL1^{I233K} displayed a reduced circularity, increased ratio between density of molecules in clusters and total density and higher fraction of molecules found within clusters, as compared to wild-type KIR2DL1. None of these parameters differed significantly between wild-type KIR2DL1 and KIR2DL1$^{Y281A/Y311A}$ (Figure 4.9 e-g). As for KIR2DS1 mutants, the analysis included cells for which total density of respective receptors detected was within comparable range and was not statistically different, in order to

ensure that observed differences do not result from differential expression (Figure 4.9 h).

Finally, cross-correlation of average cluster sizes and numbers of clusters detected in the individual cells showed that while for wild-type KIR2DL1 and KIR2DL1$^{Y281A/Y311A}$ size of clusters is relatively more constant parameter from cell to cell, for KIR2DL1^{I233K} size of clusters appears to vary more between individual cells than density of clusters (Figure 4.9 i).

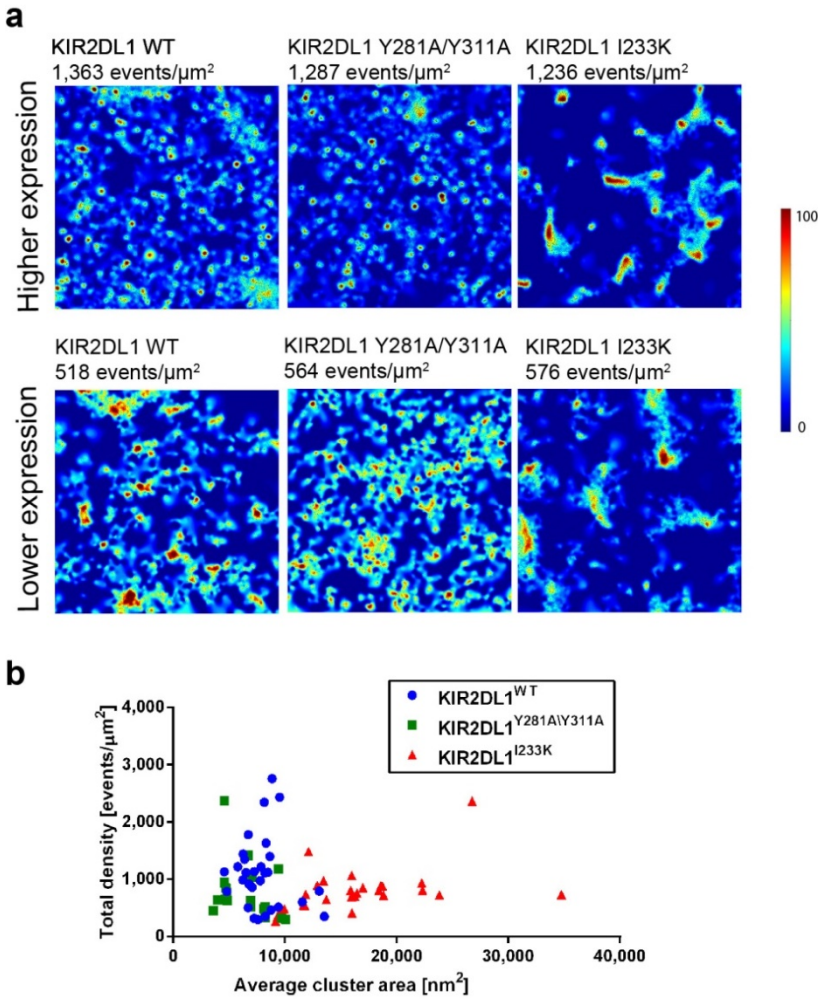

Figure 4.10 Differences in KIR2DL1^{WT}, KIR2DL1$^{Y281A/Y311A}$ and KIR2DL1^{I233K} clustering are not due to differential expression levels.
NKL/KIR2DL1-HA, NKL/KIR2DL1$^{Y281A/Y311A}$ and NKL/ KIR2DL1^{I233K} cells were stained with anti-HA mAb conjugated with AF 488 and imaged by GSD microscopy. (a) Selected 3 µm × 3 µm regions are shown as colour maps where colours correspond to the extent of clustering according to pseudo-colour scale. Regions from cells with relatively high (upper row) and low (lower row) densities of detected events are shown. (b) Total density of events plotted against average cluster area measured in individual cells. Each symbol represents the mean from several regions within one cell. Data are from 29 cells from five experiments (KIR2DL1^{WT}), 27 cells from four experiments (KIR2DL1^{I233K}) and 18 cells from three experiments (KIR2DL1$^{Y281A/Y311A}$).

In conclusion, super-resolution imaging of the wild-type KIR2DL1 and its mutated forms established that I233K substitution in the transmembrane region results in the receptor assembly into larger clusters. In contrast, tonic signalling of KIR2DL1 seems to not affect its clustering, as evidenced by the KIR2DL1$^{Y281A/Y311A}$ organization being indistinguishable for this of the wild-type KIR2DL1.

In summary, the above experiments demonstrate that presence of a positively charged residue such as lysine or arginine in transmembrane region of KIR2DL/S1 receptors promotes formation of bigger and denser clusters accommodating higher percentage of the molecules, while its absence leads to localization of lower fraction of molecules within smaller-sized clusters.

4.3.5 Expression of KIR2DL1 and KIR2DS1 in Jurkat cells

Observation of different patterns of organization for the mutated and wild-type variants of KIR2DL1 and KIR2DS1 suggested that nanoclustering of these proteins is largely controlled by their amino-acid sequence. I then set out to establish whether the differences in KIR organization are preserved in the membrane of non-NK cells. To verify this, human leukemic T cell line Jurkat was stably transfected to express KIR2DL1-HA or KIR2DS1-HA fusion proteins. Importantly, Jurkat cells are DAP-12 deficient [193], which allowed simultaneous testing whether interaction with this adaptor molecule is important for KIR2DS1 organization. To further explore if lysine at position 233 can enhance KIR clustering independent from DAP12, KIR2DL1^{I233K} mutant receptor was also expressed in Jurkat cells. All receptors were fused to the HA tag at the C-terminus.

To check whether the receptors are present at the surface of transduced cells, parental Jurkat, Jurkat/KIR2DL1-HA, Jurkat/KIR2DL1^{I233K} and Jurkat/KIR2DS1-HA cells were surface-stained with EB6 mAb conjugated to PE and analysed by flow cytometry (Figure 4.11 a). This has shown that all the receptors were expressed at the surface of Jurkat cells. KIR2DL1^{I233K} was expressed at lower level than the wild-type KIR2DL1, and KIR2DS1 was less abundant at the surface of Jurkat cells than both forms of KIR2DL1. This suggests that in the absence of DAP12, incorporation of KIR2DS1 into the cell membrane and/or its surface stability is reduced, consistent with previously published reports [342]. Nevertheless, the levels of surface expression of the three receptors overlapped to some extent, indicating that their organization could be reliably compared using the transfected cell lines.

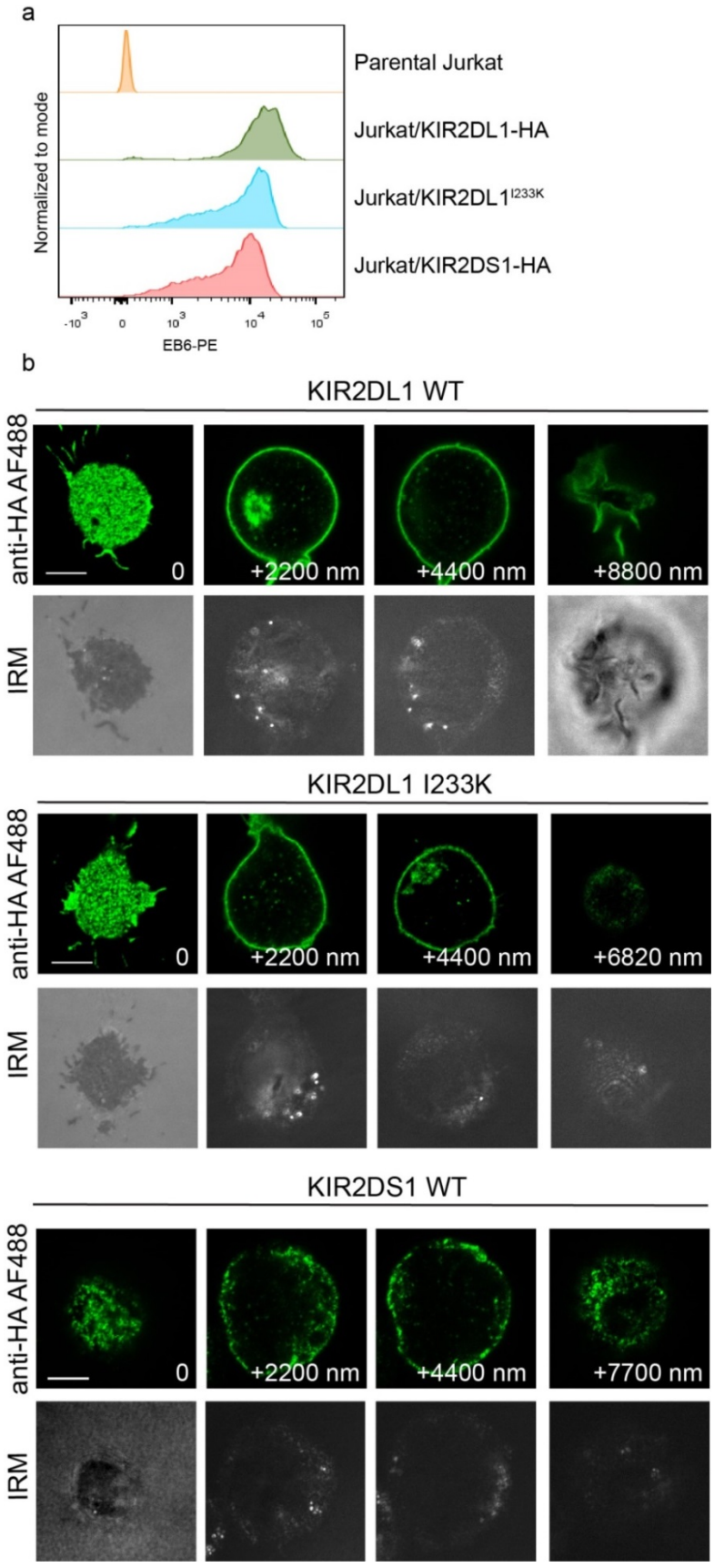

Figure 4.11 Expression of KIR2DL1-HA, KIR2DL1^{I233K} and KIR2DS1-HA mutants in Jurkat cells.

(a) Parental Jurkat, Jurkat/KIR2DL1-HA, Jurkat/ KIR2DL1^{I233K} and Jurkat/KIR2DS1-HA cells were stained with anti-KIR2DL/S1 mAb (clone EB6) conjugated to PE and analysed by flow cytometry. (b) Jurkat/KIR2DL1-HA, Jurkat/ KIR2DL1^{I233K} and Jurkat/KIR2DS1-HA cells were plated on PLL-coated glass slides, fixed, permeabilized, stained with anti-HA mAb and imaged by confocal microscopy. Localization of the proteins in the respective transfectants was assessed by visualization of KIR-derived fluorescence (upper rows) in different planes of the confocal Z stacks, for which a relative position in the Z plane was checked by imaging in IRM mode (lower rows). The most left images correspond to the membrane proximal to the glass slide and the relative position of other images is indicated in the bottom of the micrographs. Scale bars 5 μm.

The cellular localization of transfected receptors in Jurkat cells was then visualized by confocal microscopy. As before, cells were plated on the PLL-coated slides, fixed, permeabilized and stained with anti-HA mAb conjugated to AF 488. For all receptors, bright fluorescent signal could be observed in the plane of the membrane contact with glass slide and was also present in the plasma membrane within the higher Z planes (Figure 4.11 b). Similar to receptors expressed in NKL cells, a fraction of KIR2DL1-HA, KIR2DS1-HA and KIR2DL1^{I233K} was also visible within cytoplasmic vesicular structures. Overall, KIR2DL1-HA, KIR2DS1-HA and KIR2DL1^{I233K} were all present in the membrane of transfected Jurkat cells and as such these cells could be used for GSDIM experiments.

4.3.6 Analysis of KIR2DL1 and KIR2DS1 organization in Jurkat cells

To investigate if organization of KIR2DL1 and KIR2DS1 in DAP-12-deficient T cell line Jurkat matches the observations made in NKL and primary NK cells, Jurkat/KIR2DL1-HA, Jurkat/KIR2DL1^{I233K} and Jurkat/KIR2DS1-HA cells were plated on PLL-coated slides, fixed, stained with anti-HA mAb and imaged by GSDIM. The resulting super-resolution images readily suggested that, similar to what was seen in NK cells, KIR2DL1 and KIR2DS1 and KIR2DL1^{I233K} formed nanometre-scale clusters in the membrane of Jurkat T cells. Moreover, the clustering patterns they displayed closely resembled those observed in NK cells with wild type KIR2DL1 and KIR2DS1 being organized differently. Organization of KIR2DL1^{I233K} was again more reminiscent of the wild-type KIR2DS1 than KIR2DL1 (Figure 4.12 a).

The results of Ripley's K-function-based analysis were again in line with what was apparent in the reconstructed images. It indicated that in Jurkat cells KIR2DS1 is generally more clustered and forms larger clusters (L(r) – r maximum of 107.5 at r = 300 nm), as compared to wild-type KIR2DL1 (L(r) – r maximum of 29.1 at r = 160 nm). For KIR2DL1^{I233K} the function reached a peak value of 182.3 at a radius of 250 nm,

suggesting that the mutant receptor was also more clustered and formed larger clusters than wild-type KIR2LD1 (Figure 4.12 b).

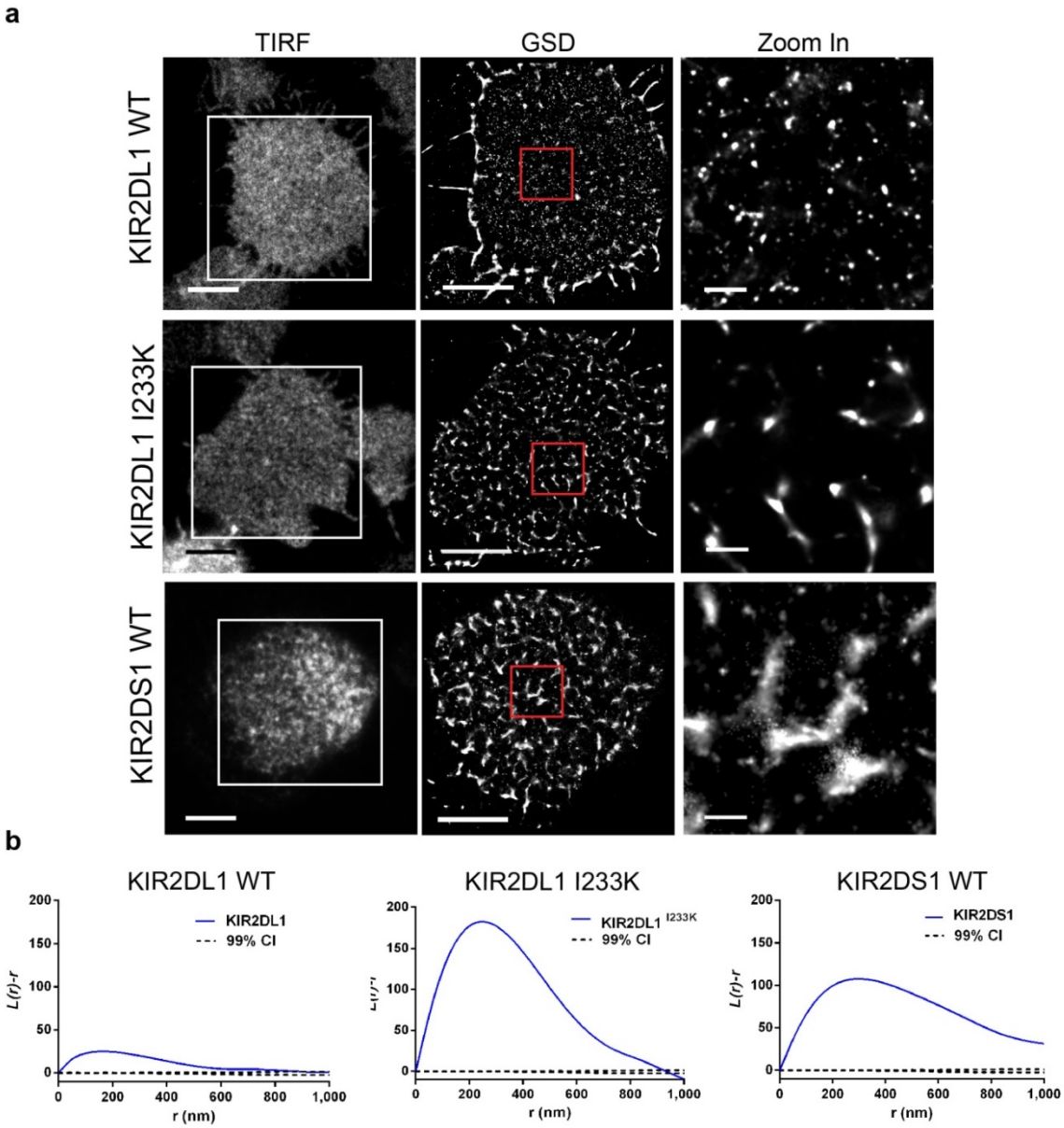

Figure 4.12 Organization of KIR2DL1-HA, KIR2DL1^{I233K} and KIR2DS1-HA visualized by TIRF and GSDIM microscopy.
(a) Representative TIRF and GSD images of Jurkat/KIR2DL1-HA, Jurkat/KIR2DL1^{I233K} and Jurkat/KIR2DS1-HA cells incubated on PLL-coated slides and stained with fluorescently labelled anti-HA mAb. Scale bars 5 µm. The 3 µm × 3 µm regions (red boxes in GSD images) are zoomed-in (scale bars 500 nm). (b) Ripley's *K* function of the events in the selected regions (red) shown in (a).

The data were then subjected to Getis and Franklin analysis. Comparison of the resulting colour-scale and binary maps of clusters, presented in the Figure 4.13, has

further confirmed that both wild-type KIR2DS1 and KIR2DL1^{I233K} assembled in larger-scale nanoclusters compared to KIR2DL1^{WT}.

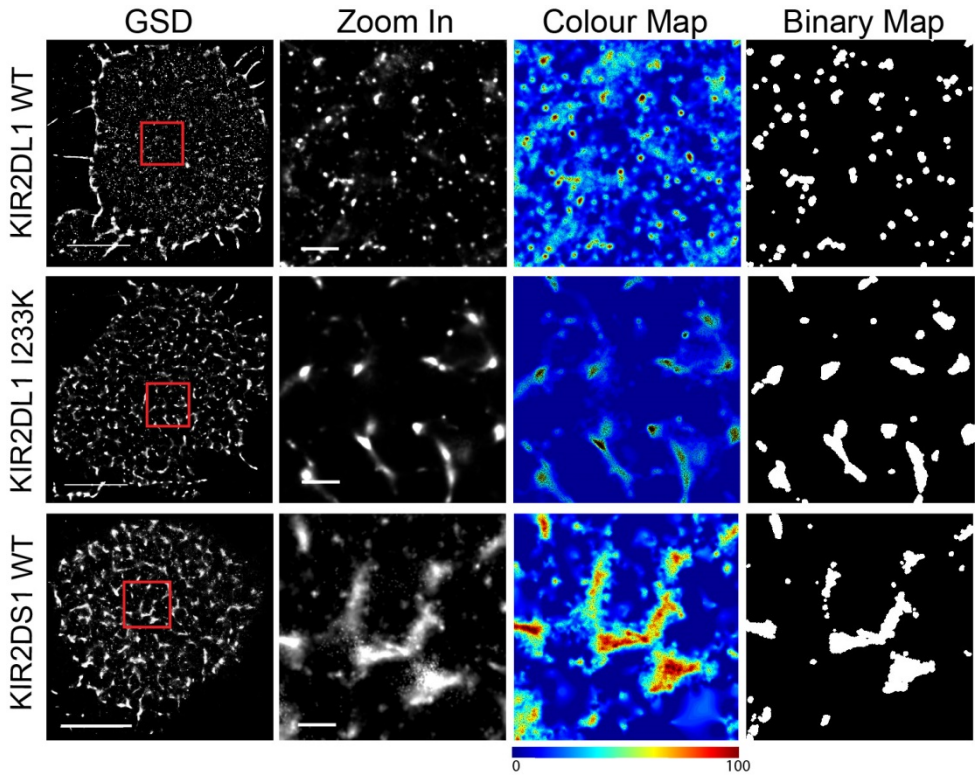

Figure 4.13 Pseudo-colour heat-maps and binary maps of clusters for KIR2DL1^{WT}, KIR2DL1^{I233K} and KIR2DS1^{WT} at the surface of Jurkat cells.
GSDIM data acquired for Jurkat/KIR2DL1-HA, Jurkat/KIR2DL1^{I233K} and Jurkat/KIR2DS1-HA cells were subjected to Getis and Franklin local point pattern analysis. The resulting colour-scale maps and binary maps of clusters are shown for selected 3 µm × 3 µm regions (red boxes in GSD images). Colours correspond to the L(30) values. To create binary maps, 50 nm disc objects were drawn around each molecule for which L(30) ≥ 65. Scale bars 5 µm in GSD images and 500 nm in zoomed-in regions.

The binary maps were then used to quantify the clustering of individual receptors expressed in Jurkat cells. This has shown that cluster area for KIR2DS1 in Jurkat (median 23,000 nm^2 with IQR 17,800 – 34,600 nm^2; corresponding to median diameter of 171 nm) was significantly larger than for KIR2DL1 (median area of 9,100 nm^2 with IQR 7,300 – 11,000 nm^2, corresponding to median diameter of 108 nm). For KIR2DL1^{I233K}, the area of nanoclusters was significantly larger than for KIR2DL1^{WT} and not significantly different from KIR2DS1 (Figure 4.14 a – b). Like in NKL cells, there was some variation in the size of clusters found within one cell. The distribution of cluster sizes differed between the tested receptors. For wild type KIR2DL1 approximately half (48.5 ± 13%) of the clusters detected had area below 5,000 nm^2, while for KIR2DS1 and KIR2DL1^{I233K} clusters of area above 15,000 nm^2 were more abundant than these below 5,000 nm^2 (Figure 4.14 c). Moreover, both KIR2DS1 and

KIR2DL1^{I233K} formed significantly less clusters at the surface of Jurkat cells, as compared to wild-type KIR2DL1 (Figure 4.14 d). Circularity of clusters was also different between the receptors, with clusters of KIR2DL1^{WT} displaying the highest circularity (Figure 4.14 e).

In addition, clusters of both KIR2DS1 and KIR2DL1^{I233K} were denser (as compared to total molecular density across the whole membrane imaged) than KIR2DL1 (median values 5.3 and 4.9-fold vs 3.9-fold; Figure 4.14 f), although the difference reached statistical significance only between the wild-type KIR2DL1 and KIR2DS1. Similarly, for both KIR2DS1 and KIR2DL1^{I233K} the fraction of molecules localized in the clusters was increased as compared to KIR2DL1^{WT}, but only the difference between wild type receptors was statistically significant (Figure 4.14 g). Importantly, although the three receptors were expressed at the surface of Jurkat cells as different levels, as detected by flow cytometry, the above analysis was conducted on cells with comparable molecular densities of the respective receptors (Figure 4.14 h).

Comparison of variation in average cluster size and density of clusters between individual cells and cross-correlation of these two parameters led to the conclusion that these two parameters for KIR2DL1^{WT}, KIR2DS1^{WT} and KIR2DL1^{I233K} in Jurkat cells follow roughly the same patterns as in NKL cells. Specifically, the average cluster size for KIR2DL1^{WT} varied between the individual cells relatively less than number of clusters detected per unit of area. In contrast, for KIR2DS1^{WT} and KIR2DL1^{I233K} average cluster sizes in different cells covered broader range, while density of clusters was less variable than for KIR2DL1 (Figure 4.14 i).

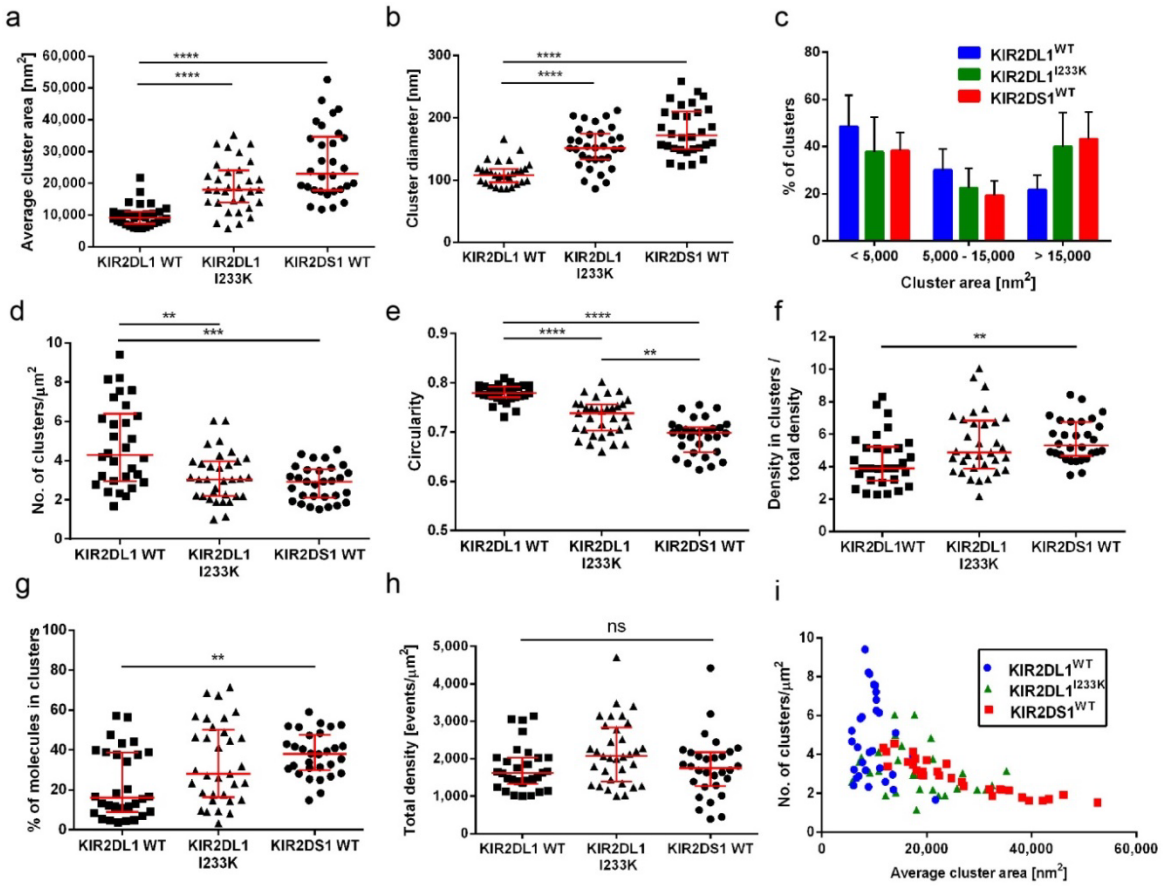

Figure 4.14 Quantitative analysis of clustering of KIR2DL1^{WT}, KIR2DL1^{I233K} and KIR2DS1^{WT} in Jurkat cells.

Average cluster area (a) and diameter (b), size distribution of clusters (c), number of clusters per µm^2 (d), average cluster circularity (e), ratio of density of events in clusters to overall membrane density (f), fraction of molecules localized within clusters (g) and overall density of detected events (h). (i) Number of clusters per µm^2 plotted against average cluster area measured in individual cells. (a - b and d - i) Each symbol represents the mean from several regions within one cell. Horizontal bars and errors represent the medians and interquartile range. (c) Bars and errors represent means and SD. Data are from 30 (KIR2DL1^{WT} and KIR2DS1^{WT}) or 32 (KIR2DL1^{I233K}) cells from three independent experiments. ns non-significant, ** $p < 0.01$, *** $p < 0.001$, **** $p < 0.0001$, Kruskal-Wallis test with Dunn's post-test.

To further ensure that observed differences are not a consequence of differential expression of the receptors, colour-scale cluster maps for cells expressing the respective receptors at similar densities were directly compared (Figure 4.15 a). As before, the comparison was made between the cells with relatively low and high expression of the transfected receptors. This has demonstrated that KIR2DS1^{WT} and KIR2DL1^{I233K} form larger clusters than KIR2DL1^{WT} at comparable low or high molecular densities. This is further illustrated in Figure 4.15 b, where average cluster areas for individual cells expressing each receptor are plotted against the density of molecules detected for individual cells. Consistent differences in cluster size of KIR2DL1^{WT},

KIR2DS1^{WT} and KIR2DL1^{I233K} are detectable across the range of different receptor densities.

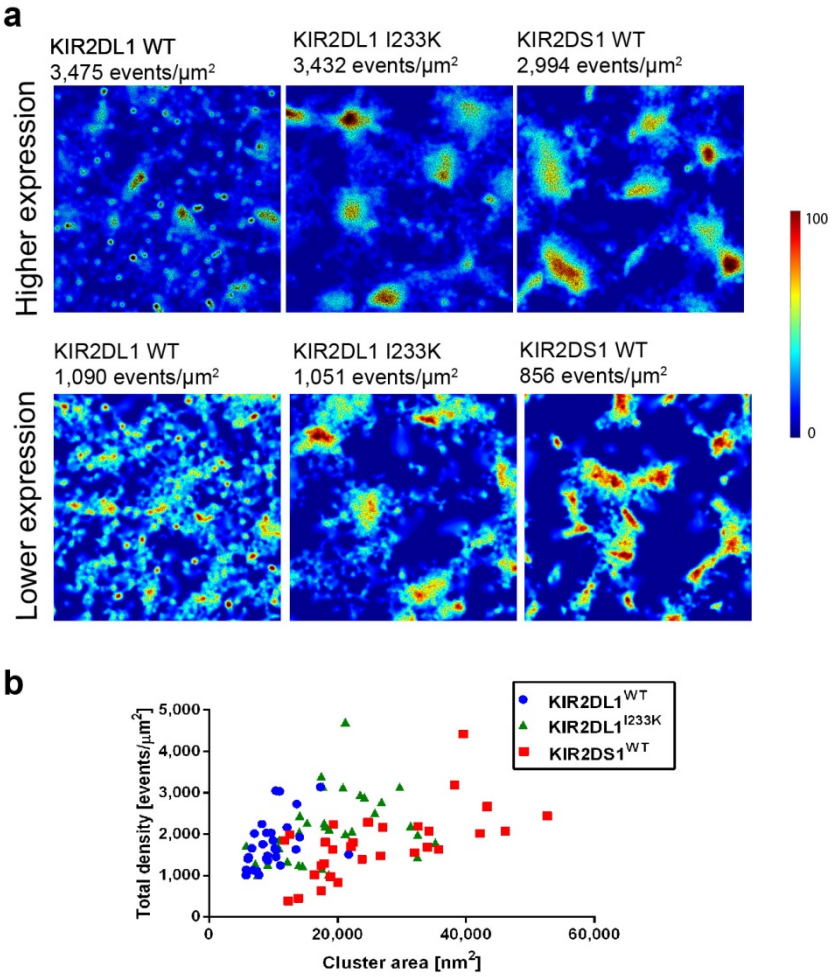

Figure 4.15 Differences in KIR2DL1^{WT}, KIR2DL1^{I233K} and KIR2DS1^{WT} clustering in Jurkat cells are not due to differential expression levels.
Jurkat/KIR2DL1-HA, Jurkat/KIR2DL1^{I233K} and Jurkat/KIR2DS1-HA cells were stained with anti-HA mAb conjugated with AF 488 and imaged by GSD microscopy. (a) Selected 3 μm × 3 μm regions are shown as colour maps where colours correspond to the extent of clustering according to pseudo-colour scale. Regions from cells with relatively high (upper row) and low (lower row) densities of detected events are shown. (b) Total density of events plotted against average cluster area measured in individual cells. Each symbol represents the mean from several regions within one cell. Data are from 30 (KIR2DL1^{WT} and KIR2DS1^{WT}) or 32 (KIR2DL1^{I233K}) cells from three independent experiments.

In summary, quantitative comparison of KIR2DL1 and KIR2DS1 clustering at the surface of Jurkat T cells demonstrated differences consistent with those observed in NKL and primary human NK cells. Despite the absence of DAP12 adaptor, KIR2DS1 formed larger and denser clusters than its inhibitory counterpart. In addition, the above experiments established that I233K substitution in the transmembrane segment of KIR2DL1 results in augmented clustering of receptor in a DAP12-independent way.

4.4 Discussion

4.4.1 Summary of results

The aim of this chapter was to establish what dictates differential patterns of clustering of KIR2DL1 and KIR2DS1 at the surface of NK cells. This question was approached by creating mutant receptors in which single amino-acids were substituted by site-directed mutagenesis. Imaging of the NKL and Jurkat cells transfected with wild-type and mutated KIR2DL1 and KIR2DS1 led to the following observations:

- Substitution of positively-charged lysine at the position 233 in KIR2DS1 sequence with neutral alanine resulted in formation of smaller, less dense clusters accommodating a lower fraction of detected molecules.
- This effect was not present when lysine 233 was substituted by another positively-charged residue, arginine.
- Substitution of isoleucine, which is found at position 233 in KIR2DL1 sequence, with lysine led to the reciprocal effect – the mutated receptor formed larger and denser clusters, as compared to the wild-type KIR2DL1.
- Substitution of the tyrosine residues within the two KIR2DL1 ITIMs with alanine residues did not change the nanometre organization of the receptor, suggesting that tonic signalling of KIR2DL1 does not affect its clustering.
- Patterns of KIR2DL1 and KIR2DS1 organization in DAP12-deficient Jurkat T cells closely resembled those observed in NK cells, indicating that interaction with DAP12 has little, if any, impact on KIR2DS1 clusters formation.
- $KIR2DL1^{I233K}$, when expressed in Jurkat cells, also formed larger and more densely packed clusters than wild-type KIR2DL1, suggesting that the effect of lysine 233 on the receptor clustering is not associated with its role in binding to DAP12.

4.4.2 Relation to earlier studies

Factors governing the nanoclustering of NK cell receptors are very poorly understood with some sparse observations published to date. To my best knowledge, the report of histidine at position 36 diminishing the self-association of KIR2DL1 molecules is the only link between the sequence and organization of an NK cell receptor described to date. In a study by Kumar *et al.* mutation of histidine 36 to alanine was shown to enhance the self-association of KIR2DL1 [333]. This was concluded from the experiments in which wild type KIR2DL1 and its mutant form with

histidine to alanine substitution at position 36 were tagged at the cytosolic tail with either the C-terminal or N-terminal fragment of a fluorescent protein Venus. The fluorescent signal is only detected in this system when both halves of the protein are in close proximity, so that the Venus reporter becomes reconstituted. Therefore, changes in Venus fluorescence can be used to assess the relative distances between tagged molecules. The authors measured them by flow cytometry and discovered that the mutant receptor displayed an increase in Venus fluorescence, indicating stronger self-association, as compared to the wild-type receptor. This effect was not detected when histidine 36 was substituted with another bulky amino-acid possessing an imidazole ring, phenylalanine. Therefore, the authors concluded that histidine 36 limits the self-association of KIR2DL1 by acting as a steric hindrance [333].

However, the actual arrangement of KIR2DL1 was not directly visualised by the authors, nor were the changes suggested by their analysis. It is therefore not completely clear how the observed increase in the fluorescence of reporter protein precisely relate to the proposed increase in clustering. Moreover, despite histidine being found also at position 36 in KIR2DS1 sequence, its influence on KIR2DS1 association was not tested. Experiments presented in Chapter 3 have established that KIR2DL1 and KIR2DS1 display strikingly different patterns of organization at the surface of NK cells with KIR2DS1 forming larger and denser clusters. This indicated that other structural properties of the molecules also have an effect on the clustering of receptors, apart from the negative regulation of clustering by histidine 36.

KIR2DL1 and KIR2DS1 have highly homologous extracellular domains, and the main body of differences between their sequences corresponds to transmembrane and intracellular regions. Thus, it seemed rational to investigate the importance of these domains for establishing KIR clustering patterns. Site-directed mutagenesis applied in this study demonstrated that enhanced clustering of KIR2DS1 is caused by the presence of lysine 233 within the transmembrane region of the receptor. This conclusion has been drawn from analysis of the receptors organization by super-resolution microscopy, which is the most direct way to study organization of any proteins. Furthermore, the effect of lysine 233 is apparent in KIR proteins when the position 36 is occupied by histidine, as evidenced by significantly larger and denser clusters detected in the super-resolution images of the mutant KIR2DL1 where isoleucine 233 was substituted by lysine.

Substitution of positively-charged residue (arginine) in the transmembrane region of NKG2D with alanine was previously shown to alter stimulation-dependent recruitment of NKG2D to detergent-resistant membrane fractions [343]. It is thus feasible that

positively-charged residues within transmembrane regions of activating NK cell receptors regulate their confinement within plasma membrane through triggering their association with cholesterol-rich microdomains. The authors of this study proposed that arginine-to-alanine mutation affected the NKG2D recruitment to the cholesterol-rich domains due to disrupting the association of NKG2D with signalling adaptor DAP10.

However, the idea that association with adaptor molecules regulates the receptor confinement in the membrane cannot be easily translated onto KIR2DS1. KIR2DS1 can be expressed at the cell surface without forming complexes with its adaptor molecule [342, 344]. This is different from for example KIR3DS1, which was demonstrated to rely on association with DAP12 for its surface expression [345]. In this and previous studies, KIR2DS1 was detected at the surface of DAP12-negative T cell line Jurkat [342, 344]. Moreover, substitution of arginine residue in the transmembrane region of NKG2D with alanine reduced the receptor expression at the surface of Baf3 murine pro-B cell line [230]. In contrast, mutant KIR2DS1 in which lysine 233 was substituted with alanine in the current study displayed a small increase in the surface expression on NKL cells, as compared to the wild-type KIR2DS1. This indicates that substitutions of positively-charged transmembrane residues in different activating receptors might have different impacts on the proteins folding and stability in the membrane. Similarly, association with the signalling adaptor might not have the same effect on the organization of different activating receptors within the plasma membrane.

In DAP12-deficient Jurkat cells, KIR2DS1 and KIR2DL1 displayed patterns of organization very similar to what was observed in NK cells, with bigger and denser clusters detected for the activating receptor. This indicated that formation of densely packed clusters might be dependent on the presence of positive charge within the transmembrane region independently of the receptor interactions with its adaptor. This is further validated by the increase in cluster size and density observed for KIR2DL1 mutant in which isoleucine 233 was substituted with lysine, observed consistently in NK cells and in Jurkat cells.

4.4.3 Significance of presented results

Different sequences of KIR2DL1 and KIR2DS1 transmembrane and intracellular domains are directly related to different types of signals transduced by these receptors. Thus, they could affect the nanometre-scale organization of KIR2DL1 and KIR2DS1 in at least two different ways. First, tonic signalling could be important for the formation of nanoclusters. To test this idea for KIR2DL1, the two tyrosine residues within the ITIMs

were mutated to alanine residues. Nanometre-scale organization of this mutated variant was found to be indistinguishable from the wild-type KIR2DL1. This indicates that tonic signalling of KIR2DL1 has little, if any, impact on its organization at the surface of NK cells. Consistent with these results, Kumar *et al*. did not detect any changes in self-association of KIR2DL1 upon mutation of both ITIM tyrosine residues to phenylalanine [333].

Substituting of lysine 233 in KIR2DS1, essential for the association with signalling adaptor, with alanine was one way to test the importance of tonic signalling for the nanometre-scale organization of the activating receptor. Substitution K233A led to striking changes in the organization of KIR2DS1. However, it was impossible to dissect precisely whether this was mediated by disruption of the tonic signalling, some independent mechanism or is caused collectively by multiple different effects.

The wild-type and mutant receptors compared in this chapter often displayed different levels of surface expression, consistent with earlier reports showing that transmembrane charged residues and association with signalling adaptors affect the stability of KIR receptors at the membrane [342, 346]. Previous studies have shown that although DAP12 is not essential for KIR2DS1 surface expression, the presence of adaptor stabilizes KIR2DS1 in the membrane, as demonstrated by increased expression of KIR2DS1 upon co-transfection with DAP12 in NKL and Jurkat cell lines. This was suggested to be the consequence of KIR-DAP12 interactions modifying the protein's glycosylation within the endoplasmic reticulum [342]. The requirements for the assembly with DAP12 have been studied in detail for KIR2DS2. Feng *et al.* demonstrated that interaction with DAP12 is largely favoured by the presence of lysine at position 9 of the transmembrane region, and even substitution of this lysine with another positively-charged residue, arginine, has significantly reduced the association of KIR2DS2 with DAP12 [346]. In light of the above studies, it seems possible that substitutions at position 233 of KIR2DS1 and KIR2DL1 affected the posttranslational modifications of these proteins, resulting in their reduced surface expression. However, the differences in the cell surface organization of wild-type and mutant KIR appear to not be directly caused by their differential expression. Tested receptors displayed the same quantitative differences in clustering across the range of molecular densities and this range was similar for each compared receptor. However, it cannot be excluded that the same factors that control the differential expression of KIR mutants could also independently contribute to the observed differences in clustering. Moreover, distinct clustering patterns of KIR2DL1 and KIR2DS1 visualized in Jurkat T cells suggest that

interaction with DAP12 is also not directly responsible for how these two receptors organize on nanometre scale.

Once at the surface, KIR2DS receptors have been shown to be stabilized by their interaction with DAP12 [342]. This was previously suggested to result from the presence of positively charged lysine being energetically unfavourable within the hydrophobic interior of the plasma membrane. DAP12 could increase stability of KIR by masking the positively charged lysine through an ionic bond with a negatively charged aspartic residue in the transmembrane region of DAP12. Alternatively, DAP12 was proposed to cover motifs on the KIR2DS molecules that could otherwise be targets for other proteins acting to regulate KIR internalization. For instance, casein kinase II phosphorylates KIR3DL1 leading to a decrease in its surface expression. The same casein kinase II phosphorylation motifs can be found within KIR2DS molecules and it was suggested that DAP12 may prevent such kinases from recognizing and phosphorylating these residues.

Although speculative, it seems feasible that self-assembly of KIR2DS1 in densely packed clusters could promote its surface stability through similar mechanisms. Tight contacts between the molecules within the cluster could also be one way to prevent the exposure of charged lysine residue to the hydrophobic membrane milieu. Such strong clustering would not be required for KIR2DL1, which does not possess a transmembrane lysine, but instead has isoleucine at position 233. The relative impact of transmembrane helices hydrophobicity on membrane insertion was used to create a 'biological' hydrophobicity scale [347]. According to the analysis by Hessa *et al*., charged residues were energetically less favourable in the transmembrane helix, especially when centrally-located (such as lysine on the 9^{th} position in transmembrane region of KIR2DS1). In contrast, isoleucine, which is present at corresponding position within KIR2DL1 sequence, was amongst the three amino-acids ranked as the most energetically-favourable in the transmembrane helix [347]. Similarly, tight clusters could be less penetrable for kinases which negatively regulate surface stability of the KIR molecules.

4.4.4 Future directions

The experiments presented in this chapter demonstrated that nanoclustering patterns of KIR2DL1 and KIR2DS1 are genetically-encoded and specifically, the presence of lysine at position 233 leads to the formation of larger and denser clusters. However, it is not clear by what mechanism is this mediated. Multiple scenarios linking

the lysine 233 with enhanced clustering could be possible in light of the current observations. In my opinion, this gap in the knowledge would be of high priority for the future studies. Some key questions to address in the future are listed below.

Firstly, although the same differences in KIR2DL1 and KIR2DS1 clustering were observed in NK cells and DAP-12 deficient Jurkat, it cannot be excluded that in the absence of DAP12 KIR2DS1 forms complexes with other adaptors, for example CD3ζ. Thus, clustering could still be facilitated by such molecular interactions. This question could be addressed with co-immunoprecipitation studies, screening for other signalling adaptors known to associate with immune receptors, which are present in Jurkat cells.

Secondly, it would be worth exploring whether the same mechanism responsible for differential expression levels of wild-type and mutated KIR2DL1 and KIR2DS1 could independently control clustering of the receptors. One possibility to investigate would be that mutations at position 233 impair the posttranslational modifications of KIR, leading to changes in expression and surface organization. For instance, it would be useful to compare the glycosylation of wild-type and mutant receptors and correlate the results with the outcome of imaging experiments. In addition, it would be very interesting to check whether different clustering patters could be related to differences in the process of membrane insertion of the particular receptors, possibly resulting from the presence or absence of polar amino-acid in the transmembrane region. An ideal experiment to establish this would be to directly image the transport of KIR2DS1 and KIR2DL1 to the plasma membrane. Such super-resolution live imaging studies would likely answer the question whether molecules are incorporated in the membrane as clusters and remain within them or maybe are incorporated into the membrane as monomers and associate later. However, such fast and potentially long lasting real-time super-resolution experiments are likely to be beyond the capabilities of the current technology.

Furthermore, it seems important to also consider the role of receptors interactions with the lipid rafts in formation of nanoclusters. The best way to study that would be to directly image the KIR receptors and fluorescently-labelled markers of lipid rafts, such as methyl-beta-cyclodextrin, by two-colour super-resolution microscopy to check if KIR clusters overlay with detected lipid rafts.

Chapter 5: The importance of nanoclusters formation for KIR2DL1 and KIR2DS1 downstream signalling.

5.1 Introduction

Following the advent of super-resolution microscopy, clustering on nanometre-scale has been described for a broad range of immune receptors from different families. Thus, it seems likely that nanoclusters might have some function in regulation of immune signalling. Multiple studies focused on comparing nanoclustering of immune receptors under resting and stimulatory conditions and some receptors have been indeed found to reorganize on nanometre scale upon ligation. For instance, clusters of TCR have been described to mix with clusters of LAT and ZAP-70 upon activation [309]. In NK cells, nanoclusters of KIR2DL1 have been observed to become smaller and denser upon ligation of either KIR2DL1 itself or NKG2D, suggesting than nanoclustering of receptors might be linked to the integration of the signals from these two receptors [224].

It is much more challenging to directly correlate these observations with activation and/or inhibition of immune cells. Although a number of studies providing some functional clues for the importance of nanoclusters constantly increases, our knowledge of this subject is still very sparse. Nevertheless, the existing reports suggest that nanoclustering can affect the immune signalling in different ways. For instance, oligomers of BCR in the membrane have been proposed to represent an autoinhibited form of BCR. This was concluded from the experiments in which wild-type IgD-BCR and its mutated form, unable to form oligomers due to mutations in transmembrane and linker regions, were expressed in insect S2 cells. To test if the defect of intrinsic oligomerization changes the signalling behaviour of the BCR, tyrosine phosphorylation of wild-type and mutant receptors was compared. Mutant IgD–BCR showed increased tyrosine phosphorylation and decreased expression on the cell surface, suggesting that BCR complexes with defects in oligomerization are hyperactive and less stably expressed on the cell surface [348].

On the other hand, Kumar *et al.* demonstrated that primary antigen-experienced T cells have larger TCR oligomers on their cell surface than naive T cells and provided genetic evidence that this is important for increased antigen sensitivity [349].

Specifically, these authors identified a mutation in the transmembrane domain of the CD3ζ chain which impaired the formation of TCR oligomers and demonstrated that MA5.8 cells transfected with the mutant CD3ζ had reduced sensitivity to antigen stimulation compared to these transfected with wild-type protein, as shown by decrease in CD69 induction and IFN-γ production [349]. Furthermore, by transducing the bone marrow precursors from *Cd3z*$^{-/-}$ mice with either wild-type or mutant CD3ζ, the authors identified a crucial role of oligomeric TCR complexes on primary T cells in enhancing the sensitivity of antigen-experienced T cells and a memory T cell response [349].

In NK cells, increased clustering of KIR2DL1 in the membrane was shown to promote its phosphorylation and constitutive association with SHP-1. This was described for the mutant form of KIR2DL1 in which a histidine residue at position 36 was substituted with alanine, leading to self-association of the receptor. The authors suggest that this could be due to reduced accessibility of ITIMs to phosphatases, which constantly dephosphorylate wild-type KIR2DL1 [333]. However, this study did not explore at all whether specific features of clusters, i.e. particular cluster size and density, are important for efficient signalling of immune receptors.

5.2 Aims

The overall aim of this thesis was to establish whether the way in which KIR2DL1 and KIR2DS1 are organized at the NK cell surface is important for these receptors function. The experiments described in the previous chapters established that both KIR2DL1 and KIR2DS1 form nanometre-scale clusters at the plasma membrane, although their specific clustering patterns are different. Therefore, a logical next step was to investigate the link between formation of nanoclusters and cellular signalling.

Unlike inhibitory receptors in NK cells, most of the activating receptors do not possess the signalling motifs within their sequence and instead rely on the association with signalling-competent adaptor proteins. It seems plausible that the way in which activating NK cell receptors and their adaptors are organized at the surface might be important for different aspects of signalling, including the thresholds and kinetics. The results presented in the previous chapter indicate that formation of KIR2DS1 clusters is independent of the presence of its signalling adaptor DAP12. Although association of KIR2DS1 and DAP12 has been demonstrated by multiple studies using biochemical methods [342, 344], their actual organization at the NK cell surface has never been characterized. Thus, the first aim of this chapter was to determine how KIR2DS1 and

DAP12 are organized with respect to each other at the surface of NK cells and whether this organization changes upon ligation of KIR2DS1.

Although a number of studies described reorganization of receptors and other signalling molecules following cellular activation [224, 309, 313] and others demonstrated that clustering can have either limiting or enhancing effect on signalling [348, 349], it remained unknown how the individual characteristics of clusters affect signalling. For instance, it is not explored whether the size of clusters is important for signalling capacity of a given receptor. To fill this gap in the knowledge, the second part of this chapter focused on imaging of KIR2DL1 and SHP-1 phosphatase, as well as KIR2DS1 and ZAP-70 kinase. This aimed to establish whether or not there is a correlation between the size of nanoclusters and phosphorylation of downstream signalling molecules.

5.3 Results

5.3.1 Imaging of endogenous DAP12 in NKL cells transfected with wild-type and mutated variants of KIR2DS1.

The association of activating KIR with DAP12 is long known to be vital for signalling [193, 237], and for some activating KIR this interaction is also essential for the surface expression [345]. KIR2DS1 however, in this and previous studies has been shown to be expressed at the surface in the absence of DAP12, i.e. in a DAP12-deficient cell line Jurkat [193, 342, 344]. Therefore, it was important to investigate how KIR2DS1 and DAP12 are organized at the cell surface and specifically, whether or not they are intermixed within the same nanoclusters. Thus, in the next step KIR2DS1 and DAP12 were imaged in NKL cells by two-channel STED microscopy.

Immunostaining of endogenous signalling molecules is challenging due to these proteins being not very abundant. Therefore, it is essential to verify the staining specificity at the start of experiments utilizing a particular antibody against endogenous signalling proteins. For this, NKL/KIR2DS1-HA cells were plated on PLL-coated slides, fixed, permeabilized and stained with an anti-DAP12 rabbit mAb, or appropriate isotype control antibody, followed by the anti-rabbit secondary antibody conjugated with AF 568. Cells were then imaged by STED microscopy using identical parameters. The comparison of fluorescence derived from the anti-DAP12 mAb and isotype control antibody is presented in the Figure 5.1. Bright staining was observed where the anti-DAP12 mAb was present, while the fluorescence was virtually absent in STED images of cells stained with the isotype control. In addition, while clusters of proteins were

readily visible in the images of anti-DAP12 mAb, in the isotype control-stained cells no aggregates of fluorescent antibodies could be observed. This has established that the tested anti-DAP12 mAb can be reliably used for visualization of endogenous DAP12 in NKL cells.

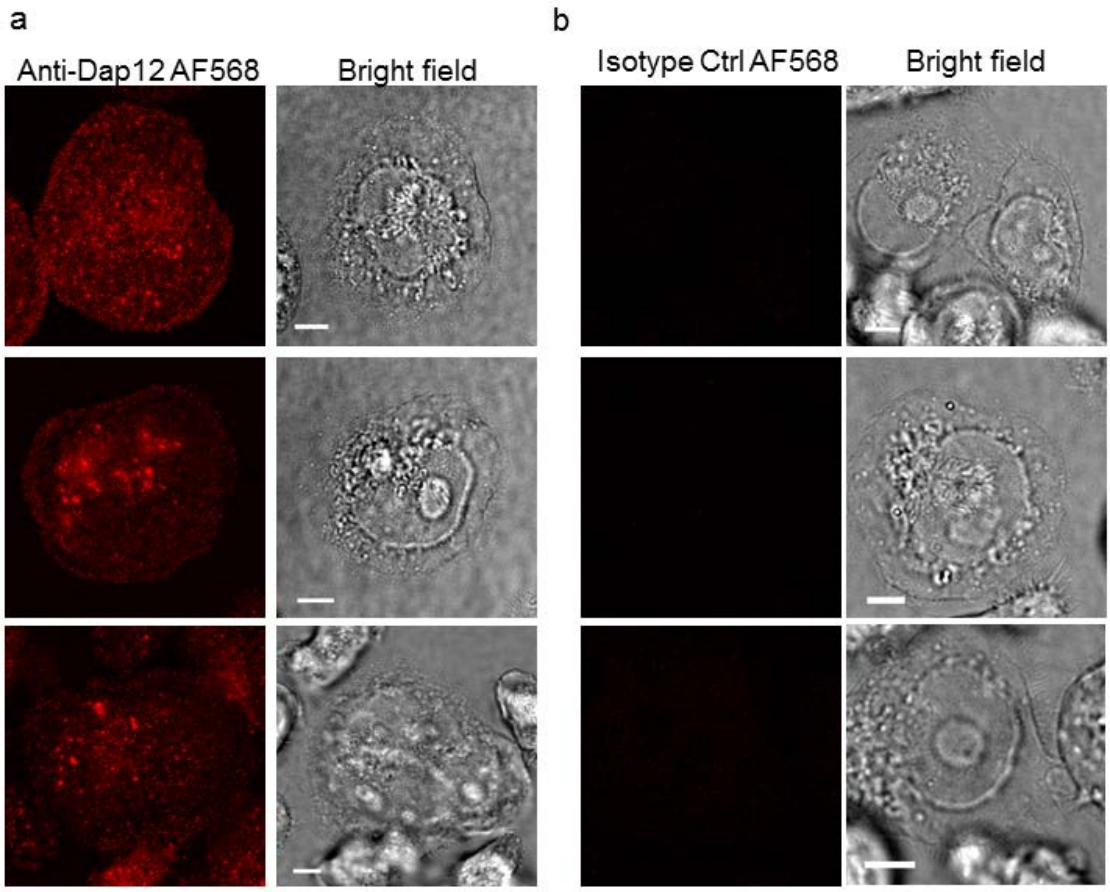

Figure 5.1 Control experiment for the specificity of anti-DAP12 mAb binding.
NKL/KIR2DS1-HA cells were plated on PLL-coated slides, fixed, permeabilized, stained with an anti-DAP12 rabbit mAb (a), or appropriate isotype control antibody (b), followed by the anti-rabbit secondary antibody conjugated with AF 568 and imaged by STED microscopy using identical parameters. Fluorescence and bright-field images are shown for three cells representative of n > 20 cells stained with the anti-DAP12 mAb (a) and isotype control antibody (b). Brightness was adjusted in an identical way in all images.

In the next step, DAP12 and wild-type and mutated variants of KIR2DS1 were visualized under non-stimulatory conditions and upon ligation of KIR2DS1 with EB6 mAb. For this, NKL/KIR2DS1-HA, NKL/KIR2DS1^{K233A} and NKL/KIR2DS1^{K233R} cells were fixed on the PLL-pre-coated slides coated with either EB6 mAb or control murine IgG1 antibody, permeabilized and stained with an anti-DAP12 rabbit mAb and secondary anti-rabbit antibody conjugated with AF568 and anti-HA antibody directly labelled with AF488. The plane of the cell contact with glass slide was imaged for all cell lines by STED microscopy using identical parameters.

Under both conditions, clusters of DAP12 were visible at the surface of all analysed cell lines. To investigate whether or not DAP12 is recruited to the synapse upon ligation of KIR2DS1, the intensity of DAP12-derived fluorescence was compared in cells incubated on EB6 or isotype-matched control antibody (Figure 5.2). For the wild-type KIR2DS1, the mean intensity value (per pixel) of fluorescent signal has significantly increased in the stimulated cells, as compared to resting cells ($p = 0.004$, Mann-Whitney test by ranks; Figure 5.2 b). This indicates that upon ligation of KIR2DS1, DAP12 is being recruited to the plasma membrane at the site of the contact.

In contrast, in NKL/KIR2DS1^{K233A} cells, the mean intensity of staining was not different between the resting and stimulated cells ($p = 0.3985$; Figure 5.3 b). The lack of DAP12 recruitment to the synapse upon KIR2DS1^{K233A} ligation was not surprising, since the presence of positively-charged transmembrane residue has been shown to be essential for the activating receptors forming complexes with DAP12 [346] and therefore substitution of lysine 233 with alanine was expected to render the receptor signalling-deficient. Disruption of the receptor-DAP12 interaction by the K233A mutation was further confirmed by a decrease in the mean intensity of DAP12 in NKL/KIR2DS1^{K233A} cells, as compared to NKL/KIR2DS1-HA cells (imaged at the same time, with identical parameters for direct comparison). DAP12-derived fluorescence was lower in NKL/KIR2DS1^{K233A} cells incubated on both control non-stimulating antibody and EB6 mAb, as compared to the NKL/KIR2DS1-HA cells in the same conditions (Figure 5.3 c). Comparison of DAP12 staining intensity in NKL/KIR2DS1^{K233R} under resting and stimulatory conditions suggested that ligation KIR2DS1^{K233R} also does not lead to the recruitment of DAP12 to the contact plane, as evidenced by no change in the fluorescence intensity ($p = 0.4402$, Mann-Whitney test by ranks; Figure 5.3 e). The amount of DAP12 imaged at the membrane of NKL/KIR2DS1^{K233R} under non-stimulatory conditions was reduced, but not significantly lower than its amount in NKL/KIR2DS1-HA cells. In contrast, when cells were incubated on EB6, the mean intensity of DAP12 staining in NKL/KIR2DS1^{K233R} was significantly lower than in NKL/KIR2DS1-HA cells imaged in the same experiments (Figure 5.3 f). This is consistent with the increase in the DAP12 intensity observed upon ligation of wild-type KIR2DS1, but not KIR2DS1^{K233R}.

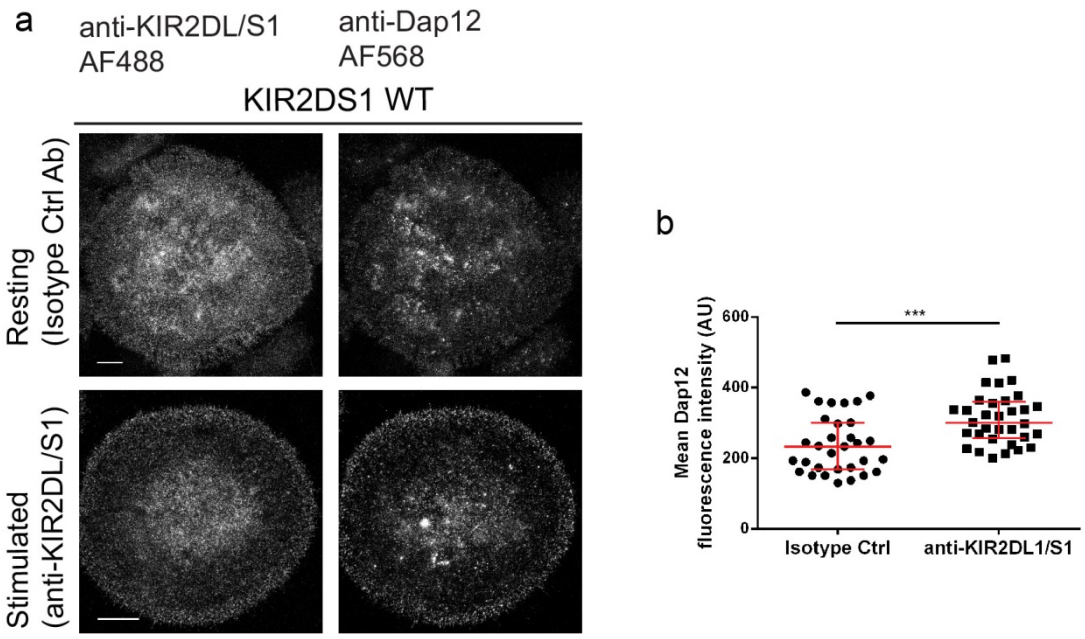

Figure 5.2 Imaging of endogenous DAP12 in unstimulated NKL/KIR2DS1-HA cells and upon KIR2DS1 ligation.

Cells were fixed on the PLL-coated slides covered with either EB6 mAb or isotype-matched control antibody, permeabilized and stained with anti-HA mAb directly labelled with AF488 and anti-DAP12 rabbit mAb and secondary anti-rabbit antibody conjugated with AF568. Representative STED images are shown in (a). Mean intensity of DAP12-derived fluorescence was compared between cells incubated on either EB6 mAb or isotype control (b). Each dot represents a value for one cell. Data are from 31 (IgG1) and 33 (EB6) cells from 2 independent experiments. Horizontal lines and bars correspond to medians and interquartile range, respectively. Scale bars 5 µm. *** $p < 0.001$, Mann-Whitney test.

The fact that amount of DAP12 detected in the membrane of resting NKL/KIR2DS1^{K233R} cells was not significantly lower than for NKL/KIR2DS1-HA - while this was the case for NKL/KIR2DS1^{K233A} cells – might suggest that K233R mutation does not abolish the interaction between KIR and DAP12 entirely. Previous studies have shown that substitution of transmembrane lysine in KIR2DS2 with arginine largely reduced its association with DAP12 but did not disrupt it completely [346]. However, the observation that DAP12 is not recruited to the contact plane upon ligation of KIR2DS1^{K233R} suggests that this mutated variant is not able to trigger the same functional outcomes as the wild-type receptor.

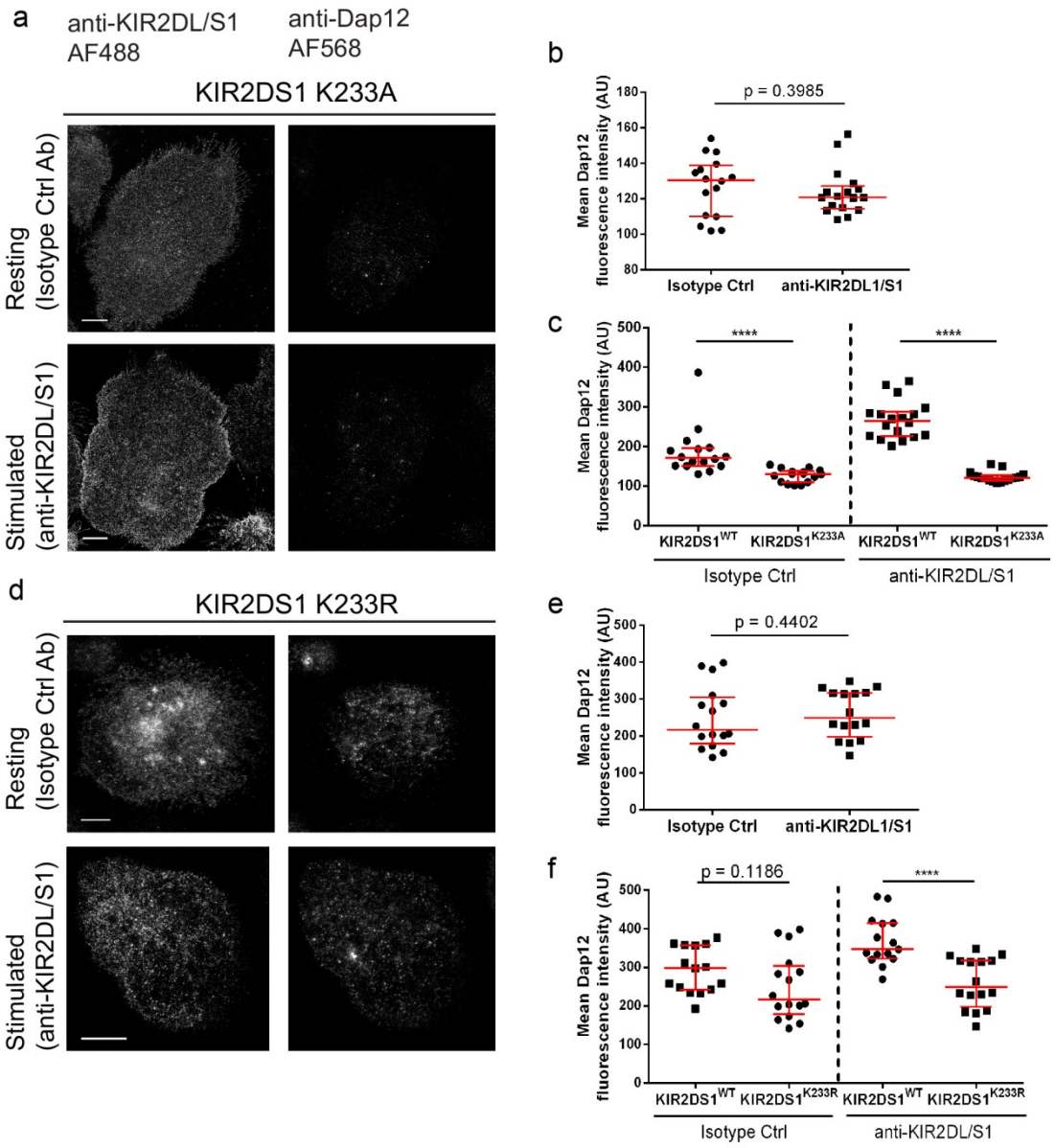

Figure 5.3 Imaging of endogenous DAP12 in unstimulated NKL/KIR2DS1^{K233A} and NKL/KIR2DS1^{K233R} cells and upon KIR2DS1 ligation.
Cells were fixed on the PLL-coated slides covered with either EB6 mAb or isotype-matched control antibody, permeabilized and stained with anti-HA mAb directly labelled with AF488 (left column in a and d) and anti-DAP12 rabbit mAb and secondary anti-rabbit antibody conjugated with AF568 (right column). Representative STED images are shown in (a) and (d). Mean intensity of DAP12-derived fluorescence was compared for each cell line incubated on either EB6 mAb or isotype control (b and e). Panels in (c) and (f) compare mean intensity of DAP12-derived fluorescence between NKL/KIR2DS1^{K233A} (c) or NKL/KIR2DS1^{K233R} (f) and NKL/KIR2DS1^{WT} cells imaged in the same experiment using identical parameters. Each dot represents a value for one cell. Data are from 15 – 18 cells from 2 independent experiments. Horizontal lines and bars correspond to medians and interquartile range, respectively. Scale bars 5 µm. **** $p < 0.0001$, Mann-Whitney test.

Taken together, these results demonstrate that upon ligation of KIR2DS1, endogenous DAP12 is recruited to the site of ligation. This effect is dependent on the formation of complexes between KIR2DS1 and DAP12 and is abrogated when this

interaction is disrupted. Moreover, disruption of KIR2DS1-DAP12 complex formation triggered by K233A substitution in the KIR2DS1 sequence results in less DAP12 being present at the surface of NKL cells, both in resting conditions and upon KIR2DS1 ligation.

5.3.2 Two-colour imaging of nanometre-scale organization of KIR2DS1 and DAP12.

Next, organization of KIR2DS1 and DAP12 was assessed in the multi-channel STED images. Like before, NKL/KIR2DS1-HA cells were plated on PLL-coated slides covered with EB6 mAb or isotype-matched control antibody and stained for KIR2DS1 with anti-HA antibody conjugated with AF 488 and for DAP12 with anti-DAP12 primary antibody followed by secondary Ab labelled with AF 568 (Figure 5.4 a). As a positive control for co-localization, the same cells were fixed on PLL-coated slides and KIR2DS1 was simultaneously labelled with EB6 mAb conjugated to Atto 488 (green channel) and with anti-HA antibody followed by specific secondary antibody conjugated to AF 568 (red channel; Figure 5.4 c).

Visual examination of the resulting STED images readily showed that in unstimulated cells clusters of KIR2DS1 and DAP12 overlapped less than the signal recorded in two channels for the positive control sample. Only partial overlapping between clusters could be observed, which appeared to mostly occur at the edges of clusters. To formally quantify the co-localization between KIR2DS1 and DAP12, Pearson's correlation coefficient was calculated for each cell. In non-stimulated cells, the values of Pearson correlation coefficient were relatively low, with a median of 0.22 and IQR 0.16 -0.27, which confirmed that clusters of KIR2DS1 and DAP12 overlap only partially (Figure 5.4 d). Interestingly, in cells stimulated on EB6 mAb the degree of mixing between clusters of KIR2DS1 and DAP12 was increased, as demonstrated by the comparison of overlaid STED images (Figure 5.4 a) and an increase of the Pearson correlation coefficient ($p = 0.004$, Kruskal-Wallis test with Dunn's post-test).

When NKL/KIR2DS1^{K233A} cells were imaged in identical experiments (Figure 5.4 b), ligation of the mutated KIR2DS1 did not trigger changes in organization of KIR2DS1^{K233A} and DAP12. No increase in Pearson correlation coefficient was observed between NKL/KIR2DS1^{K233A} cells plated on isotype or activating antibodies (Figure 5.4 d). In both resting and activated cells, median Pearson correlation coefficient was lower than in unstimulated NKL/KIR2DS1-HA cells and was equal to 0.07 (IQR -0.07 – 0.12) in resting and 0.05 (IQR -0.16 – 0.19) in stimulated cells, indicating that DAP12 and

KIR2DS1^{K233A} have roughly random mutual distribution without either significant correlation or anti-correlation between their density.

Other immune receptors, such as TCR, have been described to only partially mix with clusters of downstream signalling molecules, suggesting that such lateral contacts can be where signal propagation predominantly occurs [311]. The visual examination of multichannel STED images of wild-type KIR2DS1 and DAP12 cells suggested that these proteins often formed such lateral contacts. Edge contacts which do not result in mixing of clusters cannot be reported by measures such as Pearson correlation coefficient, which only take onto account directly overlapping areas of fluorescence in the compared channels (i.e. within one pixel). Therefore, in a complementary analysis approach, the distances between the KIR2DS1 and DAP12 cluster centroids were measured. To achieve this, the auto-threshold was applied to deconvolved STED images to produce binary maps of clusters. In the second step, for every detected KIR2DS1 cluster, a distance between its centroid and a centroid of the nearest DAP12 cluster was measured. In non-stimulated cells, the median distance between KIR2DS1 cluster centroid and centroid of the nearest DAP12 cluster was measured as 240 nm (IQR 209 – 300 nm), and when NKL cells were activated via KIR2DS1, the median distance between KIR2DS1 and DAP12 centroids significantly decreased and had a median value of 153 nm (IQR 141 – 168 nm; Figure 5.4 e).

The same analysis conducted for DAP12 and KIR2DS1^{K233A} showed that clusters of these two proteins are localized significantly further apart, with a median distance in unstimulated cells being 809 nm (IQR 593 to 1003 nm). This is consistent with the fact that KIR2DS1 ^{K233A} is not able to form complexes with DAP12, as well as the earlier observations showing that DAP12 is less abundant at the surface of NKL/KIR2DS1 ^{K233A} cells, as compared to NKL/KIR2DS1-HA.

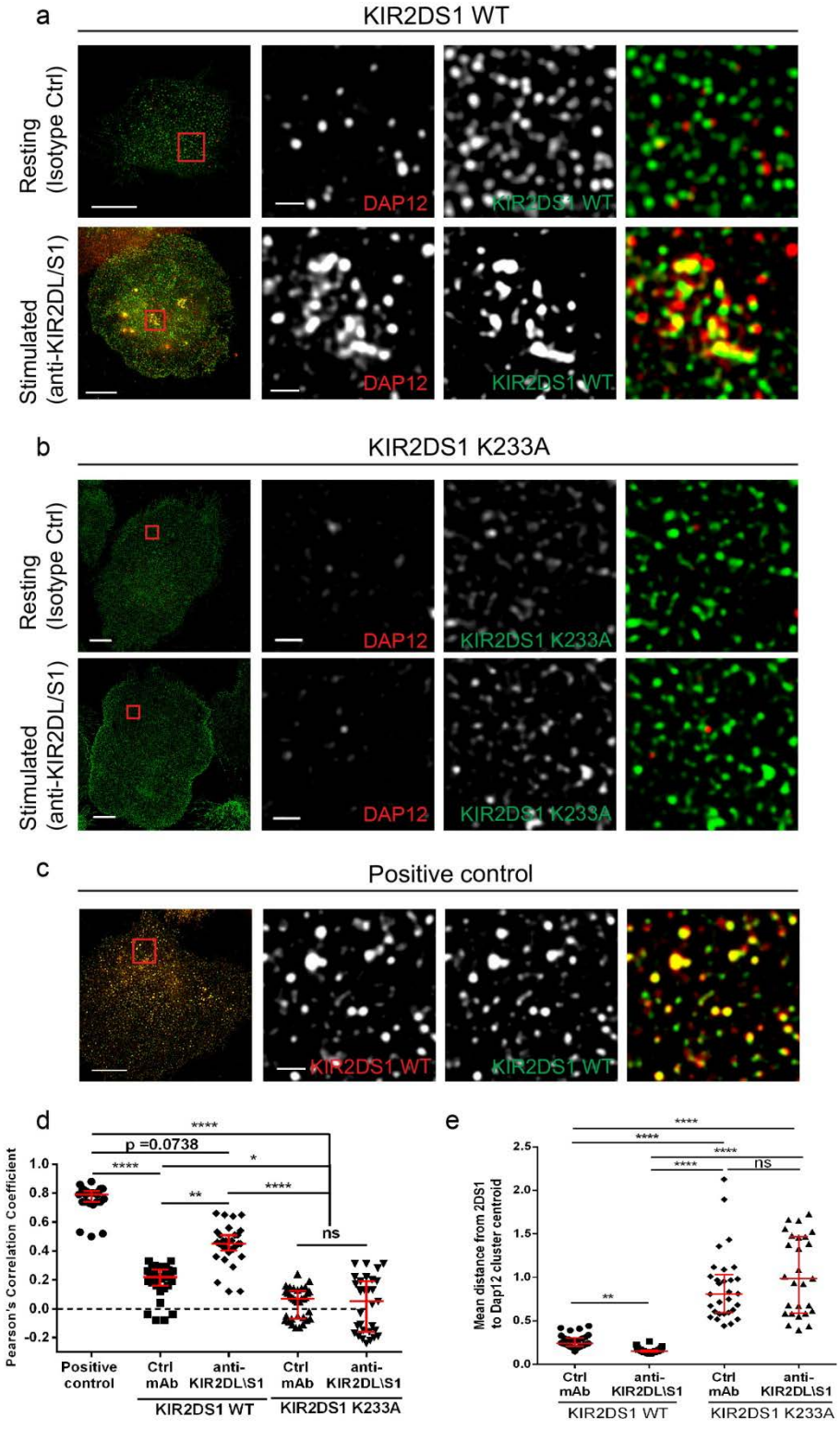

Figure 5.4 Ligation of KIR2DS1 triggers increased mixing between nano-clusters of KIR2DS1 and its associated adaptor DAP12.

NKL/KIR2DS1-HA (a) and NKL/KIR2DS1^{K233A} (b) cells on isotype-matched control mAb- (upper rows) or anti-KIR2DL/S1 mAb (clone EB6)-coated (lower rows) slides were stained with anti-HA mAb conjugated with AF488 and rabbit anti-DAP12 mAb followed by secondary anti-rabbit Ab conjugated to AF568 and imaged by STED microscopy. (c) As a positive control, NKL/KIR2DS1-HA cells incubated on PLL-coated slides were stained with anti-KIR2DL/S1 mAb conjugated with Atto 488 and rabbit anti-HA antibody followed by secondary anti-rabbit antibody

conjugated with AF 568. Representative STED images of overlaid channels and zoomed-in 3 × 3 µm regions outlined in red in STED images with channels separated and overlaid are shown. Scale bars are 5 µm in STED images and 500 nm in zoomed-in images. (d) Pearson's correlation coefficient values calculated for KIR2DS1^{WT} and DAP12 or KIR2DS1^{K233A} and DAP12 on IgG1- and anti-KIR2DL/S1 mAb-coated slides compared to KIR2DS1 stained in both channels as a positive control. (e) STED images were thresholded to create binary maps of clusters and x-y coordinates of cluster centroids were used to calculate the distances between each KIR2DS1 cluster and a nearest cluster of DAP12. Each dot represents an average of distances measured in one cell. Horizontal bars and errors represent the medians and interquartile range, respectively. The data is from 25 - 34 cells from 2 independent experiments. * = p <0.05, ** = p <0.01, **** = p <0.0001, Kruskal-Wallis test with Dunn's post-test.

In addition, the distances between clusters of DAP12 and KIR2DS1^{K233A} did not decrease upon ligation of KIR2DS1^{K233A} (median value of 989 nm; IQR 596 – 1466 nm), which further confirms that ligation of KIR2DS1 ^{K233A} does not trigger the same molecular events as the wild-type KIR2DS1. This is also in line with no increase in the amount of DAP12 present at the membrane upon ligation of KIR2DS1^{K233A}.

In summary, clusters of KIR2DS1 and its cognate signalling adaptor DAP12 in unstimulated NK cells are display only limited overlap at the membrane. However, they mix to a greater extent upon ligation of KIR2DS1, the effect which is dependent on the receptor ability to interact with DAP12 via the transmembrane lysine residue.

Visual comparison of STED images of KIR2DS1 and DAP12 in NKL/KIR2DS1-HA cells incubated on the non-stimulating antibodies and EB6 mAb indicated that in parallel to mixing of the proteins, the size of the clusters increased upon ligation of KIR2DS1 (Figure 5.4 a). To investigate whether or not this was a quantitative difference, the areas of KIR2DS1 and DAP12 clusters were measured using the binary maps of clusters created for NKL/KIR2DS1-HA cells incubated on isotype control and EB6 antibodies. This has confirmed that upon ligation of KIR2DS1, the mean area of this receptor clusters significantly increased (p = 0.0104, Mann-Whitney test; Figure 5.5 a). For DAP12, the mean size of detected clusters also increased, but not significantly.

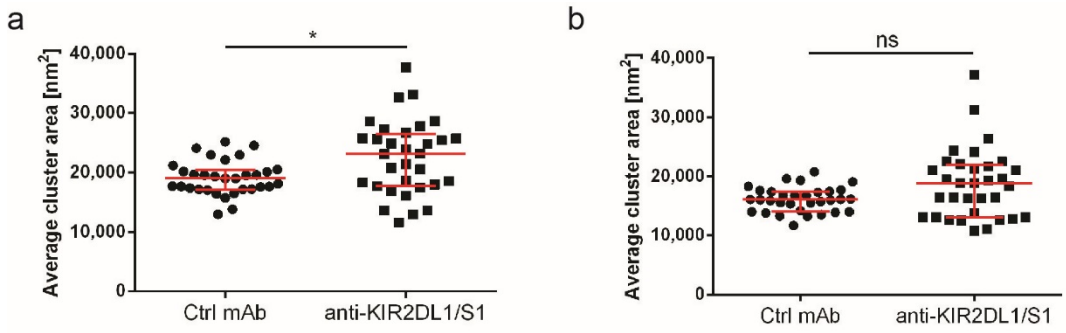

Figure 5.5 Comparison of the mean cluster area of KIR2DS1 and DAP12 in resting cells and upon ligation of KIR2DS1.
NKL/KIR2DS1-HA cells on isotype-matched control mAb- or anti-KIR2DL/S1 mAb (clone EB6)-coated slides were stained with anti-HA mAb conjugated with AF488 and rabbit anti-DAP12

mAb followed by secondary anti-rabbit Ab conjugated to AF568 and imaged by STED microscopy. For cluster measurements, STED images were thresholded to create binary maps of clusters. Each dot represents an average for one cell. Horizontal bars and errors represent the medians and interquartile range, respectively. The data is from 31 (IgG1) and 33 (EB6) cells from two independent experiments. ns non-significant, * = $p < 0.05$, Mann-Whitney test.

This has opened a question whether the increase in size of KIR2DS1 clusters is important and for example, if large clusters could preferentially interact with clusters of DAP12. Considering the arrangement of KIR2DS1 and DAP12 at the surface of resting and stimulated cells, it seemed likely that the lateral contacts between the clusters without their apparent mixing could also mediate productive signalling. Therefore, to quantify the association between clusters, a circular area around the centroid of each KIR2DS1 cluster in the multichannel STED images of NKL/KIR2DS1-HA cells resting or activated with the anti-KIR2DL/S1 mAb was screened for the presence of DAP12 clusters.

The radius of search area was equal to the radius of the KIR cluster enlarged by 78 nm or 80 nm - the values equal to the calculated 75^{th} percentiles of radii of DAP12 clusters in resting and activated cells, respectively. In this way, clusters of KIR2DS1 that either overlapped or formed edge contacts with DAP12 clusters were identified. For each analysed cell, 33^{rd} and 66^{th} percentiles (tertiles) of all KIR2DS1 cluster sizes were calculated. Next, to establish if clusters of a particular size preferably associated with DAP12, the distribution of sizes of KIR2DS1 clusters associated with DAP12 was compared against the distribution of sizes of all KIR2DS1 clusters.

For this, the percentages of KIR2DS1 clusters in contact with DAP12 which fell into the three bins designated as ‘small’, ‘medium’, or ‘large’ were calculated (Figure 5.6 a and e). Boundaries of these size bins correspond to the tertiles of all KIR2DS1 cluster sizes detected in the same cell. If KIR2DS1 clusters of all sizes formed contacts with DAP12 at equal frequency, the KIR2DS1 clusters found in contact with DAP12 should be equally distributed between these three bins – i.e. the fraction falling in each bin should be roughly 33%.

The analysis revealed that amongst the KIR2DS1 clusters associated with DAP12 in resting cells, the fraction of clusters classified as large had a median of 57% (IQR 55 – 60%), which was significantly more than the percentage of clusters classified as small (median 14%; IQR 13 – 16%), or medium (median 29%, IQR 26 – 32%). This indicated that in unstimulated cells, large KIR2DS1 clusters are more often found in contact with clusters of DAP12 (Figure 5.6 b). One possible way in which bigger clusters could form more contacts with DAP12 would be simply by covering a larger area – larger clusters with longer perimeter could support more contacts with DAP12 clusters in the plasma

membrane. Moreover, DAP12 seems to be actively transported from inside the cell to the synapse upon activation. KIR2DS1 clusters occupying a larger area could feasibly have a higher chance to be encountered by DAP12 molecules newly arriving to the membrane. To establish whether this could be a mechanism for bigger KIR2DS1 clusters preferentially associating with DAP12, experimental data acquired for each cell was compared to the simulated randomised dataset. The frequency of interactions between independently distributed clusters would be dependent on the relative densities of KIR2DS1 and DAP12 clusters and their sizes. Thus, these parameters were conserved during generation of the randomized data. To achieve this, for each imaged cell, the randomised dataset was created by keeping the positions of KIR2DS1 clusters detected in the particular cell fixed and randomly changing the positions of DAP12 clusters detected in the same cell within the boundaries demarking the cell edges. Five rounds of randomization were performed and a mean value was calculated for each cell. The relative proportions of contacts with DAP12 clusters after randomization formed by small, medium and large KIR2DS1 clusters closely resembled the result obtained for the experimental data – the likelihood of interaction with DAP12 clusters increased together with the size of KIR2DS1 clusters (Figure 5.6 c). This has shown that at the density of clusters as measured in the STED images, covering a larger area by a particular KIR2DS1 cluster could account for the observed preference for large KIR2DS1 clusters interacting with DAP12.

To check if the size could be important not only for the frequency of contacts with DAP12 clusters but also for recruiting more of the adaptor molecules to KIR2DS1 clusters, the amount of DAP12 (measured as sum of DAP12-derived fluorescence intensity) associated with KIR2DS1 clusters was then compared between the designated size bins. This has shown that in unstimulated cells, the largest KIR2DS1 clusters not only form contacts with DAP12 clusters at higher frequency, but also DAP12 clusters associated with larger KIR2DS1 clusters contain more protein (Figure 5.5 d). The same analysis was performed for NKL/KIR2DS1-HA cells incubated on EB6 mAb-covered slides (Figure 5.6 e).

This has demonstrated that upon stimulation, largest KIR2DS1 clusters are also most likely to interact with DAP12, and one third of KIR2DS1 clusters with the largest area formed approximately half of all contacts with DAP12 clusters (median 53%, interquartile range 51 – 57%; Figure 5.6 f). Again, a very similar trend has been observed in the corresponding simulated data in which DAP12 positions were randomized, indicating that in activated cells, covering a larger area by KIR2DS1 cluster could account for largest clusters preferentially interacting with DAP12.

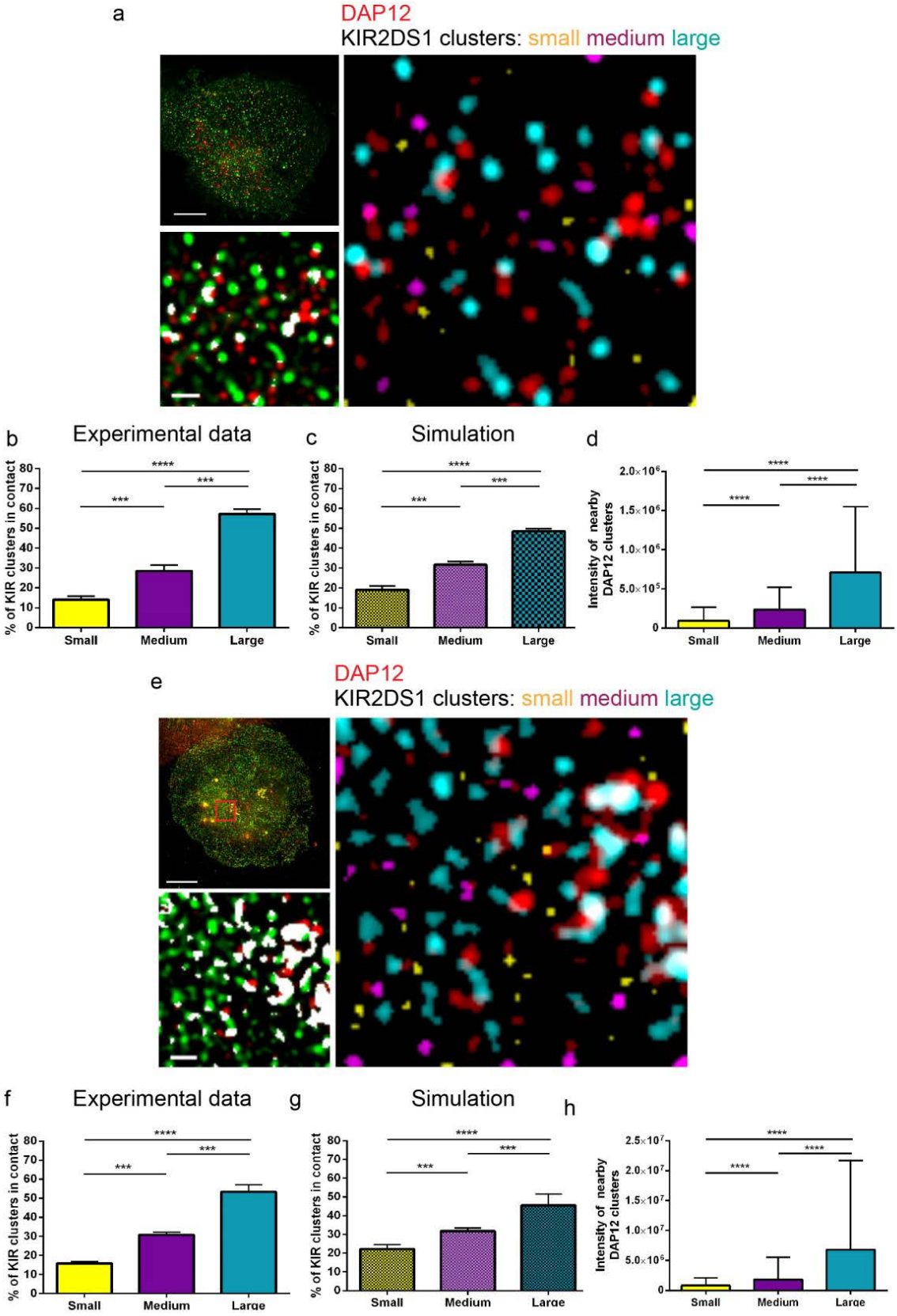

Figure 5.6 Importance of KIR2DS1 nanocluster size for association with DAP12 clusters.

NKL/KIR2DS1-HA cells were incubated for 5 min on (a –d) isotype control mAb- or (e – h) anti-KIR2DL/S1 mAb-coated slides, fixed, stained with fluorescently labelled antibodies and imaged

by two-channel STED microscopy. (a and e) STED images of cell membrane with KIR2DS1 (green) and DAP12 (red) visualized and overlaid are shown together with zoomed-in 3 µm × 3 µm regions (red boxes in STED images) in which overlapping pixels are marked in white. The same regions are shown in the right side with KIR2DS1 clusters color-coded according to size. Each size bin corresponds to a third of all KIR2DS1 clusters. (b – c and f - g) Fractions of all KIR2DS1 clusters associated with DAP12 clusters that fall into each size group calculated for the cells imaged by STED (b and f) compared to randomized data sets in which positions of KIR2DS1 clusters were conserved and positions of DAP12 clusters were randomized within the boundaries of cell area (d and g). (d and h) Sum of intensity of DAP12 clusters found nearby KIR2DS1 clusters from specified size bins. Bars and errors represent the medians and interquartile range. The data is from 31 (IgG1) and 33 (EB6) cells from two independent experiments. In (c and g), 5 rounds of randomization were run per cell and a mean value was used as the data point for this cell. *** $p < 0.001$, **** $p < 0.0001$, row-matched Friedman test with Dunn's post-test.

Comparison of DAP12 fluorescence intensity in the vicinity of differently-sized clusters has shown that similar to what was observed in resting cells, more DAP12 could be found in association with the largest KIR2DS1 clusters after KIR2DS1 ligation (Figure 5.6 h). For each size bin however, the amount of associated DAP12 was higher in stimulated cells than for the corresponding size bin in resting cells (compare values in Figures 5.6 d and 5.6 h). This is consistent with the increase in the amount of membrane-associated DAP12 observed after KIR2DS1 ligation in the previous experiments.

In summary, the above analysis indicates that both in resting cells and upon KIR2DS1 stimulation, largest clusters of KIR2DS1 are most often found in contact with DAP12 clusters.

5.3.3 Imaging of endogenous ZAP-70 in NKL cells transfected with wild-type and mutated variants of KIR2DS1.

The next step was to investigate whether similar to interaction with DAP12, specific cluster sizes of KIR2DS1 can promote or hinder its ability to recruit and activate molecules engaged in the downstream signalling, such as ZAP-70 kinase [193]. To answer this question, membrane-proximal ZAP-70 and its activated form phosphorylated on Y319 [350] had to be visualized in NKL/KIR2DS1-HA cells. To check if these proteins can be reliably labelled using commercially available antibodies, NKL/KIR2DS1-HA cells were plated on PLL-coated slides covered with EB6 mAb, fixed, permeabilized and stained with rabbit antibodies targeting either ZAP-70 or ZAP-70 pY319, or appropriate control antibody, followed by the anti-rabbit secondary antibody conjugated with AF 568. Cells were imaged by STED microscopy using identical parameters. A comparison of fluorescence derived from the anti-ZAP-70 or anti-ZAP-70 pY319 antibodies and control antibodies is presented in the Figures 5.7

and 5.8. For the antibody targeting total ZAP-70, bright staining could be observed in the plane of the cell-glass slide contact. In contrast, the fluorescent signal in STED images of cells stained with the isotype control was markedly lower. While clusters of proteins were readily visible in the STED images of anti-ZAP-70 antibody, in the isotype control-stained cells no such aggregates could be observed (Figure 5.7).

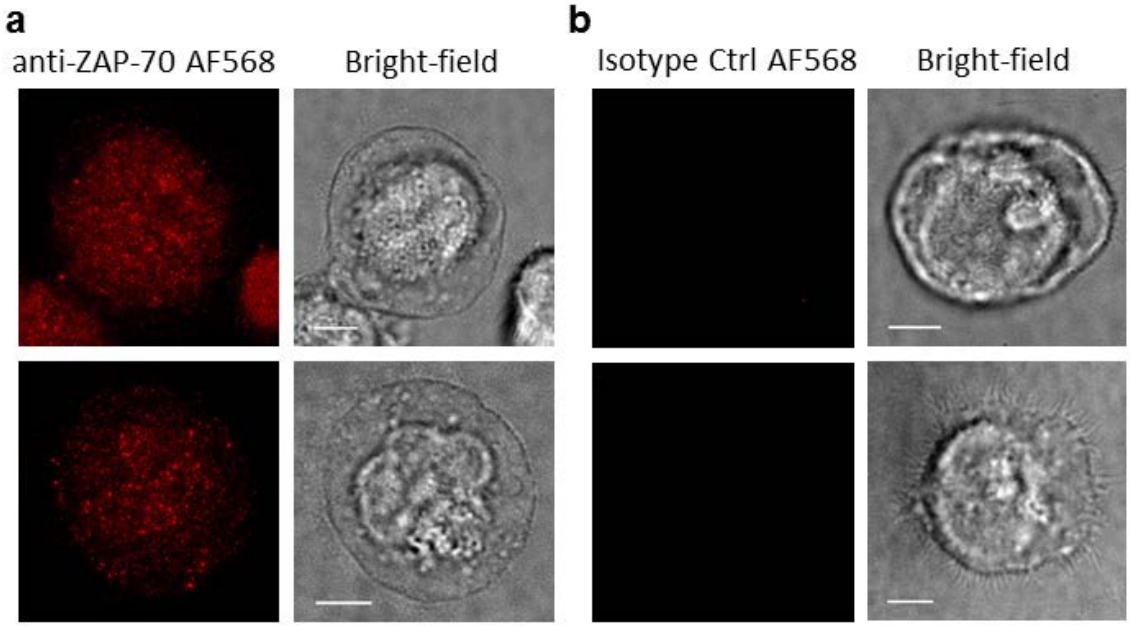

Figure 5.7 Control experiment for the specificity of anti-ZAP-70 antibody binding. NKL/KIR2DS1-HA cells were plated on PLL-coated slides covered with EB6 mAb, fixed, permeabilized, stained with an anti-ZAP-70 rabbit antibody (a), or appropriate isotype control antibody (b), followed by the anti-rabbit secondary antibody conjugated with AF 568 and imaged by STED microscopy using identical parameters. Fluorescence and bright-field images are shown for two cells representative for n > 20 cells stained with the anti-ZAP-70 antibody (a) and isotype control antibody (b). Brightness was adjusted in an identical way in all images.

For the staining with anti-ZAP-70 pY319 antibody, fluorescent signal was observed as distinct bright spots within the cell-glass slide contact plane. Importantly, in cells stained with the control antibody, such spots could not be observed and the fluorescent signal in STED images of these cells was generally very low (Figure 5.8). Taken together, these control experiments established that commercial antibodies can be reliably used for immunostaining of the ZAP-70 kinase, as well as its active phosphorylated form.

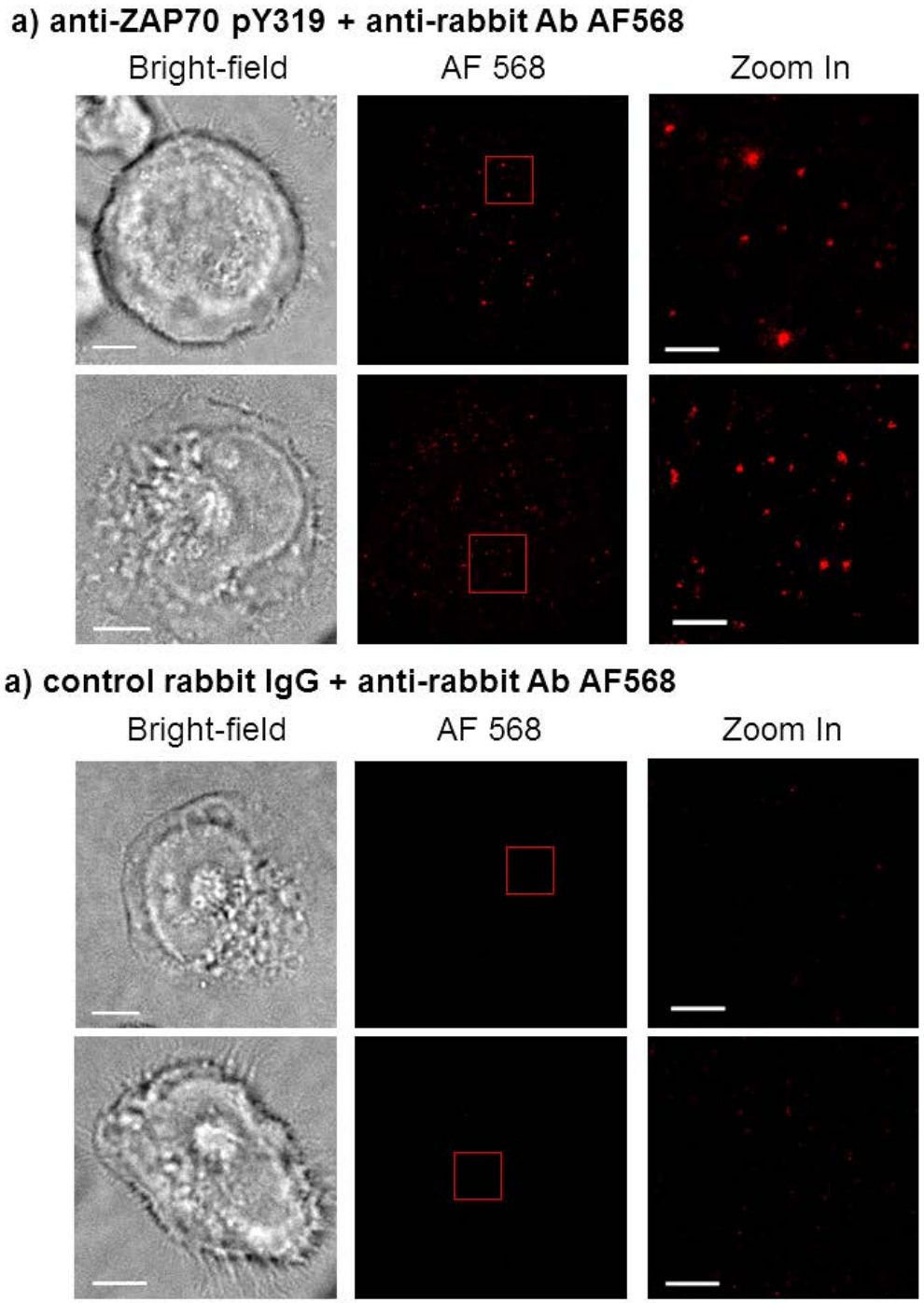

Figure 5.8 Control experiment for the specificity of anti-ZAP-70 pY319 antibody binding.
NKL/KIR2DS1-HA cells were plated on PLL-coated slides covered with EB6 mAb, fixed, permeabilized, stained with an anti-ZAP-70 pY319 rabbit antibody (a), or appropriate isotype control antibody (b), followed by the anti-rabbit secondary antibody conjugated with AF 568 and imaged by STED microscopy using identical parameters. Bright-field and fluorescence images are shown for two cells representative for n > 20 cells stained with the anti-ZAP-70 pY319 antibody (a) and isotype control antibody (b). Zoomed-In 5 µm x 5 µm regions are shown in the right column (red boxes in the STED images). Brightness was adjusted in an identical way in all images. Scale bars 5 µm in bright field images and 1 µm in zoomed-in regions.

To quantitatively compare the amount of membrane proximal ZAP-70 and ZAP-70 pY319 in resting and stimulated NKL/KIR2DS1-HA cells, cells were fixed on the slides covered with either EB6 mAb or control murine IgG1 antibody, permeabilized and stained with murine anti-HA mAb directly labelled with AF488 and rabbit anti-ZAP-70 antibody followed by secondary anti-rabbit antibody conjugated with AF568. As an additional control, NKL/KIR2DS1^{K233A} cells were treated and stained in the same way. All cells were imaged by STED microscopy using identical parameters to facilitate a direct comparison of the fluorescence intensity. For both imaged cell lines, ZAP-70 (as visualized by the antibody targeting total pool of protein) was visible at the plane of contact with the slide under resting and stimulated conditions (Figure 5.9). A clustered appearance of the membrane-proximal ZAP-70 could be readily observed upon visual examination of STED images. A comparison of the mean intensity of ZAP-70-derived fluorescence in NKL/KIR2DS1-HA cells incubated on isotype control and EB6 mAb demonstrated that the total amount of ZAP-70 at the membrane is increased upon KIR2DS1 ligation (Figure 5.9 b).

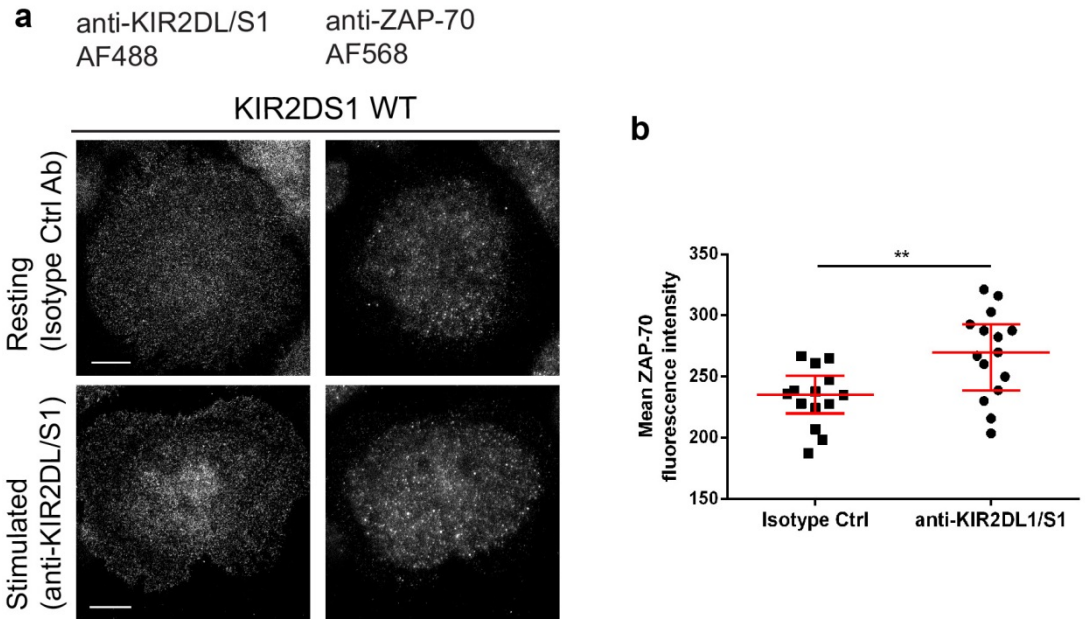

Figure 5.9 Imaging of endogenous ZAP-70 in unstimulated NKL/KIR2DS1-HA and upon KIR2DS1 ligation.
Cells were fixed on the PLL-coated slides covered with either EB6 mAb or isotype-matched control antibody, permeabilized and stained with murine anti-HA mAb directly labelled with AF488 (left column in a) and anti-ZAP-70 rabbit antibody and secondary anti-rabbit antibody conjugated with AF568 (right column). Representative STED images are shown in (a). Mean intensity of ZAP-70-derived fluorescence was compared between cells incubated on either EB6 mAb or isotype control (b). Each dot represents a value for one cell. Data are from 14 - 15 cells from two independent experiments. Horizontal lines and bars correspond to medians and interquartile range, respectively. ** $p < 0.01$, Mann-Whitney test.

No change was observed upon ligation of KIR2DS1^{K233A}, consistent with this mutant receptor being unable to transduce the signals (Figure 5.10 a). When ZAP-70-derived fluorescence was compared between NKL/KIR2DS1-HA and NKL/KIR2DS1^{K233A} cells incubated in the same conditions and imaged using identical parameters, no difference in the amount of total ZAP-70 could be observed between cells transfected with wild-type or mutant receptor under resting conditions. In contrast, more ZAP-70 was found at the membrane in NKL/KIR2DS1-HA cells incubated on EB6 mAb than in NKL/KIR2DS1^{K233A} under the same stimulation (Figure 5.10 b). Together, these results suggest that the base-line levels of ZAP-70 localized within close proximity to the membrane are independent of the tonic signalling via KIR2DS1 (as evidenced by the same amount detected in cells transfected with wild-type receptor and signalling-deficient mutant in non-stimulatory conditions). Moreover, the levels of membrane-proximal ZAP-70 increase in response to KIR2DS1 ligation.

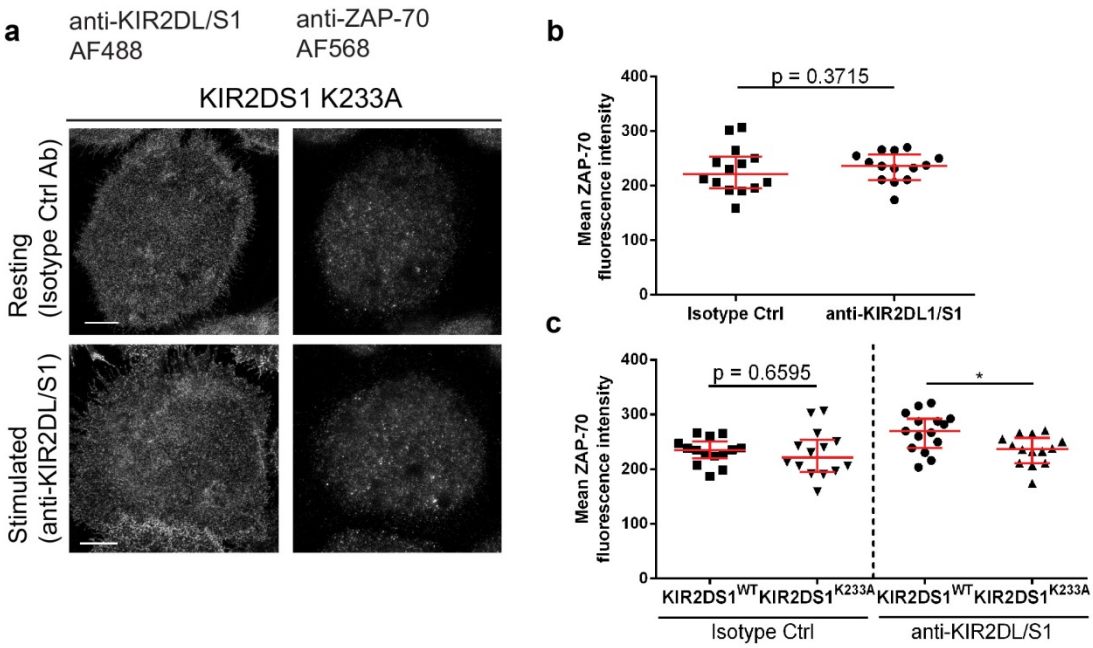

Figure 5.10 Imaging of endogenous ZAP-70 in unstimulated NKL/KIR2DS1^{K233A} cells and upon KIR2DS1 ligation.
Cells were fixed on the PLL-coated slides covered with either EB6 mAb or isotype-matched control antibody, permeabilized and stained with anti-HA murine mAb directly labelled with AF488 (left column in a) and anti-ZAP-70 rabbit antibody and secondary anti-rabbit antibody conjugated with AF568 (right column). Representative STED images are shown in (a). Mean intensity of ZAP-70-derived fluorescence was compared between cells incubated on either EB6 mAb or isotype control (b). Panel (c) compares mean intensity of ZAP-70-derived fluorescence between NKL/KIR2DS1^{K233A} and NKL/KIR2DS1-HA cells imaged in the same experiment using identical parameters. Each dot represents a value for one cell. Data are from 14 – 15 cells from two independent experiments. Horizontal lines and bars correspond to medians and interquartile range, respectively. * $p < 0.05$, Mann-Whitney test.

In similar experiments, quantitative comparison of the ZAP-70 pY319-derived fluorescence intensity in NKL/KIR2DS1-HA cells plated on isotype control and EB6 mAb demonstrated that upon ligation of KIR2DS1, the amount of membrane-proximal ZAP-70 pY319 was significantly increased (Figure 5.11 b). Importantly, this change was not observed for NKL/KIR2DS1^{K233A} cells, suggesting that the increased frequency of ZAP-70 phosphorylation was specifically related to the KIR2DS1-mediated signalling (Figure 5.12 b). Consistently, the mean intensity of ZAP-70 pY319-derived fluorescence was not statistically different between NKL/KIR2DS1-HA and NKL/KIR2DS1^{K233A} under resting conditions, but was statistically higher for NKL/KIR2DS1-HA when both cell lines were incubated on EB6-coates slides (Figure 5.12 c).

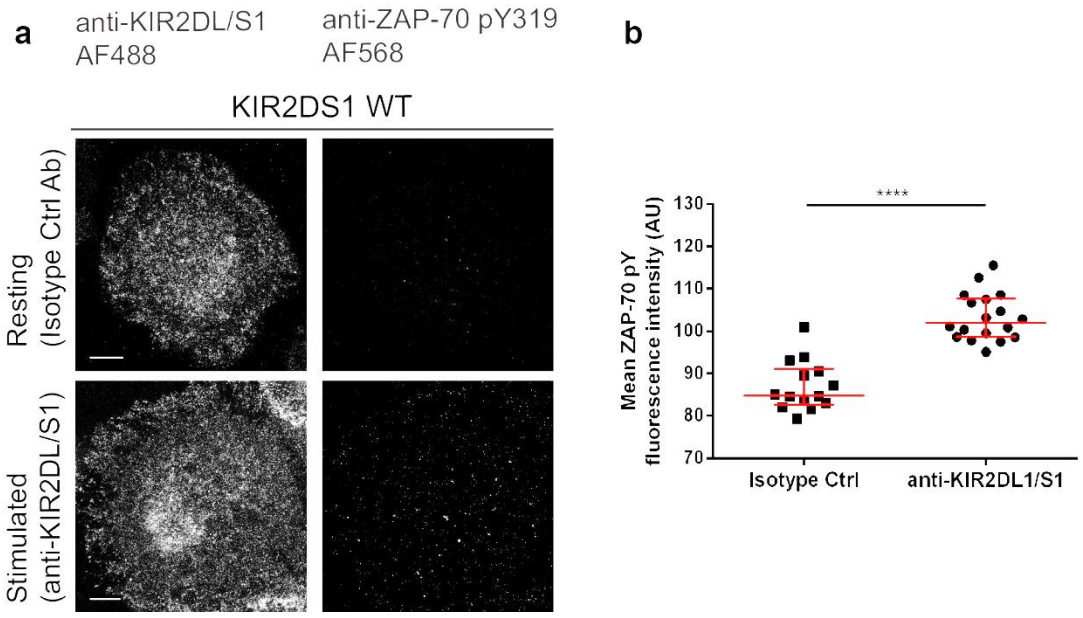

Figure 5.11 Imaging of ZAP-70 pY319 in unstimulated NKL/KIR2DS1-HA cells and upon KIR2DS1 ligation.
Cells were fixed on the PLL-coated slides covered with either EB6 mAb or isotype-matched control antibody, permeabilized and stained with anti-HA murine mAb directly labelled with AF488 (left column in a) and anti-ZAP-70 pY319 rabbit antibody and secondary anti-rabbit antibody conjugated with AF568 (right column). Representative STED images are shown in (a). Mean intensity of ZAP-70 pY319-derived fluorescence was compared between cells incubated on either EB6 mAb or isotype control (b). Each dot represents a value for one cell. Data are from 13 – 18 cells from 2 independent experiments. Horizontal lines and bars correspond to medians and interquartile range, respectively. **** $p < 0.0001$, Mann-Whitney test by ranks.

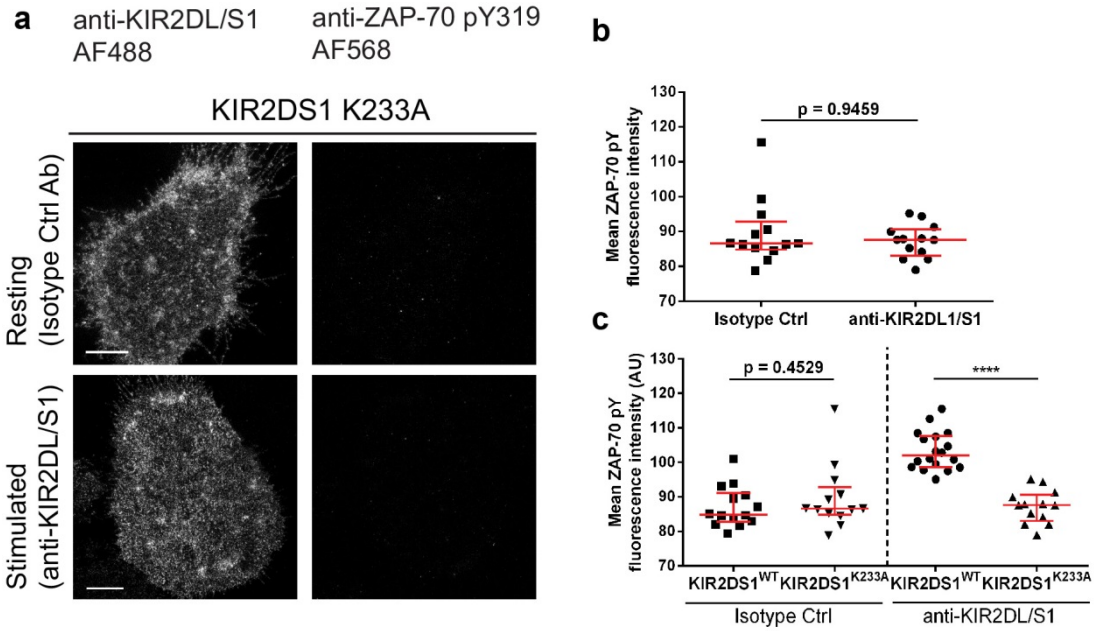

Figure 5.12 Imaging of endogenous ZAP-70 pY319 in unstimulated NKL/KIR2DS1^{K233A} cells and upon KIR2DS1 ligation.
Cells were fixed on the PLL-coated slides covered with either EB6 mAb or isotype-matched control antibody, permeabilized and stained with anti-HA murine mAb directly labelled with AF488 (left column in a) and anti-ZAP-70 pY319 rabbit antibody and secondary anti-rabbit antibody conjugated with AF568 (right column). Representative STED images are shown in (a). Mean intensity of ZAP-70 pY319-derived fluorescence was compared between cells incubated on either EB6 mAb or isotype control (b). Panel (c) compares mean intensity of ZAP-70 pY319-derived fluorescence between NKL/KIR2DS1^{K233A} and NKL/KIR2DS1-HA cells imaged in the same experiment using identical parameters. Each dot represents a value for one cell. Data are from cells from 13 – 18 cells from two independent experiments. Horizontal lines and bars correspond to medians and interquartile range, respectively. **** $p < 0.0001$, Mann-Whitney test by ranks.

Together, these experiments establish that more ZAP-70 is recruited to the proximity of plasma membrane in response to KIR2DS1 ligation, where the kinase is phosphorylated on Y536.

5.3.4 Two-colour imaging of nanometre-scale organization of KIR2DS1 and ZAP-70.

To establish whether similar to the interaction of KIR2DS1 and DAP12 clusters, size of KIR2DS1 cluster also affects its ability to recruit and activate ZAP-70, two-channel STED images of KIR2DS1 and ZAP-70 or ZAP-70 pY319 in NKL/KIR2DS1-HA cells under resting conditions and upon KIR2DS1 ligation were analysed in the way described in section 5.3.2. Briefly, distribution of sizes of KIR2DS1 clusters associated with ZAP-70 was compared against the distribution of all KIR2DS1 cluster sizes in a particular cell by splitting the clusters into tertiles, according to their measured area (Figure 5.13).

The likelihood of interaction with ZAP-70 cluster increased with the area of KIR2DS1 cluster, both in resting cells and upon KIR2DS1 ligation (Figure 5.13 a – b and e – f), with approximately half of detected contacts involving KIR2DS1 clusters falling in the last size bin. The same analysis of simulated data sets, where positions of ZAP-70 clusters were randomized within the cell, resulted in a very similar distribution of results. Thus, formation of bigger clusters promotes the interaction with ZAP-70 by increasing the chance of encountering membrane-proximal ZAP-70 clusters, both constitutively present at the membrane (as indicated by experiments on resting cells, Figure 5.13 c) and recruited to the membrane upon activation (Figure 5.13 f). In addition, comparison of ZAP-70 fluorescence localized in the vicinity of KIR2DS1 clusters of different sizes has shown that total amount of ZAP-70 associated with KIR2DS1 clusters also increases with the cluster size and is generally higher in cells incubated on EB6 mAb, consistent with the observed increase in membrane-proximal ZAP-70 levels after KIR2DS1 ligation (Figure 5.13 h).

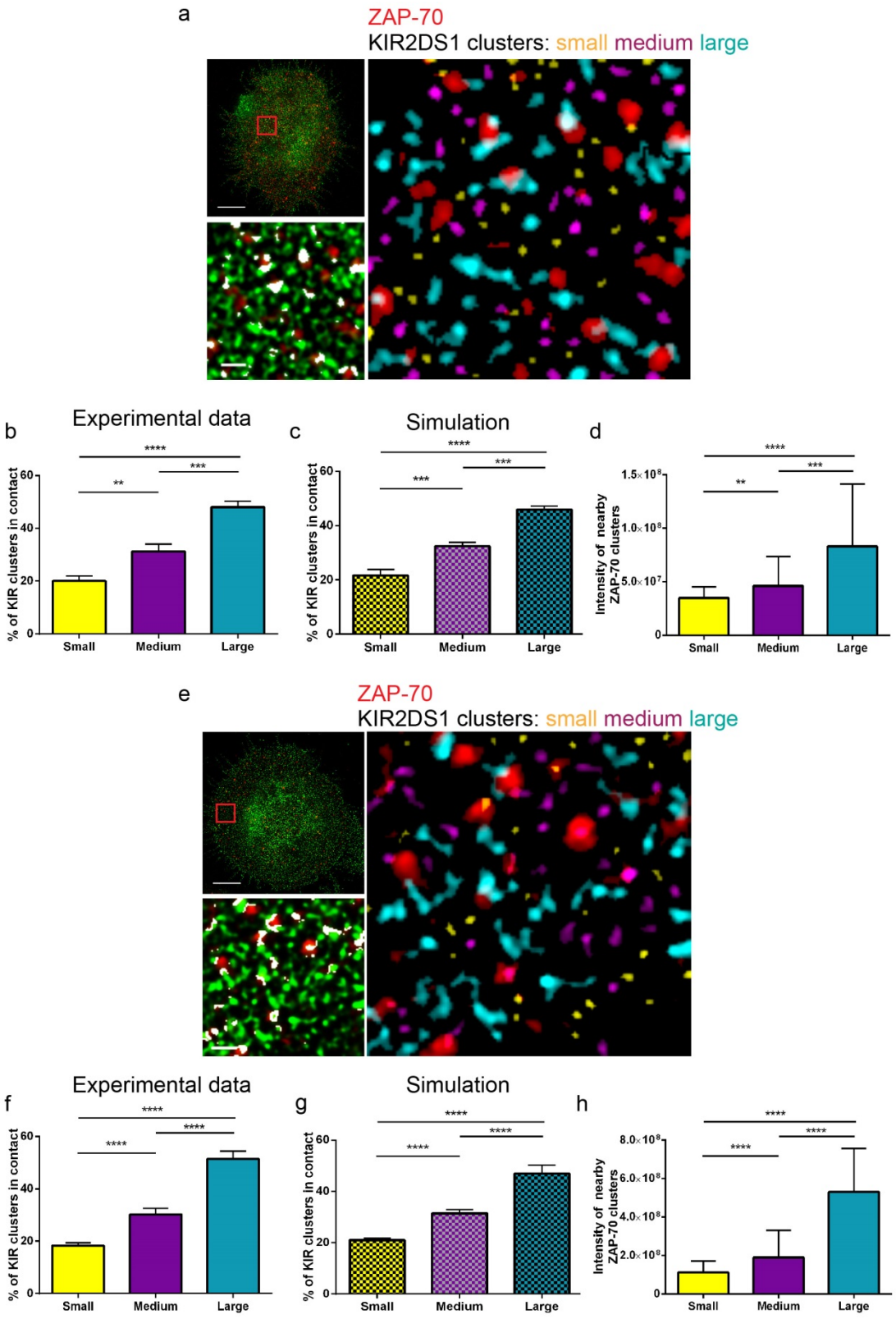

Figure 5.13 . Importance of KIR2DS1 nanocluster size for association with ZAP-70 clusters.

NKL/KIR2DS1-HA cells were incubated for 5 min on (a –d) isotype control mAb- or (e – h) anti-KIR2DL/S1 mAb-coated slides, fixed, stained with fluorescently labelled antibodies and imaged by two-channel STED microscopy. (a and e) STED images of cell membrane with KIR2DS1 (green) and ZAP-70 (red) visualized and overlaid are shown together with zoomed-in 3 × 3 µm

regions (red boxes in STED images) in which overlapping pixels are marked in white. The same regions are shown in the right side with KIR2DS1 clusters color-coded according to size. Each size bin corresponds to a third of all KIR2DS1 clusters. (b – c and f - g) Fractions of all KIR2DS1 clusters associated with ZAP-70 clusters that fall into each size group calculated for the cells imaged by STED (b and f) compared to randomized data sets in which positions of KIR2DS1 clusters were conserved and positions of ZAP-70 clusters were randomized within the boundaries of cell area (d and g). (d and h) Sum of intensity of ZAP-70 clusters found nearby KIR2DS1 clusters from specified size bins. Bars and errors represent the medians and interquartile range. The data is from 29 (IgG1) and 39 (EB6) cells from three independent experiments. In (c and g), 5 rounds of randomization were run per cell and a mean value was used as a final data point for each cell. ** $p < 0.01$, *** $p < 0.001$, **** $p < 0.0001$, row-matched Friedman test with Dunn's post-test.

Similar analysis was then performed for clusters of KIR2DS1 and ZAP-70 pY319 visualized in NKL/KIR2DS1-HA cells. In resting cells, staining of ZAP-70 pY319 displayed intensity too low for reliable identification of clusters in STED images. Thus, this interaction could only be characterized in detail for the cells activated through KIR2DS1 (Figure 5.14). This has shown that, similar to total ZAP-70, phosphorylated form of ZAP-70 is more often found in association with larger KIR2DS1 clusters. Over 50% of all KIR2DS1-ZAP-70 pY319 cluster contacts involved the KIR2DS1 clusters from the third tertile of cluster sizes (Figure 5.13 a – b). The overall distribution of sizes of KIR2DS1 clusters associated with phospho-ZAP-70 was again very similar between the experimental data and corresponding randomized datasets (Figure 5.13 c). Moreover, as indicated by differences in the fluorescence intensity, the total amount of associated ZAP-70 pY319 also increased with the area of KIR2DS1 cluster (Figure 5.13 d).

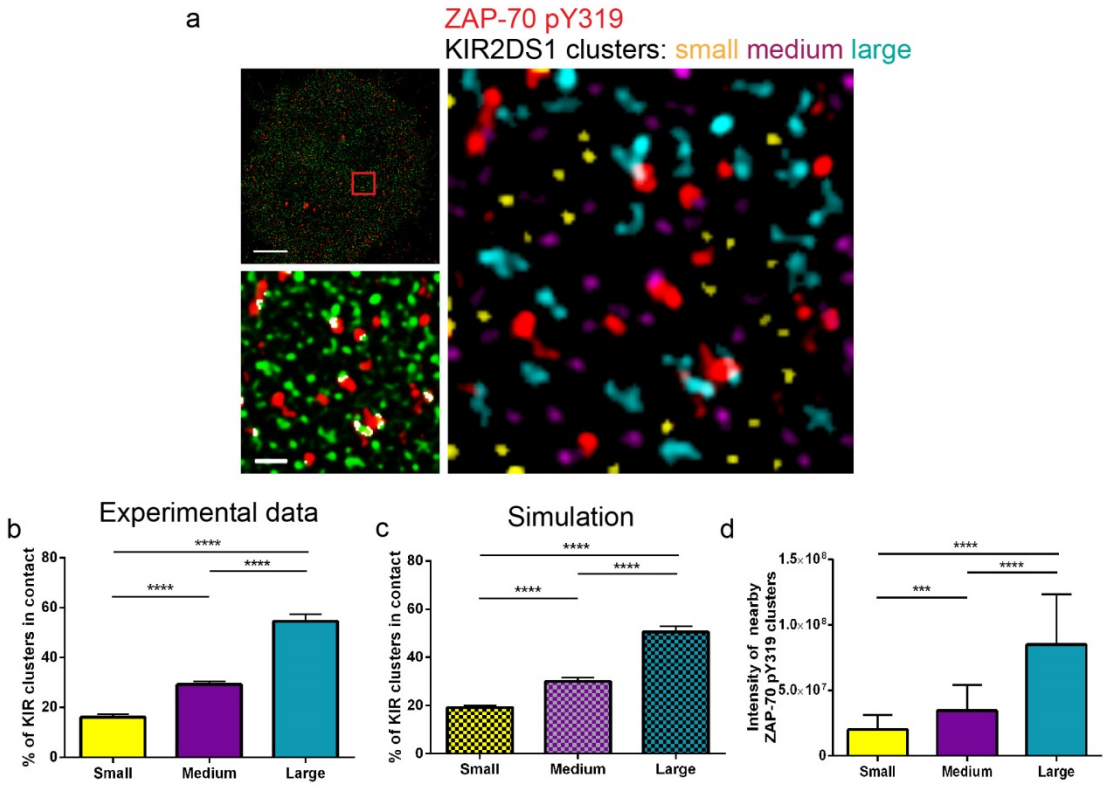

Figure 5.14 Importance of KIR2DS1 nanocluster size for association with ZAP-70 pY319 clusters.

NKL/KIR2DS1-HA cells were incubated for 5 min on anti-KIR2DL/S1 mAb-coated slides, fixed, stained with fluorescently labelled antibodies and imaged by two-channel STED microscopy. (a) STED image of cell membrane with KIR2DS1 (green) and ZAP-70 pY319 (red) visualized and overlaid is shown together with zoomed-in 3 × 3 µm region (red box in STED image) in which overlapping pixels are marked in white. The same region is shown in the right side with KIR2DS1 clusters color-coded according to size. Each size bin corresponds to a third of all KIR2DS1 clusters. (b – c) Fractions of all KIR2DS1 clusters associated with ZAP-70 pY319 clusters that fall into each size group calculated for the cells imaged by STED (b) compared to randomized data sets in which positions of KIR2DS1 clusters were conserved and positions of ZAP-70 pY319 clusters were randomized within the boundaries of cell area (c). (e) Sum of intensity of ZAP-70 pY319 clusters found nearby KIR2DS1 clusters from specified size bins. Bars and errors represent the medians and interquartile range. The data is from 36 cells from three independent experiments. In (c), 5 rounds of randomization were run per cell and a mean value was used as a final data point for each cell. *** $p < 0.001$, **** $p < 0.0001$, row-matched Friedman test with Dunn's post-test.

Together, these data suggest that larger KIR2DS1 clusters are preferentially found in association with clusters of ZAP-70 and its activated form, and ZAP-70 clusters found in contact with larger KIR2DS1 clusters contain more protein. The advantage of larger clusters can be accounted for by the increased probability of larger clusters forming interaction with independently distributed ZAP-70 clusters.

5.3.5 Imaging of endogenous SHP-1 in NKL cells transfected with wild-type and mutated variants of KIR2DL1.

The next aim was to investigate whether or not the nanocluster size was important for KIR2DL1 signalling. For this, localization of SHP-1 phosphatase, which is the most proximal molecule engaged in the signalling pathway of KIR2DL1 [109, 111], was analysed in relation to the position of KIR2DL1 clusters of different sizes. To establish whether the size of clusters could affect SHP-1 activation, SHP-1 pY536 was chosen as another target for two-colour imaging studies. Phosphorylation site Y536 has been shown to be the positive regulator of SHP-1 activity [351]. As previously, the specificity of commercially available antibodies against SHP-1 and SHP-1 pY536 was verified by comparing the staining intensity in NKL/KIR2DL1-HA cells fixed on slides covered with EB6 mAb and stained with a rat anti-SHP-1 mAb or rabbit anti-SHP-1 pY536 antibody, or appropriate control antibodies. All primary antibodies were targeted by the specific secondary antibodies conjugated with AF568. Cells were then imaged by STED microscopy using identical parameters. The comparison of fluorescence derived from the anti-SHP-1 or anti-SHP-1 pY536 antibodies and control antibodies is presented in the Figures 5.15 and 5.16. For the antibody targeting total SHP-1, bright fluorescent signal was present in the plane of the cell contact with glass slide. In contrast, the fluorescence was virtually undetectable in STED images of the cells stained with isotype control antibody. Clusters of SHP-1 were readily visible in raw STED images of cells stained with anti-SHP-1 mAb and were not present in the same cells stained with the unspecific control antibody (Figure 5.15).

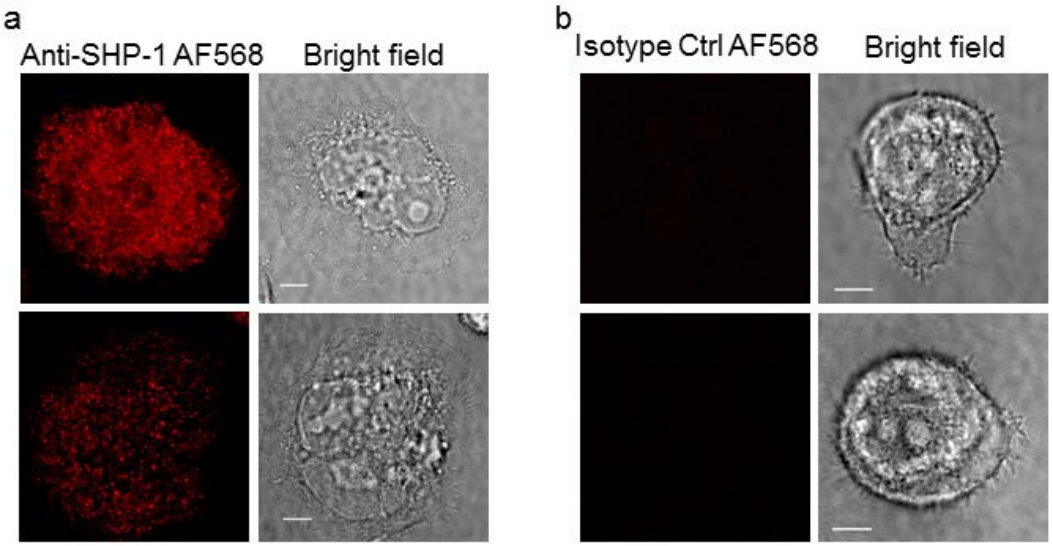

Figure 5.15 Control experiment for the specificity of anti-SHP-1 antibody binding. NKL/KIR2DL1-HA cells were plated on PLL-coated slides covered with EB6 mAb, fixed, permeabilized, stained with an anti-SHP-1 rat mAb (a), or appropriate isotype control antibody (b), followed by the anti-rat secondary antibody conjugated with AF 568 and imaged by STED microscopy using identical parameters. Bright-field and fluorescence images are shown for two cells representative of n >20 cells stained with the anti-SHP-1 antibody (a) and isotype control antibody (b). Brightness was adjusted in an identical way in all images. Scale bars 5 µm in bright-field images.

In cells stained with anti-SHP-1 pY536 antibody, fluorescent signal was mostly limited to distinct bright clusters, which were absent in the images of cells stained with the control antibody (Figure 5.16). In summary, these control experiments established that total SHP-1 and SHP-1 pY536 can be successfully visualized using commercially available antibodies.

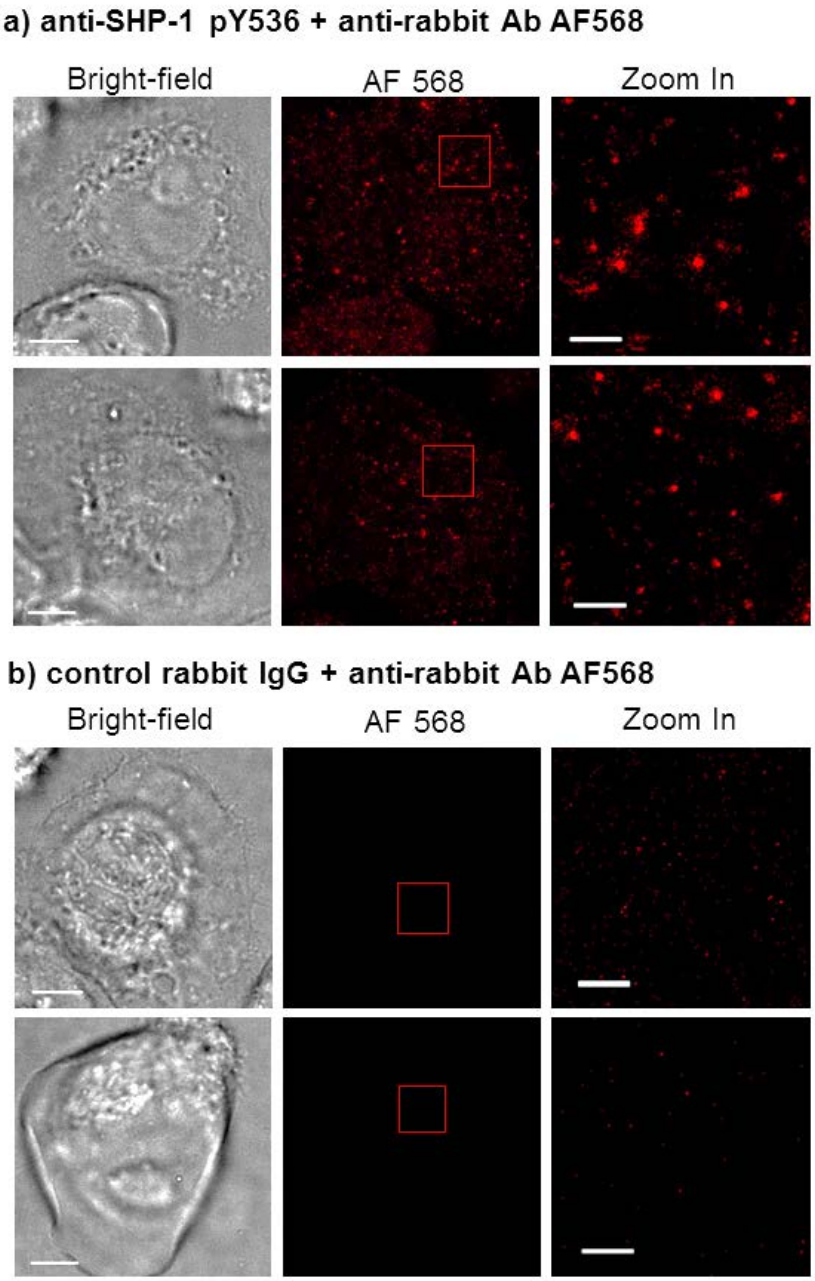

Figure 5.16 Control experiment for the specificity of anti-SHP-1 pY539 antibody binding.

NKL/KIR2DL1-HA cells were plated on PLL-coated slides covered with EB6 mAb, fixed, permeabilized, stained with an anti-SHP-1 pY536 rabbit antibody (a), or appropriate isotype control antibody (b), followed by the anti-rabbit secondary antibody conjugated with AF 568 and imaged by STED microscopy using identical parameters. Bright-field and fluorescence images are shown for two cells representative of n > 20 cells stained with the anti-SHP-1 pY536 antibody (a) and isotype control antibody (b). Zoomed-in 5 µm x 5 µm regions are shown in the right column (red boxes in the STED images). Brightness was adjusted in an identical way in all images. Scale bars 5 µm in bright-field images and 1 µm in zoomed-in regions.

To quantitatively compare the amount of membrane proximal SHP-1 and SHP-1 pY536 under resting and stimulatory conditions, NKL/KIR2DL1-HA cells were fixed on the PLL-pre-coated slides coated with either EB6 mAb or control murine IgG1 antibody, permeabilized and stained with anti-HA murine mAb directly labelled with AF488 and anti-SHP-1 antibodies followed by the appropriate secondary antibodies conjugated with AF568. In parallel, cells transfected with a signalling-deficient KIR2DL1 in which both ITIM tyrosines were mutated, NKL/KIR2DS1$^{Y281A/Y311A}$, were treated in the same way. To directly compare the SHP-1 fluorescence intensity, all cells were imaged by STED microscopy using identical parameters. SHP-1 was found in the close proximity to the membrane under resting and stimulated conditions in both tested cell lines and its clustered organization could be readily observed in the raw STED images. Quantitative comparison of the mean intensity of SHP-1-derived fluorescence in resting NKL/KIR2DL1-HA cells and upon KIR2DL1 ligation, demonstrated that the total amount of SHP-1 found near the membrane is increased upon wild-type KIR2DL1 ligation (Figure 5.17 b).

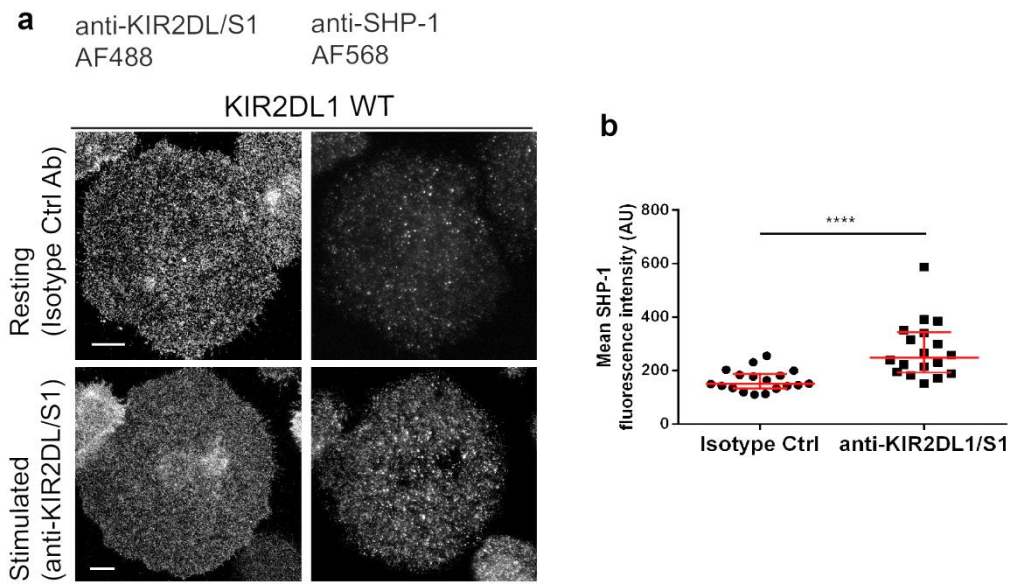

Figure 5.17 Imaging of endogenous SHP-1 in unstimulated NKL/KIR2DL1-HA cells and upon KIR2DL1 ligation.
Cells were fixed on the PLL-coated slides covered with either EB6 mAb or isotype-matched control antibody, permeabilized and stained with anti-HA murine mAb directly labelled with AF488 (left column in a) and anti-SHP-1 rat mAb and secondary anti-rat antibody conjugated with AF568 (right column). Representative STED images are shown in (a). Mean intensity of SHP-1-derived fluorescence was compared between cells incubated on either EB6 mAb or isotype control (b). Each dot represents a value for one cell. Data are from 18 cells per condition from 2 independent experiments. Horizontal lines and bars correspond to medians and interquartile range, respectively. **** $p < 0.0001$, Mann-Whitney test by ranks.

No change was observed upon ligation of KIR2DL1$^{Y281A/Y311A}$ however, which was consistent with this mutant receptor being unable to transduce the signals (Figure 5.18 b). Under non-stimulatory conditions, no difference in the amount of total SHP-1 could be observed between cells transfected with wild-type or mutated receptor. In contrast, more SHP-1 was found at the membrane in NKL/KIR2DL1-HA cells incubated on EB6 mAb than in NKL/KIR2DL1$^{Y281A/Y311A}$ under the same stimulation (Figure 5.18 c). Together, these results suggest that the base-line levels of SHP-1 localized within close proximity to the membrane are independent of the tonic signalling via KIR2DL1 (as evidenced by the same amount detected in cells transfected with wild-type receptor and signalling-deficient mutant in non-stimulatory conditions). Moreover, the levels of membrane-proximal SHP-1 increase in response to KIR2DL1 ligation.

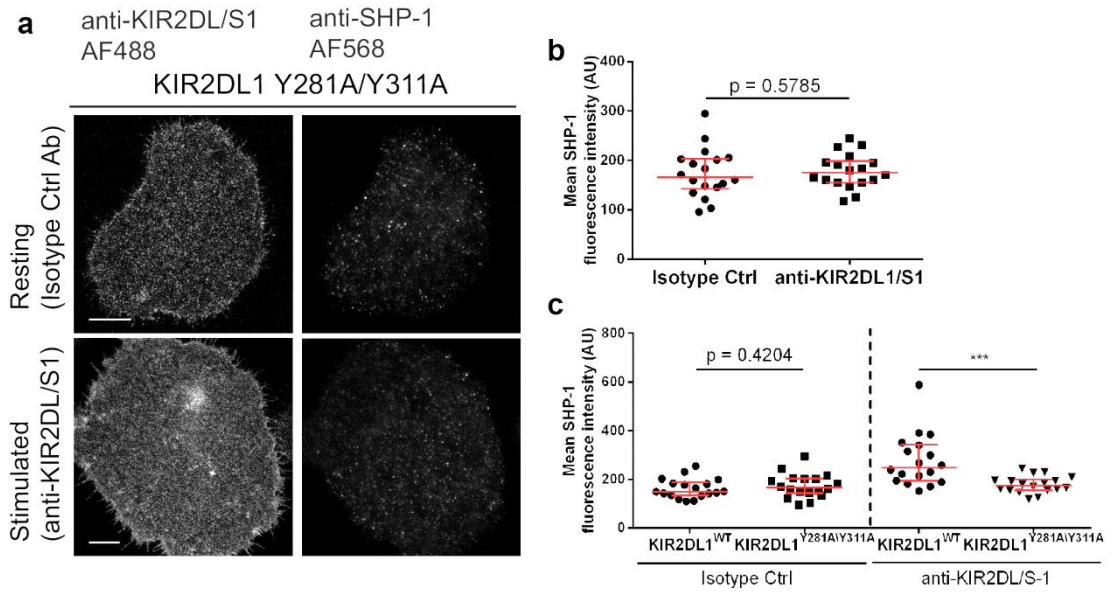

Figure 5.18 Imaging of endogenous SHP-1 in unstimulated NKL/KIR2DL1$^{Y281A/Y311A}$ cells and upon KIR2DL1 ligation.
Cells were fixed on the PLL-coated slides covered with either EB6 mAb or isotype-matched control antibody, permeabilized and stained with anti-HA murine mAb directly labelled with AF488 (left column in a) and anti-SHP-1 rat mAb and secondary anti-rat antibody conjugated with AF568 (right column). Representative STED images are shown in (a). Mean intensity of SHP-1-derived fluorescence was compared between cells incubated on either EB6 mAb or isotype control (b). Panel (c) compares mean intensity of SHP-1-derived fluorescence between NKL/KIR2DL1$^{Y281A/Y311A}$ and NKL/KIR2DL1-HA cells imaged in the same experiment using identical parameters. Each dot represents a value for one cell. Data are from 18 cells per condition from 2 independent experiments. Horizontal lines and bars correspond to medians and interquartile range, respectively. *** $p < 0.001$, Mann-Whitney test by ranks.

A comparison of SHP-1 pY536-derived fluorescence intensity in NKL/KIR2DL1-HA cells plated on isotype control or EB6 mAb demonstrated that upon ligation of KIR2DL1, the mean fluorescence of anti-SHP-1 pY536 staining significantly increases (Figure 5.19 b). However, no change in the signal intensity was observed upon ligation

of KIR2DL1$^{Y281A/Y311A}$, showing that phosphorylation of SHP-1 was specifically triggered by the KIR2DL1 signalling (Figure 5.20 b). In line with this, the mean intensity of SHP-1 pY536-derived fluorescence was not statistically different between NKL/KIR2DL1-HA and NKL/KIR2DL1$^{Y281A/Y311A}$ cells incubated on the control antibody, but was higher for NKL/KIR2DL1-HA when both cell lines were incubated on EB6-coates slides (Figure 5.20 c).

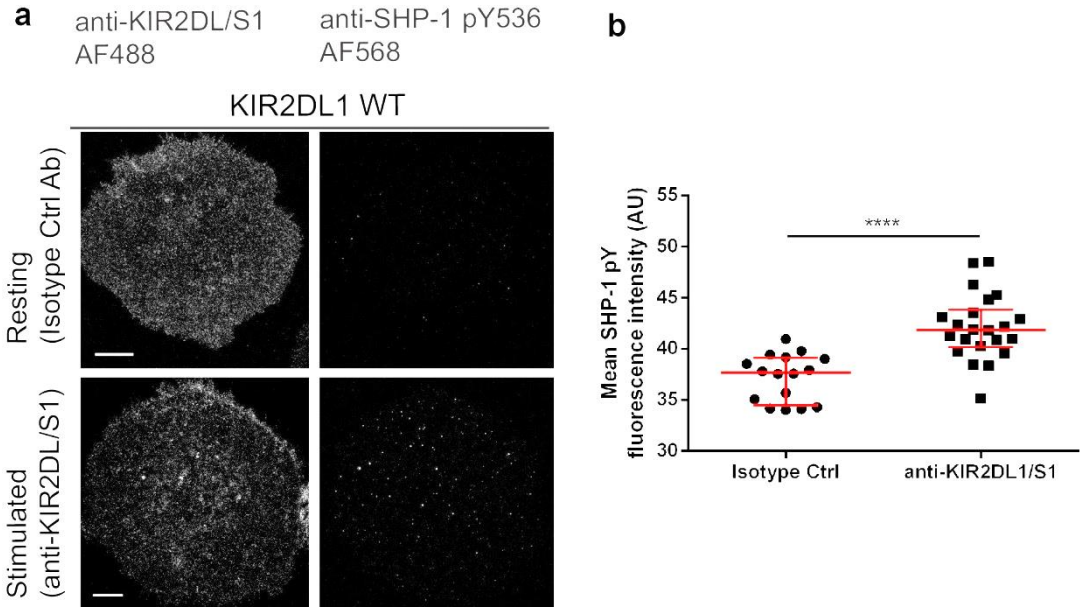

Figure 5.19 Imaging of SHP-1 pY536 in unstimulated NKL/KIR2DL1-HA cells and upon KIR2DL1 ligation.
Cells were fixed on the PLL-coated slides covered with either EB6 mAb or isotype-matched control antibody, permeabilized and stained with anti-HA murine mAb directly labelled with AF488 (left column in a) and anti-SHP-1 pY536 rabbit antibody and secondary anti-rabbit antibody conjugated with AF568 (right column). Representative STED images are shown in (a). Mean intensity of SHP-1 pY536-derived fluorescence was compared between cells incubated on either EB6 mAb or isotype control (b). Each dot represents a value for one cell. Data are from 14 - 22 cells from 2 independent experiments. Horizontal lines and bars correspond to medians and interquartile range, respectively. ns non-significant, **** $p < 0.0001$, Mann-Whitney test.

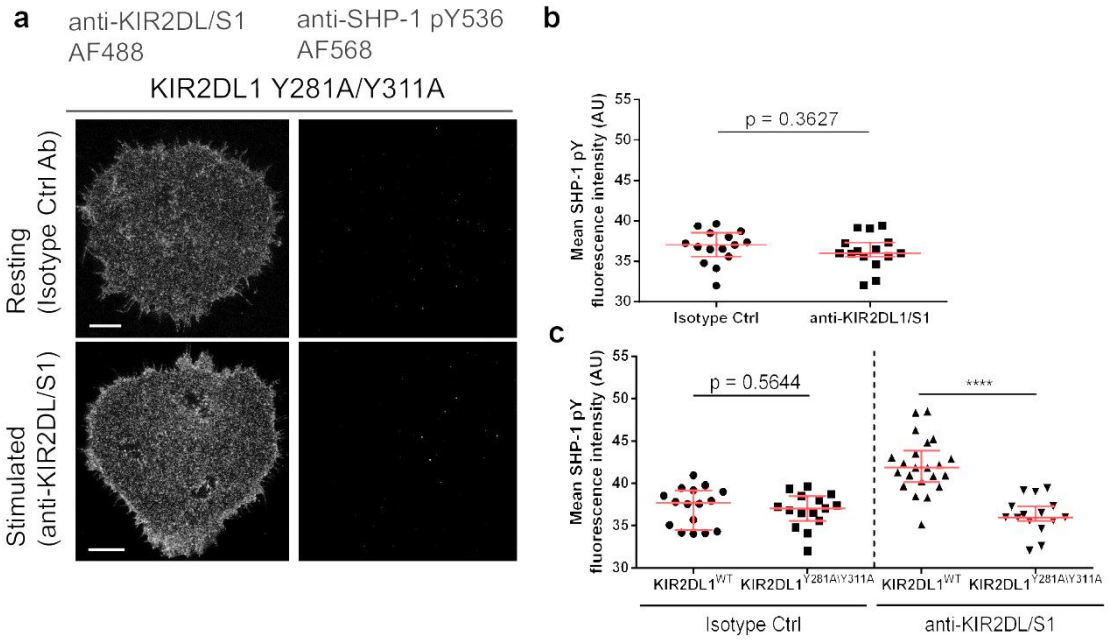

Figure 5.20 Imaging of endogenous SHP-1 pY536 in unstimulated NKL/KIR2DL1$^{Y281A/Y311A}$ cells and upon KIR2DL1 ligation.
Cells were fixed on the PLL-coated slides covered with either EB6 mAb or isotype-matched control antibody, permeabilized and stained with anti-HA murine mAb directly labelled with AF488 (left column in a) and anti-SHP-1 pY536 rabbit mAb and secondary anti-rabbit antibody conjugated with AF568 (right column). Representative STED images are shown in (a). Mean intensity of SHP-1 pY536-derived fluorescence was compared between cells incubated on either EB6 mAb or isotype control (b). Panel (c) compares mean intensity of SHP-1 pY536-derived fluorescence between NKL/KIR2DL1$^{Y281A/Y311A}$ and NKL/KIR2DL1-HA cells imaged in the same experiment using identical parameters. Each dot represents a value for one cell. Data are from cells from 14 cells per condition from 2 independent experiments. Horizontal lines and bars correspond to medians and interquartile range, respectively. **** $p < 0.0001$, Mann-Whitney test.

Together, these experiments indicate that the SHP-1 phosphatase is phosphorylated in response to the KIR2DL1 ligation and this change can be detected by STED microscopy.

5.3.6 Two-colour imaging of nanometre-scale organization of KIR2DL1 and SHP-1.

Two-channel STED images of KIR2DL1 and SHP-1 or SHP-1 pY536 were then used to investigate whether the size of KIR2DL1 clusters is important for their association with SHP-1 and activation of phosphatase. For this, size distribution of KIR2DL1 clusters associated with clusters of SHP-1 or its phosphorylated form was compared against the distribution of sizes of all KIR2DL1 clusters detected in the same cell. This demonstrated that largest KIR2DL1 clusters were most often found in association with clusters of SHP-1, both in resting NKL/KIR2DL1-HA cells and upon incubation on EB6 mAb (Figure 5.21 b and f), and SHP-1 clusters found in their vicinity contained more

SHP-1 (Figure 5.21 d and h). Comparison with simulated datasets, in which positions of SHP-1 clusters were randomized, indicated that this could be accounted for by larger clusters forming more contacts with independently distributed SHP-1 clusters, both in the absence of stimulation and upon KIR2DL1 ligation, when more SHP-1 is transported to the membrane.

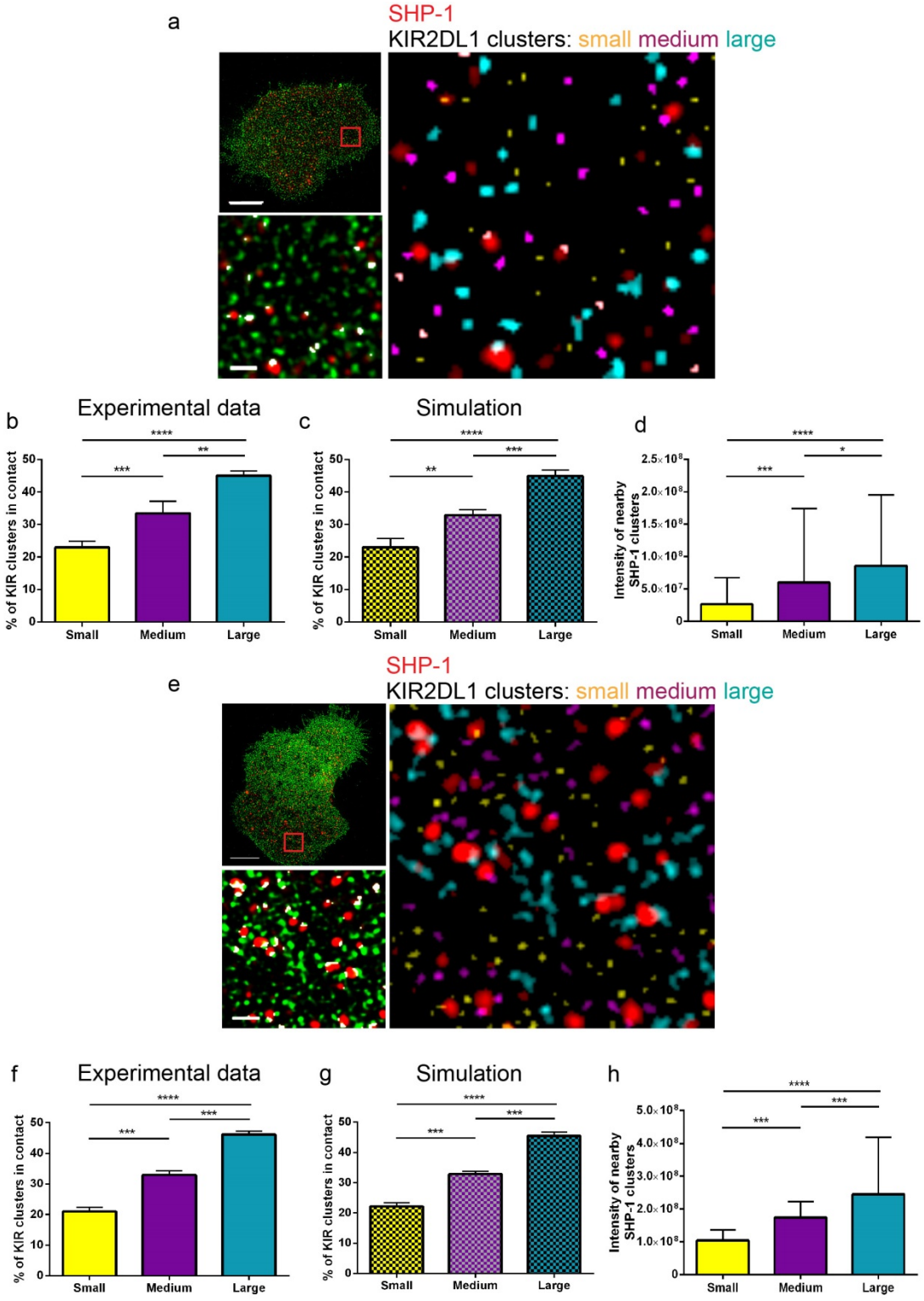

Figure 5.21 Importance of KIR2DL1 nanocluster size for association with SHP-1 clusters.

NKL/KIR2DL1-HA cells were incubated for 5 min on (a –d) isotype control mAb- or (e – h) anti-KIR2DL/S1 mAb-coated slides, fixed, stained with fluorescently labelled antibodies and imaged by two-channel STED microscopy. (a and e) STED images of cell membrane with KIR2DL1 (green) and SHP-1 (red) visualized and overlaid are shown together with zoomed-in 3 µm × 3 µm regions (red boxes in STED images) in which overlapping pixels are marked in white. The same regions are shown in the right side with KIR2DL1 clusters color-coded according to size.

Each size bin corresponds to a third of all KIR2DL1 clusters. (b – c and f - g) Fractions of all KIR2DL1 clusters associated with SHP-1 clusters that fall into each size group calculated for the cells imaged by STED (b and f) compared to randomized data sets in which positions of KIR2DL1 clusters were conserved and positions of SHP-1 clusters were randomized within the boundaries of cell area (c and g). (d and h) Sum of intensity of SHP-1 clusters found nearby KIR2DL1 clusters from specified size bins. Bars and errors represent the medians and interquartile range. The data is from 27 (IgG1) and 30 (EB6) cells from three independent experiments. In (c and g), 5 rounds of randomization were run per cell and a mean value was used as a final data point for each cell. * $p < 0.05$, ** $p < 0.01$, *** $p < 0.001$, **** $p < 0.0001$, row-matched Friedman test with Dunn's post-test.

Association between KIR2DL1 and activated form of SHP-1 phosphorylated on Y536 residue was then investigated in analogical way, except for the analysis being only possible in cells stimulated on anti-KIR2DL/S1 mAb. In resting cells, clusters of SHP-1 pY536 could not be identified due to too low intensity of overall staining. In activated cells however, the results describing interactions were similar to what was observed for the total SHP-1 – phosphorylated form of phosphatase was also preferably found in contact with the largest KIR2DL1 clusters, as indicated by both frequency of contacts and intensity of SHP-1 pY536 fluorescence increasing together with the area of KIR2DL1 clusters (Figure 5.22 b and d). The relative frequency of KIR2DL1 clusters from different size bins contacting clusters of SHP-1 pY536 was similar between the experimental data and corresponding randomized datasets (Figure 5.22 c).

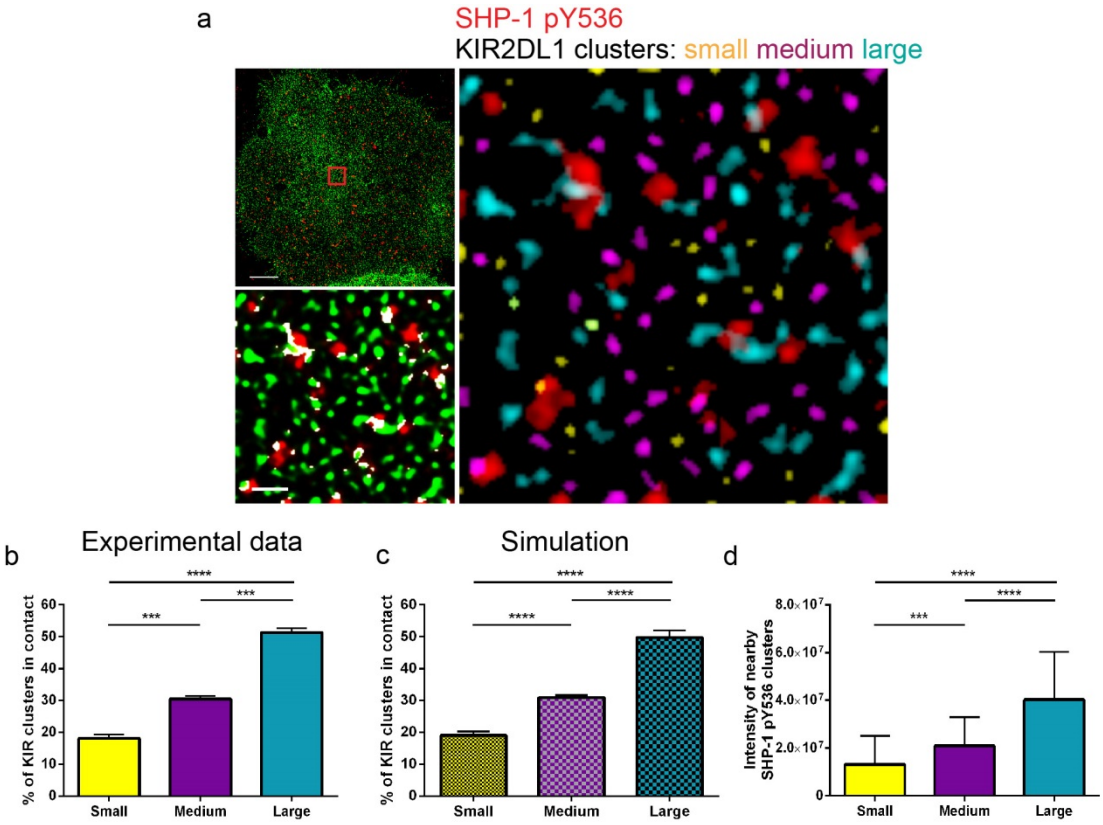

Figure 5.22 Importance of KIR2DL1 nanocluster size for association with SHP-1 pY536 clusters.
NKL/KIR2DL1-HA cells were incubated for 5 min on anti-KIR2DL/S1 mAb-coated slides, fixed, stained with fluorescently labelled antibodies and imaged by two-channel STED microscopy. (a) STED image of cell membrane with KIR2DL1 (green) and SHP-1 pY536 (red) visualized and overlaid is shown together with zoomed-in 3 × 3 µm region (red box in STED image) in which overlapping pixels are marked in white. The same region is shown in the right side with KIR2DL1 clusters color-coded according to size. Each size bin corresponds to a third of all KIR2DL1 clusters. (b – c) Fractions of all KIR2DL1 clusters associated with SHP-1 pY536 clusters that fall into each size group calculated for the cells imaged by STED (b) compared to randomized data sets in which positions of KIR2DL1 clusters were conserved and positions of SHP-1 pY536 clusters were randomized within the boundaries of cell area (c). (d) Sum of intensity of SHP-1 pY536 clusters found nearby KIR2DS1 clusters from specified size bins. Bars and errors represent the medians and interquartile range. The data is from 33 cells from three independent experiments. In (c), 5 rounds of randomization were run per cell and a mean value was used as a final data point for each cell. *** $p < 0.001$, **** $p < 0.0001$, row-matched Friedman test with Dunn's post-test.

In summary, the above results suggest that larger KIR2DL1 clusters preferentially interact with clusters of SHP-1 and are more often found in association with its activated form. Furthermore, SHP-1 clusters found in contact with larger KIR2DL1 clusters contain more protein. Comparison with randomized data indicates that this could be accounted for by increased probability of larger clusters contacting independently distributed SHP-1 clusters.

5.4 Discussion

5.4.1 Summary of results

The aim of this chapter was to investigate whether clustering of KIR2DL1 and KIR2DS1 at the surface of NK cells is important for the molecular function of these receptors. To this end, two-channel super-resolution microscopy was used to directly visualize the organization of KIR2DL1 or KIR2DS1 and the molecules engaged in their downstream signalling in resting NK cells and upon ligation of KIR. These experiments led to the following conclusions:

- Upon ligation of KIR2DS1, endogenous DAP12 is recruited to the plasma membrane. Disruption of KIR2DS1-DAP12 complex results in less DAP12 being present at the surface of NKL cells, both in resting conditions and upon KIR2DS1 ligation.
- In resting NK cells, clusters of KIR2DS1 and DAP12 display only limited overlap at the membrane, with most of the interactions occurring at the edges of clusters. However, they mix to a greater extent upon ligation of KIR2DS1.
- Ligation of KIR2DS1 leads to an increase in the size of this receptor clusters. The largest KIR2DS1 clusters form contacts with DAP12 more often than the smaller ones.
- The amount of membrane-proximal ZAP-70 kinase increases and the Y319 residue of ZAP-70 is phosphorylated in response to KIR2DS1 ligation.
- The largest clusters of KIR2DS1 are more often associated with clusters of ZAP-70 and its activated form.
- The amount of membrane-proximal SHP-1 phosphatase increases and SHP-1 is phosphorylated on the Y536 residue upon KIR2DL1 ligation.
- The largest clusters of KIR2DL1 are more often associated with clusters of SHP-1 and its activated form.

5.4.2 Relation to earlier studies

Studying of nanometre-scale organization of proteins engaged in immune cell signalling is a relatively new field of research and especially the link between the nanometre-scale arrangement of receptors and regulation of immune cells function has not been thoroughly explored. Nevertheless, a great complexity of the organization-signalling interplay is already becoming apparent. The work published so far identified multiple ways in which nanometre-scale clustering might control the signalling and

showed that clustering may increase sensitivity of signalling through some receptors (i.e. TCR [349]) but also hinder the signalling of others (i.e. BCR [348]).

For KIR2DL1, increased self-association has been proposed to enhance the signalling. Specifically, according to Kumar *et al*., H36A substitution in the KIR2DL1 sequence, which results in enhanced self-association of KIR2DL1 in the membrane, is also associated with a constitutive recruitment of SHP-1 phosphatase [333]. This was suggested to be a consequence of constitutive phosphorylation detected for the more self-associated mutant receptor. The H36A substitution in the KIR2DL1 sequence also seemed to lower the threshold for inhibition of lysis of HLA-Cw4-positive target cells. This was demonstrated by the experiments employing the 721.221-HLA-Cw4 cell line stably expressing an inhibitor of TAP, in which the amount of peptide-loaded HLA-Cw4 available to KIR2DL1 can be titrated by the addition of exogenous HLA-Cw4–specific peptide. In these experiments, KIR2DL1 H36A has been shown to more efficiently inhibit the target cell lysis when low concentrations of peptides were used. The inhibitory abilities of wild-type and mutant KIR2DL1 were similar when higher concentrations of peptides were loaded onto the cells, or when TAP-sufficient Cw4-positive targets were used. Together, these results suggest that H36A substitution in the KIR2DL1 sequence triggers constitutive phosphorylation of KIR2DL1 and recruitment of SHP-1 as well as renders the receptor more sensitive to low levels of the inhibitory ligands [333].

Despite the above study advocating the role for receptor association in enhancing the signalling, an actual arrangement of the mutant and wild-type receptor was not directly visualized in that study. Therefore, it is not clear what kind of changes in the protein organization is triggered by the H36A substitution. The assays used by the authors rely on the measurements of fluorescent signal triggered by the close proximity of two proteins and thus, the observed increase in the signal could be a result of different rearrangements. For example, only formation of KIR2DL1 dimers could be already sufficient to explain the changes observed by Kumar *et al*. Therefore, it does not seem clear that phenomenon described in the above study relates to the same level of protein association as the one described in this thesis and earlier studies using super-resolution microscopy to directly visualize the proteins nanometre-scale organization. In addition, the precise link between the change in clustering triggered by H36A substitution and strength of inhibition is obscured by the fact that although the changes described on a molecular lever seem to be irrespective of KIR2DL1 ligation, no difference in the wild-type and mutant receptor function can be observed in the absence of the ligand or when ligand is present at high densities.

Earlier work did not provide any clues about how the specific patterns of organization could affect the receptor signalling, i.e. whether formation of clusters of a certain size could be beneficial for the signal transduction and/or propagation. To my best knowledge, a direct relation between the size of KIR2DL1 clusters and the efficiency of SHP-1 recruitment and activation has never been explored before. The results presented in this chapter indicate that size of the cluster is important for signalling, as evidenced by larger KIR2DL1 and KIR2DS1 clusters being more often associated with downstream signalling molecules. In addition, the active phosphorylated forms of SHP-1 and ZAP-70 were more often found in the vicinity of larger KIR2DL1 and KIR2DS1 clusters, respectively.

Organization of KIR2DS1 at the surface of NK cells has never been studied before and consequently, nothing was known about the importance of the receptor clustering for KIR2DS1-mediated signalling. The two-colour imaging of KIR2DS1 and DAP12 unravelled that in resting cells nanoclusters of the two proteins only marginally overlap, and mix to a greater extent only after KIR2DS1 ligation. This suggested that propagation of signal is in this case associated with rearrangements of membrane proteins on nanometre scale. A convergence between nanoclusters of BCR and co-receptor CD19 was previously proposed to mediate signal amplification upon antigen stimulation of B cells [312]. Mattila *et al*. demonstrated that upon BCR stimulation, both BCR and CD19 become enriched within the signalling microclusters defined by localization of GFP-Syk [312]. Although the authors did not investigate whether BCR and CD19 clusters intermix within the microcluster boundaries or form contacts at the edges, their conclusion that bringing of BCR and CD19 together might be the mechanism of signal amplification is interesting and worth consideration. It seems feasible that mixing of KIR2DS1 and DAP12 clusters upon KIR2DS1 ligation could play a similar role in sustaining and amplification of signalling during the lifetime of the activating immune synapse.

5.4.3 Significance of presented results

Overall, the experiments presented in this chapter indicate that nanometre-scale organization of KIR2DL1 and KIR2DS1 and its changes might likely affect the thresholds and kinetics of signalling.

One example could be controlling of KIR2DS1 signalling through modification of the receptor association with DAP12. Assembly of activating KIR and DAP12 was suggested by the earlier studies to occur co-translationally. This was concluded from

the fact that KIR2DS2-DAP12 complexes could be co-precipitated from the lysate of COS cells, but were not formed in mixing experiments in which DAP12 and KIR chains had been translated separately and mixed prior to immunoprecipitation [346]. The fact that substitution of lysine 233 in KIR2DS1 sequence with alanine results in a decreased amount of DAP12 present at the plasma membrane is in line with this previously proposed scenario. It seems likely that the two proteins could be transported to the membrane as complexes, and therefore disruption of their interaction through the K233A mutation would impact transport of DAP12 to the membrane. It is interesting to speculate that this could be a mechanism of regulating the relative abundance of receptor and adaptor proteins at the membrane.

However, the arrangement of activating KIR and DAP12 after they have been inserted into the plasma membrane was never directly visualized. The results presented in this chapter indicate that both KIR2DS1 and DAP12 from nanoclusters at the surface of NK cells but perhaps surprisingly, clusters of these proteins display very limited overlap. Most of the contacts between KIR2DS1 and DAP12 clusters occur at the interfaces between them. Analysis of DAP12 association with differentially sized KIR2DS1 clusters showed that the likelihood of interaction between these protein clusters increases with increasing size of KIR2DS1 clusters. Interestingly, the frequency of small, medium and large KIR2DS1 clusters associating with DAP12 clusters closely resembled the result obtained for a simulated dataset, where positions of DAP12 clusters were randomized within the cell area. Together, this indicates that once the proteins have been incorporated into the membrane, the larger KIR2DS1 clusters would be more likely to form lateral contacts with DAP12 clusters by covering larger area.

When KIR2DS1 is ligated, the nanoclusters of KIR2DS1 and DAP12 further mix with each other and this also preferentially involves the largest KIR2DS1 clusters. Since large KIR clusters form more contacts with DAP12 already in the resting cells, it seems intuitive that mixing of clusters upon stimulation is most efficiently initiated within the areas of constitutive overlap. Furthermore, mean area of KIR2DS1 clusters increases upon the receptor ligation, which might serve to even further extend the interactions between KIR2DS1 and DAP12 clusters upon KIR2DS1 ligation. In addition, comparison of DAP12-derived fluorescence between resting and stimulated cells demonstrated that upon KIR2DS1 ligation, more DAP12 is recruited to the plasma membrane. If DAP12-containing vesicles were incorporated in the membrane in a homogenous or stochastic manner, larger KIR2DS1 clusters would again have increased chance of being encountered by the newly arriving DAP12 molecules.

The experiments presented in this chapter did not establish whether the increased overlap between KIR2DS1 and DAP12 clusters upon ligation of KIR2DS1 is triggered by mixing of pre-existing protein clusters or active transport of DAP12 to the membrane. In any case, these changes could serve to control the rate of signal amplification. In resting cells, clusters of KIR2DS1 and its adaptor DAP12 are in contact mostly at the interfaces. Since KIR2DS1 does not possess an ITAM, it can be assumed that in such arrangement, the receptors localized in the centre of cluster, without access to DAP12, are incapable of signalling. However, when nanoclusters of proteins mix with each other, more KIR2DS1 molecules would then associate with the adaptor and be capable of signalling. Thus, limited interaction between KIR2DS1 and DAP12 observed in resting cells might likely control the strength of signal at the onset of interaction with a target cell, and possibly serve to maintain a quiescent state until the threshold for activation is reached. When the ligand is encountered at sufficient levels to trigger the change in organization, increased mixing of KIR2DS1 and DAP12 clusters could provide a positive feedback-loop driving the signal propagation.

Furthermore, already in resting cells larger KIR clusters are more often found in contact with ZAP-70 clusters, which are constitutively present within the proximity of plasma membrane. Comparison with the corresponding simulated data where ZAP-70 clusters are randomly positioned showed that this can be accounted for by larger clusters forming more contacts with independently distributed ZAP-70 clusters. Such scenario is supported by the fact that abundance of ZAP-70 at the membrane is independent of KIR2DS1 tonic signalling, as evidenced by similar intensity of membrane-proximal ZAP-70-derived fluorescence observed in NKL cells transfected with wild-type KIR2DS1 and signalling-deficient KIR2DS1^{K233A}. It could be assumed that KIR2DS1 and ZAP-70 do not interact specifically in resting cells and thus, contacts between their clusters are likely to occur in a random manner.

Upon KIR2DS1 ligation, ZAP-70 clusters, as well as its activated form phosphorylated at Y536, are also more often found in association with largest KIR clusters. This could mean that upon ligation, KIR2DS1-DAP12 complex responds by simply engaging the nearest located signalling molecules, which were present in the vicinity of receptor prior to encountering of the ligand. Such scenario could reduce the time required for assembly of multicomponent complex necessary for signal transduction. It would also result in more ZAP-70 being phosphorylated within the biggest KIR clusters, which form more contacts with membrane-proximal ZAP-70 clusters prior to ligation. In line with this, in the above experiments more ZAP-70 pY319 was found in the vicinity of the largest clusters.

For KIR2DL1, clustering was previously suggested to enhance its signalling capacity by reducing the accessibility of self-associated KIR2DL1 ITIM to phosphatases, which constantly dephosphorylate wild-type KIR2DL1 in resting NK cells. This could explain why the ratio of molecules localized in clusters to monomers diffused in the membrane could be important for signalling. However, this hypothesis does not explain why an increase in the size of KIR2DL1 clusters would promote the association with SHP-1 clusters. Data presented in this chapter suggest that the influence of KIR2DL1 cluster size on downstream signalling is mediated through a similar mechanism as for KIR2DS1. Similar to ZAP-70, clusters of SHP-1 are constitutively present in the proximity of the plasma membrane and thus, covering a larger area by KIR2DL1 cluster would increase a chance of its interaction with membrane-proximal clusters of SHP-1. In line with this, the relative frequency of small, medium and large KIR2DL1 clusters for which association with SHP-1 was detected in STED images was almost identical to the simulated dataset in which positions of SHP-1 clusters were randomized. After KIR2DL1 ligation, clusters of SHP-1 pY536 are also more often found in association with largest KIR clusters, and their enrichment around the KIR2DL1 clusters of different sizes is again very similar between the experimental data and randomized datasets. Together, this suggests that upon ligation, KIR2DL1 clusters interact with and phosphorylate the nearest located SHP-1 molecules, the probability of which is regulated by larger clusters more often remaining in contact with SHP-1 clusters prior to the KIR ligation.

In summary, the data presented in this chapter demonstrated that larger clusters of KIR2DL1 and KIR2DS1 preferentially associate with clusters of downstream signalling molecules. Comparison with the simulated data showed that this could be accounted for by the larger clusters more often overlapping with independently distributed clusters of downstream molecules. After the receptors ligation, activated forms of ZAP-70/SHP-1 are also more often found in the vicinity of the largest clusters and as indicated by comparison with randomized datasets, this also can be a result of clusters covering a larger area. Together, these observations lead to a model in which covering a larger area by a cluster promotes the interaction between the independently distributed clusters of receptors and downstream molecules and in turn, increases the chance that upon ligation a particular cluster of KIR will be in contact with signalling molecules and will rapidly trigger their phosphorylation.

5.4.4 Future directions

Experiments presented in this chapter provided some interesting insights into the spatial arrangement of receptors and downstream signalling molecules but also provoked a number of important questions. The observation that KIR2DS1 and DAP12 are not strictly co-clustered at the surface of NK cells is puzzling, considering that KIR and DAP12 chains were previously suggested to assemble co-translationally. It would be interesting to investigate whether these proteins might be transported to the membrane together, and then become rearranged within the cell membrane. For this, KIR2DS1 and DAP12 would have to be tagged with fluorescent proteins, such as GFP or its variants, to enable monitoring their trafficking within the cell by live-time imaging.

Relation between the cluster size and signalling efficiency is also worth studying in more detail. The mutated receptors created in this study displayed altered clustering phenotype, but were of limited use for studying the link between organization and function. KIR2DS1^{K233A} mutant is incapable of signalling independently of its organization, as the substitution disrupts KIR2DS1 association with DAP12. KIR2DL1^{I233K} mutant however, could be potentially of use for investigating the clustering-mediated enhancement of signalling capacity. However, results involving this receptor would be obscured by that it can be likely involved in both inhibitory and activating signalling. Although the ability of KIR2DL1^{I233K} to form complexes with DAP12 was not investigated here, previous studies suggested that only the lysine residue at position 9 in transmembrane region is sufficient to trigger association with DAP12, even when all other residues are substituted with leucine residues [346]. Although not ideal, one way to overcome this issue could be to investigate this receptor function in DAP12-deficient cell lines, i.e. Jurkat. Importantly, wild-type KIR2DL1 and KIR2DL1 ^{I233K} are expressed at different levels at the surface of Jurkat cells and this problem would crucially have to be addressed before any conclusions regarding the receptor function could be drawn.

Large KIR clusters seem to be preferentially involved in signal transduction due to more frequent association with membrane-proximal signalling molecules. This is suggested by the experiments specifically analysing the interactions of KIR2DL1 and SHP-1 and KIR2DS1 and ZAP-70. The logical next step would be to analyse the positions of other signalling molecules in relation to KIR clusters of different sizes. This seems exceptionally important for KIR2DS1, for which downstream signalling pathway includes multiple proteins of different functions. Specifically, Syk family kinases and LAT protein seem to be important targets for the future imaging studies. Such experiments would lead to deeper understanding of how the multicomponent signalling

complexes are assembled during the signal transduction. The ultimate goal would be to establish how the molecular events following ligation of receptors truly relate to what is often pictured as sequential interactions of multiple cytoplasmic proteins.

Chapter 6: Conclusions

6.1 Overview

As part of our innate immune system, NK cells are able to kill target cells without prior priming and therefore, their activity has to be tightly controlled. Indeed, NK cells do not rely on one dominant activating receptor like T cells or B cells, but instead are controlled by combined signals from multiple activating and inhibitory receptors. However, how the signals from multiple receptors are integrated and translated into an appropriate response is poorly understood. Application of imaging studies to probe NK cell contacts with target cells has demonstrated that the outcome of interaction is not only governed by the quantity of receptor-ligand interactions, but is also affected by the specific organization of surface molecules. Advances in the field of microscopy have later established that such interplay between the receptors organization and activity can occur on different scales and includes formation of immune synapse, which typically occupies tens of micrometres, as well as assembly of receptors into smaller structures. More recently, super-resolution microscopy enabled the observation of nanometre-scale clusters or receptors, which are constitutively present at the surface of NK cells and other immune cells. Immune receptor nanoclusters were often found to undergo changes under different stated of immune cell activation, which has drawn the attention to their possible role in signalling. However, to the date very little is known about how such clusters are formed and whether or not they are important for the regulation of NK cells activity. Experiments presented in this thesis aimed to narrow this gap in the knowledge by studying the nanometre-scale clustering of NK cell receptors KIR2DL1 and KIR2DS1. To summarize briefly, this investigation has established that:

- KIR2DL1 and KIR2DS1 display differential organization patters at the surface of NK cells, with an activating receptor forming larger and denser clusters.
- Formation of bigger clusters by KIR2DS1 is linked to the presence of lysine residue at position 233 in amino-acid sequence.
- Bigger clusters of KIR2DL1 and KIR2DS1 are more often found in contact with clusters of downstream signalling molecules and these molecules are more often phosphorylated in the proximity of bigger KIR clusters. Larger area of clusters can account for this effect by promoting the interactions with

independently distributed clusters of membrane-proximal signalling molecules in resting cells and upon KIR ligation.

6.2 Potential significance of distinct clustering patterns of KIR2DL1 and KIR2DS1

Since assembly of receptors into bigger clusters seems to promote KIR2DL1 and KIR2DS1 signalling via similar mechanisms, it is intriguing why these two receptors would display such strikingly different patterns of organization at the surface of resting NK cells. Specifically, if bigger clusters are more efficient at transducing the signal – why would KIR2DL1 form clusters significantly smaller than KIR2DS1?

One reason for this difference could be that activating signalling pathways in NK cells are considerably more complex than those downstream the inhibitory receptors. First, activating receptors are commonly devoid of signalling motifs and rely on the association with adaptor molecules Thus, to initiate the signal, the receptors and cognate adaptors have to be in contact. Second, signalling pathways downstream of activating NK cell receptors are known to be complicated and involve multiplicity of kinases, scaffold proteins and adaptor proteins [144]. In contrast, inhibitory receptors act via activation of SHP-1, which is believed to then target the membrane proximal components of activating signalling cascade [115]. Therefore, it seems possible that activating receptor clusters would have to be bigger in order to form enough interactions with adaptor molecule clusters and also increase the probability that more of the downstream signalling components will be present in the immediate vicinity of the cluster and therefore can be engaged and activated immediately upon ligation. In light of this idea, it is interesting to note that the same lysine 233 residue that facilitates interaction of KIR2DS1 with DAP12 is also responsible for this receptor forming bigger and denser clusters.

An alternative reason could be that KIR2DL1 has evolved to achieve an optimal degree of inhibition rather than the maximum possible. It cannot be excluded that formation of bigger clusters by KIR2DL1 could facilitate too extensive interaction between the receptor and SHP-1. In turn, even low densities of inhibitory ligands could trigger very strong inhibitory signal, which couldn't be overcome easily enough in a situation when activating ligands are presented at the surface of the same target cell. In other words, limiting the size of KIR2DL1 clusters could be important for tuning the NK cell responsiveness.

6.3 The role for receptor clustering in NK cell signalling

The link between formation of clusters and signal transduction was first suggested by a number of reports describing changes in receptor organization upon activation of immune cells. The precise role for nanoclusters, however, was not understood, although it was generally considered that they could serve as 'signalling platforms'.

The current views of immune cells signalling often assume that downstream signalling molecules are actively recruited to the receptors after the specific ligand is encountered. However, some pools of intracellular signalling molecules are constitutively present in the vicinity of the membrane, such as demonstrated in this study for SHP-1 and ZAP-70. Although they most likely do not form specific interactions with non-ligated receptors, clusters of receptors, signalling adaptors and downstream molecules can form stochastic contacts in resting cells. Therefore, it seems feasible that upon receptor ligation, the multicomponent signalling complex can be most efficiently formed by engaging the closest localized signalling components than by recruiting the molecules from other parts of cytoplasm. This could mean that efficiency of assembling the molecular complex in the vicinity of a particular receptor cluster would depend on this cluster remaining in contact with signalling components already prior to ligation. Such scenario is supported by the experiments showing that increased size of KIR clusters promotes their contacts with ZAP-70 and SHP-1 clusters, as revealed by super-resolution imaging, and does it to exactly the same extent as can be expected in the situation when clusters of signalling molecules are distributed randomly.

The molecular model for NK cell receptor signalling proposed here assumes that engaging of the most proximal signalling components would be the most efficient and fast way to initiate the signalling. Thus, it would mean that at the onset of signalling, the pools of signalling proteins constitutively present at the plasma membrane play a crucial role. Active recruitment of signalling components to the membrane, which is part of the response to the receptors ligation, most likely occurs after the initial threshold for productive signalling has been already reached. Therefore, newly recruited pools of downstream molecules might be more important for maintenance and propagation of the signal.

In summary, it seems likely that the model in which larger area of clusters accounts for forming more contacts with downstream signalling components and in turn, controls the likelihood of their activation, could apply to the responses of diverse receptors. In support of this, results presented in this thesis indicate that for both inhibitory KIR2DL1

and activating KIR2DS1, assembly into bigger clusters might promote the signalling via similar mechanisms.

6.4 Closing remarks

The work presented in this thesis has shown that nanometre-scale organization of NK cell receptors and other signalling molecules is yet another factor that adds to the complexity of NK cell signalling. As demonstrated here by the example of inhibitory receptor KIR2DL1 and activating receptor KIR2DS1, NK cell receptors display distinct patterns of clustering on nanometre scale. Importantly, these patterns of organization seem to be important for the receptors association with downstream signalling molecules, and consequently, affect the signal transduction upon ligation. To fully comprehend the link between the nanometre-scale organization of membrane proteins and regulation of NK cell activity, further studies are necessary. These should concentrate on correlating the imaging techniques used in this study with other approaches to investigate the functional effects of receptors clustering and its changes. In conclusion, the results presented in this work highlight the need for multidisciplinary studies investigating the biology of immune cells.

References

1. Kiessling, R., E. Klein, and H. Wigzell, *"Natural" killer cells in the mouse. I. Cytotoxic cells with specificity for mouse Moloney leukemia cells. Specificity and distribution according to genotype.* Eur J Immunol, 1975. **5**(2): p. 112-7.
2. Herberman, R.B., M.E. Nunn, and D.H. Lavrin, *Natural cytotoxic reactivity of mouse lymphoid cells against syngeneic acid allogeneic tumors. I. Distribution of reactivity and specificity.* Int J Cancer, 1975. **16**(2): p. 216-29.
3. Galy, A., et al., *Human T, B, natural killer, and dendritic cells arise from a common bone marrow progenitor cell subset.* Immunity, 1995. **3**(4): p. 459-73.
4. Huntington, N.D., C.A. Vosshenrich, and J.P. Di Santo, *Developmental pathways that generate natural-killer-cell diversity in mice and humans.* Nat Rev Immunol, 2007. **7**(9): p. 703-14.
5. Blum, K.S. and R. Pabst, *Lymphocyte numbers and subsets in the human blood. Do they mirror the situation in all organs?* Immunol Lett, 2007. **108**(1): p. 45-51.
6. Ritz, J., et al., *Characterization of functional surface structures on human natural killer cells.* Adv Immunol, 1988. **42**: p. 181-211.
7. Sivori, S., et al., *p46, a novel natural killer cell-specific surface molecule that mediates cell activation.* J Exp Med, 1997. **186**(7): p. 1129-36.
8. Fogler, W.E., et al., *NK cell infiltration into lung, liver, and subcutaneous B16 melanoma is mediated by VCAM-1/VLA-4 interaction.* J Immunol, 1996. **156**(12): p. 4707-14.
9. Glas, R., et al., *Recruitment and activation of natural killer (NK) cells in vivo determined by the target cell phenotype. An adaptive component of NK cell-mediated responses.* J Exp Med, 2000. **191**(1): p. 129-38.
10. Orange, J.S., *Human natural killer cell deficiencies.* Curr Opin Allergy Clin Immunol, 2006. **6**(6): p. 399-409.
11. Lunemann, S., et al., *Compromised function of natural killer cells in acute and chronic viral hepatitis.* J Infect Dis, 2014. **209**(9): p. 1362-73.
12. Alter, G., et al., *HIV-1 adaptation to NK-cell-mediated immune pressure.* Nature, 2011. **476**(7358): p. 96-100.
13. Alter, G., et al., *Differential natural killer cell-mediated inhibition of HIV-1 replication based on distinct KIR/HLA subtypes.* J Exp Med, 2007. **204**(12): p. 3027-36.
14. Leung, K.N. and G.L. Ada, *Induction of natural killer cells during murine influenza virus infection.* Immunobiology, 1981. **160**(3-4): p. 352-66.
15. Stein-Streilein, J. and J. Guffee, *In vivo treatment of mice and hamsters with antibodies to asialo GM1 increases morbidity and mortality to pulmonary influenza infection.* J Immunol, 1986. **136**(4): p. 1435-41.
16. Azeredo, E.L., et al., *NK cells, displaying early activation, cytotoxicity and adhesion molecules, are associated with mild dengue disease.* Clin Exp Immunol, 2006. **143**(2): p. 345-56.
17. Marquardt, N., et al., *The Human NK Cell Response to Yellow Fever Virus 17D Is Primarily Governed by NK Cell Differentiation Independently of NK Cell Education.* J Immunol, 2015. **195**(7): p. 3262-72.
18. Daniels, K.A., et al., *Murine cytomegalovirus is regulated by a discrete subset of natural killer cells reactive with monoclonal antibody to Ly49H.* J Exp Med, 2001. **194**(1): p. 29-44.
19. Bodduluru, L.N., et al., *Natural killer cells: the journey from puzzles in biology to treatment of cancer.* Cancer Lett, 2015. **357**(2): p. 454-67.
20. Wu, J. and L.L. Lanier, *Natural killer cells and cancer.* Adv Cancer Res, 2003. **90**: p. 127-56.

21. Waldhauer, I. and A. Steinle, *NK cells and cancer immunosurveillance.* Oncogene, 2008. **27**(45): p. 5932-43.
22. Smyth, M.J., N.Y. Crowe, and D.I. Godfrey, *NK cells and NKT cells collaborate in host protection from methylcholanthrene-induced fibrosarcoma.* Int Immunol, 2001. **13**(4): p. 459-63.
23. Smyth, M.J., et al., *New aspects of natural-killer-cell surveillance and therapy of cancer.* Nat Rev Cancer, 2002. **2**(11): p. 850-61.
24. Shankaran, V., et al., *IFNgamma and lymphocytes prevent primary tumour development and shape tumour immunogenicity.* Nature, 2001. **410**(6832): p. 1107-11.
25. Imai, K., et al., *Natural cytotoxic activity of peripheral-blood lymphocytes and cancer incidence: an 11-year follow-up study of a general population.* Lancet, 2000. **356**(9244): p. 1795-9.
26. Poirot, L., C. Benoist, and D. Mathis, *Natural killer cells distinguish innocuous and destructive forms of pancreatic islet autoimmunity.* Proc Natl Acad Sci U S A, 2004. **101**(21): p. 8102-7.
27. Alba, A., et al., *Natural killer cells are required for accelerated type 1 diabetes driven by interferon-beta.* Clin Exp Immunol, 2008. **151**(3): p. 467-75.
28. Dotta, F., et al., *Coxsackie B4 virus infection of beta cells and natural killer cell insulitis in recent-onset type 1 diabetic patients.* Proc Natl Acad Sci U S A, 2007. **104**(12): p. 5115-20.
29. Erkeller-Yusel, F., et al., *Lymphocyte subsets in a large cohort of patients with systemic lupus erythematosus.* Lupus, 1993. **2**(4): p. 227-31.
30. Erkeller-Yuksel, F.M., P.M. Lydyard, and D.A. Isenberg, *Lack of NK cells in lupus patients with renal involvement.* Lupus, 1997. **6**(9): p. 708-12.
31. Hervier, B., et al., *Phenotype and function of natural killer cells in systemic lupus erythematosus: excess interferon-gamma production in patients with active disease.* Arthritis Rheum, 2011. **63**(6): p. 1698-706.
32. Park, Y.W., et al., *Impaired differentiation and cytotoxicity of natural killer cells in systemic lupus erythematosus.* Arthritis Rheum, 2009. **60**(6): p. 1753-63.
33. Oliviero, B., et al., *Natural killer cell functional dichotomy in chronic hepatitis B and chronic hepatitis C virus infections.* Gastroenterology, 2009. **137**(3): p. 1151-60, 1160 e1-7.
34. Tatsumi, T. and T. Takehara, *Impact of NK cells on chronic hepatitis C and hepatocellular carcinoma.* Hepatol Res, 2015.
35. Ni, Z., et al., *Expression of chimeric receptor CD4zeta by natural killer cells derived from human pluripotent stem cells improves in vitro activity but does not enhance suppression of HIV infection in vivo.* Stem Cells, 2014. **32**(4): p. 1021-31.
36. Zhen, A., et al., *HIV-specific Immunity Derived From Chimeric Antigen Receptor-engineered Stem Cells.* Mol Ther, 2015. **23**(8): p. 1358-67.
37. Rosario, M., et al., *The IL-15-Based ALT-803 Complex Enhances FcgammaRIIIa-Triggered NK Cell Responses and In Vivo Clearance of B Cell Lymphomas.* Clin Cancer Res, 2015.
38. Sconocchia, G., et al., *NK cells and T cells cooperate during the clinical course of colorectal cancer.* Oncoimmunology, 2014. **3**(8): p. e952197.
39. Semeraro, M., et al., *Natural killer cell mediated immunosurveillance of pediatric neuroblastoma.* Oncoimmunology, 2015. **4**(11): p. e1042202.
40. Jiang, W., et al., *hIL-15 gene-modified human natural killer cells (NKL-IL15) augments the anti-human hepatocellular carcinoma effect in vivo.* Immunobiology, 2014. **219**(7): p. 547-53.
41. Knorr, D.A. and D.S. Kaufman, *Pluripotent stem cell-derived natural killer cells for cancer therapy.* Transl Res, 2010. **156**(3): p. 147-54.

42. Colucci, F. and C.M. Cilio, *Taming killer cells may halt diabetes progression.* Nat Immunol, 2010. **11**(2): p. 111-2.
43. Lanier, L.L., et al., *The relationship of CD16 (Leu-11) and Leu-19 (NKH-1) antigen expression on human peripheral blood NK cells and cytotoxic T lymphocytes.* J Immunol, 1986. **136**(12): p. 4480-6.
44. Cooper, M.A., et al., *Human natural killer cells: a unique innate immunoregulatory role for the CD56(bright) subset.* Blood, 2001. **97**(10): p. 3146-51.
45. Fehniger, T.A., et al., *CD56bright natural killer cells are present in human lymph nodes and are activated by T cell-derived IL-2: a potential new link between adaptive and innate immunity.* Blood, 2003. **101**(8): p. 3052-7.
46. Monks, C.R., et al., *Three-dimensional segregation of supramolecular activation clusters in T cells.* Nature, 1998. **395**(6697): p. 82-6.
47. Davis, D.M., et al., *The human natural killer cell immune synapse.* Proc Natl Acad Sci U S A, 1999. **96**(26): p. 15062-7.
48. Dustin, M.L., et al., *A novel adaptor protein orchestrates receptor patterning and cytoskeletal polarity in T-cell contacts.* Cell, 1998. **94**(5): p. 667-77.
49. Liu, D., et al., *Integrin-dependent organization and bidirectional vesicular traffic at cytotoxic immune synapses.* Immunity, 2009. **31**(1): p. 99-109.
50. Stinchcombe, J.C., et al., *The immunological synapse of CTL contains a secretory domain and membrane bridges.* Immunity, 2001. **15**(5): p. 751-61.
51. Stinchcombe, J.C., et al., *Centriole polarisation to the immunological synapse directs secretion from cytolytic cells of both the innate and adaptive immune systems.* BMC Biol, 2011. **9**: p. 45.
52. Mentlik, A.N., et al., *Rapid lytic granule convergence to the MTOC in natural killer cells is dependent on dynein but not cytolytic commitment.* Mol Biol Cell, 2010. **21**(13): p. 2241-56.
53. Campi, G., R. Varma, and M.L. Dustin, *Actin and agonist MHC-peptide complex-dependent T cell receptor microclusters as scaffolds for signaling.* J Exp Med, 2005. **202**(8): p. 1031-6.
54. Orange, J.S., et al., *The mature activating natural killer cell immunologic synapse is formed in distinct stages.* Proc Natl Acad Sci U S A, 2003. **100**(24): p. 14151-6.
55. Rak, G.D., et al., *Natural killer cell lytic granule secretion occurs through a pervasive actin network at the immune synapse.* PLoS Biol, 2011. **9**(9): p. e1001151.
56. Brown, A.C., et al., *Remodelling of cortical actin where lytic granules dock at natural killer cell immune synapses revealed by super-resolution microscopy.* PLoS Biol, 2011. **9**(9): p. e1001152.
57. Liu, D., et al., *Two modes of lytic granule fusion during degranulation by natural killer cells.* Immunol Cell Biol, 2011. **89**(6): p. 728-38.
58. Cohnen, A., et al., *Surface CD107a/LAMP-1 protects natural killer cells from degranulation-associated damage.* Blood, 2013. **122**(8): p. 1411-8.
59. Lopez, J.A., et al., *Perforin forms transient pores on the target cell plasma membrane to facilitate rapid access of granzymes during killer cell attack.* Blood, 2013. **121**(14): p. 2659-68.
60. Thiery, J., et al., *Perforin activates clathrin- and dynamin-dependent endocytosis, which is required for plasma membrane repair and delivery of granzyme B for granzyme-mediated apoptosis.* Blood, 2010. **115**(8): p. 1582-93.
61. Bossi, G. and G.M. Griffiths, *Degranulation plays an essential part in regulating cell surface expression of Fas ligand in T cells and natural killer cells.* Nat Med, 1999. **5**(1): p. 90-6.
62. Johnsen, A.C., et al., *Regulation of APO-2 ligand/trail expression in NK cells-involvement in NK cell-mediated cytotoxicity.* Cytokine, 1999. **11**(9): p. 664-72.

63. Fauriat, C., et al., *Regulation of human NK-cell cytokine and chemokine production by target cell recognition.* Blood, 2010. **115**(11): p. 2167-76.
64. Fehniger, T.A., et al., *Differential cytokine and chemokine gene expression by human NK cells following activation with IL-18 or IL-15 in combination with IL-12: implications for the innate immune response.* J Immunol, 1999. **162**(8): p. 4511-20.
65. Wolk, K., et al., *Cutting edge: immune cells as sources and targets of the IL-10 family members?* J Immunol, 2002. **168**(11): p. 5397-402.
66. Street, S.E., E. Cretney, and M.J. Smyth, *Perforin and interferon-gamma activities independently control tumor initiation, growth, and metastasis.* Blood, 2001. **97**(1): p. 192-7.
67. Snijders, A., et al., *High-level IL-12 production by human dendritic cells requires two signals.* Int Immunol, 1998. **10**(11): p. 1593-8.
68. Gerosa, F., et al., *Reciprocal activating interaction between natural killer cells and dendritic cells.* J Exp Med, 2002. **195**(3): p. 327-33.
69. Adam, C., et al., *DC-NK cell cross talk as a novel CD4+ T-cell-independent pathway for antitumor CTL induction.* Blood, 2005. **106**(1): p. 338-44.
70. Anfossi, N., et al., *Human NK cell education by inhibitory receptors for MHC class I.* Immunity, 2006. **25**(2): p. 331-42.
71. Arstila, T.P., et al., *A direct estimate of the human alphabeta T cell receptor diversity.* Science, 1999. **286**(5441): p. 958-61.
72. Karre, K., et al., *Selective rejection of H-2-deficient lymphoma variants suggests alternative immune defence strategy.* Nature, 1986. **319**(6055): p. 675-8.
73. Ljunggren, H.G. and K. Karre, *In search of the 'missing self': MHC molecules and NK cell recognition.* Immunol Today, 1990. **11**(7): p. 237-44.
74. Karlhofer, F.M., R.K. Ribaudo, and W.M. Yokoyama, *MHC class I alloantigen specificity of Ly-49+ IL-2-activated natural killer cells.* Nature, 1992. **358**(6381): p. 66-70.
75. Colonna, M. and J. Samaridis, *Cloning of immunoglobulin-superfamily members associated with HLA-C and HLA-B recognition by human natural killer cells.* Science, 1995. **268**(5209): p. 405-8.
76. Wagtmann, N., et al., *Molecular clones of the p58 NK cell receptor reveal immunoglobulin-related molecules with diversity in both the extra- and intracellular domains.* Immunity, 1995. **2**(5): p. 439-49.
77. Correa, I., L. Corral, and D.H. Raulet, *Multiple natural killer cell-activating signals are inhibited by major histocompatibility complex class I expression in target cells.* Eur J Immunol, 1994. **24**(6): p. 1323-31.
78. Garni-Wagner, B.A., et al., *A novel function-associated molecule related to non-MHC-restricted cytotoxicity mediated by activated natural killer cells and T cells.* J Immunol, 1993. **151**(1): p. 60-70.
79. Mandelboim, O., et al., *Recognition of haemagglutinins on virus-infected cells by NKp46 activates lysis by human NK cells.* Nature, 2001. **409**(6823): p. 1055-60.
80. Garg, A., et al., *Vimentin expressed on Mycobacterium tuberculosis-infected human monocytes is involved in binding to the NKp46 receptor.* J Immunol, 2006. **177**(9): p. 6192-8.
81. Jarahian, M., et al., *Activation of natural killer cells by newcastle disease virus hemagglutinin-neuraminidase.* J Virol, 2009. **83**(16): p. 8108-21.
82. Rosental, B., et al., *Proliferating cell nuclear antigen is a novel inhibitory ligand for the natural cytotoxicity receptor NKp44.* J Immunol, 2011. **187**(11): p. 5693-702.
83. Arnon, T.I., et al., *Inhibition of the NKp30 activating receptor by pp65 of human cytomegalovirus.* Nat Immunol, 2005. **6**(5): p. 515-23.

84. Pogge von Strandmann, E., et al., *Human leukocyte antigen-B-associated transcript 3 is released from tumor cells and engages the NKp30 receptor on natural killer cells.* Immunity, 2007. **27**(6): p. 965-74.
85. Brandt, C.S., et al., *The B7 family member B7-H6 is a tumor cell ligand for the activating natural killer cell receptor NKp30 in humans.* J Exp Med, 2009. **206**(7): p. 1495-503.
86. Bahram, S., et al., *Nucleotide sequence of the human MHC class I MICA gene.* Immunogenetics, 1996. **44**(1): p. 80-1.
87. Bahram, S. and T. Spies, *Nucleotide sequence of a human MHC class I MICB cDNA.* Immunogenetics, 1996. **43**(4): p. 230-3.
88. Cosman, D., et al., *ULBPs, novel MHC class I-related molecules, bind to CMV glycoprotein UL16 and stimulate NK cytotoxicity through the NKG2D receptor.* Immunity, 2001. **14**(2): p. 123-33.
89. Eagle, R.A., et al., *ULBP6/RAET1L is an additional human NKG2D ligand.* Eur J Immunol, 2009. **39**(11): p. 3207-16.
90. Vivier, E., et al., *Structure and function of the CD16:zeta:gamma complex expressed on human natural-killer cells.* Int J Cancer Suppl, 1992. **7**: p. 11-4.
91. Nakajima, H., et al., *Activating interactions in human NK cell recognition: the role of 2B4-CD48.* Eur J Immunol, 1999. **29**(5): p. 1676-83.
92. Braud, V.M., et al., *HLA-E binds to natural killer cell receptors CD94/NKG2A, B and C.* Nature, 1998. **391**(6669): p. 795-9.
93. Borrego, F., et al., *Recognition of human histocompatibility leukocyte antigen (HLA)-E complexed with HLA class I signal sequence-derived peptides by CD94/NKG2 confers protection from natural killer cell-mediated lysis.* J Exp Med, 1998. **187**(5): p. 813-8.
94. Bottino, C., et al., *Identification of PVR (CD155) and Nectin-2 (CD112) as cell surface ligands for the human DNAM-1 (CD226) activating molecule.* J Exp Med, 2003. **198**(4): p. 557-67.
95. Stanietsky, N., et al., *The interaction of TIGIT with PVR and PVRL2 inhibits human NK cell cytotoxicity.* Proc Natl Acad Sci U S A, 2009. **106**(42): p. 17858-63.
96. Fuchs, A., et al., *Cutting edge: CD96 (tactile) promotes NK cell-target cell adhesion by interacting with the poliovirus receptor (CD155).* J Immunol, 2004. **172**(7): p. 3994-8.
97. Moretta, A., et al., *Existence of both inhibitory (p58) and activatory (p50) receptors for HLA-C molecules in human natural killer cells.* J Exp Med, 1995. **182**(3): p. 875-84.
98. Samaridis, J. and M. Colonna, *Cloning of novel immunoglobulin superfamily receptors expressed on human myeloid and lymphoid cells: structural evidence for new stimulatory and inhibitory pathways.* Eur J Immunol, 1997. **27**(3): p. 660-5.
99. Lepin, E.J., et al., *Functional characterization of HLA-F and binding of HLA-F tetramers to ILT2 and ILT4 receptors.* Eur J Immunol, 2000. **30**(12): p. 3552-61.
100. Rosen, D.B., et al., *Cutting edge: lectin-like transcript-1 is a ligand for the inhibitory human NKR-P1A receptor.* J Immunol, 2005. **175**(12): p. 7796-9.
101. Ito, M., et al., *Killer cell lectin-like receptor G1 binds three members of the classical cadherin family to inhibit NK cell cytotoxicity.* J Exp Med, 2006. **203**(2): p. 289-95.
102. Lebbink, R.J., et al., *Collagens are functional, high affinity ligands for the inhibitory immune receptor LAIR-1.* J Exp Med, 2006. **203**(6): p. 1419-25.
103. Parham, P., *Influence of KIR diversity on human immunity.* Adv Exp Med Biol, 2005. **560**: p. 47-50.
104. Vance, R.E., et al., *Mouse CD94/NKG2A is a natural killer cell receptor for the nonclassical major histocompatibility complex (MHC) class I molecule Qa-1(b).* J Exp Med, 1998. **188**(10): p. 1841-8.
105. Cosman, D., et al., *A novel immunoglobulin superfamily receptor for cellular and viral MHC class I molecules.* Immunity, 1997. **7**(2): p. 273-82.

106. Vitale, M., et al., *The leukocyte Ig-like receptor (LIR)-1 for the cytomegalovirus UL18 protein displays a broad specificity for different HLA class I alleles: analysis of LIR-1 + NK cell clones.* Int Immunol, 1999. **11**(1): p. 29-35.
107. Long, E.O., *Negative signaling by inhibitory receptors: the NK cell paradigm.* Immunol Rev, 2008. **224**: p. 70-84.
108. Daeron, M., et al., *Immunoreceptor tyrosine-based inhibition motifs: a quest in the past and future.* Immunol Rev, 2008. **224**: p. 11-43.
109. Burshtyn, D.N., et al., *Recruitment of tyrosine phosphatase HCP by the killer cell inhibitor receptor.* Immunity, 1996. **4**(1): p. 77-85.
110. Burshtyn, D.N., et al., *Conserved residues amino-terminal of cytoplasmic tyrosines contribute to the SHP-1-mediated inhibitory function of killer cell Ig-like receptors.* J Immunol, 1999. **162**(2): p. 897-902.
111. Fry, A.M., L.L. Lanier, and A. Weiss, *Phosphotyrosines in the killer cell inhibitory receptor motif of NKB1 are required for negative signaling and for association with protein tyrosine phosphatase 1C.* J Exp Med, 1996. **184**(1): p. 295-300.
112. Bruhns, P., et al., *Differential roles of N- and C-terminal immunoreceptor tyrosine-based inhibition motifs during inhibition of cell activation by killer cell inhibitory receptors.* J Immunol, 1999. **162**(6): p. 3168-75.
113. Gupta, N., et al., *Negative signaling pathways of the killer cell inhibitory receptor and Fc gamma RIIb1 require distinct phosphatases.* J Exp Med, 1997. **186**(3): p. 473-8.
114. Hof, P., et al., *Crystal structure of the tyrosine phosphatase SHP-2.* Cell, 1998. **92**(4): p. 441-50.
115. Stebbins, C.C., et al., *Vav1 dephosphorylation by the tyrosine phosphatase SHP-1 as a mechanism for inhibition of cellular cytotoxicity.* Mol Cell Biol, 2003. **23**(17): p. 6291-9.
116. Graham, D.B., et al., *Vav1 controls DAP10-mediated natural cytotoxicity by regulating actin and microtubule dynamics.* J Immunol, 2006. **177**(4): p. 2349-55.
117. Vitale, M., et al., *NKp44, a novel triggering surface molecule specifically expressed by activated natural killer cells, is involved in non-major histocompatibility complex-restricted tumor cell lysis.* J Exp Med, 1998. **187**(12): p. 2065-72.
118. Pende, D., et al., *Identification and molecular characterization of NKp30, a novel triggering receptor involved in natural cytotoxicity mediated by human natural killer cells.* J Exp Med, 1999. **190**(10): p. 1505-16.
119. Kruse, P.H., et al., *Natural cytotoxicity receptors and their ligands.* Immunol Cell Biol, 2014. **92**(3): p. 221-9.
120. Joyce, M.G. and P.D. Sun, *The structural basis of ligand recognition by natural killer cell receptors.* J Biomed Biotechnol, 2011. **2011**: p. 203628.
121. Esin, S., et al., *Functional characterization of human natural killer cells responding to Mycobacterium bovis bacille Calmette-Guerin.* Immunology, 2004. **112**(1): p. 143-52.
122. Wu, W., et al., *Regulation of apoptosis by Bat3-enhanced YWK-II/APLP2 protein stability.* J Cell Sci, 2012. **125**(Pt 18): p. 4219-29.
123. Bauer, S., et al., *Activation of NK cells and T cells by NKG2D, a receptor for stress-inducible MICA.* Science, 1999. **285**(5428): p. 727-9.
124. Pende, D., et al., *Major histocompatibility complex class I-related chain A and UL16-binding protein expression on tumor cell lines of different histotypes: analysis of tumor susceptibility to NKG2D-dependent natural killer cell cytotoxicity.* Cancer Res, 2002. **62**(21): p. 6178-86.
125. Smyth, M.J., et al., *NKG2D function protects the host from tumor initiation.* J Exp Med, 2005. **202**(5): p. 583-8.
126. Guerra, N., et al., *NKG2D-deficient mice are defective in tumor surveillance in models of spontaneous malignancy.* Immunity, 2008. **28**(4): p. 571-80.

127. Wu, J., et al., *DAP10 and DAP12 form distinct, but functionally cooperative, receptor complexes in natural killer cells.* J Exp Med, 2000. **192**(7): p. 1059-68.
128. Wu, J., et al., *An activating immunoreceptor complex formed by NKG2D and DAP10.* Science, 1999. **285**(5428): p. 730-2.
129. Seyfizadeh, N., et al., *A molecular perspective on rituximab: A monoclonal antibody for B cell non Hodgkin lymphoma and other affections.* Crit Rev Oncol Hematol, 2016. **97**: p. 275-90.
130. Feugier, P., *A review of rituximab, the first anti-CD20 monoclonal antibody used in the treatment of B non-Hodgkin's lymphomas.* Future Oncol, 2015. **11**(9): p. 1327-42.
131. Clynes, R.A., et al., *Inhibitory Fc receptors modulate in vivo cytotoxicity against tumor targets.* Nat Med, 2000. **6**(4): p. 443-6.
132. Cartron, G., et al., *Therapeutic activity of humanized anti-CD20 monoclonal antibody and polymorphism in IgG Fc receptor FcgammaRIIIa gene.* Blood, 2002. **99**(3): p. 754-8.
133. Parolini, S., et al., *X-linked lymphoproliferative disease. 2B4 molecules displaying inhibitory rather than activating function are responsible for the inability of natural killer cells to kill Epstein-Barr virus-infected cells.* J Exp Med, 2000. **192**(3): p. 337-46.
134. Latour, S., et al., *Binding of SAP SH2 domain to FynT SH3 domain reveals a novel mechanism of receptor signalling in immune regulation.* Nat Cell Biol, 2003. **5**(2): p. 149-54.
135. Dong, Z., et al., *The adaptor SAP controls NK cell activation by regulating the enzymes Vav-1 and SHIP-1 and by enhancing conjugates with target cells.* Immunity, 2012. **36**(6): p. 974-85.
136. Latour, S., et al., *Regulation of SLAM-mediated signal transduction by SAP, the X-linked lymphoproliferative gene product.* Nat Immunol, 2001. **2**(8): p. 681-90.
137. Eissmann, P., et al., *Molecular basis for positive and negative signaling by the natural killer cell receptor 2B4 (CD244).* Blood, 2005. **105**(12): p. 4722-9.
138. Waggoner, S.N., et al., *Absence of mouse 2B4 promotes NK cell-mediated killing of activated CD8+ T cells, leading to prolonged viral persistence and altered pathogenesis.* J Clin Invest, 2010. **120**(6): p. 1925-38.
139. Colucci, F., J.P. Di Santo, and P.J. Leibson, *Natural killer cell activation in mice and men: different triggers for similar weapons?* Nat Immunol, 2002. **3**(9): p. 807-13.
140. Vely, F. and E. Vivier, *Natural killer cell receptor signaling pathway in mammals.* Sci STKE, 2005. **2005**(292): p. cm7.
141. Jiang, K., et al., *Pivotal role of phosphoinositide-3 kinase in regulation of cytotoxicity in natural killer cells.* Nat Immunol, 2000. **1**(5): p. 419-25.
142. Cella, M., et al., *Differential requirements for Vav proteins in DAP10- and ITAM-mediated NK cell cytotoxicity.* J Exp Med, 2004. **200**(6): p. 817-23.
143. Billadeau, D.D., et al., *NKG2D-DAP10 triggers human NK cell-mediated killing via a Syk-independent regulatory pathway.* Nat Immunol, 2003. **4**(6): p. 557-64.
144. Vivier, E., J.A. Nunes, and F. Vely, *Natural killer cell signaling pathways.* Science, 2004. **306**(5701): p. 1517-9.
145. Bryceson, Y.T., et al., *Synergy among receptors on resting NK cells for the activation of natural cytotoxicity and cytokine secretion.* Blood, 2006. **107**(1): p. 159-66.
146. Bryceson, Y.T., H.G. Ljunggren, and E.O. Long, *Minimal requirement for induction of natural cytotoxicity and intersection of activation signals by inhibitory receptors.* Blood, 2009. **114**(13): p. 2657-66.
147. Brown, A.C., et al., *Super-resolution imaging of remodeled synaptic actin reveals different synergies between NK cell receptors and integrins.* Blood, 2012. **120**(18): p. 3729-40.
148. Valiante, N.M., et al., *Functionally and structurally distinct NK cell receptor repertoires in the peripheral blood of two human donors.* Immunity, 1997. **7**(6): p. 739-51.

149. Fernandez, N.C., et al., *A subset of natural killer cells achieves self-tolerance without expressing inhibitory receptors specific for self-MHC molecules.* Blood, 2005. **105**(11): p. 4416-23.
150. Kim, S., et al., *Licensing of natural killer cells by host major histocompatibility complex class I molecules.* Nature, 2005. **436**(7051): p. 709-13.
151. Andersson, S., et al., *KIR acquisition probabilities are independent of self-HLA class I ligands and increase with cellular KIR expression.* Blood, 2009. **114**(1): p. 95-104.
152. Guia, S., et al., *Confinement of activating receptors at the plasma membrane controls natural killer cell tolerance.* Sci Signal, 2011. **4**(167): p. ra21.
153. Thomas, L.M., M.E. Peterson, and E.O. Long, *Cutting edge: NK cell licensing modulates adhesion to target cells.* J Immunol, 2013. **191**(8): p. 3981-5.
154. Forslund, E., et al., *Microchip-Based Single-Cell Imaging Reveals That CD56dimCD57-KIR-NKG2A+ NK Cells Have More Dynamic Migration Associated with Increased Target Cell Conjugation and Probability of Killing Compared to CD56dimCD57-KIR-NKG2A- NK Cells.* J Immunol, 2015. **195**(7): p. 3374-81.
155. Sakisaka, T. and Y. Takai, *Biology and pathology of nectins and nectin-like molecules.* Curr Opin Cell Biol, 2004. **16**(5): p. 513-21.
156. Chan, C.J., M.J. Smyth, and L. Martinet, *Molecular mechanisms of natural killer cell activation in response to cellular stress.* Cell Death Differ, 2014. **21**(1): p. 5-14.
157. Shibuya, A., et al., *DNAM-1, a novel adhesion molecule involved in the cytolytic function of T lymphocytes.* Immunity, 1996. **4**(6): p. 573-81.
158. Stanietsky, N., et al., *Mouse TIGIT inhibits NK-cell cytotoxicity upon interaction with PVR.* Eur J Immunol, 2013. **43**(8): p. 2138-50.
159. Chan, C.J., et al., *The receptors CD96 and CD226 oppose each other in the regulation of natural killer cell functions.* Nat Immunol, 2014. **15**(5): p. 431-8.
160. Castriconi, R., et al., *Natural killer cell-mediated killing of freshly isolated neuroblastoma cells: critical role of DNAX accessory molecule-1-poliovirus receptor interaction.* Cancer Res, 2004. **64**(24): p. 9180-4.
161. Tahara-Hanaoka, S., et al., *Tumor rejection by the poliovirus receptor family ligands of the DNAM-1 (CD226) receptor.* Blood, 2006. **107**(4): p. 1491-6.
162. Liu, S., et al., *Recruitment of Grb2 and SHIP1 by the ITT-like motif of TIGIT suppresses granule polarization and cytotoxicity of NK cells.* Cell Death Differ, 2013. **20**(3): p. 456-64.
163. Li, M., et al., *T-cell immunoglobulin and ITIM domain (TIGIT) receptor/poliovirus receptor (PVR) ligand engagement suppresses interferon-gamma production of natural killer cells via beta-arrestin 2-mediated negative signaling.* J Biol Chem, 2014. **289**(25): p. 17647-57.
164. Brooks, A.G., et al., *NKG2A complexed with CD94 defines a novel inhibitory natural killer cell receptor.* J Exp Med, 1997. **185**(4): p. 795-800.
165. Carretero, M., et al., *Specific engagement of the CD94/NKG2-A killer inhibitory receptor by the HLA-E class Ib molecule induces SHP-1 phosphatase recruitment to tyrosine-phosphorylated NKG2-A: evidence for receptor function in heterologous transfectants.* Eur J Immunol, 1998. **28**(4): p. 1280-91.
166. Lanier, L.L., et al., *Association of DAP12 with activating CD94/NKG2C NK cell receptors.* Immunity, 1998. **8**(6): p. 693-701.
167. Beziat, V., et al., *CMV drives clonal expansion of NKG2C+ NK cells expressing self-specific KIRs in chronic hepatitis patients.* Eur J Immunol, 2012. **42**(2): p. 447-57.
168. Guma, M., et al., *Expansion of CD94/NKG2C+ NK cells in response to human cytomegalovirus-infected fibroblasts.* Blood, 2006. **107**(9): p. 3624-31.
169. Stewart, C.A., et al., *Recognition of peptide-MHC class I complexes by activating killer immunoglobulin-like receptors.* Proc Natl Acad Sci U S A, 2005. **102**(37): p. 13224-9.

170. Sivori, S., et al., *Natural killer cells expressing the KIR2DS1-activating receptor efficiently kill T-cell blasts and dendritic cells: implications in haploidentical HSCT.* Blood, 2011. **117**(16): p. 4284-92.
171. Graef, T., et al., *KIR2DS4 is a product of gene conversion with KIR3DL2 that introduced specificity for HLA-A*11 while diminishing avidity for HLA-C.* J Exp Med, 2009. **206**(11): p. 2557-72.
172. Martinet, L. and M.J. Smyth, *Balancing natural killer cell activation through paired receptors.* Nat Rev Immunol, 2015. **15**(4): p. 243-54.
173. Stanietsky, N. and O. Mandelboim, *Paired NK cell receptors controlling NK cytotoxicity.* FEBS Lett, 2010. **584**(24): p. 4895-900.
174. Harel-Bellan, A., et al., *Natural killer susceptibility of human cells may be regulated by genes in the HLA region on chromosome 6.* Proc Natl Acad Sci U S A, 1986. **83**(15): p. 5688-92.
175. Moretta, A., et al., *A novel surface antigen expressed by a subset of human CD3- CD16+ natural killer cells. Role in cell activation and regulation of cytolytic function.* J Exp Med, 1990. **171**(3): p. 695-714.
176. Wilson, M.J., et al., *Plasticity in the organization and sequences of human KIR/ILT gene families.* Proc Natl Acad Sci U S A, 2000. **97**(9): p. 4778-83.
177. Trowsdale, J., et al., *The genomic context of natural killer receptor extended gene families.* Immunol Rev, 2001. **181**: p. 20-38.
178. Vilches, C., C.M. Gardiner, and P. Parham, *Gene structure and promoter variation of expressed and nonexpressed variants of the KIR2DL5 gene.* J Immunol, 2000. **165**(11): p. 6416-21.
179. Selvakumar, A., et al., *Genomic organization and allelic polymorphism of the human killer cell inhibitory receptor gene KIR103.* Tissue Antigens, 1997. **49**(6): p. 564-73.
180. Dohring, C., J. Samaridis, and M. Colonna, *Alternatively spliced forms of human killer inhibitory receptors.* Immunogenetics, 1996. **44**(3): p. 227-30.
181. Torkar, M., et al., *Isotypic variation of novel immunoglobulin-like transcript/killer cell inhibitory receptor loci in the leukocyte receptor complex.* Eur J Immunol, 1998. **28**(12): p. 3959-67.
182. Uhrberg, M., et al., *Human diversity in killer cell inhibitory receptor genes.* Immunity, 1997. **7**(6): p. 753-63.
183. Jiang, W., et al., *Copy number variation leads to considerable diversity for B but not A haplotypes of the human KIR genes encoding NK cell receptors.* Genome Res, 2012. **22**(10): p. 1845-54.
184. Hsu, K.C., et al., *Killer Ig-like receptor haplotype analysis by gene content: evidence for genomic diversity with a minimum of six basic framework haplotypes, each with multiple subsets.* J Immunol, 2002. **169**(9): p. 5118-29.
185. Shilling, H.G., et al., *Allelic polymorphism synergizes with variable gene content to individualize human KIR genotype.* J Immunol, 2002. **168**(5): p. 2307-15.
186. Norman, P.J., et al., *Distribution of natural killer cell immunoglobulin-like receptor sequences in three ethnic groups.* Immunogenetics, 2001. **52**(3-4): p. 195-205.
187. Witt, C.S., et al., *Population frequencies and putative haplotypes of the killer cell immunoglobulin-like receptor sequences and evidence for recombination.* Transplantation, 1999. **68**(11): p. 1784-9.
188. Gardiner, C.M., et al., *Different NK cell surface phenotypes defined by the DX9 antibody are due to KIR3DL1 gene polymorphism.* J Immunol, 2001. **166**(5): p. 2992-3001.
189. Selvakumar, A., U. Steffens, and B. Dupont, *Polymorphism and domain variability of human killer cell inhibitory receptors.* Immunol Rev, 1997. **155**: p. 183-96.
190. Fan, Q.R., E.O. Long, and D.C. Wiley, *Crystal structure of the human natural killer cell inhibitory receptor KIR2DL1-HLA-Cw4 complex.* Nat Immunol, 2001. **2**(5): p. 452-60.

191. Fan, Q.R., et al., *Structure of the inhibitory receptor for human natural killer cells resembles haematopoietic receptors.* Nature, 1997. **389**(6646): p. 96-100.
192. Boyington, J.C., et al., *Crystal structure of an NK cell immunoglobulin-like receptor in complex with its class I MHC ligand.* Nature, 2000. **405**(6786): p. 537-43.
193. Lanier, L.L., et al., *Immunoreceptor DAP12 bearing a tyrosine-based activation motif is involved in activating NK cells.* Nature, 1998. **391**(6668): p. 703-7.
194. Albert, E.D., et al., *Nomenclature for factors of the HLA system, 2002.* Tissue Antigens, 2002. **60**(5): p. 407-464.
195. Marsh, S.G., et al., *Killer-cell immunoglobulin-like receptor (KIR) nomenclature report, 2002.* Hum Immunol, 2003. **64**(6): p. 648-54.
196. Biassoni, R., et al., *Amino acid substitutions can influence the natural killer (NK)-mediated recognition of HLA-C molecules. Role of serine-77 and lysine-80 in the target cell protection from lysis mediated by "group 2" or "group 1" NK clones.* J Exp Med, 1995. **182**(2): p. 605-9.
197. Winter, C.C. and E.O. Long, *A single amino acid in the p58 killer cell inhibitory receptor controls the ability of natural killer cells to discriminate between the two groups of HLA-C allotypes.* J Immunol, 1997. **158**(9): p. 4026-8.
198. Biassoni, R., et al., *Role of amino acid position 70 in the binding affinity of p50.1 and p58.1 receptors for HLA-Cw4 molecules.* Eur J Immunol, 1997. **27**(12): p. 3095-9.
199. Moretta, A., et al., *P58 molecules as putative receptors for major histocompatibility complex (MHC) class I molecules in human natural killer (NK) cells. Anti-p58 antibodies reconstitute lysis of MHC class I-protected cells in NK clones displaying different specificities.* J Exp Med, 1993. **178**(2): p. 597-604.
200. Colonna, M., et al., *HLA-C is the inhibitory ligand that determines dominant resistance to lysis by NK1- and NK2-specific natural killer cells.* Proc Natl Acad Sci U S A, 1993. **90**(24): p. 12000-4.
201. Moesta, A.K., et al., *Synergistic polymorphism at two positions distal to the ligand-binding site makes KIR2DL2 a stronger receptor for HLA-C than KIR2DL3.* J Immunol, 2008. **180**(6): p. 3969-79.
202. Moesta, A.K. and P. Parham, *Diverse functionality among human NK cell receptors for the C1 epitope of HLA-C: KIR2DS2, KIR2DL2, and KIR2DL3.* Front Immunol, 2012. **3**: p. 336.
203. Liu, J., et al., *Activating killer cell immunoglobulin-like receptor 2DS2 binds to HLA-A*11.* Proc Natl Acad Sci U S A, 2014. **111**(7): p. 2662-7.
204. Ciccone, E., et al., *Involvement of HLA class I alleles in natural killer (NK) cell-specific functions: expression of HLA-Cw3 confers selective protection from lysis by alloreactive NK clones displaying a defined specificity (specificity 2).* J Exp Med, 1992. **176**(4): p. 963-71.
205. Rajagopalan, S. and E.O. Long, *A human histocompatibility leukocyte antigen (HLA)-G-specific receptor expressed on all natural killer cells.* J Exp Med, 1999. **189**(7): p. 1093-100.
206. Rajagopalan, S., et al., *Activation of NK cells by an endocytosed receptor for soluble HLA-G.* PLoS Biol, 2006. **4**(1): p. e9.
207. Le Page, M.E., et al., *Killer Ig-like receptor 2DL4 does not mediate NK cell IFN-gamma responses to soluble HLA-G preparations.* J Immunol, 2014. **192**(2): p. 732-40.
208. Thananchai, H., et al., *Cutting Edge: Allele-specific and peptide-dependent interactions between KIR3DL1 and HLA-A and HLA-B.* J Immunol, 2007. **178**(1): p. 33-7.
209. Cella, M., et al., *NK3-specific natural killer cells are selectively inhibited by Bw4-positive HLA alleles with isoleucine 80.* J Exp Med, 1994. **180**(4): p. 1235-42.

210. Gumperz, J.E., et al., *The Bw4 public epitope of HLA-B molecules confers reactivity with natural killer cell clones that express NKB1, a putative HLA receptor.* J Exp Med, 1995. **181**(3): p. 1133-44.
211. Pende, D., et al., *The natural killer cell receptor specific for HLA-A allotypes: a novel member of the p58/p70 family of inhibitory receptors that is characterized by three immunoglobulin-like domains and is expressed as a 140-kD disulphide-linked dimer.* J Exp Med, 1996. **184**(2): p. 505-18.
212. Hansasuta, P., et al., *Recognition of HLA-A3 and HLA-A11 by KIR3DL2 is peptide-specific.* Eur J Immunol, 2004. **34**(6): p. 1673-9.
213. Kollnberger, S., et al., *Cell-surface expression and immune receptor recognition of HLA-B27 homodimers.* Arthritis Rheum, 2002. **46**(11): p. 2972-82.
214. Goodridge, J.P., et al., *HLA-F and MHC class I open conformers are ligands for NK cell Ig-like receptors.* J Immunol, 2013. **191**(7): p. 3553-62.
215. Mandelboim, O., et al., *Enhancement of class II-restricted T cell responses by costimulatory NK receptors for class I MHC proteins.* Science, 1996. **274**(5295): p. 2097-100.
216. Arase, H., et al., *Direct recognition of cytomegalovirus by activating and inhibitory NK cell receptors.* Science, 2002. **296**(5571): p. 1323-6.
217. Rajagopalan, S. and E.O. Long, *The direct binding of a p58 killer cell inhibitory receptor to human histocompatibility leukocyte antigen (HLA)-Cw4 exhibits peptide selectivity.* J Exp Med, 1997. **185**(8): p. 1523-8.
218. Fadda, L., et al., *Peptide antagonism as a mechanism for NK cell activation.* Proc Natl Acad Sci U S A, 2010. **107**(22): p. 10160-5.
219. Deng, L., et al., *Molecular architecture of the major histocompatibility complex class I-binding site of Ly49 natural killer cell receptors.* J Biol Chem, 2008. **283**(24): p. 16840-9.
220. Vales-Gomez, M., et al., *Kinetics of interaction of HLA-C ligands with natural killer cell inhibitory receptors.* Immunity, 1998. **9**(3): p. 337-44.
221. Almeida, C.R. and D.M. Davis, *Segregation of HLA-C from ICAM-1 at NK cell immune synapses is controlled by its cell surface density.* J Immunol, 2006. **177**(10): p. 6904-10.
222. Vitale, M., et al., *Negative signalling via the P58/NKR for HLA.C alleles.* Eur J Histochem, 1994. **38 Suppl 1**: p. 69-76.
223. Biassoni, R., et al., *The human leukocyte antigen (HLA)-C-specific "activatory" or "inhibitory" natural killer cell receptors display highly homologous extracellular domains but differ in their transmembrane and intracytoplasmic portions.* J Exp Med, 1996. **183**(2): p. 645-50.
224. Pageon, S.V., et al., *Superresolution microscopy reveals nanometer-scale reorganization of inhibitory natural killer cell receptors upon activation of NKG2D.* Sci Signal, 2013. **6**(285): p. ra62.
225. Feuchtinger, T., et al., *Cytolytic activity of NK cell clones against acute childhood precursor-B-cell leukaemia is influenced by HLA class I expression on blasts and the differential KIR phenotype of NK clones.* Bone Marrow Transplant, 2009. **43**(11): p. 875-81.
226. Almeida, C.R., et al., *Human NK cells differ more in their KIR2DL1-dependent thresholds for HLA-Cw6-mediated inhibition than in their maximal killing capacity.* PLoS One, 2011. **6**(9): p. e24927.
227. Mandelboim, O., et al., *Natural killer activating receptors trigger interferon gamma secretion from T cells and natural killer cells.* Proc Natl Acad Sci U S A, 1998. **95**(7): p. 3798-803.
228. Pittari, G., et al., *NK cell tolerance of self-specific activating receptor KIR2DS1 in individuals with cognate HLA-C2 ligand.* J Immunol, 2013. **190**(9): p. 4650-60.

229. Vales-Gomez, M., et al., *Differential binding to HLA-C of p50-activating and p58-inhibitory natural killer cell receptors.* Proc Natl Acad Sci U S A, 1998. **95**(24): p. 14326-31.
230. Watzl, C., C.C. Stebbins, and E.O. Long, *NK cell inhibitory receptors prevent tyrosine phosphorylation of the activation receptor 2B4 (CD244).* J Immunol, 2000. **165**(7): p. 3545-8.
231. Abeyweera, T.P., E. Merino, and M. Huse, *Inhibitory signaling blocks activating receptor clustering and induces cytoskeletal retraction in natural killer cells.* J Cell Biol, 2011. **192**(4): p. 675-90.
232. Liu, D., M.E. Peterson, and E.O. Long, *The adaptor protein Crk controls activation and inhibition of natural killer cells.* Immunity, 2012. **36**(4): p. 600-11.
233. Bari, R., et al., *Significant functional heterogeneity among KIR2DL1 alleles and a pivotal role of arginine 245.* Blood, 2009. **114**(25): p. 5182-90.
234. Flores-Villanueva, P.O., et al., *Control of HIV-1 viremia and protection from AIDS are associated with HLA-Bw4 homozygosity.* Proc Natl Acad Sci U S A, 2001. **98**(9): p. 5140-5.
235. Martin, M.P., et al., *Epistatic interaction between KIR3DS1 and HLA-B delays the progression to AIDS.* Nat Genet, 2002. **31**(4): p. 429-34.
236. O'Connor, G.M., et al., *Functional polymorphism of the KIR3DL1/S1 receptor on human NK cells.* J Immunol, 2007. **178**(1): p. 235-41.
237. Carr, W.H., et al., *Cutting Edge: KIR3DS1, a gene implicated in resistance to progression to AIDS, encodes a DAP12-associated receptor expressed on NK cells that triggers NK cell activation.* J Immunol, 2007. **178**(2): p. 647-51.
238. Martin, M.P., et al., *Innate partnership of HLA-B and KIR3DL1 subtypes against HIV-1.* Nat Genet, 2007. **39**(6): p. 733-40.
239. Gaudieri, S., et al., *Killer immunoglobulin-like receptors and HLA act both independently and synergistically to modify HIV disease progression.* Genes Immun, 2005. **6**(8): p. 683-90.
240. Barbour, J.D., et al., *Synergy or independence? Deciphering the interaction of HLA Class I and NK cell KIR alleles in early HIV-1 disease progression.* PLoS Pathog, 2007. **3**(4): p. e43.
241. Khakoo, S.I., et al., *HLA and NK cell inhibitory receptor genes in resolving hepatitis C virus infection.* Science, 2004. **305**(5685): p. 872-4.
242. Venstrom, J.M., et al., *HLA-C-dependent prevention of leukemia relapse by donor activating KIR2DS1.* N Engl J Med, 2012. **367**(9): p. 805-16.
243. Pende, D., et al., *Anti-leukemia activity of alloreactive NK cells in KIR ligand-mismatched haploidentical HSCT for pediatric patients: evaluation of the functional role of activating KIR and redefinition of inhibitory KIR specificity.* Blood, 2009. **113**(13): p. 3119-29.
244. Hsu, K.C., et al., *Improved outcome in HLA-identical sibling hematopoietic stem-cell transplantation for acute myelogenous leukemia predicted by KIR and HLA genotypes.* Blood, 2005. **105**(12): p. 4878-84.
245. Chen, D.F., et al., *Differential impact of inhibitory and activating Killer Ig-Like Receptors (KIR) on high-risk patients with myeloid and lymphoid malignancies undergoing reduced intensity transplantation from haploidentical related donors.* Bone Marrow Transplant, 2012. **47**(6): p. 817-23.
246. Miller, J.S., et al., *Missing KIR ligands are associated with less relapse and increased graft-versus-host disease (GVHD) following unrelated donor allogeneic HCT.* Blood, 2007. **109**(11): p. 5058-61.

247. Hsu, K.C., et al., *KIR ligands and prediction of relapse after unrelated donor hematopoietic cell transplantation for hematologic malignancy.* Biol Blood Marrow Transplant, 2006. **12**(8): p. 828-36.
248. Bari, R., et al., *Effect of donor KIR2DL1 allelic polymorphism on the outcome of pediatric allogeneic hematopoietic stem-cell transplantation.* J Clin Oncol, 2013. **31**(30): p. 3782-90.
249. Moffett, A. and F. Colucci, *Co-evolution of NK receptors and HLA ligands in humans is driven by reproduction.* Immunol Rev, 2015. **267**(1): p. 283-97.
250. Apps, R., et al., *Conformation of human leucocyte antigen-C molecules at the surface of human trophoblast cells.* Immunology, 2008. **124**(3): p. 322-8.
251. Apps, R., et al., *Natural-killer cell ligands at the maternal-fetal interface: UL-16 binding proteins, MHC class-I chain related molecules, HLA-F and CD48.* Hum Reprod, 2008. **23**(11): p. 2535-48.
252. King, A., et al., *Surface expression of HLA-C antigen by human extravillous trophoblast.* Placenta, 2000. **21**(4): p. 376-87.
253. King, A., et al., *HLA-E is expressed on trophoblast and interacts with CD94/NKG2 receptors on decidual NK cells.* Eur J Immunol, 2000. **30**(6): p. 1623-31.
254. Apps, R., et al., *A homodimeric complex of HLA-G on normal trophoblast cells modulates antigen-presenting cells via LILRB1.* Eur J Immunol, 2007. **37**(7): p. 1924-37.
255. King, A., C. Birkby, and Y.W. Loke, *Early human decidual cells exhibit NK activity against the K562 cell line but not against first trimester trophoblast.* Cell Immunol, 1989. **118**(2): p. 337-44.
256. King, A. and Y.W. Loke, *Human trophoblast and JEG choriocarcinoma cells are sensitive to lysis by IL-2-stimulated decidual NK cells.* Cell Immunol, 1990. **129**(2): p. 435-48.
257. Kopcow, H.D., et al., *Human decidual NK cells form immature activating synapses and are not cytotoxic.* Proc Natl Acad Sci U S A, 2005. **102**(43): p. 15563-8.
258. Xiong, S., et al., *Maternal uterine NK cell-activating receptor KIR2DS1 enhances placentation.* J Clin Invest, 2013. **123**(10): p. 4264-72.
259. Hiby, S.E., et al., *Maternal activating KIRs protect against human reproductive failure mediated by fetal HLA-C2.* J Clin Invest, 2010. **120**(11): p. 4102-10.
260. Hiby, S.E., et al., *Association of maternal killer-cell immunoglobulin-like receptors and parental HLA-C genotypes with recurrent miscarriage.* Hum Reprod, 2008. **23**(4): p. 972-6.
261. Hiby, S.E., et al., *Combinations of maternal KIR and fetal HLA-C genes influence the risk of preeclampsia and reproductive success.* J Exp Med, 2004. **200**(8): p. 957-65.
262. Nakimuli, A., et al., *A KIR B centromeric region present in Africans but not Europeans protects pregnant women from pre-eclampsia.* Proc Natl Acad Sci U S A, 2015. **112**(3): p. 845-50.
263. Ozturk, O.G., F.D. Gun, and G. Polat, *Killer cell immunoglobulin-like receptor genes in patients with breast cancer.* Med Oncol, 2012. **29**(2): p. 511-5.
264. Marin, D., et al., *KIR2DS1 genotype predicts for complete cytogenetic response and survival in newly diagnosed chronic myeloid leukemia patients treated with imatinib.* Leukemia, 2012. **26**(2): p. 296-302.
265. Niepieklo-Miniewska, W., et al., *Protective effect of the KIR2DS1 gene in atopic dermatitis.* Gene, 2013. **527**(2): p. 594-600.
266. Hou, Y.F., et al., *Disparate distribution of activating and inhibitory killer cell immunoglobulin-like receptor genes in patients with systemic lupus erythematosus.* Lupus, 2010. **19**(1): p. 20-6.
267. Martin, M.P., et al., *Cutting edge: susceptibility to psoriatic arthritis: influence of activating killer Ig-like receptor genes in the absence of specific HLA-C alleles.* J Immunol, 2002. **169**(6): p. 2818-22.

268. Luszczek, W., et al., *Gene for the activating natural killer cell receptor, KIR2DS1, is associated with susceptibility to psoriasis vulgaris.* Hum Immunol, 2004. **65**(7): p. 758-66.
269. Davidovits, P. and M.D. Egger, *Scanning laser microscope.* Nature, 1969. **223**(5208): p. 831.
270. Davidovi.P and M.D. Egger, *Scanning Laser Microscope for Biological Investigations.* Applied Optics, 1971. **10**(7): p. 1615-&.
271. Borg, C., et al., *NK cell activation by dendritic cells (DCs) requires the formation of a synapse leading to IL-12 polarization in DCs.* Blood, 2004. **104**(10): p. 3267-75.
272. Nedvetzki, S., et al., *Reciprocal regulation of human natural killer cells and macrophages associated with distinct immune synapses.* Blood, 2007. **109**(9): p. 3776-85.
273. Krzewski, K., et al., *Formation of a WIP-, WASp-, actin-, and myosin IIA-containing multiprotein complex in activated NK cells and its alteration by KIR inhibitory signaling.* J Cell Biol, 2006. **173**(1): p. 121-32.
274. Masilamani, M., et al., *CD94/NKG2A inhibits NK cell activation by disrupting the actin network at the immunological synapse.* J Immunol, 2006. **177**(6): p. 3590-6.
275. Lagrue, K., et al., *The central role of the cytoskeleton in mechanisms and functions of the NK cell immune synapse.* Immunol Rev, 2013. **256**(1): p. 203-21.
276. Eriksson, M., et al., *Inhibitory receptors alter natural killer cell interactions with target cells yet allow simultaneous killing of susceptible targets.* J Exp Med, 1999. **190**(7): p. 1005-12.
277. Freiberg, B.A., et al., *Staging and resetting T cell activation in SMACs.* Nat Immunol, 2002. **3**(10): p. 911-7.
278. Treanor, B., et al., *Microclusters of inhibitory killer immunoglobulin-like receptor signaling at natural killer cell immunological synapses.* J Cell Biol, 2006. **174**(1): p. 153-61.
279. Kohler, K., et al., *Matched sizes of activating and inhibitory receptor/ligand pairs are required for optimal signal integration by human natural killer cells.* PLoS One, 2010. **5**(11): p. e15374.
280. Bryceson, Y.T., et al., *Cytolytic granule polarization and degranulation controlled by different receptors in resting NK cells.* J Exp Med, 2005. **202**(7): p. 1001-12.
281. Cartwright, A.N., J. Griggs, and D.M. Davis, *The immune synapse clears and excludes molecules above a size threshold.* Nat Commun, 2014. **5**: p. 5479.
282. Tschopp, J., D. Masson, and S. Schafer, *Inhibition of the lytic activity of perforin by lipoproteins.* J Immunol, 1986. **137**(6): p. 1950-3.
283. Axelrod, D., *Cell-substrate contacts illuminated by total internal reflection fluorescence.* J Cell Biol, 1981. **89**(1): p. 141-5.
284. Axelrod, D., *Total internal reflection fluorescence microscopy.* Methods Cell Biol, 1989. **30**: p. 245-70.
285. Bunnell, S.C., et al., *T cell receptor ligation induces the formation of dynamically regulated signaling assemblies.* J Cell Biol, 2002. **158**(7): p. 1263-75.
286. Harwood, N.E. and F.D. Batista, *The cytoskeleton coordinates the early events of B-cell activation.* Cold Spring Harb Perspect Biol, 2011. **3**(2).
287. Kaizuka, Y., et al., *Mechanisms for segregating T cell receptor and adhesion molecules during immunological synapse formation in Jurkat T cells.* Proc Natl Acad Sci U S A, 2007. **104**(51): p. 20296-301.
288. Bastiaens, P.I. and A. Squire, *Fluorescence lifetime imaging microscopy: spatial resolution of biochemical processes in the cell.* Trends Cell Biol, 1999. **9**(2): p. 48-52.
289. Wu, P. and L. Brand, *Resonance energy transfer: methods and applications.* Anal Biochem, 1994. **218**(1): p. 1-13.

290. Betzig, E., et al., *Imaging intracellular fluorescent proteins at nanometer resolution.* Science, 2006. **313**(5793): p. 1642-5.
291. Hess, S.T., T.P. Girirajan, and M.D. Mason, *Ultra-high resolution imaging by fluorescence photoactivation localization microscopy.* Biophys J, 2006. **91**(11): p. 4258-72.
292. Manley, S., et al., *High-density mapping of single-molecule trajectories with photoactivated localization microscopy.* Nat Methods, 2008. **5**(2): p. 155-7.
293. Owen, D.M., et al., *Optical techniques for imaging membrane domains in live cells (live-cell palm of protein clustering).* Methods Enzymol, 2012. **504**: p. 221-35.
294. MacGillavry, H.D. and T.A. Blanpied, *Single-Molecule Tracking Photoactivated Localization Microscopy to Map Nano-Scale Structure and Dynamics in Living Spines.* Curr Protoc Neurosci, 2013. **2**(220): p. 2.20.1-2.20.19.
295. Baumann, S., et al., *Live cell imaging of endosomal trafficking in fungi.* Methods Mol Biol, 2015. **1270**: p. 347-63.
296. Rust, M.J., M. Bates, and X. Zhuang, *Sub-diffraction-limit imaging by stochastic optical reconstruction microscopy (STORM).* Nat Methods, 2006. **3**(10): p. 793-5.
297. Bates, M., et al., *Multicolor super-resolution imaging with photo-switchable fluorescent probes.* Science, 2007. **317**(5845): p. 1749-53.
298. Huang, B., et al., *Whole-cell 3D STORM reveals interactions between cellular structures with nanometer-scale resolution.* Nat Methods, 2008. **5**(12): p. 1047-52.
299. Heilemann, M., et al., *Subdiffraction-resolution fluorescence imaging with conventional fluorescent probes.* Angew Chem Int Ed Engl, 2008. **47**(33): p. 6172-6.
300. Jones, S.A., et al., *Fast, three-dimensional super-resolution imaging of live cells.* Nat Methods, 2011. **8**(6): p. 499-508.
301. Kohl, J., et al., *Ultrafast tissue staining with chemical tags.* Proc Natl Acad Sci U S A, 2014. **111**(36): p. E3805-14.
302. Hell, S.W. and J. Wichmann, *Breaking the diffraction resolution limit by stimulated emission: stimulated-emission-depletion fluorescence microscopy.* Opt Lett, 1994. **19**(11): p. 780-2.
303. Gottfert, F., et al., *Coaligned dual-channel STED nanoscopy and molecular diffusion analysis at 20 nm resolution.* Biophys J, 2013. **105**(1): p. L01-3.
304. Donnert, G., et al., *Macromolecular-scale resolution in biological fluorescence microscopy.* Proc Natl Acad Sci U S A, 2006. **103**(31): p. 11440-5.
305. Donnert, G., et al., *Two-color far-field fluorescence nanoscopy.* Biophys J, 2007. **92**(8): p. L67-9.
306. Lukinavicius, G., et al., *Fluorogenic probes for live-cell imaging of the cytoskeleton.* Nat Methods, 2014. **11**(7): p. 731-3.
307. Schamel, W.W., et al., *Coexistence of multivalent and monovalent TCRs explains high sensitivity and wide range of response.* J Exp Med, 2005. **202**(4): p. 493-503.
308. Lillemeier, B.F., et al., *TCR and Lat are expressed on separate protein islands on T cell membranes and concatenate during activation.* Nat Immunol, 2010. **11**(1): p. 90-6.
309. Sherman, E., et al., *Functional nanoscale organization of signaling molecules downstream of the T cell antigen receptor.* Immunity, 2011. **35**(5): p. 705-20.
310. Williamson, D.J., et al., *Pre-existing clusters of the adaptor Lat do not participate in early T cell signaling events.* Nat Immunol, 2011. **12**(7): p. 655-62.
311. Sherman, E., V. Barr, and L.E. Samelson, *Super-resolution characterization of TCR-dependent signaling clusters.* Immunol Rev, 2013. **251**(1): p. 21-35.
312. Mattila, P.K., et al., *The actin and tetraspanin networks organize receptor nanoclusters to regulate B cell receptor-mediated signaling.* Immunity, 2013. **38**(3): p. 461-74.

313. Maity, P.C., et al., *B cell antigen receptors of the IgM and IgD classes are clustered in different protein islands that are altered during B cell activation.* Sci Signal, 2015. **8**(394): p. ra93.
314. Mace, E.M. and J.S. Orange, *Lytic immune synapse function requires filamentous actin deconstruction by Coronin 1A.* Proc Natl Acad Sci U S A, 2014. **111**(18): p. 6708-13.
315. Robertson, M.J., et al., *Characterization of a cell line, NKL, derived from an aggressive human natural killer cell leukemia.* Exp Hematol, 1996. **24**(3): p. 406-15.
316. Shimizu, Y., et al., *Transfer and expression of three cloned human non-HLA-A,B,C class I major histocompatibility complex genes in mutant lymphoblastoid cells.* Proc Natl Acad Sci U S A, 1988. **85**(1): p. 227-31.
317. Fauriat, C., et al., *Education of human natural killer cells by activating killer cell immunoglobulin-like receptors.* Blood, 2010. **115**(6): p. 1166-74.
318. Falco, M., et al., *Combined genotypic and phenotypic killer cell Ig-like receptor analyses reveal KIR2DL3 alleles displaying unexpected monoclonal antibody reactivity: identification of the amino acid residues critical for staining.* J Immunol, 2010. **185**(1): p. 433-41.
319. Verschueren, H., *Interference reflection microscopy in cell biology: methodology and applications.* J Cell Sci, 1985. **75**: p. 279-301.
320. Vicidomini, G., et al., *STED nanoscopy with time-gated detection: theoretical and experimental aspects.* PLoS One, 2013. **8**(1): p. e54421.
321. Ovesny, M., et al., *ThunderSTORM: a comprehensive ImageJ plug-in for PALM and STORM data analysis and super-resolution imaging.* Bioinformatics, 2014. **30**(16): p. 2389-90.
322. Sage, D., et al., *Quantitative evaluation of software packages for single-molecule localization microscopy.* Nat Methods, 2015. **12**(8): p. 717-24.
323. Izeddin, I., et al., *Wavelet analysis for single molecule localization microscopy.* Opt Express, 2012. **20**(3): p. 2081-95.
324. Thompson, R.E., D.R. Larson, and W.W. Webb, *Precise nanometer localization analysis for individual fluorescent probes.* Biophys J, 2002. **82**(5): p. 2775-83.
325. Stallinga, S. and B. Rieger, *Accuracy of the gaussian point spread function model in 2D localization microscopy.* Opt Express, 2010. **18**(24): p. 24461-76.
326. Smith, C.S., et al., *Fast, single-molecule localization that achieves theoretically minimum uncertainty.* Nat Methods, 2010. **7**(5): p. 373-5.
327. Huang, F., et al., *Simultaneous multiple-emitter fitting for single molecule super-resolution imaging.* Biomed Opt Express, 2011. **2**(5): p. 1377-93.
328. Mlodzianoski, M.J., et al., *Sample drift correction in 3D fluorescence photoactivation localization microscopy.* Opt Express, 2011. **19**(16): p. 15009-19.
329. Perry, G.L.W., *SpPack: spatial point pattern analysis in Excel using Visual Basic for Applications (VBA).* Environmental Modelling & Software, 2004. **19**(6): p. 559-569.
330. Soares, H., et al., *Regulated vesicle fusion generates signaling nanoterritories that control T cell activation at the immunological synapse.* J Exp Med, 2013. **210**(11): p. 2415-33.
331. Manders, E.M., et al., *Dynamics of three-dimensional replication patterns during the S-phase, analysed by double labelling of DNA and confocal microscopy.* J Cell Sci, 1992. **103 (Pt 3)**: p. 857-62.
332. Torreno-Pina, J.A., et al., *Enhanced receptor-clathrin interactions induced by N-glycan-mediated membrane micropatterning.* Proc Natl Acad Sci U S A, 2014. **111**(30): p. 11037-42.
333. Kumar, S., et al., *A single amino acid change in inhibitory killer cell Ig-like receptor results in constitutive receptor self-association and phosphorylation.* J Immunol, 2015. **194**(2): p. 817-26.

334. Culley, F.J., et al., *Natural killer cell signal integration balances synapse symmetry and migration.* PLoS Biol, 2009. **7**(7): p. e1000159.
335. Ripley, B.D., *Modeling Spatial Patterns.* Journal of the Royal Statistical Society Series B-Methodological, 1977. **39**(2): p. 172-212.
336. Getis, A. and J. Franklin, *Second-Order Neighborhood Analysis of Mapped Point Patterns.* Ecology, 1987. **68**(3): p. 473-477.
337. Hayley, M., S. Bourbigot, and V. Booth, *Self-association of an activating natural killer cell receptor, KIR2DS1.* PLoS One, 2011. **6**(8): p. e23052.
338. Valitutti, S., et al., *Serial triggering of many T-cell receptors by a few peptide-MHC complexes.* Nature, 1995. **375**(6527): p. 148-51.
339. Saka, S.K., et al., *Multi-protein assemblies underlie the mesoscale organization of the plasma membrane.* Nat Commun, 2014. **5**: p. 4509.
340. Tavano, R., et al., *CD28 interaction with filamin-A controls lipid raft accumulation at the T-cell immunological synapse.* Nat Cell Biol, 2006. **8**(11): p. 1270-6.
341. Kusumi, A., et al., *Single-molecule tracking of membrane molecules: plasma membrane compartmentalization and dynamic assembly of raft-philic signaling molecules.* Semin Immunol, 2005. **17**(1): p. 3-21.
342. Mulrooney, T.J., P.E. Posch, and C.K. Hurley, *DAP12 impacts trafficking and surface stability of killer immunoglobulin-like receptors on natural killer cells.* J Leukoc Biol, 2013. **94**(2): p. 301-13.
343. Gutgemann, S.A., et al., *Recruitment of activating NK-cell receptors 2B4 and NKG2D to membrane microdomains in mammalian cells is dependent on their transmembrane regions.* Eur J Immunol, 2015. **45**(4): p. 1258-69.
344. VandenBussche, C.J., et al., *Dramatically reduced surface expression of NK cell receptor KIR2DS3 is attributed to multiple residues throughout the molecule.* Genes Immun, 2009. **10**(2): p. 162-73.
345. Trundley, A., et al., *Allelic expression patterns of KIR3DS1 and 3DL1 using the Z27 and DX9 antibodies.* Eur J Immunol, 2007. **37**(3): p. 780-7.
346. Feng, J., M.E. Call, and K.W. Wucherpfennig, *The assembly of diverse immune receptors is focused on a polar membrane-embedded interaction site.* PLoS Biol, 2006. **4**(5): p. e142.
347. Hessa, T., et al., *Recognition of transmembrane helices by the endoplasmic reticulum translocon.* Nature, 2005. **433**(7024): p. 377-81.
348. Yang, J. and M. Reth, *Oligomeric organization of the B-cell antigen receptor on resting cells.* Nature, 2010. **467**(7314): p. 465-9.
349. Kumar, R., et al., *Increased sensitivity of antigen-experienced T cells through the enrichment of oligomeric T cell receptor complexes.* Immunity, 2011. **35**(3): p. 375-87.
350. Di Bartolo, V., et al., *Tyrosine 319, a newly identified phosphorylation site of ZAP-70, plays a critical role in T cell antigen receptor signaling.* J Biol Chem, 1999. **274**(10): p. 6285-94.
351. Zhang, Z., et al., *The role of C-terminal tyrosine phosphorylation in the regulation of SHP-1 explored via expressed protein ligation.* J Biol Chem, 2003. **278**(7): p. 4668-74.

Appendix 1: Sequence alignment for KIR2DL1 and KIR2DS1 alleles used in this study.

In other sections of this thesis numbering of amino-acid positions excludes the leader peptide.

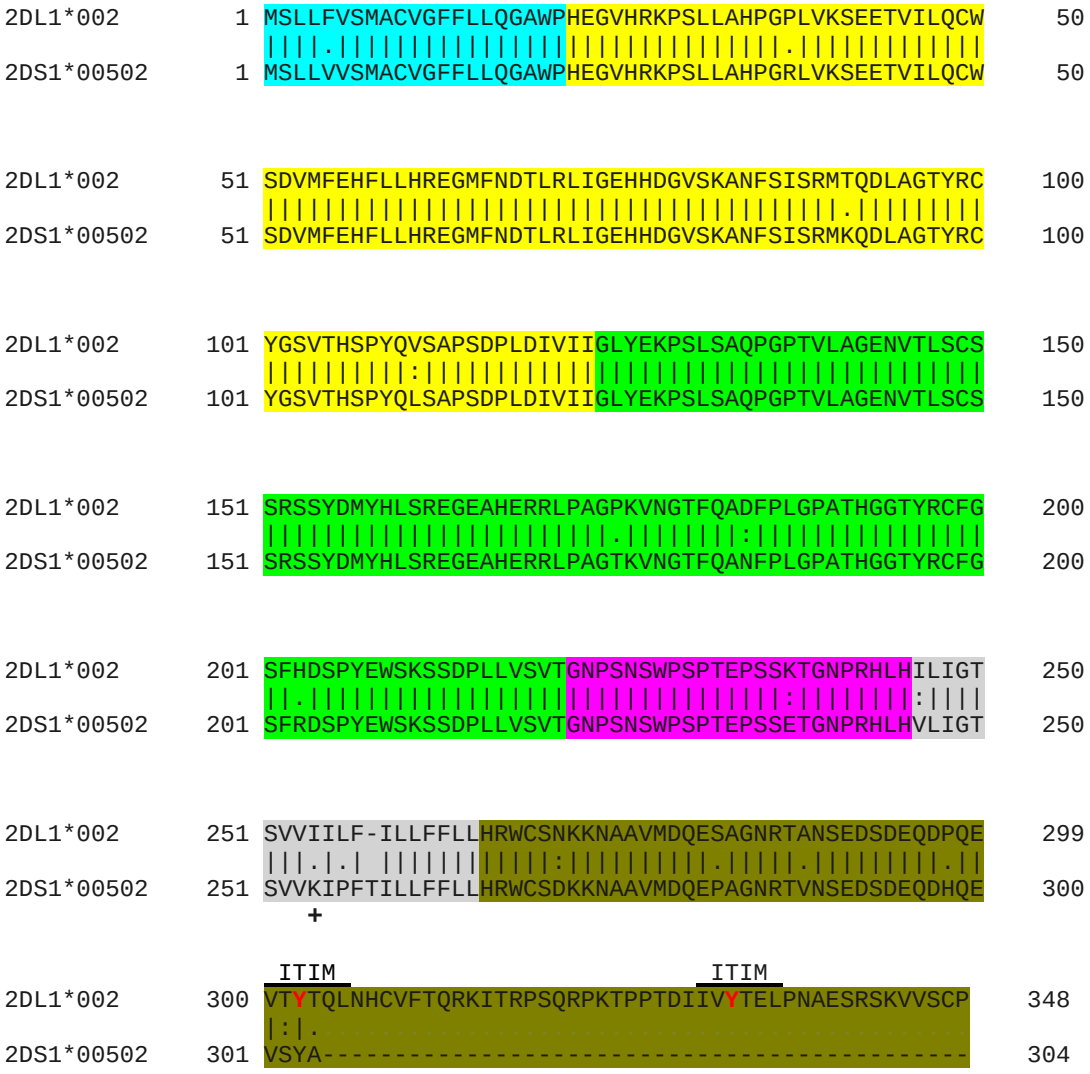

\+ Position 254 (233 in numbering excluding signal peptide):
Lysine in KIR2DS1 WT and KIR2DL1^{I233K}
Alanine in KIR2DS1^{K233A}
Arginine in KIR2DS1^{K233R}
Isoleucine in KIR2DL1 WT

ITIM Positions of ITIMs in KIR2DL1 sequence
Tyrosines marked in **red** are substituted with alanines in KIR2DL1$^{Y281A/Y311A}$